A comparative analysis of Purkinje cells across species combining modelling, machine learning, and information theory

Submitted to the University of Hertfordshire in partial fulfilment
of the requirements of the degree of Doctor of Philosophy

Kirsty Kidd

July 2017

There have been a number of computational modelling studies that aim to replicate the cerebellar Purkinje cell, though these typically use the morphology of rodent cells. While many species, including rodents, display intricate dendritic branching, it is not a universal feature among Purkinje cells. This study uses morphological reconstructions of 24 Purkinje cells from seven species to explore the changes that occur to the cell through evolution and examine whether this has an effect on the processing capacity of the cell. This is achieved by combining several modes of study in order to gain a comprehensive overview of the variations between the cells in both morphology and behaviour.

Passive and active computational models of the cells were created, using the same electrophysiological parameters and ion channels for all models, to characterise the voltage attenuation and electrophysiological behaviour of the cells. These results and several measures of branching and size were then used to look for clusters in the data set using machine learning techniques. They were also used to visualise the differences within each species group. Information theory methods were also employed to compare the estimated information transfer from input to output across each cell.

Along with a literature review into what is known about Purkinje cells and the cerebellum across the phylogenetic tree, these results show that while there are some obvious differences in morphology, the variation within species groups in electrophysiological behaviour is often as high as between them. This suggests that morphological changes may occur in order to conserve behaviour in the face of other changes to the cerebellum.

Contents

Chapter 1

Introduction

Purkinje cells are found in all cerebella, which in turn are found in all vertebrates. Both the cerebellum and the Purkinje cells become more intricate structures as the emergence of the animal becomes more phylogenetically recent, but there are many elements of cerebellar organisation that are consistent from fish through to mammals. These cells have been studied extensively over many years, but much of this research has concerned rodent cerebella, and little has been done to examine other taxa.

This study is intended as a first step in exploring a range of Purkinje cells from different species. This exploration is executed as a comparison of the available cells in three areas: the differences of the form, or morphology of the cells; the electrophysiology of the cells, and the capacity of the cells for information transfer. As a first step, the aim of this study is to find potential functional relationships between morphology and cell behaviour that could be looked at in a larger scale study in the future.

Quantifying the morphology of the neurons begins the exploration. This allows for statistical analysis of the morphology and comparison across the models, as well as the ability to look for correlation between the morphology and electrophysiology. Computational models of neurons were created using morphology files created from digital traces of Purkinje cells and electrophysiological parameters drawn from experimentation to simulate the output of the neurons. These outputs become a quantification of cell behaviour, and can be analysed and compared in the same way as the morphological metrics.

These two steps allow for some analysis of the effect of morphology on the behaviour of Purkinje cells, and which morphological features may have the most influence. The next step is to apply clustering techniques to explore whether the features extracted in the previous steps have strong enough relationships to classify the cells into discrete groups, particularly whether these groups can be divided by species.

Lastly, the output of the cell models can also be analysed to explore the effect of morphological and electrophysiological differences on the information transfer capacity of cells. Using information theoretical techniques, this can also

be quantified and compared across the cells to look for significant differences that could be investigated in more detail in a larger study.

Using the research methods described above, several contributions to the field of computational neuroscience were made. The morphological analysis is very preliminary but indicates that there are trends with phylogenetic rank, particularly in the amount of branching in dendrites.

Modelling with passive parameters revealed that the main difference between species when stimulating different points across the dendritic tree was the maximum amplitude recorded at soma. This correlates with the differences in size between the species groups. Cell size does not correlate with phylogenetic rank, but is statistically distinct for each species. The models with active parameters corroborated with existing research to show that peak amplitude and time to peak is independent from distance to soma in the Purkinje cell, extending these results to the dendritic structures from different species groups used here.

The cluster analysis is also very preliminary, as the sample set is very small. Few clusters were comprised of observations from a single species, but there were species that tended to be clustered together. The species subsets that were found are closely phylogenetically related, suggesting that phylogenetic correlations may be found if the same analysis was performed on a larger dataset.

Finally, the transfer entropy results confirmed estimations that in most cases, the Purkinje cell models require at least 50 synchronous parallel fibre inputs to affect action at the soma. It also indicates that the distance of inputs was also important to how much transfer entropy is calculated.

This dissertation begins with a summary of what is known about the cerebellum in different vertebrate groups. Chapter 2 includes a general overview of the organisation of the cerebellum and Purkinje cell electrophysiology, but a large section is devoted to investigating what is already known about Purkinje cells from different species and how this is expressed in morphology and behaviour.

As a large component of this study is the creation and use of computational models, the next chapter provides some background on how this is achieved. This gives a detailed explanation of compartmental modelling and on the Purkinje cell model created by De Schutter and Bower (1994a) that was the basis of the models used in this study.

The following chapter introduces the Purkinje cells that were digitally traced for use in computational modelling. The methods used to quantify and analyse the morphology of the cells are given here as are the results. These metrics become the morphological component of the clustering analysis that takes place in chapter 6.

Chapter 5 explains the creation of the computational models and the experimentation that the models are used for. The results of these experiments, listed and discussed in this chapter, are also used in the clustering analysis. They make up two feature vectors; one to describe the characteristics of models with passive electrophysiology, and one for models with active electrophysiology.

The clustering analysis is an important aspect of this study, as it offers a chance to look for patterns in the morphological and electrophysiological results across the different cells. The methods of clustering and corresponding results

are discussed here.

Finally, chapter 7 represents a first step into an information theoretical analysis of the Purkinje cell. Some background on the use of information theory is given, as are the methods used to calculate a metric called transfer entropy, which was used to characterise information transfer in each model. This chapter ends with a discussion of the results and comparison between species groups.

These threads are brought together in the final chapter and discussed with the outlook that this work should be a starting point for increased study outside of rodent species.

Chapter 2

Purkinje Cells and the Cerebellum

2.1 Introduction

The subject of this study is the cerebellar Purkinje cell, a key component of cerebellar circuitry across all vertebrate species. The cerebellum has been studied extensively throughout the history of neuroscience, the layout of its circuitry has come to be well understood with developments in preparing and imaging brain tissue. Some elements of cerebellar circuitry were first described very early in the field of neuroscience by the pioneering work of Santiago Ramon y Cajal (Rámon y Cajal, 1911). The existence of some other elements, and the numerousness of elements, have been more recent discoveries as the finesse of neuronal experimentation techniques increased.

This chapter is a summary of the cerebellum, Purkinje cells, and the changes that appear in these structures across evolution. While there has been a long history of studies on Purkinje cells, the majority of studies have been performed on species from a single family of animals. This has lead to a huge amount of information on rodents and very little on any other family, which in turn means there is little comparative work on Purkinje cells or the cerebellum as a whole. This chapter is intended to summarise and compare what is known on the cerebellum of different species.

Section 2.2 is a background on the cerebellum, an important area of the brain that is densely packed with neurons and well-connected to many other brain regions. The following section, 2.3, provides further details on the anatomy and physiology of the Purkinje cell itself. This is followed by Section 2.4, a review of the literature looking at different aspects of the cerebella of different species, in order to make a catalogue of cerebellar features and, where possible, the earliest times these features arose. Finally, these threads are joined and summarised in Section 2.5.
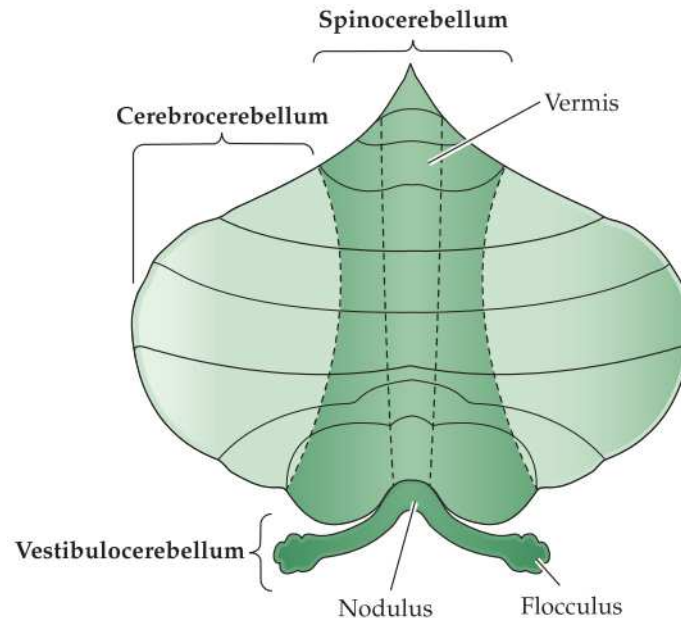
Figure 2.1: Simplified diagram of the cerebellum taken from (Purves et al., 2012). The cerebellar hemispheres (not labelled here) are comprised of the tissue either side of the vermis. In this diagram each hemisphere would include the cerebrocerebellum and a portion of the spinocerebellum.

2.2   Cerebellar Anatomy

The cerebellum has been found to be present in all vertebrates with varying degrees of complexity (Bell, 2002). It is situated in a posterior area of the cranial cavity, close to the brain stem and forming the roof of the fourth ventricle (Llinás et al., 2004). Size can vary greatly, the tight foliation in mammalian cerebella allows for very long structures to be packed into relatively small cavities. The human cerebellum, once unfolded, is over 2m long (Sultan and Bower, 1998).

More advanced vertebrates will display larger, more foliated, cerebella with increased neuronal density and variety. In contrast, the cerebella in amphibians and some fish and reptiles are flat, ovoid structures. In mammals and birds, the larger folds are used to classify ten lobules along the vermis. As other vertebrates tend to have much less foliation, they are divided in other ways (Miyamura and Nakayasu, 2001). The mammalian cerebellar cortex can be most simply described as three distinct areas, the vermis, the hemispheres and the flocculus (see Figure 2.1). The vermis is the central portion of the cerebellum, from which the hemispheres protrude either side of the sagittal plane. The flocculus also protrudes from each side, but is separate from the main hemispheres. For all
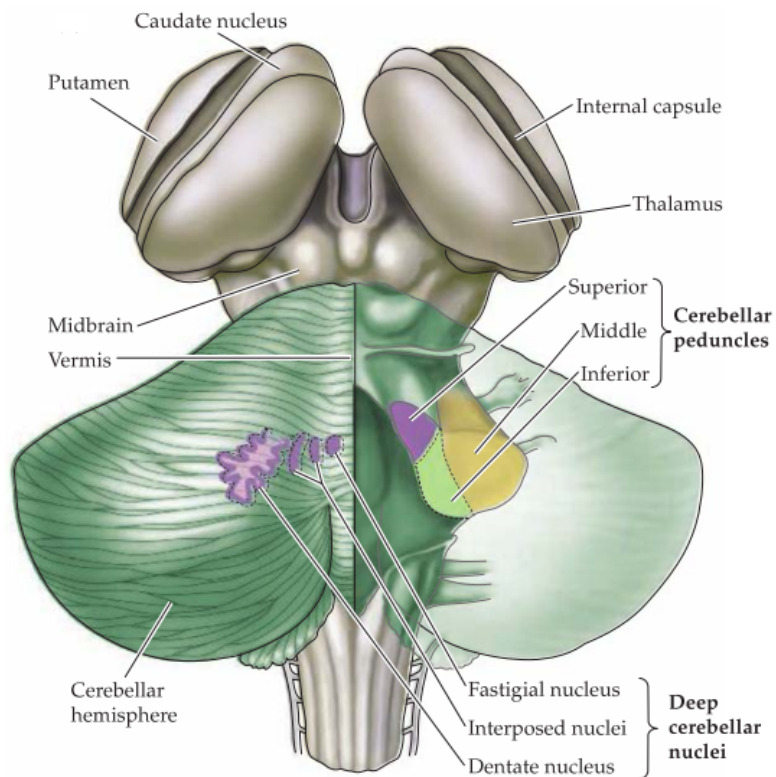
Figure 2.2: As shown in Purves et al. (2012), a detailed diagram of the mammalian brain stem and cerebellum. A hemisphere is removed to show the cerebellar peduncles

vertebrates, excepting teleost fist, the cerebella contains deep cerebellar nuclei (DCN), clusters of neurons within the white matter. The DCN receives afferent connections from Purkinje cells, which are the only output from the cerebellar cortex.

The cerebellum is well-connected to other areas of the brain and to the brain stem. Inputs (afferent connections) and outputs (efferent connections) connect to and from the cerebellum through three peduncles, large groupings of fibres, that are found between the brain stem and the cerebellum (see Figure 2.2). These peduncles are a feature as early as elasmobranch sharks (Farrell, 2011) and teleost fish (Finger, 1978), despite the fish lacking any DCN, which is the only source of efferent axons from the cerebellum in other species. The connections differ by species but the cerebellum projects to areas such as the thalamus and superior colliculus, the functions of which include sensory and motor co-ordination. Afferent connections arise from regions including the pons and the spinal cord (Purves et al., 2012).
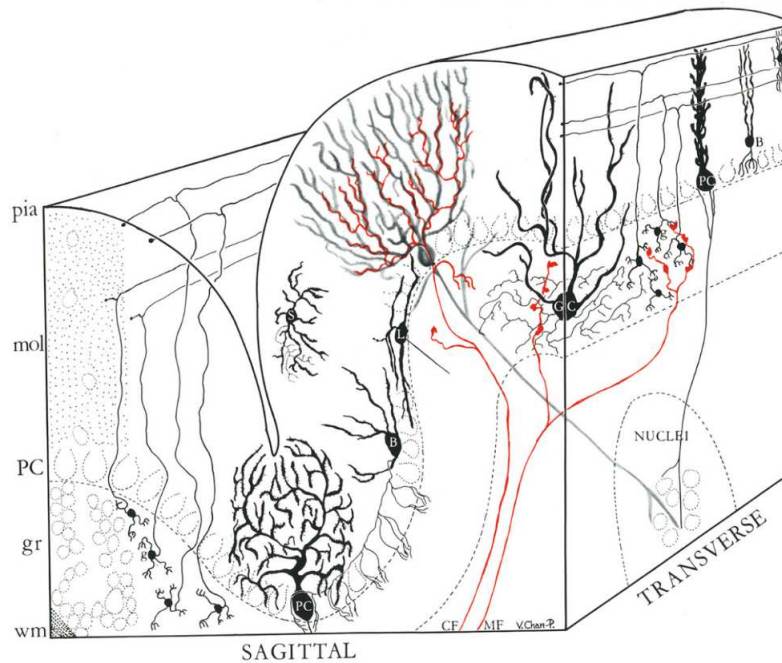
Figure 2.3: Cross-section of the cerebellum as depicted in (Palay and Chan-Palay, 2012) detailing the layers that have been found within the cerebellar cortex and the various cells that are found in each layer. At the left of the diagram, each of the layers are specified: Deepest in the cerebellum is the white matter (wm), followed by the granular layer (gr), the Purkinje layer (PC), molecular layer (mol), and pial surface (pia). The granular layer contains the numerous granule cells (g) as well as Golgi cells (GC). Somas of the Purkinje cell (PC) are contained within the Purkinje layer, as are Lugaro cells (L). The molecular layer contains the inhibitory stellate cells (S) and basket cells (B). The diagram also shows, in red, the afferent climbing and mossy fibres (CF, MF), and the deep cerebellar nuclei.

Most cerebellar cortices share an organisational structure of three distinct layers, each populated by a different cell type (as can be seen in Figure 2.3). These are the granular layer, which is the deepest layer and largely populated by granule cells; the Purkinje cell layer, where the somas of Purkinje cells are found; and the molecular layer, which includes the parallel fibres and Purkinje cell dendritic trees.

In its mammalian form, the cerebellar circuitry includes the inhibitory Purkinje cell receiving excitatory input from two different sources. A strong excitatory input is provided by the climbing fibre, which originates from the inferior olive in the medulla oblongata. Each Purkinje cell receives input from only a single climbing fibre, which makes thousands of connections on the soma and smooth primary dendrites. The climbing fibre itself will branch before it reaches the Purkinje cell layer, allowing each climbing fibre to make contact with several Purkinje cells (Llinás et al., 2004).

The second excitatory input comes from parallel fibres, the axons of granule cells, and the ascending segments of these axons. Granule cells synapse onto Purkinje cells, the inhibitory interneurons (stellate and basket cells), and Golgi cells, which in turn inhibit the granule cells. Both granule and Golgi cells receive excitatory input from mossy fibres. Parallel fibers extend perpendicularly from the planar Purkinje cell dendritic trees, and can pass through approximately 450 of these trees in mammals, while contacting at least 300 Purkinje spines (Ito, 2006). Each mammalian Purkinje cell can receive 150,000-200,000 of these inputs.

Also receiving parallel fibre input are the inhibitory interneurons, often known in mammals as stellate and basket cells, although they can be considered a single cell type (Sultan and Bower, 1998; Ito, 2006). Stellate cells are thought to be found in all but the most primitive cerebella, although they were often thought to be absent in some vertebrates, such as amphibians, as the cells can be small and far fewer in number in comparison to mammals (Bloedel and Llinas, 1969; Hillman, 1969). Stellate cells are found in the molecular layer and synapse on Purkinje cells, mostly in the dendritic tree although they can also reach the soma. Basket cells are named for the basket-like structure they form around Purkinje cell somas, creating a strong inhibition. This structure is only found in mammal and bird cerebella (Voogd and Glickstein, 1998). The cells are found lower in the cerebellum than stellate cells, allowing them to also receive some excitation from climbing fibres and inhibition from the Purkinje cell axon. A simplified breakdown of which cerebellar features appear in which class of animal can be found in Table 2.1 in Section 2.4.

Traditionally the cerebellum has been thought of as being largely engaged with fine motor control, although there is evidence that it is involved with sensory processing (Bell et al., 2008). There is a general consensus that the cerebellum has some involvement in movement, although debates remain on the extent and nature of that involvement.

Theories of directly controlling movement are drawn from studies of people and animals where the cerebellum of the subject is damaged or removed. This does not lead to any losses in senses or movement, but a loss of control. Impair-

ment in gait is a common effect of cerebellar lesions in humans, for example. However, to say that this is the only function of the cerebellum ignores the many afferent connections from disparate regions of the brain. Cerebellar circuitry receives a large amount of sensory information, including vision, sound, touch, proprioception and even blood flow (Bower, 1994). To accommodate this, alternate theories suggest that the cerebellum acts to refine movements based on sensory information (Braitenberg and Preissl, 1994) or that it integrates the information from other systems but then passes it on for other structures to make decisions (Bloedel, 1992).

Other theories include the cerebellum as a bank of learned movements, or otherwise involved in learning new movements – a theory that dates back to Marr (1969) and Albus (1971) who suggested that the climbing fibre acts as a teaching or error signal to Purkinje cells, effecting the strength of parallel fibre inputs. Each of the theories mentioned have some degree of supporting experimental evidence, but there is yet to be a definitive theory of cerebellar function.

2.3   Purkinje Cells

Residing in the cerebellar cortex (as seen in Figure 2.3), the Purkinje cell is the recipient of a large number of both excitatory and inhibitory inputs, and is a key component of cerebellar circuitry. The morphology of Purkinje cells differs across the taxa, but its unique position and organisation in the cerebellum is constant.

With the cell's large size and distinctive dendritic branching, the Purkinje cell was one of the earliest distinguished cells, being described by Jan Purkyně in 1837. This was before Camillo Golgi discovered a silver staining technique which exclusively targets cells and their processes, making them much easier to distinguish from surrounding tissue. This early discovery combined with the unique features of the Purkinje cell - the large number of inputs, its centrality to cerebellar circuitry, and its position as the only output of the cerebellar cortex in almost all vertebrates - mean that it has been the subject of a vast number of studies over the 180 years since it was first described.

2.3.1   Anatomy

The cerebellar cortex has three distinct layers of cells. Closest to the DCN is the granule cell layer, densely packed with tiny granule cells. Above this is the Purkinje layer, where the somas of Purkinje cells sit in a neat row, as though in a queue. At the very top of the cortex is the molecular layer. The Purkinje cell dendritic trees stretch up into this layer, where the long, straight parallel fibres weave through the branches.
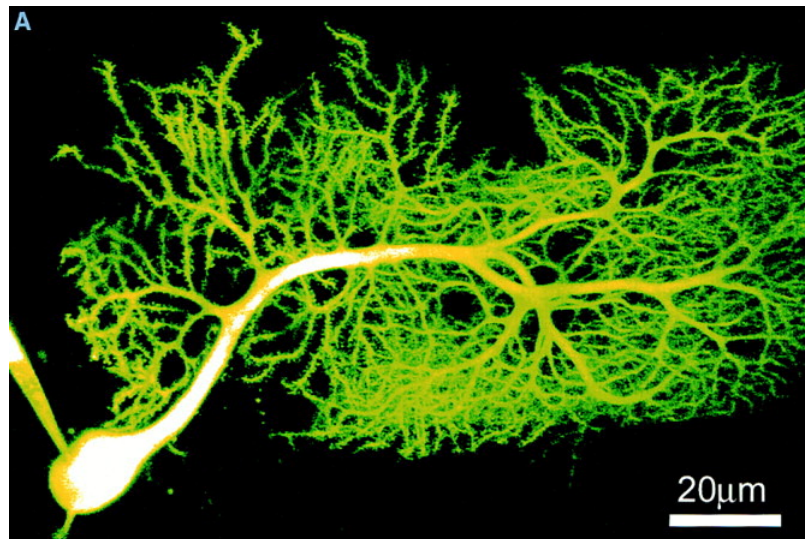
Figure 2.4: Multiphoton image of a fluorescent-dyed Purkinje cell in slice (Denk and Svoboda, 1997, fig. 3)

2.3.1.1   Morphology

One of the largest cells in the central nervous system, the Purkinje cell is prominent in the cerebellum for its size, complexity, and its large number of inputs. Purkinje somas are typically tear-shaped (e.g. Figure 2.4) rather than spherical. When creating their guinea pig Purkinje models, Rapp et al. (1994) estimated the average diameter of the somas to be approximately 25 μm, although size varies between species. The size of the cell itself will also vary by species. The three guinea pig cells modelled in this study - that use the same morphology as the Rapp et al. (1994) models - average 280 μm maximum width and 258 μm maximum height. A constant feature across species is the cell having a much smaller depth than its width or height, so that it is almost flat. The average depth of the three guinea pig cells is 38 μm.

Figure 2.4 also shows the complex dendritic branching that characterises the Purkinje cell in many species. Mammalian species are famous for their structure, which is also present in birds and some reptiles. The cells modelled in this study show how branching can differ, particularly in fish and turtles (examples shown in Figure 4.1).

This intricate morphology allows the Purkinje cell to sample inputs from huge numbers of parallel fibres and inhibitory interneurons. Parallel fibres synapse onto small protrusions called spines (visible in Figure 2.4, shown in detail in Figure 2.5) that cover much of the surface of Purkinje cell dendrites. The number of spines is unclear, and seems to vary across species (see Section 2.4 for more on this), but has been estimated at approximately 150,000 in rats (Harvey and Napper, 1991).
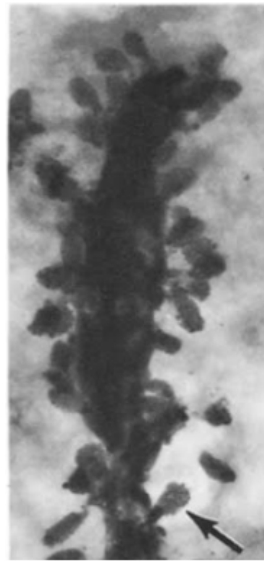
Figure 2.5: Single Purkinje cell branch showing dendritic spines (Palay and Chan-Palay, 2012, fig. 26A)

2.3.1.2 Connections

The characteristic Purkinje morphology allows for a large number of parallel fibres to make multiple connections on each dendritic tree. The Purkinje cell dendritic tree is almost flat, extending up and out much like a fan. This allows the Purkinje cells to sit closely together on a single plane, similarly to books on a shelf. At the same time, the dense branching seen in most species is well suited for creating synapses with the many parallel fibres that travel through the layer.

   The thinner branches of the Purkinje dendritic trees are studded with spines that make contact with the parallel fibres. Originating in the granular layer, the parallel fibres are the axons of granule cells. The granular layer is densely populated with these small cells, one of the most numerous cell types in the central nervous system (Purves et al., 2012). Each one provides the Purkinje cell a small excitatory input, many parallel fibres firing synchronously are required to affect firing. Barbour (1993) estimates that 50 parallel fibres firing at the same time can excite a Purkinje cell in this way. Parallel fibres project upwards from the granule layer, synapsing onto Purkinje cells as ascending segments, before bifurcating in a "T" shape and synapsing on the Purkinje cell's dendritic spines as parallel fibres. The length that parallel fibres can extend appears to vary between species, reaching on average 6 mm in cats (Brand et al., 1976), chickens and rhesus monkeys (Mugnaini, 1983), but only 4.5 mm in rats (Pichitpornchai et al., 1994).

   Purkinje cells also get a large excitatory input from climbing fibres. Climbing

fibres extend into the cerebellum from cells found in the inferior olive, a brain stem nucleus. Each Purkinje cell will receive input from only a single climbing fibre. In contrast to the numerous granule cells, there are fewer inferior olivary cells than Purkinje cells. The axons of these will branch in to 10 climbing fibres on average (Llinás et al., 2004). Each fibre covers a large portion of the soma and main dendrite, "climbing" up the cell and making a large number of synapses. Climbing fibre excitation produces a unique response known as a complex spike (Eccles et al., 1966b) (see Section 2.3.2 for more).

Purkinje cells also receive inhibitory input to both dendrites and soma. Sometimes described separately as stellate and basket cells, there is evidence that these are classes of a single type of inhibitory interneuron (Sultan and Bower, 1998). Stellate-type interneurons are located higher in the molecular layer and make connections with Purkinje dendrites. They tend to be smaller the higher in the cortex they are, and are far more numerous than Purkinje cells. Basket-type interneurons sit closer to the Purkinje layer, and are more morphologically complex than stellate cells. Their axons extend through the Purkinje layer, where they branch off and create woven structures around the somas, inspiring their name. Basket cells are also more numerous than Purkinje cells, and up to 50 have been known to synapse onto a single Purkinje cell (Llinás et al., 2004).

The Purkinje cell itself is an inhibitory cell. In most species, their axons leave the cerebellar cortex to provide inhibition to the cells in the DCN, making it the only efferent cell in the cortex. Teleost fish lack DCN, so the Purkinje cells there instead terminate on eurydendroid cells.

Cerebellar circuitry is more complicated than the Purkinje cell integrating the array of inputs described here into a single output. Other neurons and fibres exist in cerebellar circuitry without synapsing directly on to Purkinje cells, such as Golgi cells and mossy fibres. There are also many loops of information that occur within this circuitry. For example, the Purkinje cell axon extends downwards past the granule layer to contact DCN neurons, but it can also branch and extend upwards to make connections with Golgi and basket cells (Llinás et al., 2004), as well as other Purkinje cells (Palay and Chan-Palay, 2012).

2.3.2   Physiology

As the only efferent cell of the cerebellar cortex, the Purkinje cell spiking behaviours have been carefully studied. Purkinje spiking patterns depend greatly on the source of excitation, based on the ions that cause the change in membrane potential. Additionally, Purkinje cells are also known to fire spontaneously in vivo, without any apparent input (Bower and Woolston, 1983).

Parallel fibres synapse onto Purkinje cells on the magnitude of hundreds of thousands. These small excitatory inputs are linked to "simple" spiking, a train of action potentials common to all neurons, driven by the activation of sodium channels (an example spike train can be seen in Figure 3.7). Simple spiking in Purkinje cells typically occurs at frequencies of 30-100 Hz (Armstrong
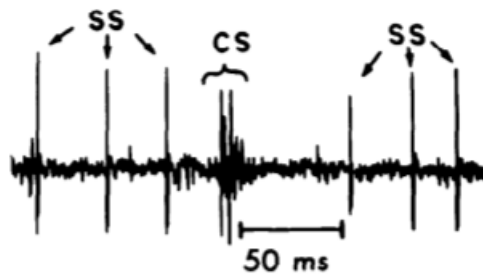
Figure 2.6: Recordings from a rat Purkinje cell soma showing simple spikes (labeled SS) and complex spikes (CS) and the suppression of simple spiking caused by a complex spike (Bower and Woolston, 1983, fig. 1D)

and Rawson, 1979) at irregular intervals that approximately follow a Poisson distribution (Bower and Woolston, 1983).

The excitatory input from climbing fibres is so strong that it decreases the effect of parallel fibre input, silencing simple spikes (see Figure 2.6), and causes the firing of a complex spike. The complex spike typically lasts approximately 20ms, containing several spikelets and reaching a peak amplitude of 40 mV (Llinás et al., 2004), such as in Figure 2.7. Across multiple activations, the unique shape and timing of a complex spike is relatively constant. Complex spiking is much rarer than simple spiking, occurring at a frequency of approximately 1-2.5 Hz (Armstrong and Rawson, 1979). Unlike the sodium driven simple spikes, complex spikes occur when calcium channels are activated.

Faithful recreation of both spiking behaviours in computational models require the model to include not just a replication of the excitatory input, but also of the background inhibitory input of stellate cells (De Schutter and Bower, 1994b). Many studies of Purkinje cells are executed in an *in vitro* environment, usually electrode stimulation of neurons in thin slices of cerebellar material. Current injection experiments of this type produce a bursting response in Purkinje cell that is never seen *in vivo*, show in Figure 2.8. This is likely due to the lack of inhibition as De Schutter and Bower discovered a similar bursting effect when simulating parallel fibre input without any stellate cell input.

2.4 Evolution of the Cerebellum

While the cerebellum has been the subject of a great many studies in the last hundred years, there is little variation on the animal species that these studies use. There is a large volume of data available on mammals, primates and rodents are particularly well represented, while other taxa are far less explored. This section is intended to summarise the available knowledge of the cerebellum and Purkinje cells across the phylogenetic tree. Tables 2.1 and 2.2 are intended to serve as overviews of which point in evolution certain cerebellar features (such as basket-type interneurons, Table 2.1) or Purkinje cell ion channels (Table 2.2)
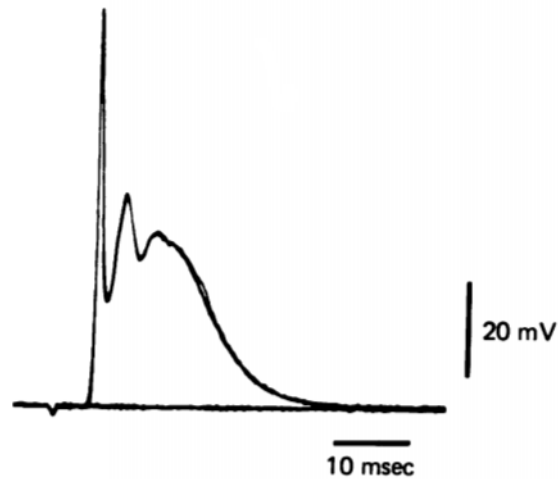
Figure 2.7: A complex spike recorded from a guinea pig Purkinje cell (Llinás and Sugimori, 1980a, fig. 1D)

are first confirmed to exist.

2.4.1 Cyclostomata

Fish of the group cyclostomata are vertebrates which lack a jaw, such as the lamprey eel. Living species are thought to date back to the late Devonian period, approximately 360-375 million years ago (Gess et al., 2006). In hagfish, the region thought to be the cerebellum is not clearly differentiated from the cerebellum-like acousticolateralis area, with some disagreement on whether a cerebellum is actually present. Purkinje-like cells in the possible cerebellar region have been found to be large and not unlike those seen in mammals of early developmental ages (Paulin, 1993).

2.4.2 Elasmobranchii

Elasmobranchii, a subclass of the class of cartilaginous fish also known as Chondrichthyes, includes sharks and rays. The subclass is thought to have originated in the late Devonian period approximately 370 million years ago (Jacquemin et al., 2016), although living species only date back to the early Jurassic period 195 million years ago (Kriwet et al., 2009).

Modern elasmobranch fish have been found to have cerebella that are larger than those seen in teleost fish of the same size (Paulin, 1993). Interestingly, a study of shark cerebella found that some sharks show cerebellar foliation (Yopak et al., 2007), a trait that had previously been thought to have been restricted to mammals, birds, and alligators (Larsell, 1932). The extent of foliation varies greatly between orders of shark, the evolutionarily older squalomorph and
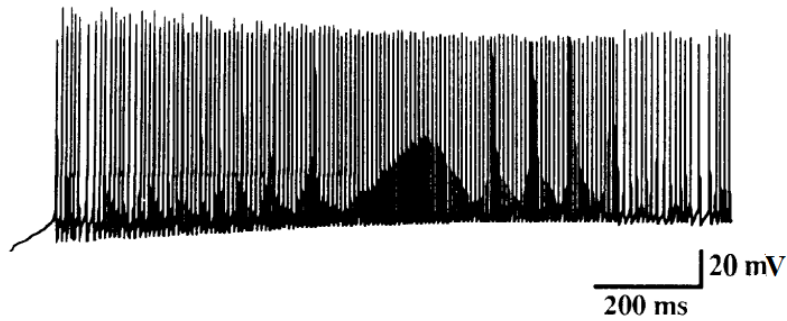
(a) Current injection at 0.5 nA
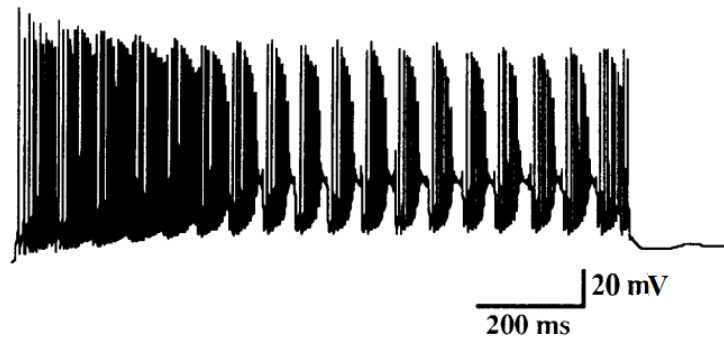
(b) Current inject at 2.0 nA

Figure 2.8: Recordings from the soma of a computational model of a guinea pig Purkinje cell when replicating current injection in vitro (De Schutter and Bower, 1994a, fig. 3A,C).

Vertebrate Group/Species	Cerebellar Foliation	DCN	BEC*	Stellate Cells	Basket Cells
Cyclostomata	a	a	u	u	a
Elasmobranchii	s	p	p	p	a
Teleostei	a	a	p	p	a
Frog	a	s$^+$	p	p$^\diamond$	a
Turtle	a	p	p	p	u
Alligator	p	p	p	p	u
Neornithes	p	p	p	p	p
Guinea Pig	p	p	p	p	p

Table 2.1: Which cerebellar features are found in groups of vertebrates. KEY: a-confirmed absent, p-confirmed present, s-only confirmed present in some species, u-unknown/unconfirmed/disputed. *BEC (Basic Excitatory Circuitry) comprises Purkinje cells, parallel fibres and climbing fibres. +Single deep cerebellar nucleus, disputed in some species. $\diamond$Far fewer stellate-type interneurons are present than found in mammals.
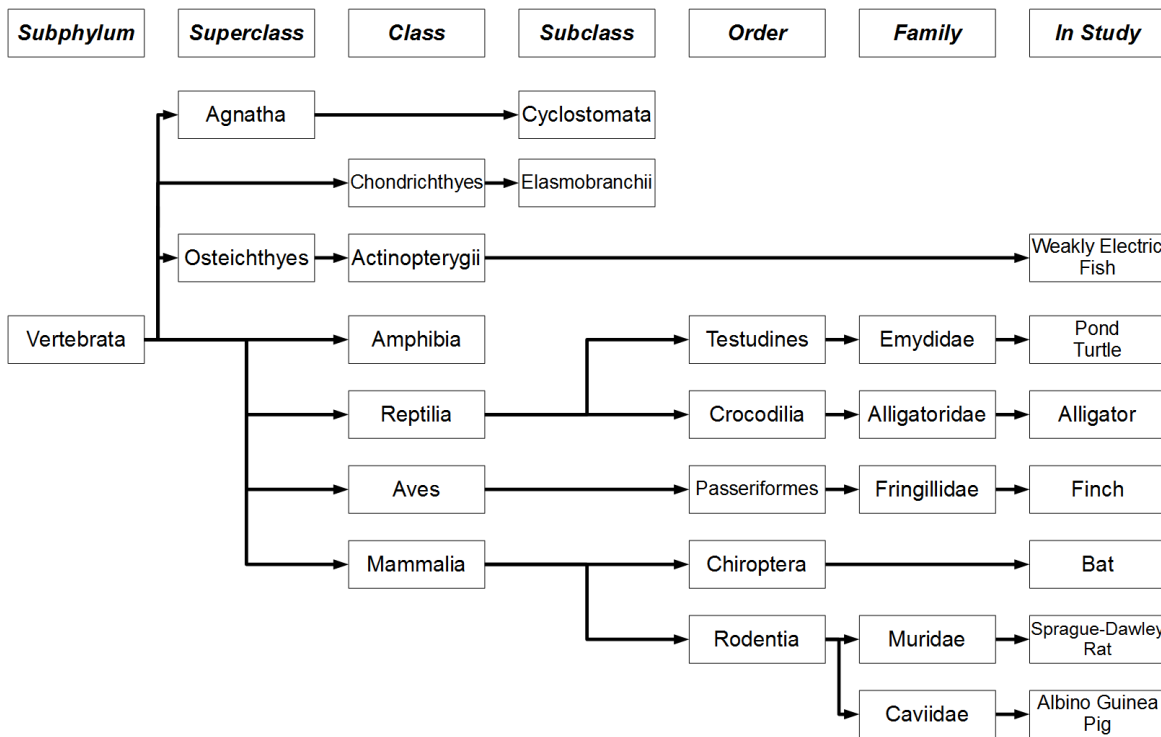
Figure 2.9: A subsection of the phylogenetic tree that shows the positions of the species used in this study, with as much detail as is known (see Chapter 4 for more details), as well as other vertebrates that are discussed in Section 2.4.

Vertebrate Group/Species	Fast Na	Persistent Na	P-Type Ca	T-Type Ca	DR*	Ca-Dependent K	Other
Cyclostomata	u	u	u	u	u	u	
Elasmobranchii	u	u	u	u	u	u	
Teleostei	p	u	u	u	u	u	
Frog	u	u	u	u	u	u	
Turtle	u	p	p	u	u	p	Cl-+
Alligator	u	u	u	u	u	u	
Neornithes	p	u	p	u	u	p	
Guinea Pig	p	p	p	p	p	p	

Table 2.2: Which types of ion channel have been found in the Purkinje cells of different vertebrate groups. KEY: a-confirmed absent, p-confirmed present, s-only confirmed present in some species, u-unknown/unconfirmed/disputed. *Delayed Rectifier. +See (Hounsgaard and Midtgaard, 1989) for more information

squatinomorph sharks have flat cerebella. Galeomorphii, a more recent order, show foliation in their cerebella, although the amount of foliation still varies greatly between habitat and predatory strategy (Yopak et al., 2007).

Studies in the dogfish cerebellum have found that the Purkinje cells resemble those found in other vertebrates in many ways. They show characteristic dendritic flatness, are organised in the typical 'shelved' manner (Llinás and Nicholson, 1971). The cells show less branching than mammals or amphibians, with spine density estimated at 6-7 per 10 μm (Paul and Roberts, 1977). There were also groups of spines found on the soma of Purkinje cells. These groupings are known as 'pincushions' and are terminated on by climbing fibres. They have previously been found on the cells of amphibians and teleost fish (Alvarez-Otero et al., 1993). The cerebellar circuitry is present as described in the introduction, with the exception of basket-type inhibitory interneurons. The presence of climbing fibres had been disputed, but they have since been found to be present. They are considered more primitive than in some other vertebrates as they do not extend into the molecular layer (Alvarez-Otero et al., 1993).

2.4.3 Teleostei

Teleostei is an infraclass of the class Actinopterygii (ray-finned fish) and comprises the vast majority of known, living species of fish. The earliest found fossils date to the Triassic period, around 200-250 million years ago (Greenwood et al., 1966), with many extant species first appearing in a period of mass diversification during the Mesozoic era 250-66 million years ago (Near et al., 2012).

In contrast to the mammalian and avian cerebella, which are divided into ten lobules, the teleost cerebellum has been found to contain only three main divisions: the valvula cerebelli, the corpus cerebelli, and the crista cerebellaris (Miyamura and Nakayasu, 2001). Most vertebrates also have a Purkinje layer between the granular and molecular layers that spans the cerebellum where the somas of Purkinje cells are situated. In the teleost cerebellum, however, the layers are less defined and Purkinje cells are found in 'zones' in the valvula and corpus cerebelli. For the most part, the Purkinje cells in these zones are still positioned by the 'shelved' organisation observed in other vertebrates, but there is more evidence of irregularities closer to the corpus cerebelli (Miyamura and Nakayasu, 2001). There are no Purkinje cells found in the corpus cerebellaris, which is also thought to be evolutionarily the oldest region of the teleost cerebellum (Miyamura and Nakayasu, 2001). A major difference between teleosts and higher vertebrates is the lack of deep cerebellar nuclei in the former. As there are no deep cerebellar nuclei neurons, the Purkinje cell axons terminate on eurydendroid cells, which mediate the cerebellar output. This is a dramatic difference as the Purkinje cells act as an interneuron, rather than the position they hold as sole efferent cell of the cerebellar cortex in other vertebrates. The eurydendroid cells also extend their dendrites to receive input from parallel fibres (Hashimoto and Hibi, 2012).

2.4.3.1   Mormyridae

The mormyrids are a family of teleost fish, commonly known as elephantfish, which have particularly large cerebella (Paulin, 1993). In comparison to another teleost, the zebrafish, mormyrids also have a more complex cerebellar structure (Hashimoto and Hibi, 2012). Han et al. (2007) described the central lobe of the mormyrid cerebellum as having three layers: the granular, ganglionic (containing the Purkinje cells) and the molecular, which also included stellate-type inhibitory interneurons.

Purkinje cells of mormyrid fish have large dendrites that branch sparsely and have spines on the secondary and tertiary branches. Their electrophysiological responses are different to those recorded in other vertebrates, with very low amplitude (typically less than 30 mV) sodium spikes and the climbing fibre response consisting of an all-or-nothing excitatory post-synaptic potential (EPSP) rather than the mammalian complex spike (de Ruiter et al., 2006) (spiking in the Purkinje cell is detailed in Section 2.3.2, action potentials in general can be found in Section 3.2.2.2). Despite these differences in behaviour, the conductance of sodium channels in mormyrid fish Purkinje cells were found to be very similar to those in the cells of rats. When the amplitude of the excitatory post-synaptic conductance (EPSC) in the fish was scaled up, as it was very small, it was found to be close in shape to those in the rats; rise times were also very similar (de Ruiter et al., 2006). A figure from the paper showing similar sodium currents following a simulated complex spike has been reprinted as Figure 2.10 for reference.

To further investigate the sodium channel densities and distributions in rat and mormyrid Purkinje cells, de Ruiter et al. (2006) performed channel staining in the both the soma and dendrites of the cells. They found that the two species have similar results for three types of sodium channel. Staining for two types of sodium channel, Nav1.2 and Nav1.6, strongly showed in the soma and dendrites in both species. Both species also showed strong staining in the soma for channel Nav1.1, but only weak traces in the dendrites. Table 2.3 shows the average value of several features of sodium channels after correcting for input capacitance to account for differences in soma size between the two species. Furthermore, the study also found that input resistance for Purkinje cells in both species in slice were very similar; $84.8 \pm 18.5 \ M\Omega$ in rats and $81.3 \pm 13.1 \ M\Omega$ in fish. Using a dynamic clamp, sodium traces were recorded in response to a simulated complex spike. Despite complex spiking not occurring naturally in the mormyrid fish, the responses in both species were of a similar shape once differences in scale were accounted for (de Ruiter et al., 2006).

2.4.4   Amphibia

The first amphibians have been dated as emerging in the late Devonian period (over 360 million years ago) (Carroll, 1977; Vitt and Caldwell, 2013) as descendants of lobe-finned fish with small primitive lungs. All living amphibian species belong to the subclass lissamphibia. The time period that lissamphibia
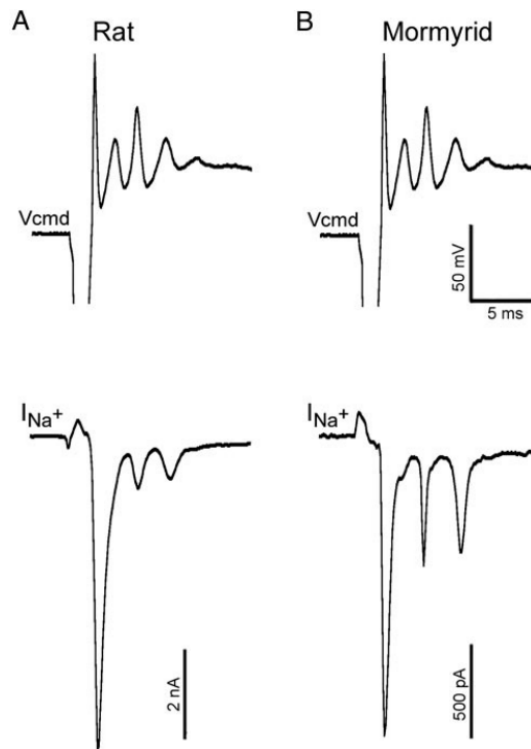
Figure 2.10: The top row shows the simulated complex spike applied to each cell in vitro. The bottom traces show the sodium current recorded in the rat (left) and fish (right) cells. The scale bars show the difference in amplitude between the cells (de Ruiter et al., 2006, fig. 8).

Property	Fish	Rat
Current Peak (pA/pF)	179 ± 59	189 ± 57
Decay Time (ms)	0.47 ± 0.05	0.31 ± 0.049
Rise Time (ms)	0.39 ± 0.008	0.38 ± 0.052

Table 2.3: Comparison of fast inactivating sodium channel properties in fish and rat Purkinje cells in (de Ruiter et al., 2006) given as species averages and standard error.

diversified to include extant species is contested, but assumed to be within the last 300 million years (Marjanović and Laurin, 2007).

As in cyclostomata, the amphibian cerebellum is very simple and primitive. Comparisons in size to both land-based and aquatic vertebrates show the amphibian cerebellum to be particularly small (Paulin, 1993). It has been suggested that the amphibian cerebellum lacks the inhibitory interneurons found in higher vertebrates (Llinás et al., 1969), but this has been disproved for frogs (Bloedel and Llinas, 1969).

2.4.4.1   Frogs

Frogs are widely-distributed and numerous, exhibiting a high amount of species variation. The earliest confirmed frog fossils date back to the early Triassic period. They also have a more advanced cerebellum than many other amphibians, having been described as having a higher resemblance to the reptile cerebellum than those of other amphibians (Hillman, 1969).

Purkinje cells are again found with the typical organisation, with flat dendritic trees perpendicular to parallel fibres, between the granular and molecular layers. The cells also have spiny pincushions around the soma, as previously described in elasmobranchii (Alvarez-Otero et al., 1993) and teleost fish, where climbing fibres terminate (Hillman, 1969). It has been estimated that the climbing fibre makes approximately 300 synapses on the soma and primary dendrites (Bloedel and Llinas, 1969), in comparison to the nearly 30,000 estimated for mammalian cells (Ito, 2006). The Purkinje cells response to climbing fibre activation resembles the response as recorded in cats, pigeons, and alligators in similar studies (Bloedel and Llinas, 1969).

Early studies suggested that the frog cerebellum lacked any inhibitory interneurons. Stellate-type interneurons have since been found, although they were described as small and are present in much smaller numbers than in mammals. Studies of bullfrog Purkinje cells using local stimulation suggest that these cells receive very little inhibition (Bloedel and Llinas, 1969).

The Purkinje cells have far fewer spines in the secondary and tertiary branches than has been estimated in mammals, approximately 3-4,000 spines per cell. Purkinje cell dendritic trees are also far less densely-branched than mammalian cells; Hillman (1969) described the primary dendrite as particularly long and suggested that the less complex dendritic trees would be less adept at sampling a large range of parallel fibres than their mammalian counterparts. However, a later study (Llinás, 1971a) based on work by Hillman estimates the number of granule cells as approximately 1.6×10^6, which is an order of magnitude smaller than the lowest estimates in mammals. The methods used to find this number are not included, but if accurate would suggest that the level of branching in frog Purkinje cells is adequate for the number of inputs.

2.4.5   Reptilia

It is known that the ancestors of both reptile and bird species first appeared during the Carboniferous period, around 320 million years ago (Vitt and Caldwell, 2013). However, continued dispute on the definition of reptile makes it difficult to know when the first ancestors of modern species began to appear. Debates also occur on the proper classification of the families of turtles and crocodilians (a group including crocodiles and alligators). Turtles, appearing in the late Jurassic around 155 million years ago (Joyce, 2007), are unlike any other reptile, and have historically been classified with extinct reptiles rather than living groups (Vitt and Caldwell, 2013). Crocodilians date back to the Triassic period (250 million years ago) and are phylogenetically closer to birds than other reptiles (Benton and Clark, 1988).

The reptile cerebellum shows a series of advancements over amphibians; there is an increase in the number of granule cells (becoming closer to the numbers typically found in mammals) and the Purkinje cells are both larger and more numerous. Additionally, the reptile cerebellum appears to have the earliest examples of basket-type interneurons providing inhibition to Purkinje cell somas. Basket-type interneurons were identified in the turtle (Larsell, 1932) and chameleon (Rámon y Cajal, 1911), but not in the alligator (Llinás et al., 1968), although Llinás et al. did describe the alligator as having stellate cells which terminate on the Purkinje soma without forming a basket. The basket-type interneurons in turtles are not positioned closely to the Purkinje cells and have very long axons in comparison to those in mammals, which terminate on up to 2-3 Purkinje cells (Larsell, 1932).

2.4.5.1   Turtle

Like in most reptiles, the turtle cerebellum is a flat ovoid with no signs of folding (Larsell, 1932), but still has three clear layers of cells (Hounsgaard and Midtgaard, 1988). Chan and Nicholson (1986) describe turtle Purkinje cells as having dendritic trees similar to those seen in elasmobranch fish, with a maximum soma diameter of roughly 30 μm.

While stellate-type interneurons are present, it has been proposed that they may have a diminished inhibitory effect on Purkinje cells in comparison to results from alligator and mammalian cells (Chan and Nicholson, 1986). Later studies of in vitro turtle stellate-type interneuron and Purkinje cells found that in certain conditions, input to the dendritic tree from a single inhibitory interneuron could cause a reduction in the Purkinje cell firing. However, as the effect of a single cell could be easily nullified by an increase in depolarisation in the Purkinje cell, it is suggested that inhibiting the Purkinje cell from dendritic inputs would require several stellate-type cells firing simultaneously (Midtgaard, 1992). A single stellate-type input has a varied effect on a climbing fibre response, related to the timing of each input. Inhibitory input just after the start of the climbing fibre response could severely shorten the duration of the response. With the correct timing, single inhibitory inputs were capable of reducing the calcium

influx required for complex spiking (Midtgaard, 1992).

Turtle Purkinje cells produce firing patterns that are much like those which have been used to exemplify Purkinje cells in other vertebrates, as shown by Hounsgaard and Midtgaard (1988). When measuring the voltage response in the soma of Purkinje cells to current injection in vitro (Hounsgaard and Midtgaard, 1988, fig. 1), the recorded firing patterns were very similar to those seen in mammals (Llinás and Sugimori, 1980a, fig. 4) under the same conditions. The same study also shows that these firing patterns are the result of the turtle Purkinje cells having the same voltage-activated ion channels as have been found in other vertebrates. Fast action potentials indicate sodium channels, while slower spikes are due to calcium channels. Potassium channels have also been confirmed. A typical behaviour in mammalian Purkinje cells is hyperpolarisation of the cell following the activation of a large calcium conductance. Behaviourally, this is seen as an inhibition of spiking following climbing fibre induced complex spiking, which has also been observed in the turtle Purkinje cells (Hounsgaard and Midtgaard, 1989).

2.4.5.2 Alligator

The alligator cerebellum is an interesting area of study as it possesses many features that are more similar to the cerebella of birds and mammals. For example, cerebellar folding is found in the alligator (Larsell, 1932), where most reptiles have flat ovoid cerebella. Foliation is characteristic in birds and mammals and is very rare in other vertebrates, but there are exceptions found even in elasmobranch fish. Alligator cerebella also show distinct segmentations (Larsell, 1932) and while the molecular and granular layers are thin, similar to those of the turtle, they also show the first evidence of a true single layer of Purkinje cells (Llinás et al., 1968).

In terms of cerebellar circuitry, the expected Purkinje cells, parallel and climbing fibres, and stellate-type interneurons are all present. Llinás et al. (1968) described some of the inhibitory interneurons as terminating on Purkinje somas; acting as proto basket-type interneurons, although they did not create a 'basket' around the soma. The Purkinje cells in alligator embryos were described by Larsell (1932) as being well-developed, with dendritic processes comparable to those of mammals.

Recordings of action potentials from the soma of alligator Purkinje cells were similar to those observed in both cats and frogs (Llinás et al., 1968).

2.4.6 Aves

There is some debate over the distinction between birds and their ancestors, the theropod dinosaurs, making it difficult to determine when the first birds would have emerged, but as mentioned in the previous section, early reptile-bird ancestors appeared around 320 million years ago (Vitt and Caldwell, 2013), and the archosauria group that includes ancestors of birds and crocodillians first emerged around 250 million years ago (Benton and Clark, 1988).

The bird cerebellum is a thin sheet of folded grey matter, as in mammals, but it is narrow and shows most variation between species through its length. Bird cerebella have been found to contain both dendrite-terminating and basket-type inhibitory interneurons. Comparative studies (Sultan, 2005) of bird cerebella found that enlargements in the cerebellum as the brain became larger were region-specific rather than uniform, which is likely to also be true of other vertebrates. It is possible that the particular region enlargements are behaviour-driven, for example the cerebellum of owls have enlargements in the vestibular and specific somatosensory regions associated with the tail area, suggesting these changes could aid night-time flight. Birds that are known for flight dexterity, such as falcons and swifts, do not have particularly long cerebella. This is indicative that flight skill is not correlated with cerebellar size (Sultan, 2005).

Foliation is a feature of all avian cerebella, but there are differences in the degree of foliation across species. A comparative study of 91 bird species (Iwaniuk et al., 2006a) found that cerebellar foliation is most correlated with the body, overall brain, and cerebellum size of the species. Of these, the overall brain volume has the largest correlation with cerebellar foliation. This is particularly true in corvid and parrot species, which have large brains but small, highly foliated cerebella. Foliation allows for an increase in the number of neurons, particularly Purkinje cells, without increasing the size of the cerebellum. The increase in cells could mean an increase in cerebellar processing; a higher level of foliation also correlates with tool use in birds. In terms of phylogenetics, the study found that some orders of birds consistently show higher foliation than others. Seabirds, parrots and penguins have the highest cerebellar foliation, with the lowest levels are found in pigeons, nightjars and waterfowl (Iwaniuk et al., 2006a).

A study of the Purkinje cells of pigeons confirmed the presence of voltage-gated ion channels and found their electrophysiological behaviour to be comparable to that seen in alligators (Llinás and Hess, 1976). The same work finds that some dendritic spikes in pigeon Purkinje cells are produced by a slow calcium current.

2.4.7   Mammalia

As with birds and reptiles, the appearance of the first mammals is a matter of debate, depending on how mammals are defined. By the traditional definition, put forward in the late 19th century, the earliest fossils that could be classed as mammals are from the late Triassic era, 225 million years ago (Lyell, 1871). Whether this group of animals, known as haramiyidans, are considered mammals is disputed. A more recent classification by Rowe (1988) suggests that mammals should be defined by the extant species. This would place the most recent common ancestor at 163-186 million years ago based on when the three extant mammal groups split (Messer et al., 1998).

On average, the mammalian cerebellum makes up 13.5% of the total brain volume (Clark et al., 2001), although there is variation between orders. When both are plotted as logarithms, the proportion of body weight to brain weight is

usually estimated at 0.66 (Jerison, 1973), i.e. $\log(w_{brain}) = 0.66 \log(w_{body})$. In a study of 14 mammalian and 1 avian cerebella, the proportionality between the logarithm of cerebellar weight and the logarithm of body weight was calculated as 0.72 (Sultan and Braitenberg, 1993). Their study also showed that mammalian cerebella all generally conform to an arrow-like shape, whereas birds and reptiles are more rectangular. In small mammals, cerebellar width is found to increase greatly with surface area. In larger mammals, excepting humans, this increase is still present but much more subtle (Sultan and Braitenberg, 1993). Comparative studies have also found that cell size and dendritic complexity appear to increase proportionately with cerebellum size in mammals (Maseko et al., 2012). However, there is also an inverse relationship between size and neuronal density (Jacobs et al., 2014).

Monotremes (egg-laying mammals) have been described as having "large and unusual" (Paulin, 1993) cerebella, which is possibly linked to their having electroreceptors in their beaks. The comparison of vertebrate cerebella by Paulin (1993) also found that cetaceans have larger cerebella in comparison to land mammals. However, in the Sultan and Braitenberg (1993) comparative study it was found that of their samples, the cow has the longest anterior to posterior extension. In pinnipeds, such as seals, the dorsal and ventral paraflocculus and paramedian lobe are particularly enlarged (Paulin, 1993).

The Purkinje cells of mammals tend to have more complex branching than in other animal groups. One exception is the humpback whale, whose Purkinje cells have straight, vertical dendritic processes, not dissimilar to those seen in fish. This type of branching was not observed in manatees, another aquatic mammal, or giraffes, which belong to the order cetartiodactyla along with whales (Jacobs et al., 2014, fig. 4). The spine density on Purkinje cells has been estimated in several studies using different species and methods. A relatively early study in 1957 by Fox and Barnard estimated that Purkinje cells in the macaque average at 1.5 spines per μm. Spine density in mice, cats, and humans was measured at 4.4 spines per μm. In frogs it drops to 1.1 spines per μm (Shelton, 1985). However, a 1988 study (Napper and Harvey) using different counting methods found that the number of spines per μm on rat Purkinje spiny branchlets was between 17.2-17.6, depending on the method used. Using these estimates, the total number of spines per cell could be between 154,000 and 175,000 in rats.

As parallel fibres synapse on the Purkinje cell spiny branchlets, an increase in the number of spines on the cell, and in the spread of the dendritic tree, could be an adaption to the population of granule cells also increasing. The small, densely-packed neurons are the most numerous cells in the brain, constituting over half of the total number of cells in the mammalian central nervous system (Heck and Sultan, 2002). A study of the cat cerebellum by Palkovits et al. (1971) calculated the total number of granule cells to be in the range of 2.2×10^9 and Harvey and Napper (1988) estimated the total to be 9.2×10^7 in rat cerebella. Most recently, Andersen et al. (1992) calculated the number of granule cells in the human cerebellum to be approximately 10^{11}.

2.4.7.1   Bats

There are two major groups of bats, the microchiropterans (microbats) and the megachiropterans (megabats). Microbats are mostly insectivores and rely on echo-location, while megabats largely eat fruit and rely on their vision; it has been suggested that their brains resemble the brains of certain types of primates (Paulin, 1993).

A study of the microbat cerebellum showed that they share the typical mammalian cerebellar architecture, including the Purkinje cell zones which are visible from antigen immunoreactivity. Immunoreactivity is the body showing some response to the introduction of some antigen - a foreign substance. It also has some more unique features thought to be related to bats being capable of flight and using echolocation (Kim et al., 2009). The main difference between the microbat cerebellum and those of other mammals is the large proportion of Purkinje cells in lobule I that are immunopositive to the antigen zebrin II. This type of expression is more typical of avian rather than mammalian cerebella (Kim et al., 2009), suggesting this is an example of convergent evolution and possibly an adaption to the cerebellum to optimise for flight. The study by Kim et al. (2009) goes on to describe enlarged sections of the VI/VII lobules, which are thought to be responsive to auditory stimuli, suggesting it may have developed for echolocation.

2.4.7.2   Guinea Pigs

Studies of the guinea pig Purkinje cell found that the spiny dendrites make up 81-85% of the total dendritic length, although an actual count of spines has not been made. The cells were also found to have over 400 terminal points to their dendritic trees (Rapp et al., 1994). In an electrophysiological study, six active channels have been confirmed in guinea pig Purkinje cells. These are inactivating and non-inactivating sodium channels that are found at or near the soma, spike generating calcium channels found in dendrites, and voltage- and calcium-dependent potassium currents also found in the dendrites (Llinás and Sugimori, 1980a). Table 2.2 lists these channels against what channels have been confirmed in the Purkinje cells of other species groups.

Following on from these studies, computer models of hybrid guinea pig/rat Purkinje cells[1] by De Schutter and Bower (1994a; 1994b) (explored in more detail in Section 3.3) that replicated the firing patterns of cells in vitro were able to find out more about the electrophysiological behaviour of the cells. Modelling only the excitatory inputs to the Purkinje cell was not sufficient for the model to accurately replicate behaviour, as the calcium produced spikes were non-complex. This reflects the results in teleost fish, which lack inhibitory inputs and produce an all-or-nothing response rather than a complex spike to calcium currents.

---

[1] The cell morphology was traced from guinea pig cells, but much of the voltage clamp data used to model behaviour was taken from studies using rats.

Further to this, the De Schutter and Bower modelling studies (1994a; 1994b) also found that complex spiking from climbing fibre activation was dependent on both calcium and calcium-activated potassium channels. The shape of the complex spike could be altered by changing the maximum conductance of climbing fibre synapses. These studies were also able to cast doubt on a long-standing belief originally put forward by Llinás and Nicholson (1971) in a study of alligator Purkinje cells. This was the description of dendritic 'hot-spots', thought to be caused by regions in Purkinje dendrites where calcium channel densities were higher than other areas. The models used by De Schutter and Bower have uniform calcium channel distribution across the dendritic tree, but they were still able to produce the 'mosaic'-like patterns of calcium concentration that have been given as evidence of variable channel densities. They go on to suggest that differences in calcium concentration are a consequence of the morphology of spiny dendrites.

2.4.7.3   Elephants

Elephants have been found to have the largest cerebella relative to their size in mammals (Maseko et al., 2012). They demonstrate the typical mammalian cerebellar circuitry, although all cerebellar neurons in the elephant tend to have much higher volumes than has been seen in other mammals. The total dendritic length of neurons also tended to be higher than other mammals, but to a far lesser degree (Jacobs et al., 2014). This cellular enlargement is particularly evident in the Lugaro cell, a cerebellar interneuron, more so than any other cell types. The extreme size of Lugaro cells appears to be a change unique to elephants (Maseko et al., 2012). Purkinje cells in elephants are very densely-branched and heavily spined. As with the other cerebellar neurons, they are also very large in size, with somatic volume averaging at 8507.75 μm (Maseko et al., 2012), which is roughly twice the volume of the soma of any of the cells in our own studies.

2.4.7.4   Primates

Primates are known to have large cerebella. In humans, the cerebellum is wider than would be expected given trends in mammalian cerebella (Sultan and Braitenberg, 1993). A study of the cerebella of haplorhine primates, a suborder of primates spanning apes, monkeys, and tarsiers, found a positive correlation between cerebellar weight and life-span. A second, lesser, positive correlation between cerebellar weight and female reproductive age was also found. This was also true for the whole brain, but a stronger correlation was found with the cerebellum (Voogd and Glickstein, 1998).

The number of inhibitory interneurons in the human molecular layer of the cerebellum is estimated at 1.5×10^9, a marked increase in comparison to other vertebrates. The cells were also found to be more morphologically complex than those in the cerebella of other vertebrates (Sultan, 1999).

2.4.8 Comparing Cerebella

2.4.8.1 Circuitry

Evolutionarily, the first inhibitory inputs to the Purkinje cells are the stellate-type interneurons. As shown in Table 2.1, these cells that provide inhibition to the Purkinje cell dendritic tree have been described in all cerebella but that of the cyclostomes. Neurons that match the description of basket-type interneurons and terminate on the Purkinje cell soma in reptiles have been reported as far back as 1911 in Rámon y Cajal's description of the chameleon cerebellum, as well as more recently in alligators (Llinás et al., 1968). It has been suggested that the introduction of basket-type inhibitory neurons synapsing on to the Purkinje cell soma was related to these species having large cerebella and therefore a larger number of interneurons among reptiles (Sultan and Bower, 1998; Sultan, 1999).

Rámon y Cajal was also the first proponent of basket and stellate cells being morphological variations of the same cell type, and that the morphological differences were linked to the depth of the neuron in the cerebellar cortex. The morphology of the stellate-type interneurons in turtles also appeared to vary based on the depth of the cell. Chan and Nicholson (1986) were able to classify these interneurons into three groups based on cells that were less than 200 μm, 200-400 μm, or more than 400 μm from the cerebellar surface. This idea was further explored by performing principal component analysis on the morphological descriptions and positions of rat cerebellar inhibitory interneurons (Sultan and Bower, 1998). The population of 26 cells was not definitively separated as 'stellate' and 'basket' cells, but showed a smoother transition based on the depth of the cell.

Cerebellar structure and organisation also appears to be fairly constant across vertebrates. Changes to the cerebellum to account for specialisations in particular species are often expressed as an enlargement in a specific region rather than a change in organisation. Immunoreactivity to zebrin II in Purkinje cells also shows a conserved alternation between positive and negative expression, which demonstrates groupings or 'zones' of Purkinje cells in all tested vertebrates, although the meaning of this is unclear.

The planar dendritic trees and positioning of Purkinje cells is a feature of all cerebella. Higher vertebrates have increased dendritic complexity which allows them to efficiently sample the input of large numbers of parallel fibres. In mammals, the number of dendritic spines where the parallel fibres synapse has been estimated at 1.5 spines per μm in macaques (Fox and Barnard, 1957), 4.4 spines per μm in cats, mice, and humans (Shelton, 1985), and 17.4 spines per μm in rats (Napper and Harvey, 1988), while in frogs the estimation is only 1.1 spines per μm (Shelton, 1985). It is likely that this lower estimate is more similar to other vertebrates with sparsely-branched Purkinje cells, such as teleost and elasmobranch fish. However, the spine estimates may change if calculated again using more modern methodologies, much like the differences seen in the mammalian estimates. There are very few studies which attempt to provide a

count of granule cells in the cerebellum due to their incredible numerousness. The estimate for the frog cerebellum, 1.6×10^6, is much lower than that given for rats (9.2×10^7), cats (2.2×10^9), and humans (10^{11}). Assuming the numbers are accurate, it is possible that the more complex dendritic trees and large number of spines of mammalian Purkinje cells are a specific adaption to increasing populations of granule cells through evolution.

A computer model of a hybrid guinea pig/rat Purkinje cell indicated that a lack of inhibitory input would prevent a cell from being able to produce complex spikes. The mormyrid fish has been shown not to produce a complex spike from climbing fibre input. While teleost cerebella include input to Purkinje cell dendrites from inhibitory interneurons, it is possible that this input is too small for complex spiking to occur.

2.4.8.2 Ion Channels and Electrophysiology

There are very few studies that attempt to characterise ion channels in Purkinje cells in non-mammalian species. With the notable exception of de Ruiter et al.'s (2006) work in mormyrid fish, most studies of Purkinje cell active channels have taken place on rodent cells. Table 2.2 shows the types of ion channels found in guinea pig Purkinje cell dendrites in a study by Llinás and Sugimori (1980b) and whether they have been found in other species. This is telling of how little this area has been explored experimentally. de Ruiter et al. (2006) demonstrated the similarity in rise and decay time constants, as well as the shape of the conductance of sodium channels between fish and rats. This is suggestive that there has been some conservation in channel conductance, despite differences in electrophysiological behaviour.

Conversely, there is also a lot of evidence for similarities in the electrophysiological behaviour of Purkinje cells across species, at least in vitro. Both the fish and rat cells responded to a simulated complex spike in a similar way, with the main difference being scale of response. Recordings of voltage change in response to current injection at soma and the firing patterns of turtle Purkinje cells are also very similar to recordings made in mammals, suggesting that similar channel dynamics are also present in this species (Hounsgaard and Midtgaard, 1988, 1989). In various studies by Llinás (Llinás et al., 1968; Llinás and Hess, 1976; Llinás et al., 1969), there are similarities noted in the electrophysiological behaviour in Purkinje cells of alligators, pigeons, and frogs. Furthermore, the computational model of a Purkinje cell by De Schutter and Bower (1994a,b) was able to accurately replicate the firing patterns and electrophysiological behaviours of in vitro cells. This model used the morphology of a guinea pig cell and simulated ten voltage-dependent ion channels, distributed in varying densities between the dendrites and soma. The same parameters were used for cell models that used the traced morphology of two other guinea pig Purkinje cells and the results proved to be robust, with only minor variations where differences in size changed channel density. The model results were also fairly robust to changes in channel density, although they were far more sensitive to alterations of the high-threshold calcium channel or either of the calcium de-

pendent potassium channels. These results seem to validate computer models of Purkinje cells that use experimental data from different species, or use a single set of electrophysiological properties across different morphological traces, including the use of identical ion channel densities. However, when simulating spines, there should be differences in spine density that are proportional to the dendritic complexity of the cell.

2.5   Conclusion

In all vertebrates, the basic cerebellar circuitry consists of Purkinje cells with excitatory input from granule cell axons bifurcating as parallel fibres and a climbing fibre input originating from the inferior olive. Axons of Purkinje cells then terminate on either DCN neurons or eurydendroid cells where the vertebrate lacks DCN. Across evolution, the cells making up cerebellar circuitry have grown in both number and type, with a particular increase in the numbers of granule cells and the introduction of the inhibitory interneurons.

Overall, these findings point towards substantial conservation of structure and circuitry in the cerebellum over evolution. The differences between fish and mammal cerebella largely amount to an increase in cell numbers and a related increase in neuronal complexity. This is particularly true if inhibitory interneurons in the cerebellum are considered to be variations of the same cell type, rather than separate cells. Assuming that granule cell population estimates are accurate, it is likely that the increased dendritic complexity of mammalian and avian Purkinje cells in comparison to fish and amphibians is an adaption of the cell to allow it to receive input from the increased number of parallel fibres. Descriptions of the frog cerebellum suggest that the number of inhibitory interneurons increased along with the number of excitatory granule cells. While cerebellar organisation is constant; all vertebrates have granular, Purkinje, and molecular layers, cerebellar size and foliation also see an increase over time. It seems possible that while the cerebellum performs the same function in all vertebrates, this function becomes more sophisticated through evolution.

Chapter 3

Passive and Active Models of Electrical Activity in Neurons

3.1 Introduction

This chapter provides some background to the computational modelling of neurons and how it is able to simulate the behaviour of these complex systems.

The work in this chapter lays the necessary foundation for understanding the experimentation performed in Chapters 5 and 7. It summarises the knowledge first put forward over 50 years ago by researchers such as Rall in passive modelling, and Hodgkin and Huxley in understanding the electrical activity within neurons, as well as more modern work in computational modelling by De Schutter and Bower.

Throughout this chapter and the rest of the work, the terms "passive" and "active" are used as shorthand for simulations that use only constant electrophysiological parameters, and those that use both constant and voltage-dependent parameters.

Section 3.2 describes the mathematics and reasoning for building computational models of neurons that are biologically realistic in terms of both morphology and behaviour. This begins with representing complex dendritic structures as a series of cylinders in Section 3.2.1, and introducing the electrical parameters necessary for modelling the movement of current through the cylinders. Section 3.2.2 builds on modelling with passive parameters to also include active parameters for modelling ion channels. Finally, Section 3.3 is a summary of the Purkinje cell model created by De Schutter and Bower (1994a,b,c), an important community model that has informed many Purkinje models since its publication, including those used in this study.

3.2 Compartmental Modelling

Computational models of neurons can be created in many ways depending on the desired level of biological realism. A very abstract model will exclude chemical gradients and ion channels, possibly even simplifying electrophysiological behaviour to a binary decision much like a Boolean gate. This kind of model will also lack morphological detail, often existing only as a cell body or point neuron. A very simplified neuron is useful in network models where computational power may be a limiting factor, but is unsuitable for the analysis described in this work.

Each of the models used in this study has a biologically accurate neuronal morphology and use electrical parameters (described in Section 3.2.1) based on in vitro or in vivo studies of electrophysiological behaviour. These include resistance and capacitance parameters based on studies of rat Purkinje cells. The models can be used with just this information as models of the passive electrophysiology, as the work in Section 5.2.1 shows. They can also be expanded upon and given descriptions of voltage-dependent ion channels (see Section 3.2.2 for an explanation of active ion channels) to model the active properties demonstrated in many neurons, Purkinje cells included. This allows for a more biologically realistic model.

In this study, all the models have a detailed cell morphology, each of which has been traced from real Purkinje cells from different species. The complex dendritic form is broken down into a series of cylindrical compartments, which makes both the equations for calculating voltage attenuation and the description of the morphology a much simpler task. Some of the experimentation in this study called for models of passive electrophysiology only (Section 5.2.1), while others required active channels to be included in the models (Sections 5.2.2 and 7.3.3). This section provides an explanation of the mechanics behind each type of model and the differences between them.

3.2.1 Passive Parameters

Passive cable theory describes the movement of current along a cylinder, without any of the non-linearities caused by active ion channels. When modelling neurons, each cylinder, or compartment, is representative of a finite section of a dendrite. The length of compartments is very important for accurate modelling. While these lengths may be determined by a need for morphological accuracy, e.g. splitting a compartment into two to replicate a bend in the dendrite, more often the length of a compartment is limited so it may be considered isopotential. This means that the membrane potential, or voltage, is considered the same at any point of the compartment surface; this simplifies the mathematics greatly. The membrane potential is the difference in the electrical potential inside the membrane and the electrical potential of the extracellular environment.

Splitting a dendritic tree from a single structure into a series of cylinders, first introduced by Rall (1964) has several benefits. Firstly, it allows the equations for finding voltage to be simplified into a series of discrete differential equations

Extracellular

r_m c_m

Intracellular
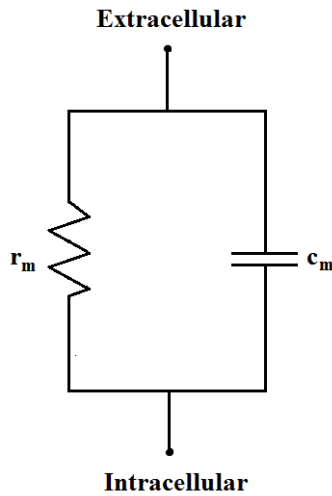
Figure 3.1: A diagram of a patch of passive membrane (or single compartment) represented as an RC circuit.

rather than a far more complex - and computationally intensive - continuous differential equation. It also allows for morphological features such as the tapering of dendritic diameters to be properly modelled. Additionally, splitting a neuron into different compartments also allows for electrical constants, such as the passive parameters described in this section, to be set as different values in somatic and dendritic compartments (Segev and Burke, 1998).

3.2.1.1   RC Circuits

A passive compartmental neuron model is designed like a series of basic resistor-capacitor (RC) circuits (Rall, 1959), due to the similarities between the behaviour of an RC circuit and a passive neuronal membrane when injected with a step current. An RC circuit contains a resistor and capacitor in a simple parallel circuit, as shown in Figure 3.1. When modelling neurons, the dendrites are imagined as cables, with the resistance and capacitance being properties of that cable. The resistance of a cable describes the difficulty of reaching a given level of current through the cable, or more accurately, how much voltage is required to maintain a level of current. A cable with a high resistance will require a larger voltage to maintain current than a cable with a lower resistance. Conductance is the inverse of resistance, describing the ease of movement of current, or the level of current given the current voltage.

In cable theory, resistance is described by the membrane resistance and axial resistivity. Axial resistivity describes the flow of current within the cable as described previously. The walls of dendritic cables are permeable to ions, meaning that it is also possible to lose current through the dendritic membrane. Membrane resistance describes how difficult it is for current to flow in this way. Den-

dritic membrane is much more insulated than the core, making this membrane resistance often much higher than axial resistivity (Segev, 1998). As described below, resistance and conductance are dependent not only on the material the cable is made from, but also the dimensions of the cable. Axial resistivity will increase with the length of cable, and decrease if the cable becomes wider. The membrane also has a capacitance, which is how much electrical charge can be stored in the membrane, with a higher capacitance indicating that more charge can be held.

Calculating the voltage at any point in the cable requires several features of the cable and the input to be characterised: the resistance of the membrane (r_m) and resistivity of the cable (r_a) in ohms, the capacitance of the membrane (c_m) in farads, and the input current (I) in amperes. Additionally, the passive electrical parameters (r_m, r_a, c_m) are dependent on the the length and diameter of the cable. Specific parameters for the membrane resistance and capacitance represent the values for a square centimetre (or metre in some notations), which can then be scaled to dendritic compartments. The axial resistivity scales with length as well as area. Scaling is performed with the following equations:

$$r_m = \frac{R_m}{\pi dl} \tag{3.1}$$

$$r_a = \frac{4lR_a}{\pi d^2} \tag{3.2}$$

$$c_m = \pi dl C_m \tag{3.3}$$

where d is the compartment diameter, and l the length. The specific resistances and capacitance are constant values that represent the physical properties of the medium.

Axial resistivity, r_a, is the resistance to current flow within the cable and decreases as the cable diameter increases, therefore decreasing voltage attenuation. Membrane resistance also decreases with increases in diameter, but this means that it is easier for current to leak through the membrane. Voltage can also drop by current charging the membrane capacitance. This also increases with compartment diameter as it indicates an increase in storage capacity. Current that is not lost crossing or charging the membrane is measured as a function of time (t) since injection and distance (x) from input site.

These parameters can then be used to find the length and time constants that describe the change in voltage and the speed of that change within and between compartments. Within a closed RC circuit, a circuit without axial current flow, the total current is equal to the capacitive current and the resistive current. This total current is zero when no external current is applied. This is known as Kirchhoff's Circuit Law. When current is injected into the circuit, the voltage of the circuit for any given time can be found be solving equation 3.4, where t is time and I_{inj} is the injected current.

$$c_m \frac{dV}{dt} + \frac{V}{r_m} = I_{inj} \tag{3.4}$$

The general solution for Equation 3.4 is given in Equation 3.5, which assumes the resting potential of the membrane is zero. It shows that when a positive current is injected continuously, the voltage will increase exponentially towards $V = IR$.

$$V(t) = IR(1 - e^{-t/\tau_m})\ (3.5)$$

3.2.1.2 The Membrane Time Constant and The Length Constant

Equation 3.5 introduces the membrane time constant τ_m(Rall, 1969a). When injecting a steady current over time, at the point at which $t = \tau_m$, the voltage $V(t)$ will have reached 63.2% $(1 - 1/e)$ of its value after infinite time has passed. The time constant is dependent on the passive properties of the membrane (see equation 3.6) and is an important descriptor of the behaviour of the membrane, as it governs how quickly it responds to the onset of current, and how quickly the voltage attenuates once the current injection ends. The time constant will usually be found in the range of 10-100 ms (Dayan and Abbott, 2001).

$$\tau_m = r_m c_m\ (3.6)$$

The length constant λ is an important parameter for voltage attenuation across distance. Given an infinite length of cable, the voltage at distance λ from point x on the cable has always attenuated to 36.8% $(1/e)$ of the voltage measured at x, which is an exponential decrease. The length constant is defined as:

$$\lambda = \sqrt{\frac{r_m}{r_a}}\ (3.7)$$

The length of compartments is often derived from the branching structure of the dendrite, but long sections can be split based on their electrotonic length. The electrotonic length of a cable is the length divided by the length constant, which quantifies the distance from a current injection site to the point where the voltage has attenuated to 36.8% $(1/e)$ of its original magnitude. Splitting compartments to a fraction of the length constant (often to less than 0.1) improves the accuracy of calculations. The process of resizing dendritic compartments based on their electrotonic length is known as re-meshing the cell. Figure 3.2 shows two diagrams of two of the cells from this study with each compartment drawn using its electrotonic length rather than its physical dimensions. Images of the compartmental models can be found in Section 4.2. To make this image, the electrotonic length of each compartment was recorded using neuroConstruct 1.6 (Gleeson et al., 2007). This length vector was then used to replace the original length vector for compartments in the Trees Toolbox (Cuntz et al., 2010) construct for dendritic trees. The Trees Toolbox tree plotting function was then used to make the dendrogram.

With both the length and time constants, the full cable equation to find voltage V at point x and time t is (Segev, 1998):
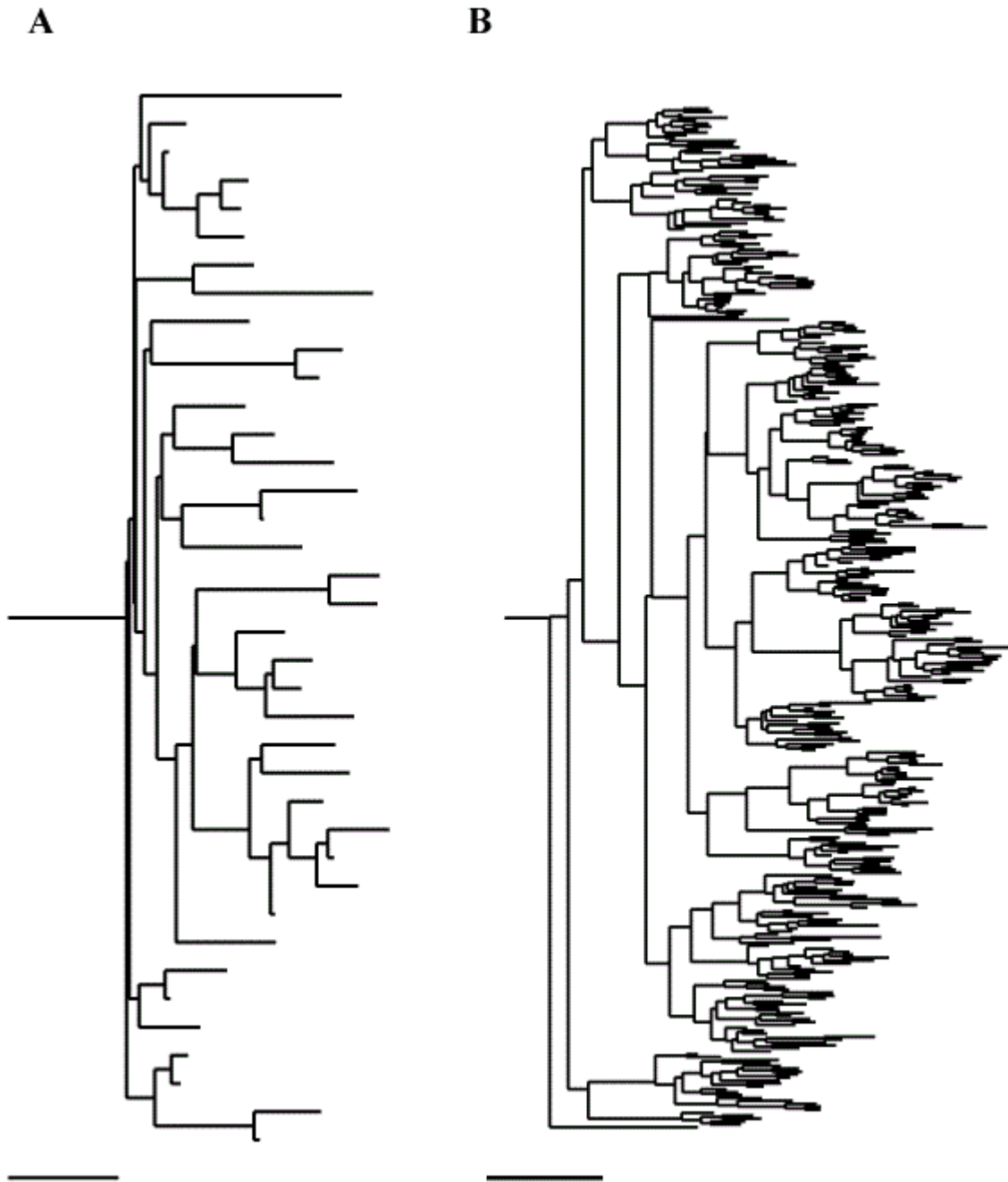
Figure 3.2: Dendrograms are a visual representation of the electrical compactness of neural dendritic trees. The length of each compartment is scaled based on its electrotonic length. *A* is the dendrogram for the fish Purkinje cell used in this study, while *B* shows the same for one of the rat cells. Scale bar shows λ
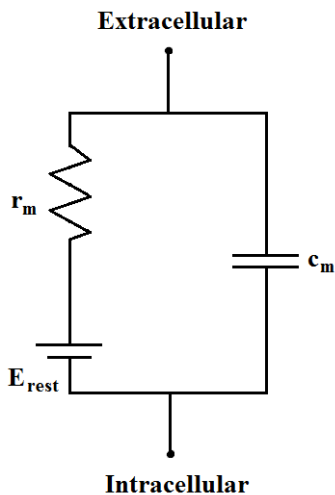
Figure 3.3: The resting potential is displayed as a battery on the circuit diagram for the compartment, as there is a difference between the intracellular resting potential and the extracellular potential, and this requires movement of charged ions to maintain.

$$\lambda^2 \frac{\partial^2 V}{\partial x^2} - \tau_m \frac{\partial V}{\partial t} - V = 0 \qquad (3.8)$$

3.2.1.3   The Resting Potential

In the preceding sections, the resting potential of the compartment is assumed to by $0\ mV$. This is mathematically simpler, but is biologically unrealistic. A cell's resting potential is the value of the membrane potential that the cell returns to when not receiving any injected current. Many neurons have a resting potential of approximately $-65\ mV$ (Sterratt et al., 2011). This means that the intracellular potential is $65\ mV$ lower than the potential of the extracellular environment. To maintain this difference in potential, the compartment must have a source of voltage, depicted in Figure 3.3 as a battery.

Voltage in neurons is created by the movement of charged ions through the membrane. Neuronal membrane is largely made of lipids, which is impossible for the ions to move through, but also has channels that can selectively allow ions through. Were these ion channels not selective, the ions would diffuse such that their concentrations in the intra- and extracellular media became uniform. These selective channels disrupt this diffusion enough to allow for differences in concentrations of ions within and outside the cell. An ion channel can be passively or actively permeable to ions, and is selectively permeable to specific types of ion. Active ion channels, discussed in the Section 3.2.2, are open to the movement of ions only in response to changes in the environment. Passive ion

channels do not vary how permeable they are to ions.

The movement of positively charged ions out of the cell causes the cell to become negatively charged. Many neurons have a larger concentration of potassium ions, which are positively charged, within the cell than there are extracellularly (Sterratt et al., 2011). This difference between the concentrations means that, given a permeable channel, the potassium ions will diffuse following their concentration gradient (meaning that the particles move from where there is a high concentration to where the concentration is lower). With this movement of ions and creation of a negative charge, there is then an electrical pull for positively charged ions to move into the cell. This pull can be strong enough to force the ions to move against their concentration gradient. Given time, these two forces will create a net flux (flux referring to the number of ions moving across the cell membrane) to become zero, and for the potential for this ion to become stable. This is known as the equilibrium or reversal potential for the ion type.

Finding the reversal potential for a single ion can be achieved by solving the Nernst (1888) Equation, given that the concentrations for the ion inside and outside the membrane is known. For example, Equation 3.9 shows the Nernst equation for sodium. The first term includes R, the universal gas constant, and F, the Faraday constant. T is the temperature in Kelvin, as thermal energy is an aid in ion movement across a membrane, and z_{Na} is the charge of the ion, which is $+1$ in the case of sodium. The second term is the ratio of sodium concentrations inside and outside of the cell.

$$E_{NA} = \frac{RT}{z_{Na}F} \ln \frac{[Na_{out}]}{[Na_{in}]} \tag{3.9}$$

In the absence of active ion channels, the resting membrane potential is equal to the reversal potential of a passive channel called the leak conductance, which is mainly permeable to potassium. A leak conductance models the loss of current through the dendritic membrane, the inverse of the membrane resistance. When active channels are present, the resting membrane potential becomes a function of the reversal potentials of any active channels that are open at rest and the leak conductance.

3.2.1.4 Joining Compartments

The previous segments of this section have described the electrical diagrams of a single patch of passive membrane, and therefore a single compartment. The first step towards replicating real neuronal morphology is to join compartments to simulate a length of dendrite. Current moving within a compartment, as opposed to through the membrane, will flow from the point of injection along the cable in both directions. The intracellular medium is not a perfect conductor, having a resistance (see Equation 3.2) that increases with the length of the compartment and decreases with the compartment cross section area.

In Figure 3.4, there are three joined compartments labelled x, y, and z. Kirchhoff's law, as described in Section 3.2.1.1 applies across compartments as
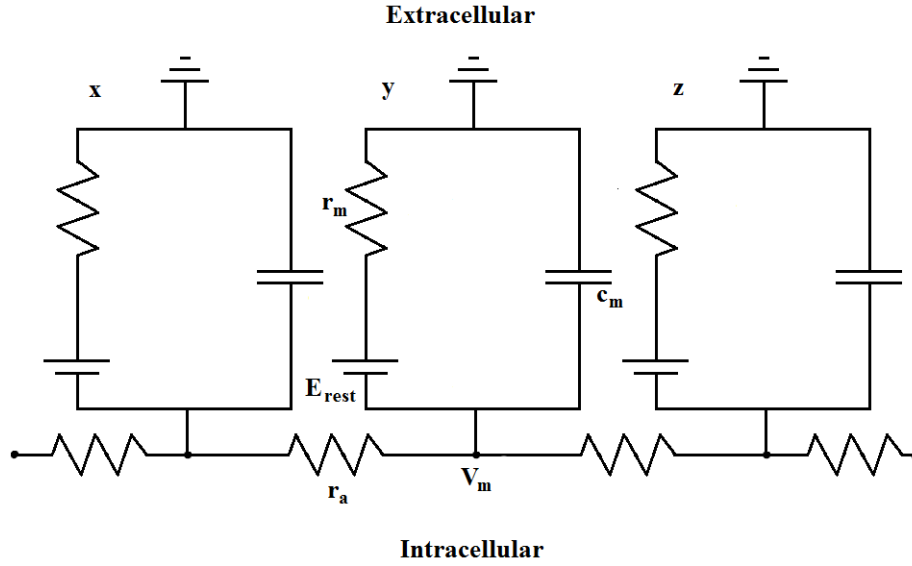
Figure 3.4: Electrical diagram of several compartments in series. The extracellular environment is assumed to be 0 mV, this is depicted in the diagram as going to ground

well as within single compartments. Total current is still the sum of capacitive and resistive currents, with the inclusion of current flowing through the axial resistance. This change to Equation 3.4 is reflected in Equation 3.10. Note also the inclusion of the resting potential - as it is no longer assumed to be 0, membrane voltage must be taken as the difference between the current and resting potentials.

$$c_m \frac{dV_y}{dt} + \frac{V_y - E_{rest}}{r_m} + \frac{V_x - V_y}{r_a} + \frac{V_z - V_y}{r_a} = I_{inj} \qquad (3.10)$$

This is accurate for a length of dendrite, but changes again when the dendrite branches or ends. Cable theory gives three types of dendrite endings: sealed, leaky, and the killed or dead end. These are known as boundary conditions. In his work on cable theory, Rall (1969b) solved the cable equation for each type of end, but the sealed end is the best approximation of a dendritic tip. This is because dendrites taper towards the tips, their diameter becomes smaller towards the end. This means a decrease in the surface area of the membrane, which increases the axial resistivity until no current flows at all (Rall and Agmon-Snir, 1998).

3.2.2   Adding Active Channels

In the previous section, the building blocks for a passive neuronal model were described and joined into a section of neurite in Figure 3.4. While it is a useful

starting point, this model is still incomplete for simulating realistic neurons as it lacks the active ion channels that have been found in many dendrites, and more crucially, any realistic sources of input. To simulate a biological neuron and its electrophysiological responses fully, the model will need to include synaptic channels to receive input, and active ion channels that adjust their permeability to different ions depending on the membrane voltage or on ionic concentrations within the cell.

With synaptic inputs come changes to membrane potential. In a cell receiving input, these are called post-synaptic potentials (PSPs). These can be depolarising excitatory potentials (EPSPs), or hyperpolarising inhibitory potentials (IPSPs). Synaptic potentials spread from the point of input, typically in the dendrites of neurons. If an EPSP, or a sum of EPSPs, creates a strong enough change in the membrane potential in the soma or axon, the neuron may produce an action potential. This is a brief increase in potential above 0 mV before falling below the resting potential. Action potentials, or spikes, are incredibly important to neuronal communication.

3.2.2.1 Synaptic Channels

In the voltage equations throughout Section 3.2.1, the source of current is assumed to be a step or continuous current injection, replicating stimulation from an electrode. For a cell in vivo, input is received from other cells synapsing onto the dendritic processes. The area of the pre-synaptic neuron that contacts the post-synaptic neuron contains synaptic vesicles that carry neurotransmitters that travel into the post-synaptic neuron when stimulated by an action potential (Dayan and Abbott, 2001). The neurotransmitters then bind to ionotropic receptors in the post-synaptic neuron, which triggers the opening of ionic channels. Neurons also contain metabotropic receptors; when neurotransmitters bind to these receptors they instead trigger a cascade of signalling processes within the cell.

Unlike the passive membrane parameters described in the previous section, that are independent constants, active synaptic and ionic channels will have dependencies on membrane voltage or ion concentrations that change their conductance. This change in conductance is denoted in electrical diagrams as a variable resistor (see Figure 3.5). Some types of neurotransmitter-mediated synaptic channel can be accurately modelled using only time dependencies (Segev and Burke, 1998).

The time-dependent synaptic channel shown in Figure 3.5 adds a new path for current through the membrane in comparison to the passive case in Figure 3.3. As such, the voltage equation, following Kirchhoff's law of current, must also gain a new term. It is also important to note that although they are represented as resistors in electrical diagrams, synaptic and ionic channels are defined by their conductance (inverse of resistance) rather than their resistance. This will also be reflected in the notation for voltage equations in this section, such as Equation 3.11, as is the change from injected current I_{inj} to simply the membrane current I_m.
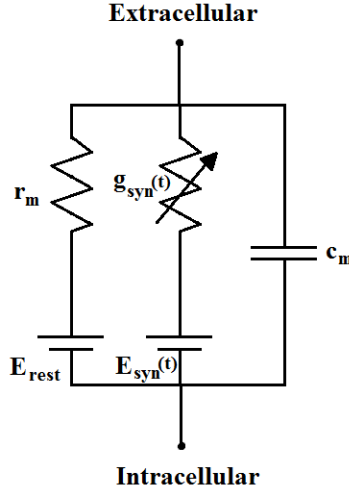
Figure 3.5: Electrical diagram of a single compartment containing passive parameters and a variable resistor representing a time-dependent synaptic channel

$$c_m \frac{dV}{dt} + \frac{V - E_{rest}}{r_m} + g_{syn}(V - E_{syn}) = I_m \qquad (3.11)$$

The updated voltage equation (Equation 3.11) now has three terms reflecting the three paths for current through the membrane that are shown in Figure 3.5, satisfying Kirchhoff's law of current. While the synaptic conductance is voltage-independent in this instance, it is not a constant. The change to a time-dependent conductance can be approximated in several ways, with two of the most accurate and widely-used being alpha functions (Rall, 1967) and dual exponential functions.

An alpha function uses a single exponential and time constant that governs both the rise and decay of the conductance following an input spike stimulating the release and binding of neurotransmitters. The function assumes an exponential decay time and a proportional rise time to reach peak conductance (Roth and van Rossum, 2009).

$$g_{syn}(t) = \bar{g}_{syn} \frac{t - t_i}{\tau} e^{1 - \frac{t - t_i}{\tau}} \qquad (3.12)$$

In Equation 3.12, the conductance at time t, following the arrival of input at time t_i, is dependent on the time passed since the input and on the maximum possible conductance $\bar{g}_{syn}$. Having rise and decay times correlated in this way can give good approximations to some synapse types but this is unrealistic and not suitable for all models. When the modelled synapse requires rise and decay times to be independent, it is necessary to use a dual exponential function. The models used in this study use independent rise and decay times for the modelling of synaptic channels. As is indicated in the name, a dual exponential function

models both the rise and decay phases of the conductance with a separate exponential, as shown in Equation 3.13, where τ_1 is the rise time and τ_2 is the decay time of the conductance.

$$g_{syn}(t) = \bar{g}_{syn} \frac{\tau_1 \tau_2}{\tau_1 - \tau_2} (e^{1 - \frac{t - t_i}{\tau_1}} - e^{1 - \frac{t - t_i}{\tau_2}}) \tag{3.13}$$

Typically the rise time constant is much shorter than that of the decay time, due to many neurotransmitters binding to the synaptic channels much more quickly than they unbind (Roth and van Rossum, 2009).

While some synaptic channels can be accurately modelled with only a dependence on time, the same cannot be said of all synaptic channels, nor of many ion channels, the permeability of which are dependent on the intracellular and membrane conditions. The addition of these types of channels is the difference between the "passive" models that have been described so far and "active" models. NMDA-type (N-methyl-D-aspartate) receptive synaptic channels are dependent on both the concentration of magnesium ions and the membrane voltage due to magnesium blocking the channel when the membrane potential is at rest or lower (Mel, 1993). In this case, the function for channel conductance appears as in Equation 3.14; in which τ_1 and τ_2 are the rise and decay times as before, η is the magnesium dependency ($0.33/mM$), $[Mg^{2+}]$ is the concentration of magnesium ions ($1mM$), and γ is the voltage dependency ($0.06/mV$) (Mel, 1993).

$$g_{NMDA} = \bar{g}_{NMDA} \frac{e^{-t/\tau_1} - e^{-t/\tau_2}}{1 + \eta[Mg^{2+}]e^{\gamma V_m}} \tag{3.14}$$

3.2.2.2 The Action Potential

A commonality of all neurons is the ability to produce an action potential, also known as a spike. This is the neuron's method of communication - an all-or-none non-linear phenomena, a fleeting increase in voltage once a threshold of depolarisation is met, followed by a refractory period where the membrane potential dips below its resting state (see Figure 3.6). The term all-or-none refers to the fact that the membrane potential must meet some threshold before a spike will fire, but the amplitude and shape of the spike will always be the same regardless of how high above the threshold the depolarisation becomes before the spike fires (Hodgkin et al., 1952). All-or-none describes a binary condition, there is either a spike fired or there is no spike, it is not possible to have partial spikes.

The amplitude of an action potential is typically 100 mV above the resting potential, as seen in Figure 3.6, and lasts for approximately 1 ms (Dayan and Abbott, 2001). This sudden rise in voltage can be linked to the opening of sodium and sometimes calcium channels as the membrane potential increases. Sodium and calcium ions both carry a positive charge (calcium ions carry two positive charges), meaning a sudden influx of these ions into the neuron will rapidly increase the membrane potential.
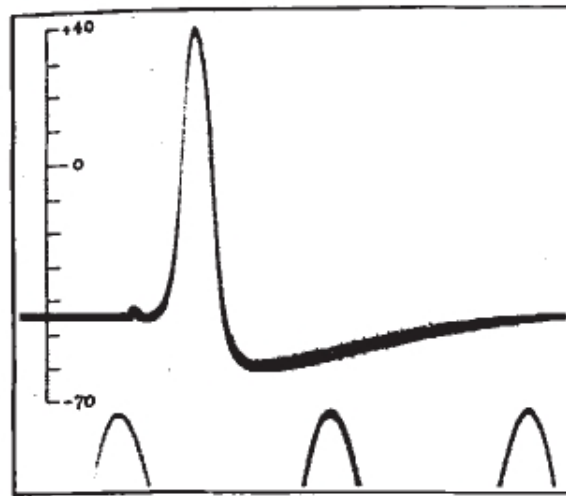
Figure 3.6: An action potential recorded from the squid giant axon (Hodgkin and Huxley, 1939, fig. 2)

Following the spike is the refractory period. This lull in the membrane potential is caused by the opening of potassium channels that has been triggered either by voltage or by the increase in concentration of calcium ions. The opening of these channels causes the positively charged potassium ions to leave the neuron due to the low concentration of potassium in the extracellular medium. The refractory period is notable not just because the membrane potential drops below the resting value, but also because the cell remains incapable of depolarising to the point of producing another spike for several milliseconds.

Action potentials are incredibly important to the function of the brain. Changes in neuron membrane potential that do not reach the threshold required for spiking have only a very local effect (Purves et al., 2012). How local sub-threshold fluctuations can be are explored in the modelling experiments in Chapter 5. An action potential can travel across a single neuron but can also travel the length of axons to affect other neurons; spiking is the language of the brain, and the only way to carry information through the brain and central nervous system.

3.2.2.3   Active Ion Channels

Adding ion channels to a model is important for verisimilitude, but any active channels will add non-linearities that greatly increase the unpredictability and complexity of the model. Ion channels are pores in the membrane that are predominantly permeable to one type of ion, allowing it to move through the cell membrane. Much like the NMDA-type synaptic channels discussed in Section 3.2.2.1, ion channels are typically dependent on the intracellular environment; whether or not they allow ions to pass through the membrane will change based

on factors like the membrane potential and the concentration of other ions. The movement of charged ions creates current. The total current created by ion channels is simply the sum of each individual channel current:

$$I_{ion} = \sum_c I_c = \sum_c G_c(V_m - E_c) \tag{3.15}$$

Some ion channels become permeable to ions when the membrane potential increases or decreases to a given threshold, making them voltage-dependent. These channels are often modelled using schemes first devised by Hodgkin and Huxley in 1952. These schemes are remarkable as Hodgkin and Huxley were able to create them before the structure and biology of ion channels was known. The original schemes were designed to simulate the sodium and potassium channels found in the squid giant axon. The series of papers that explain the Hodgkin-Huxley (HH) model are rooted in earlier work, including a 1949 paper by Hodgkin and Katz that investigated the possibility of membrane potential effecting intracellular concentrations of sodium and potassium. These two ion channels became the basis of the HH model.

The making of the HH model - a series of kinetic schemes and equations describing action potentials - was possible due to both new technology in the form of voltage and space clamping (Marmont, 1949; Cole, 1968), and the fortuitous physiology of the squid giant axon. Voltage and space clamping uses pairs of dual electrodes to "clamp" the membrane potential to a desired voltage, and to keep that voltage uniform across a section of membrane. These new techniques were vital to explore whether or not voltage-dependent mechanisms exist in the squid giant axon.

Using the squid giant axon was essential for the success of Hodgkin and Huxley's studies of ion channels for two reasons. Firstly, the sheer size of the axon - up to 1 mm in diameter - was unique in allowing for the insertion of electrodes for the space and voltage clamping, particularly given that the electrodes used at the time were larger than the ones used today. Additionally, the squid giant axon has a much simpler electrophysiology than many other axons as the sodium and potassium channels are effectively the only channels that are voltage-dependent. This simplicity stems from the simple function of the giant axon. It is understood to be involved with the movement of the squid's mantle, used to propel the squid through water, resulting in a regular firing pattern that doesn't require a complex system of ion channels to achieve (Bower and Beeman, 1998).

To find the effect of a single ion channel, Hodgkin and Huxley used what is known as the ion substitution method, where ions are removed from the extracellular environment (Sterratt et al., 2011). In this case, sodium ions were removed from the extracellular medium to reduce the sodium current to negligible levels. Voltage clamp results from cells in this medium could then be compared to results from those in a standard seawater medium to find the effect of sodium channels. This would not have been so simple if the squid axon had a larger number of ion channels effecting the overall ion conductance (Nelson and Rinzel, 1998).

With this new information on the voltage-dependencies of sodium and potassium channels in the squid axon, the next step was to create a mathematical model that could emulate this behaviour. First, each channel is given a number of gates that could be in an "open" or a "closed" state to ions. Each gate of a channel needs to be in it's "open" state for the channel itself to be considered open to the movement of ions. The transition of gates between the open and closed states are described using a first-order kinetic scheme (see Equation 3.16), meaning that the two states have rates of transitioning and there is a set probability that a gate will be in a given state at time t. By convention, the transition rate constant to open a gate is written as $\alpha_i(V)$ and to close as $\beta_i(V)$, with each being voltage-dependent. The probability that the gate is in either state is simply p_i to be open and $1 - p_i$ to be closed, though these can be extrapolated in larger systems to represent the fraction of gates open or closed rather than a probability (Nelson and Rinzel, 1998).

$$\frac{dp_i}{dt} = \alpha_i(V)(1 - p_i) - \beta_i(V)p_i \tag{3.16}$$

An open channel, one that has all its gates in the open state, adds a small constant amount to the total conductance for channels of that type. This means that the total conductance for that channel is proportional to the probability that gates are currently in their open state (Equation 3.17), given that this probability is proportional to the number of open gates in a large number of channels.

$$G_{chan} = \bar{g}_{chan} \prod_i p_i \tag{3.17}$$

Equation 3.18 shows the simplest case for finding the total conductance of a channel type, using potassium as an example. Potassium is modelled using four gates that all use the same kinetic scheme, the probability of the gates being in the open state are denoted here as n rather than p_n, using the Hodgkin and Huxley naming convention.

$$G_K = \bar{g}_K n^4 \tag{3.18}$$

Not all ion channels can be modelled with a single gate type in this way. The sodium channel from the HH model is one such example, using three m gates and an h gate (Equation 3.19). Sodium channels cannot be modelled in the same way as those for potassium as sodium channels will inactivate where giant squid axon potassium channels do not. Activation refers to the rise in conductance with the depolarisation of the membrane potential; if the conductance reaches a maximum point and decays back to its resting state while the membrane potential remains depolarised, that channel has inactivated (Sterratt et al., 2011).

$$G_{Na} = \bar{g}_{Na} m^3 h \tag{3.19}$$

Channels that are dependent on ion concentration, such as the two calcium-dependent potassium channels used in this study and the De Schutter-Bower model (discussed in Section 3.3), still have a number of gates that each have a probability to be in the open or closed states. Equation 3.16 holds true for both activating and inactivating voltage-dependent channels, and also for the calcium dependent channels. The difference in dependencies can be see in the equations for the gating functions. In the HH model, the voltage-dependent gating functions for potassium are given as in Equation 3.20:

$$\alpha_i(V) = 0.01 \frac{V+55}{1 - e^{(-V+55)/10}}, \qquad \beta(V) = 0.125 e^{(-(V+65)/80)} \qquad (3.20)$$

In De Schutter and Bower's paper, the equations for the activation of the calcium-dependent channels was given as shown in Equations 3.21, 3.22 where z represents the probability of the calcium-dependent gates being open, or p_z.

$$\frac{dz}{dt} = \frac{z_\infty - z}{\tau_z} \qquad (3.21)$$

$$z_\infty = \frac{1}{1 + \frac{A}{[Ca^{2+}]}} \qquad (3.22)$$

τ_z in Equation 3.21 is the time constant of the channel and A in Equation 3.22 the dissociation constant; molecules have the ability to bind together, a dissociation constant for a molecule is the ratio between the concentration of unbound molecules and the concentration of bound molecule products once their concentrations have reached equilibrium (Sterratt et al., 2011). z_∞ is the limiting value, this can also be found for the voltage-dependent equations by dividing through Equation 3.16 by $\alpha_i(V) + \beta_i(V)$, as seen in Equations 3.23, 3.24 (Dayan and Abbott, 2001) (where i refers to the p_i for some generic channel).

$$\tau_i(V) \frac{di}{dt} = i_\infty(V) - i \qquad (3.23)$$

$$\tau_i(V) = \frac{1}{\alpha_i(V) + \beta_i(V)} \qquad (3.24)$$

This means that the limiting factor for the generic voltage-dependent channel i is defined as Equation 3.25.

$$i_\infty(V) = \frac{\alpha_i(V)}{\alpha_i(V) + \beta_i(V)} \qquad (3.25)$$

The HH model is described here as it is still used in modelling today, including in the GENESIS simulations undertaken in this study.

3.3 De Schutter-Bower Purkinje Model

The De Schutter-Bower computer model of a hybrid guinea pig/rat Purkinje cell is one of the most studied and shared models in the field. Much like the models used in this study, it began as a passive model (Rapp et al., 1994) and was later updated to include ion channels (De Schutter and Bower, 1994a,b,c). These channels were tuned until the firing frequencies and patterns elicited from the model under different inputs matched those seen in in vitro experimentation. Since then the active model has been used by many laboratories for testing the performance and computational function of the Purkinje cell using different techniques; from channel blocking (Miyasho et al., 2001) to pattern recognition (De Schutter and Steuber, 2009).

The earliest model of a Purkinje cell reconstructed from real anatomical data was created by Shelton in 1985. This was a passive model built to replicate the morphology of a rat Purkinje cell, although the electrophysiological data used to tune the passive parameters of the model was from guinea pig cells. Three later models, each reproducing the morphology of a guinea pig Purkinje cell, were designed by Rapp et al. in 1992. These were also passive models, with the passive parameters derived using experimental data obtained specifically for this purpose. Originally written for a program called SPICE (Vladimirescu and Pederson, 1981), the descriptions of the morphology of these cells were translated to the GENESIS platform (Bower et al., 2003) before being used by De Schutter and Bower.

Purkinje cells are known to have thousands of spiny protrusions across their dendritic trees. For the De Schutter-Bower model, De Schutter and Bower estimated that a guinea pig Purkinje cell would have approximately 150,000 spines based on the work by Harvey and Napper (1991). Due to what is cited as a lack of data on the position and shape of spines for rat or guinea pig cells, De Schutter and Bower only explicitly modelled spines when simulating input from granule cells, and modelled them implicitly when simulating current injections. To implicitly model spines they mimicked the presence of spines by expanding the membrane surface of dendritic compartments that were designated part of a spiny branchlet. The dendrites were separated into categories based on their diameter; connected to the soma is the main dendrite, which includes the compartments with the largest diameters. The first compartments branching from the main dendrite are known as the "smooth" or "thick" dendrites, once the diameter thins to beneath a threshold these become the "spiny" dendrites. The increase to membrane surface of spiny compartments was based on the estimations of spine surface area in rat Purkinje cells by Harris and Stevens (1988), where each spine was assumed to have a membrane surface of 1.33 μm^2. When modelled explicitly, spines were made up of two compartments, a spherical head and cylindrical neck. Each spine head had a diameter of 0.54 μm and each neck a diameter of 0.2 μm and length of 0.66μm. Due to computational limitations, De Schutter and Bower were unable to explicitly model 150,000 spines. They chose to model approximately 1% of the estimated number of spines, and compensated for the reduction in spines, and by extension reduction in synapses, by

still including some increase to membrane surface area and increasing the firing rate at each synapse.

Taking new experimental data to increase the accuracy of models was an important precedent set by Rapp et al. (1994). Unfortunately, the De Schutter-Bower studies found that the passive parameters used by Rapp et al. (1994) did not allow the model to replicate Purkinje firing patterns once the active ion channels were added to the cell. It was particularly important to significantly raise the membrane resistance (R_m) in the soma to avoid dampening the effect of incoming current. This change meant that the soma of the active model has an R_m of 10 $k\Omega cm^2$ compared to 0.44 $k\Omega cm^2$ in the original passive model; the active dendrites have a lowered R_m, 30 $k\Omega cm^2$ from the passive 110 $k\Omega cm^2$. More modern Purkinje cells models use a single R_m value for both soma and dendrites, as is the case for the Roth and Häusser models (2001), the passive parameters of which were also used in the current work. Membrane capacitance (C_m) and axial resistivity (R_a) were unchanged from the passive model at 1.64 $\mu F/cm^2$ and 250 Ωcm^2 respectively.

The model included a leak current, with a reversal potential of -80 mV, in addition to the voltage-activated channels described below. When the model lacked background inputs, the model was considered to be modelling in vitro behaviour and had a steady resting potential of -68 mV. The inclusion of background excitatory and inhibitory inputs allowed for the modelling of in vivo behaviour. In this state, the model would fire sporadically, and was able to replicate Purkinje cell behaviour more accurately. When this background input was provided, the membrane potential did not return to -68 mV, even if the input was later stopped. Instead, the model would return to a semi-stable state of -50 to -55 mV. This followed other evidence at the time that background input had an effect on the passive electrical properties in pyramidal (Bernander et al., 1991) and Purkinje cells (Rapp et al., 1992).

Ten ion channels were then added to the model based on in vitro, voltage clamp and single channel studies of Purkinje cells. While the majority of these studies use rat cells for their experimentation, Hounsgaard and Midtgaard (1988) and Llinás and Sugimori (1980a,b) use in vitro recordings from turtle and guinea pig cells respectively. Channels added included two sodium, two calcium and several potassium channels. These are listed in full along with their reversal potentials in Table 3.1. Each of the voltage-gated channels have their conductance modelled using the Hodgkin-Huxley-type equations (1952), while the calcium-gated channels have an additional term for calcium activation.

De Schutter and Bower did not distribute the ion channels equally over the neuron model. Using trial and error, and based on what was known about their distribution across the cell, the distributions and densities of the active channels were varied until the model was able to accurately replicate the firing patterns and frequencies of both Purkinje cells in vitro using current injections, and the firing patterns characteristic of Purkinje cells in vivo.

Sodium channels were added to the soma compartment, fast potassium channels were added to both the soma and main dendrite. The entire dendrite has calcium and calcium-activated potassium channels distributed throughout. Af-

Channel Name	Reversal Potential (mV)
Fast Sodium	45
Persistent Sodium	45
P-Calcium	135
T-Calcium	135
Anomalous Rectifier	-30
Delayed Rectifier	-85
Persistent Potassium	-85
A	-85
BK Calcium-activated Potassium	-85
K2 Calcium-activated Potassium	-85

Table 3.1: The 10 active channels added to the De Schutter and Bower model, and used in the cell models in the current studies, with their reversal potentials

ter testing different channel densities, De Schutter and Bower found that the smooth and spiny dendrites did not require different densities for accurate replication. The full channels used and their reversal potentials (see Sections 3.2.1 and 3.2.2 for an explanation of reversal potentials in passive and active models respectively) can be seen in Table 3.1. The channels were chosen by De Schutter and Bower following studies on channels in Purkinje cells by Hounsgaard and Midtgaard (1988) and Llinás and Sugimori (1980a,b, 1992). Equations for the channel kinetics for the anomalous rectifier were based on Spain et al. (1987), and those for the delayed rectifier and slow persistent potassium current on (Yamada et al., 1989).

Channel conductance was determined by the product of the voltage-dependent gates (both activating and inactivating), and the calcium-dependent gates where applicable. This is shown in Equation 3.26 where m represents the activating voltage-dependent gates, h the inactivating voltage-dependent gates, and z the activating calcium-dependent gates (De Schutter and Bower, 1994a).

$$G(V, [Ca^{2+}], t) = \bar{g}m(V,t)^p h(V,t)^q z([Ca^{2+}], t)^r \qquad (3.26)$$

De Schutter and Bower derived their equations for the voltage-dependent channels based on the original work of Hodgkin and Huxley, with the channel kinetics parameters (e.g. peak conductance) gathered from experimental data where possible. These equations, and those for the calcium-dependent channels, are described in detail in Section 3.2.2.3.

The inclusion and tuning of each of these channels was critical to allow the model to successfully recreate the distinctive firing patterns of the Purkinje cell. It was especially important that the model was able to capture the two different modes of firing, the steady simple spiking linked to sodium channels, and the infrequent complex spikes that occur due to calcium channels. An explanation of the differences between these firing patterns and traces of these patterns as seen in different species can be found in Section 2.3.2.
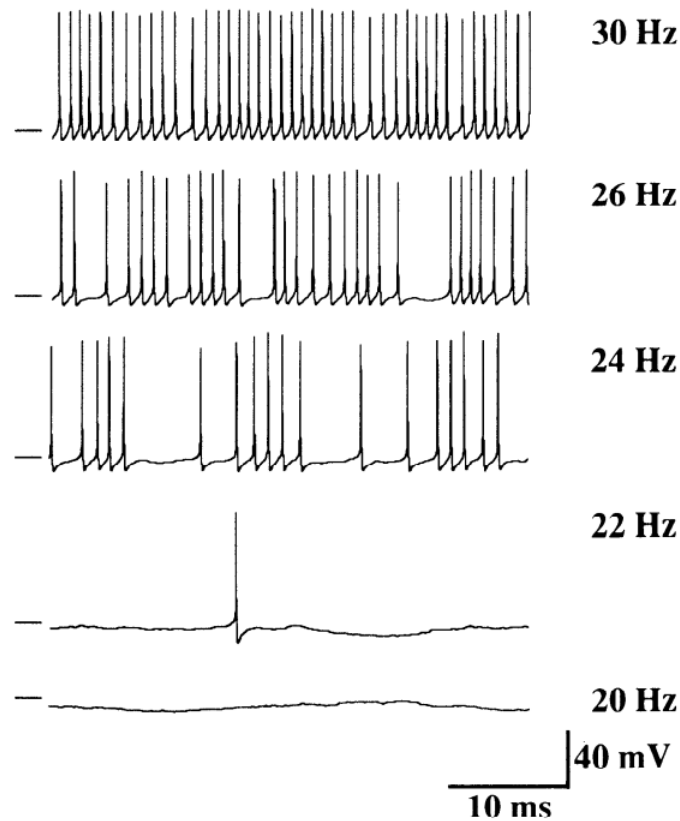
Figure 3.7: Simple spiking observed in the De Schutter-Bower Purkinje cell model following asynchronous excitatory firing from granule cells and 1 Hz inhibitory firing from stellate cells (De Schutter and Bower, 1994b, fig. 7)

The fast sodium channel is particularly important for spiking in Purkinje cells, as it governs depolarisation in the soma. It is especially associated with simple spiking, which refers to a series of spikes with a regular amplitude and interval. A replication of this firing pattern from the De Schutter-Bower model can be seen in Figure 3.7, which was recorded from the soma compartment following the asynchronous firing of modelled granule cell synapses and stellate synapses firing at 1 Hz.

Voltage plateau responses at soma are thought to be caused by the channel known as the persistent sodium channel. In the De Schutter-Bower model the two sodium channels have similar slopes, but different thresholds of activation, based on a variety of steady-state clamping data. The two calcium channels, T- and P-type, both have several published studies on their activation and inactivation. T-type calcium channels are inactivating with a low threshold of activation, while P-type is a high-threshold channel that inactivates slowly.
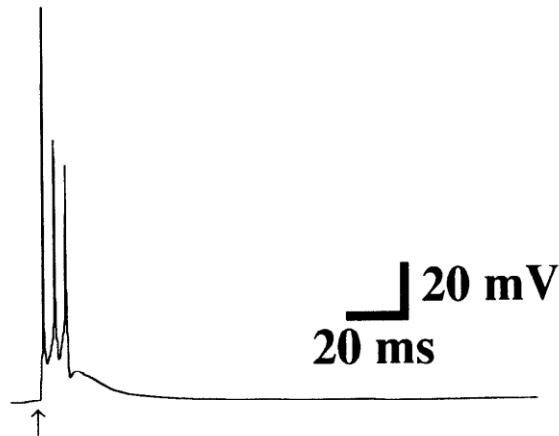
Figure 3.8: A complex spike recreated by the De Schutter-Bower Purkinje model (De Schutter and Bower, 1994b, fig. 1A). The arrow indicates when the climbing fibre input was activated.

Calcium channels, particularly the P-type channels, are involved with complex spiking - a unique firing pattern than occurs when a climbing fibre fires on to a Purkinje cell. Complex spikes have an unusual shape (see Figure 3.8 for the De Schutter-Bower model recreation) and a longer refractory period due to the activation of BK potassium channels.

In addition, the model also has four potassium channels. Two of these, the persistent and "A" types, are voltage-gated, while the "BK" and "K2" channels are calcium-gated. The two voltage-gated potassium channels were modelled from limited electrophysiological data, as was the K2 channel. There were several experiments available to draw on for the BK channel parameters, though they suffered from contradictions. Also included in the model are an anomalous rectifier and a delayed rectifier. These help the flow of potassium ions into the cell, helping to return it to the resting potential. The calcium-gated potassium channels also serve this purpose, repolarising the cell following calcium generated spiking. The properties of active ion channels are explored in more detail in Section 3.2.2.

One major area which lacked experimental data was the distribution of the channels across the cell. This meant that the distribution of channels in the model was largely based on speculation by Llinás and Sugimori (1980a,b). However, a parameter search was undertaken in order to test how sensitive the model was to changes in channel density and distribution. The P-type calcium and calcium-gated potassium channels were most sensitive to changes, while the voltage-gated potassium channels could withstand larger changes without affecting the behaviour of the model.

This model has endured as a community model as it is a strong and accurate recreation of a mammalian Purkinje cell. It was made possible due to the

reconstruction of true dendrite morphology, a large amount of experimental data into ion channels, and the passive modelling work that preceded it.

3.4 Conclusion

Neuronal modelling can be achieved on a scale of abstraction versus realism, from a binary logic gate to a series of complex equations that aim to replicate the minutiae of biochemistry and biophysics. In this chapter, the knowledge required for reaching the level of modelling used in this study is described, as well as a landmark Purkinje cell model that was the foundation for this work.

Compartmental models are widely used across the fields of neuroscience and computer science as they simplify mathematics for faster computations, while maintaining accuracy, and allow for the replication of cell morphology. The simplest compartmental models specify only passive electrophysiological parameters to describe current flow. These parameters are constant, they do not change with the environment or with time, and are proportionate to the size of compartments. Passive models are often only a foundation to more complicated models, as many neurons have ion channels through their membranes that are selectively permeable based on the intracellular environment.

These active channels are important for accurately replicating changes to membrane potential within a single cell, and even more so for creating realistic "spiking" mechanisms. The action potential - or spike - is vital for the effectiveness of the central nervous system. A method for modelling the underlying systems of the action potential put forward by Hodgkin and Huxley in 1952 earned the authors a Nobel Prize, and is still used in simulations today.

This chapter closes with an example of these modelling principles in use, the 1994a model of a guinea pig Purkinje cell created by De Schutter and Bower. This model was the first to include active channels and to be shared between different research groups as a "community" model, allowing it to be used in many different contexts.

Chapter 4

Morphology of Purkinje Cells from Various Species

4.1 Introduction

This chapter details the morphological data that was provided for this study, what is known of its history, and the methods used to quantify morphology and statistically differentiate each cell. This includes a discussion of the limitations of the data, in terms of both quantity and towards the representation of the full phylogenetic tree.

The quantification of morphology is principally performed through the creation of a feature vector for use in clustering experiments. However, this is also the first step in the exploration of Purkinje cells across species that this study aims to achieve, and is intended to create metrics for the morphology of these cells that may be able to give more context to electrophysiological results as well as being interesting in their own right. Purkinje cells are famed for the complexities of their dendritic branching, but this is clearly something that differs between species (see Figure 4.1) rather than a constant feature. Quantifying elements of morphology is essential for being able to meaningfully compare these elements in different cells.

The origin of the data and discussions of its limitations are important points for this study, particularly for the use of clustering techniques in Chapter 6, and are discussed here with the aim of defining the scope of these results.

Firstly, in Section 4.2, what is known of the origin of the morphological data used in this study is described, followed by an explanation of any changes to this data made for the study, such as the re-meshing of cells. Sections 4.3 and 4.4 detail the different techniques used to quantify the morphological data and some statistical tests performed, and the results of each. The final section is an evaluation of this data and how generalisable the results of this study can be considered given their limitations.

4.2   The Morphological Data

The morphological data used in this study, with the exception of the guinea pig data (the history of which are detailed in Section 3.3), are all Microlucida traces of Purkinje cells performed by the former Bower group at the University of Texas Health Science Center. Tracing is the process of copying the morphology of stained cells under a microscope and onto a computer. The cell morphology files were received either in a standardised format called "SWC", or formatted for use with the GENESIS simulator.

Both types of files describe the form of neurons as a series of geometric shapes with a diameter and three co-ordinates in space that typically describe the location of one end of a cylinder. The GENESIS files differentiate the soma compartment as a sphere, and can also describe the position of shapes with two sets of co-ordinates (usually start and end points of cylinders). A single set of co-ordinates will describe an end point, with the co-ordinates of the parent shape assumed to be the starting point.

Each shape becomes a compartment once the cell is modelled. For this reason, the length of cylinders must be amended according to the specific membrane capacitance, membrane resistance and axial resistivity (see Section 3.2.1.1). Ideally these values would have been derived from experimentation on the cells in vitro, but the use of these parameters found in similar cells is a reasonable alternative.

Amending the number of compartments based on these parameters is known as re-meshing. In this study, the programme CVAPP (Cannon et al., 1998) was used to re-mesh the cells using parameters derived by Roth and Häusser (2001) from rat Purkinje cells (the values used are discussed in Section 5.2.1). The aim of re-meshing is to reduce the electrotonic length of each compartment to no more than 10% of the length constant, λ (the length constant is explored in Section 3.2.1.2). This is necessary for the accuracy of voltage and current estimations in compartmental modelling.

Figure 4.1 shows a sample of the cells modelled in this study, displaying the variety of sizes (the scale bar in each panel is 50 μm long) and dendritic complexities exhibited across the cells, as visualised using the neuroConstruct software (Gleeson et al., 2007). The remainder of cells are given in Appendix A.

Unfortunately, when the cells were received, there was no longer any record of the origin of the cells. This means that the number of donor animals per species, the ages of the animals, and the position in the cerebellum that the cells were harvested from is all unknown. As much detail as is known about the specific families of animals that the cells were sourced from is given in Figure 2.9.

(a) Fish

(b) Alligator 1

(c) Turtle 3

(d) Finch 3

(e) Bat 5

(f) Guinea pig 1

(g) Rat 4
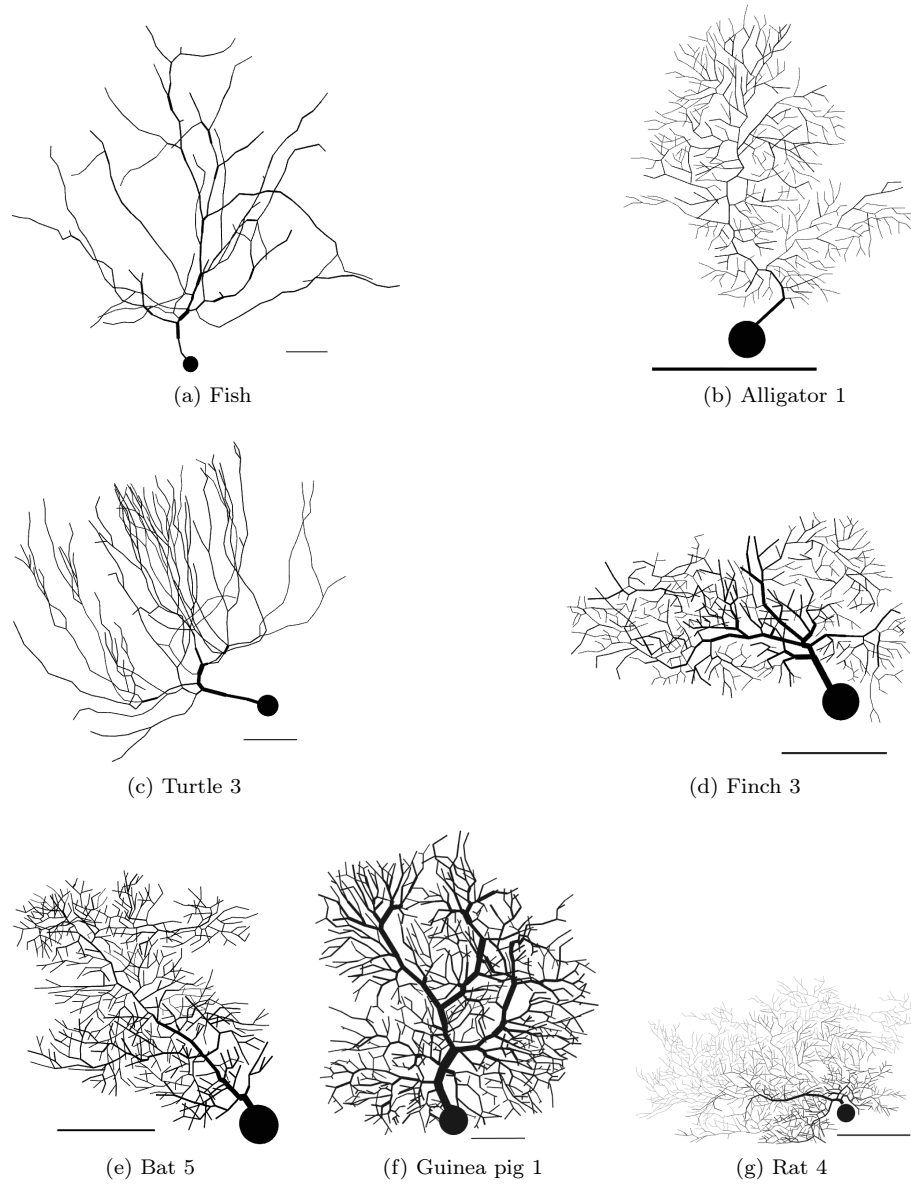
Figure 4.1: A selection of cells used in this study, spanning the different species. In each panel, the scale bar shows 50 μm.

4.3   Methods

Exploring the Purkinje cell morphology was a two-step process. First, elements of the morphology needed to be quantified. Metrics that quantified the size of the cells could be derived from the morphology files with very little processing, such as the average radius of dendritic compartments or the total volume of the cell. Some of the branching metrics required a little more processing of the tree structures of the dendrites, the methods used are described in more detail in this section.

These metrics were principally recorded for use in the clustering work described in Chapter 6, but were also used to quantify the variance in morphology both within and between species groups. This second step of exploration used statistical analysis to concretely define the differences and similarities between the dendritic structures of the cells.

4.3.1   Quantifying the Morphology

The simplest metrics to find were the physical measurements of the cell; the average radius of dendritic compartments, total dendritic length (both in μm), total dendritic surface area (μm^2), and total dendritic volume (μm^3) were all gathered using tools in the model generation software neuroConstruct (Gleeson et al., 2007). neuroConstruct also lists the electrotonic length (dimensionless) of each compartment, so is also the source of the average electrotonic length of dendritic compartments. The number of dendritic compartments and the radius of the soma were both known from the morphology files. The number of dendritic spines was also known from the morphology files, as they were generated in GENESIS. Based on the De Schutter and Bower (1994a) model, it was estimated that approximately 94% of the dendritic compartments should have spinal compartments added, leaving just the thickest 6% without spines. GENESIS will add one spine to each compartment with a radius below a given threshold. Trial and error was used to find the threshold in each model that produced ˜94% coverage.

Most of the metrics listed here could be gathered using pre-existing tools, but two were written as Matlab (The MathWorks, 2013) functions specifically for this work. The first was a function to find the Horton-Strahler number (Horton, 1945; Strahler, 1952) of each dendritic tree. The Horton-Strahler number was originally designed to analyse river networks, but has since been applied to many different hierarchical structures, including L-systems and respiratory systems. To begin the algorithm, each leaf node is given an H-S number of one. The number of a parent node is based on its children; if the children have the same H-S number i, the parent is assigned $i + 1$. When the children are unequal, the parent takes on the highest H-S number of its children. This continues through the tree until it reaches the root node, the H-S number of which becomes the number assigned to the entire tree.

The second Matlab script calculated a related measure to the H-S number, the average or maximum bifurcation ratio of a tree. It is found by dividing the

H-S number at compartment c by that of its parent $c + 1$. Averaging this ratio across the whole tree gives an indication of how evenly the tree bifurcates across its branches.

Three other branching measures, maximum branch order, maximum and average path length and average tree asymmetry, were all taken using the Trees Toolbox (Cuntz et al., 2010), a collection of functions written for analysing and plotting dendritic trees in Matlab. The number of branching and terminal points were also gathered from Trees Toolbox. Path length is a simple measure which counts the number of compartments between the root and each terminal point. As dendritic compartments are split into compartments based on either branch points or electrotonic length, which is derived from the membrane resistance and axial resistivity and the diameter of the compartment, this measure can be considered as encompassing the average compartment diameter as well as branching.

Branching order is a similar measure to the Horton-Strahler number calculated from root to tips, rather than the reverse, and is simpler to calculate. With the root node given a branching order of zero, a compartment will inherit the branching order of its parent if there was no branch point, otherwise it will increment by one. The maximum branching order of the tree is therefore the path from root to tip with the most branch points.

The final branching measure used is tree asymmetry, a measure that can only be taken at the branch points of the tree. It is a ratio based on the count of terminal points in each sub-tree from that branch point; that is, if the sum of terminal points on one sub-tree is x and the sum from the other sub-tree is y, the tree asymmetry is calculated as: $\frac{x}{(x+y)}$, but only if $x < y$. In all other cases the asymmetry is listed as NaN. The average tree asymmetry is calculated from all non-NaN numbers.

4.3.2 Statistical Analysis of Morphological Features

Once the morphological metrics described in the previous section were gathered for each cell, the mean was taken for each metric across the species groups. These were then plotted as bar charts with 95% confidence intervals (shown in Section 4.4) to determine which metrics, if any, displayed possible correlations with phylogenetic rank that would warrant further investigation.

Kendall rank correlation coefficients (Kendall, 1938), or τ, were calculated for features that appeared to have a strong correlation with phylogenetic rank. The Kendall rank test is a non-parametric test for ordinal data. Non-parametric tests are desirable for small sample sets, such as the data used in this study, as it makes no assumptions on the distribution the sample set is from. This is beneficial for smaller datasets as it is less likely a small sample can accurately represent the distribution it was taken from. Another benefit to non-parametric testing over parametric analysis of variance (ANOVA) tests is that the reliability of results does not depend on the dataset having a low variance. Rank testing allows for observed values to be compared against ordered groups - in this case phylogenetic order.

The Kendall rank test compares the ranks of two vectors of the same size (X and Y) by pairing elements of the vectors and checking whether they are "concordant" or "discordant". When the observations comprising a pair (x_i, y_i) are both larger or both smaller than a second pair (x_j, y_j), then the observations are concordant. Conversely, if $x_i < x_j$ and $y_i > y_j$ then x_i and y_i are discordant. A pair is neither concordant nor discordant if either observation is equal to the compared value.

When the number of concordant and discordant pairs are found, Kendall's rank coefficient can then be calculated as in Equation 4.1, where n_{con} is the number of concordant pairs, n_{dis} the number of discordant pairs, and z is the number of elements in vectors X and Y.

$$\tau = \frac{n_{con} - n_{dis}}{z(z-1)/2} \tag{4.1}$$

This version of Kendall's τ is also called τ_A, and makes no adjustments for the tied values that are not considered concordant or discordant. The implementation of Kendall's τ used in this study, a built-in Matlab (The MathWorks, 2013) function, does adjust for tied values and is often referred to as τ_B (Kendall, 1945). This is given in Equation 4.2, where z_0 is the total number of pairs ($z(z-1)/2$), z_1 is the number of tied values in vector X, and z_2 the number of tied values in vector Y (see Equation 4.3).

$$\tau_B = \frac{n_{con} - n_{dis}}{\sqrt{(z_0 - z_1)(z_0 - z_2)}} \tag{4.2}$$

$$z_u = \sum_i t_i(t_i - 1)/2 \tag{4.3}$$

Kendall's τ is ranged between -1 and 1. $\tau = 1$ would mean that the rankings of vector X are identical to that of Y, -1 means that the rankings are exactly opposite in the two vectors, and 0 would indicate no relationship.

The Kruskal-Wallis test (Kruskal and Wallis, 1952) is also a non-parametric statistical measure for ordinal data. Where Kendall's rank coefficient test examines the hypothesis that there is a relationship between rank and data, the Kruskal-Wallis test examines the hypothesis that the groups in the same have statistically significant differences in medians. The first step in a Kruskal-Wallis test is to rank the data by size across all observations, the smallest observation given rank 1 and equal values are all given the average rank of the number of equal values. The ranks of the observations are then summed for each group. With these gathered, the Kruskal-Wallis test is performed as in Equation 4.4, where N is the total number of observations, C the number of groups, n_i the number of observations in group i, and R_i the summed ranks for group i.

$$H = \frac{12}{N(N+1)} \sum_{i=1}^{C} \frac{R_i^2}{n_j} - 3(N+1) \tag{4.4}$$

When there are ties in the observations, H is adjusted by Equation 4.5, which increases the value by 0-1 depending on the number of ties. $T = t^3 - t$, with t as the number of observations in a given tie, then summed over all tie groups.

$$H_t = \frac{H}{\left(1 - \frac{\sum T}{N^3 - N}\right)} \qquad (4.5)$$

Higher values of H point towards the medians of groups being statistically different. Given a large enough dataset, H has a χ^2 distribution, however the size of the dataset in this study does not meet this requirement, so the p-values might overestimate the probability of the null hypothesis (that the medians of each group are equal) being true.

4.4 Results

The previous section detailed how the morphological metrics were found for each cell and how these metrics were analysed based on species groups. Full listings of the morphological metrics are given in Appendix B. Metrics were averaged over species and tested by Kendall's τ and Kruskal-Wallis H to look for metrics that seem to change with or against phylogenetic rank or that could differentiate species groups. Metrics were also plotted as bar charts (examples shown in the next section) to aid visualisation of the statistical results.

The Kendall's rank coefficient test revealed very few of the morphological metrics have a strong relationship with phylogenetic rank. The most significant results are given in Table 4.1, full results can be found in Appendix C. Only two of the metrics, the number of terminal points (Figure 4.3) and the Horton-Strahler number (Figure 4.2), were statistically significant to $p < 0.05$. The p-values used were two-tailed, so a low p-value suggests that the null hypothesis - that there is no correlation between the metric and phylogenetic rank - has a very low probability and can be rejected.

Branching metrics are found to have a stronger relationship with phylogenetic rank than measures of cell size. All five of the size metrics, including average radius of dendritic compartments and total dendritic length, have τ scores close to zero and high p-values.

Table 4.2 shows the morphological metrics that scored a significant result with the Kruskal-Wallis test when no outlying results were removed, suggesting that at least one of the species groups is statistically different from the others in that respect.

The significant Kruskal-Wallis metrics are less branching-centric than the Kendall's rank correlation results. The number of terminal points averaged over species has p-values < 0.05 for both statistical measures. This suggests a positive relationship with phylogenetic rank, but also that at least one species group is statistically different to the others. Figure 4.3 plots the average species values with 95% confidence intervals. The variance in the turtle group does

Metric	τ	p (2-tailed)
nDendC	0.619	0.069
nDendSp	0.619	0.069
nBrP	0.619	0.069
nTrmP	0.714	0.030
H-S	0.781	0.017
avgDendCmpEL	-0.619	0.069

Table 4.1: Significant Kendall's τ results when averaging morphological features over full species groups. KEY: nDendC: Number of dendritic compartments; nDendSP: Number of dendritic spines; nBrP: Number of branch points; nTrmP: Number of terminal points; H-S: Horton-Strahler numbers; avgDendCmpEL: Average dendritic compartment electrotonic length
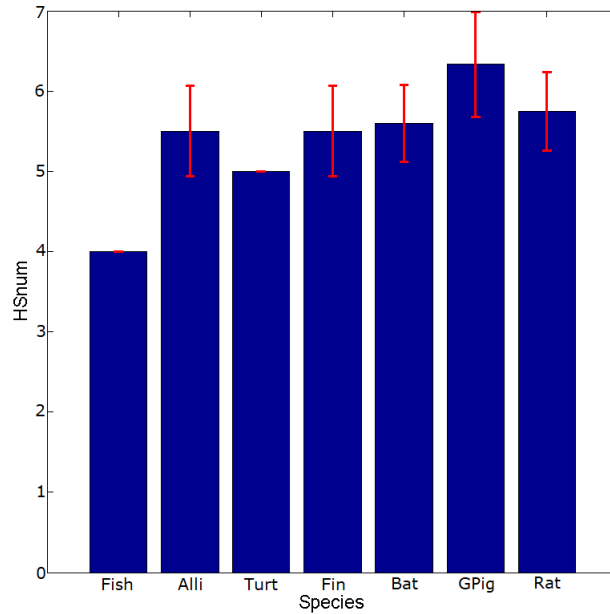
Figure 4.2: The Horton-Strahler number for each model averaged over species with 95% confidence intervals

Metric	H	p
nBrP	15.362	0.018
nTrmP	16.231	0.013
maxBO	13.666	0.034
totLen	14.417	0.025
totSurfA	16.701	0.010
totVol	12.612	0.050
avgDendCmpRad	15.446	0.017
avgDendCmpEL	10.804	0.003

Table 4.2: Morphological features with statistically significant H values, taken over the full dataset. KEY nBrP: Number of branch points; nTrmP: Number of terminal points; maxBO: Maximum branch order; totLen: Total dendritic length; totSurfA: Total dendritic surface area; totVol: Total dendritic volume; avgDendCmpRad: Average dendritic compartment radius; avgDendCmpEL: Average dendritic compartment electrotonic length

not overlap with any other species, potentially pointing it out as the independent group. The turtle group also has non-overlapping intervals in Figure 4.6, showing the average electrotonic length of dendritic compartments, and in all the other statistically significant branching metrics. In two of the size-based metrics, total dendritic surface area (Figure 4.4) and total volume, the guinea pig group has no overlap in confidence intervals. The second two size-based metrics, such as the average radius of dendritic compartments shown in Figure 4.5, had no species that was clearly visually differentiated.

4.5 Discussion

Unfortunately there are many limitations with the dataset of Purkinje cell models used in this study. Firstly, very little was recorded about the animals that the cells were harvested from, greatly limiting what is known about them. The age and number of donor animals are both unknown, as is the original cerebellar location of the cells. This makes it impossible to say if variance within species groups can be explained by any of these factors. Purkinje cells change and grow rapidly in young animals (Altman, 1972), so the age of the donor animals could account for much of the morphological variance.

Another important feature that is unknown about the cells is the specific taxonomy; the term "species" is used to name the groups throughout this study, but the specific species of animal donors was unknown excepting the guinea pig (Cavia porcellus) and rat (Rattus norvegicus) (see Figure 2.9 for the extent of what is known for each species). Identifying the species used would be informative for this study, but a larger problem is that the range of species used does not reflect the breadth of extant taxa. For example, the fish cell used in this study was harvested from a weakly electric fish, examples of which from both
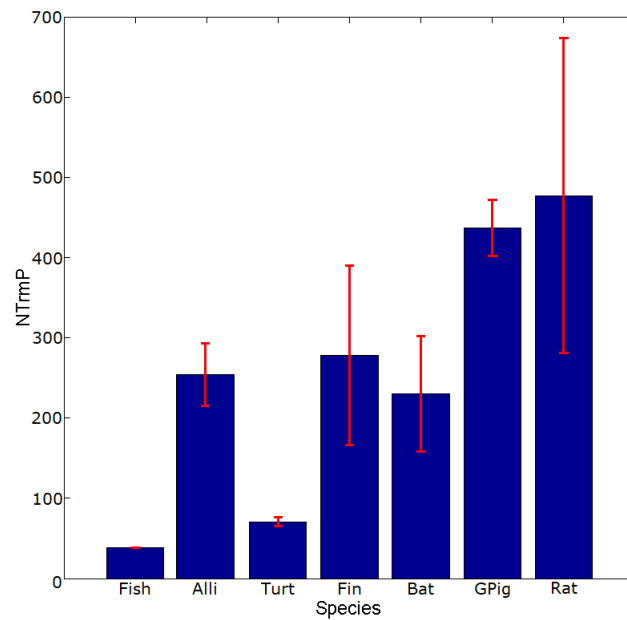
Figure 4.3: The number of terminal points (end of dendrites) in each model averaged over species with 95% confidence intervals
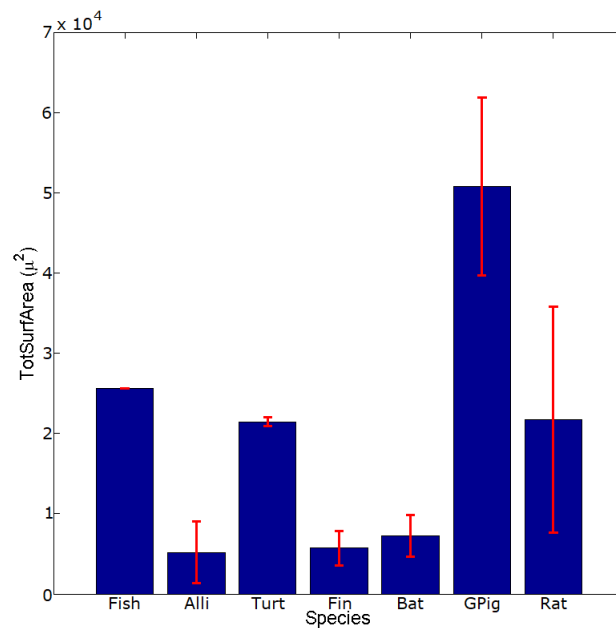
Figure 4.4: The total surface area (μ^2) of dendritic compartments in each model averaged over species with 95% confidence intervals
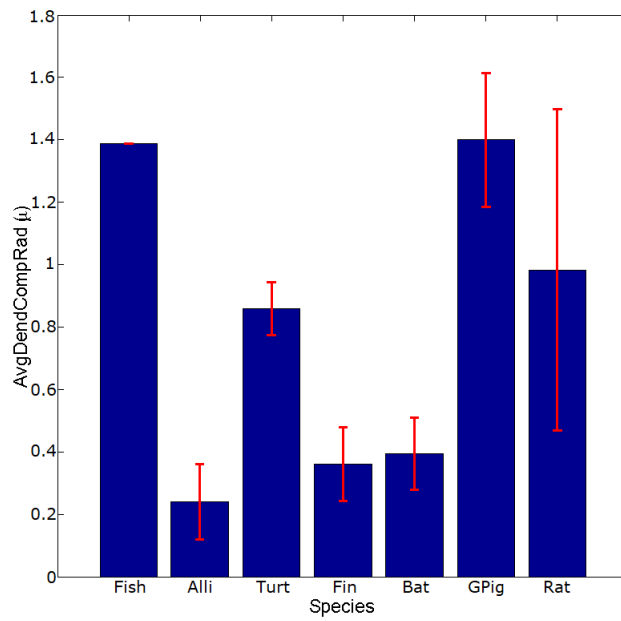
Figure 4.5: The average radium of dendritic compartments in each model averaged over species with 95% confidence intervals
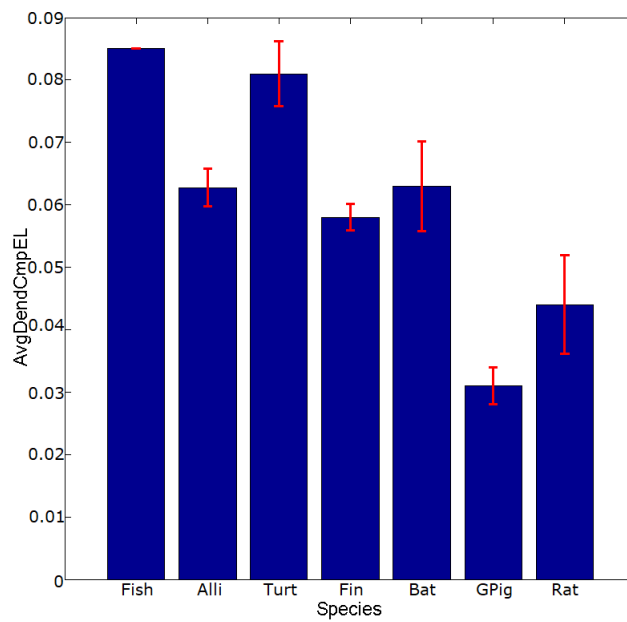
Figure 4.6: The average electrotonic length of dendritic compartments in each model averaged over species with 95% confidence intervals

the mormyridae and gymnotiformes have enlarged cerebella in comparison to other fish due to their electrical sense (Paulin, 1993). A better species range would include non-electric and elasmobranch examples at the very least. Furthermore, the reptile species with representatives in this study are both unlike the majority of reptiles; alligators are considered to be evolutionarily closer to birds than other reptiles (Benton and Clark, 1988), while the place of turtles within the class Reptilia has long been debated (DeBraga and Rieppel, 1997) due to their differences to other species.

Exacerbating the problem of poor representation is the small sample size of both individual species and the dataset overall. The small size makes it difficult to assume that the samples represent their species, and therefore make it difficult to extend the results of this study to the wider population. This low number of samples minimises the generalisability of comparisons, statistical analysis, and of clustering, for which even samples numbering in the hundreds would be considered low.

These problems highlight the need for a greater variety of animals used in neurological study. A majority of studies use rodent cells and models, which are not generalisable to all vertebrates, as even the small sample used in this study shows.

Chapter 5

Modelled Electrophysiology of Purkinje Cells from Various Species

5.1 Introduction

In this chapter, the theoretical concepts explained in Chapter 3 and the morphological data described in Section 4.2 are put into practice to create compartmental models representing the Purkinje cells of different species. There were three different comparisons made across the set of experiments; the effect of passive or active electrophysiology on the model's behaviour, the effect of implicitly or explicitly modelling dendritic spines, and the differences in voltage traces when impulses are moving toward or away from the soma. This work aims to explore a second aspect of the Purkinje cells - the mechanisms by which they are able to function.

These experiments were designed to characterise the behaviour of the cells and to look for any differences that may be explained by either the cell morphology or by the species. The results were intended to be interesting as an exploration of these models, but also to be used as features for clustering. The experiments needed to measure a number of behaviours so that the feature vectors could reasonably be considered as a characterisation of the electrophysiology of each cell. This chapter serves to describe these experiments, their outcomes, and the meaning of these outcomes and whether the results meet the needs of the clustering work.

Section 5.2 details the models used in these experiments, how the experiments were constructed, and what was measured in each case. The section following this then reports the results of the experimentation. Each of these sections is split into subsections covering the experiments using models with passive electrophysiology, and those that use active electrophysiology. Finally,

the last section is a discussion of these results and what they may mean for the development of behaviour through evolution.

5.2 Methods

All modelling was performed using the GENESIS platform (Bower et al., 2003), specialised neuronal modelling software. GENESIS reads morphology files and solves the passive electrical equations and those for Hodgkin-Huxley models of ion channels. Cell morphology must be translated to a series of cylindrical and spherical objects to be readable by GENESIS. This allows for the electrical equations to be completed for a series of small compartments each with a constant diameter, simplifying the problem greatly. The compartmental modelling technique is described in more detail in Section 3.2. Cerebellar Purkinje cells are known to have a large number of their dendritic branches to be studded with spines, small growths that act as contact points for the axons of other cells. The GENESIS simulator allows these spines to be modelled explicitly as small cylindrical compartments (the spine 'neck') connected to a spherical compartment (the 'head'), or implicitly by expanding the surface area of dendritic membrane to account for the missing spines. Explicitly modelled spines are attached to dendritic compartments based on compartment diameter. In this case, spines were added one for each compartment with a maximum diameter that was adjusted for each species such that ~94% compartments included a spine. This study includes experiments that use both types of approximation, using the same methods as described in Section 3.3.

The same passive and active electrophysiological parameters were used for all of the cell models, despite the cells originating from different species. This decision was made for several reasons. Deriving unique electrical parameters for computational models requires data from in vivo or in vitro experimentation. Unfortunately, there has been little exploration in this area with the exception of rat cells, so these data do not exist for the species used in this study. Additionally, where experimentation has taken place on Purkinje cells from other species, spiking patterns have been shown to be similar in shape and frequency (de Ruiter et al., 2006), this is given more discussion in Section 2.4.8.2. This suggests that the electrical parameters of the cells must also be similar. Studies where morphological and electrical parameters are based on data from different species are common in the history of Purkinje modelling (Shelton, 1985; De Schutter and Bower, 1994a,b) where experimental data were often incomplete, as are studies in which the same parameters are used in several cells with successful results (Rapp et al., 1994). Using the same parameters for all models also allows for any differences in behaviour between the cells due to their morphology to be clearly differentiated.

All experiments used a simulation time step of 0.02 ms, but were recorded at a time step 0.1 ms.

5.2.1 Passive Modelling

5.2.1.1 Model Parameters

Passive modelling, detailed in Section 3.2.1, has been a integral method of investigating Purkinje cells since the earliest models (Shelton, 1985) as it forms the groundwork for more biologically detailed models. Modelling active ion channels also introduces non-linearities to the electrophysiology that can make it harder to discern the effects of morphology, or if there are any such effects.

In these experiments, the passive electrical parameters were set uniformly across the cells, using the following values from Roth and Häusser (2001): Specific membrane resistance R_m, 122 $k\Omega cm^2$, specific capacitance C_m, 0.77 $\mu F cm^{-2}$, and specific axial resistivity R_a, 115 Ωcm. These values are the averages of parameters derived by Roth and Häusser for four different adult rat Purkinje cells. These passive parameters were kept the same across the different cells used, and were also constant between the soma and dendrites of individual cells.

The passive models also include a leak current, a non-voltage-dependent channel first used in the Hodgkin and Huxley (1952) models of the giant squid axon to model passive properties in the conductance equations. Using the same values originally used in De Schutter and Bower (1994a,b) Purkinje models, the reversal potential of the leak conductance E_{leak} and the resting potential E_{rest} was set to -68 mV (further explained in Section 3.2.1.3).

In order to model the reception of input spikes, the cell must have an input site with a synaptic channel. Unlike the voltage-gated ion channels used in active models, these synaptic channels respond with a change in conductance that is modelled as an explicit function of time (these functions are explained in Section 3.2.2.1). In all the experiments described here, each run attached a single bi-exponential AMPA receptor synaptic channel to the model to act as input site for a simulated spike from another cell. In spined models the channel would be included in the spine head, where parallel fibres typically make synaptic contacts with Purkinje cells. When the models did not explicitly include spines, the channel would be attached directly to the dendritic compartment. Synaptic conductance parameters were also set using values from Roth and Häusser (2001): maximum conductance g_{max}, 1^{-6} mS, reversal potential E_k, 0 mV, rise time τ_0, 0.2 ms, and decay time τ_1, 3 ms.

As part of the exploration of the Purkinje cell models, both the passive and active model experimentation was run using models with implicitly and explicitly modelled dendritic spines. Both the implicit and the explicit spines were modelled in the same way as those used in the De Schutter-Bower model (see Section 3.3). In the De Schutter and Bower guinea pig morphology, the diameter threshold for adding a spine to a compartment or expanding the membrane surface to simulate a spine was set at 3.17 μm. This threshold was varied in the other cells so that the proportion of spiny compartments was approximately the same.

The cells in this study were all re-meshed using the software CVAPP (Can-

non et al., 1998) (using the passive parameters described in Section 5.2.1) prior to being used in any modelling experiments. Re-meshing is the process of finding the optimal compartmentalisation of a cell morphology based on the branching and passive electrophysiological parameters.

5.2.1.2 Experiments with Passive Models

Once the passive models of the cells were created, GENESIS scripts were written with the intention of characterising the passive electrophysiological behaviour of these cells, and specifically the differences in behaviour that may be attributable to differences in morphology. The results of this experimentation can be found in Section 5.3.

The first experiment performed used the spineless (implicitly modelled spines) models to gauge the voltage attenuation across each cell. In each run of the experiment, a synaptic channel was placed on one of the dendritic compartments and stimulated with a single simulated spike. The voltage in the cell soma was recorded for 1.5 seconds. The input was initiated after half a second to give the cell time to settle to rest if necessary; this first half second was not included in the data analysis. These results were used to gather statistics that could be used to characterise the behaviour of each model, including the maximum amplitude recorded at soma and the time taken to reach that maximum.

Following this, the experiment was repeated using the spined (explicitly modelled spines) models, with the synaptic channel added for each run to a spine head rather than a dendritic compartment. Although the spineless models have the membrane surface area increased to compensate for the missing spines, running the experiment on both types of model allowed us to investigate whether or not the explicitly modelled spines have an effect on attenuation.

As neurons tend to be more electrically compact when travelling from soma to dendrites than the reverse, the voltage attenuation was also measured when travelling from soma to dendrites. To test the voltage attenuation in this direction, the synaptic channel was placed on the soma and it was activated with the same single spike. Voltage was recorded at each dendritic compartment for the same time span as the previous passive model experiments.

Statistics taken from the results of these tests were used to make a feature vector in order to attempt to summarise the passive electrophysiological behaviour of each of the cells. The feature vector was then used to look for clusters in the data and visualise the differences between and within species (explored in Chapter 6).

5.2.2 Active Modelling

5.2.2.1 Model Parameters

The active models used in this work use the same reconstructions of cell morphology and passive parameters as previously discussed, with the exception of the resting potential E_{rest}, and reversal potential of the leak current E_{leak}. This

starting resting potential is raised slightly from the value used in the passive model to -55 mV, due to the addition of active channels in the De Schutter and Bower model leading to a new semi-stable resting potential at approximately that value. The reversal potential of the leak conductance is decreased to -80 mV to provide a hyperpolarising current to slightly counteract the depolarising ion channels to help stabilise the model at rest.

Ten voltage-dependent ion channels were added to the models, using the same channel types and parameters (such as those for the reversal potential and maximum conductance) as those used by De Schutter and Bower (1994a,b). A more detailed look at the ion channels added to the model can be found in Section 3.3.

5.2.2.2   Experiments with Active Models

The active models were used in two sets of experimentation, the first was a direct comparison to the investigation of the passive models, and the second was to provide spiking data for information theoretical analysis. The methods used in the information theoretical analysis are described in Section 7.3.3, and the results of this analysis in Section 7.4.

To be comparable to the results of the passive modelling experiments, the active models simulated dendrites with voltage and ion-dependent ion channels as described in Section 3.3, but the soma was kept passive. The passive experimentation was designed to explore voltage attenuation and how this changes with dendritic morphology, and measured this by looking at the magnitude and delay of voltage responses. Passively modelling the soma compartment stopped the model from producing spikes. Spikes are described as all-or-nothing events, if the membrane potential depolarises to a given threshold, a spike is produced. As shown in Figure 3.7, there is little variation in the amplitude of spikes. Voltage attenuation could still be examined in a spiking model - to explore whether or not a spike is produced - but this approach would not allow the results of passive and active experimentation to be directly compared.

As with the passive models, two experiments in this set measured the voltage at soma while a single spike input is given to either a single dendritic compartment or spine – with different experiments for implicitly and explicitly modelled spines. In the third experiment the set-up was reversed and voltage was measured at each dendritic compartment following a single spike input to the soma. In all three cases a single synaptic channel was added to the model for the input site.

5.3   Results

Both the passive and active modelling experiments were intended to characterise the electrophysiological behaviour of the cells in three ways: the maximum voltage recorded in a target somatic/dendritic compartment following stimulation, the time taken to reach this maximum, and how much attenuation the

voltage suffers between the input and target sites. These three goals were true for all versions of the Purkinje cell models.

The maximum voltage and time to reach the maximum were simply taken from the recorded voltage traces. Voltage attenuation was measured in both the dendrite to soma direction and vice versa. Voltage attenuation is defined here as the proportion of the input voltage retained in the recording site compared to the input site, by dividing the peak amplitude at the input site by that of the recorded site (see Equation 5.1, where $\bar{V}$ represents the mean maximum voltage amplitude recorded) (Koch, 2004). To get a single value per cell, the mean peak amplitude was found. Rather than averaging across the entire dendritic tree, a subset of compartments was used. These compartments were taken from the endpoints of branches, specifically any dendritic compartment without a child, also called a terminal compartment. For example, when finding attenuation from dendritic inputs to the soma, the mean peak amplitude at terminal compartments was divided by the mean peak amplitude recorded at the soma when receiving input from a terminal compartment.

$$V_{att} = \bar{V}_{in}/\bar{V}_{rec} \tag{5.1}$$

5.3.1 Passive Modelling

5.3.1.1 Stimulating Dendritic Compartments and Measuring Somatic Voltage

The first experimental condition monitored the voltage at the soma compartment while a simulated spike was delivered to a single dendritic compartment. The voltage amplitude is reported here as the change in voltage from the resting potential of the models, which was -68 mV in each case.

The plots in Figure 5.1 show the results for three of the cell models, where each data point is the peak voltage amplitude measured at the soma plotted against the distance to the soma of the compartment that received input. Trend lines were computed using polynomial regression, the coefficients of which can be found in Table 5.1 for both Figures 5.1 and 5.2. The regression coefficients for all of the models are given in Appendix D (Table D.1), and additional voltage and time plots showing examples from other species can be found in Appendix E (Figures E.1, E.2). The coefficients given for these plots are the slope, intercept and R^2. The slope and intercept describe the trend line as they are terms in the regression equation used to generate it. The polynomial for this trend line, as calculated by Matlab (The MathWorks, 2013) is given in Equation 5.2: the intercept is represented by b_{n+1} and the slope by terms b_1 to b_n, with x as the independent variable (distance to soma) and y as the dependent variable (peak amplitude or time to reach peak amplitude). The coefficient of determination, or R^2, is a measure of good fit, giving a value to how well the trend line fits the data. R^2 is a number between 0 and 1, with a higher value indicating a better fit An adjusted R^2 was used that gives a penalty for each additional degree added to the polynomial, as without the adjustment R^2 will increase with each term

Species	Peak Amplitude			Time to Reach Peak Amplitude		
	Slope	Intercept	R^2	Slope	Intercept	R^2
Fish	[-0.006, 0.009, 0.014, -0.006, -0.034]	0.024	0.892	[-0.047, 0.050, 0.039, 1.812]	7.453	0.964
Alligator 2	[-0.019, 0.037, -0.021]	0.013	0.913	[0.162, 2.224]	7.332	0.967
Guinea pig 2	[-0.000, 0.002, -0.008]	0.015	0.913	[-0.100, -0.212, 0.391, 3.938]	9.995	0.910

Table 5.1: Slope and intercept terms for the regression equations for the plots shown in Figures 5.1 and 5.2, and the coefficient of determination (adjusted R^2) for each trend line.

added regardless of the significance of the term.

$$y = b_1 x^n + b_2 x^{n-1} + ... + b_n x + b_{n+1} \qquad (5.2)$$

Many of the peak amplitude over distance graphs (examples in Figure 5.1, further examples in Appendix E) all show a decreasing slope in peak amplitude as the input source moves further from the soma. This can also be seen in Table 5.1 (full listing in Appendix D). The negative sign of the covariance indicates the decrease in voltage with the increase in distance.

The main difference demonstrated in these graphs is the scale of the peak amplitude. The species average maximum amplitudes for this set of experiments are recorded in Figure 5.3, both with the full species results and with some outlying results removed. These graphs show a general downward trend in maximum amplitude as the species become more phylogenetically recent.

In many of the graphs showing the time taken to reach peak amplitude against distance from the soma, the increase in time appears linear, and in all cases the covariance between the time and distance was positive (Table 5.3). For some of the graphs this is also backed up by slopes created by a first degree polynomial equation with a high fit. An example of this is the alligator example in Figure 5.2. In other graphs, there seem to be some dendritic branches that delayed peak amplitude more than others, such as the example Finch in the appendix E.2. This particular example displays some of the more complex dendritic branching in all the models (Finch 4 A.4), suggesting that branching could be a factor in any delays to peak amplitude. This was explored further, by plotting the average and maximum time taken to reach peak amplitude at soma against the number of branching points in the model (Figure 5.4, regression coefficients and coefficient of correlation in Table 5.4). Unfortunately it was found that the trend line failed to fit the data well and the coefficient of correlation R did not point strongly to a linear relationship, particularly for the maximum time.

The average voltage attenuated in each species, calculated as in 5.1 and then averaged over species, is shown in Figure 5.5. Higher numbers indicate a higher attenuation. When averaging over all the models, there seems to be little relationship between voltage attenuation and phylogenetics. However, once some outlying results were removed from the average, voltage attenuation is
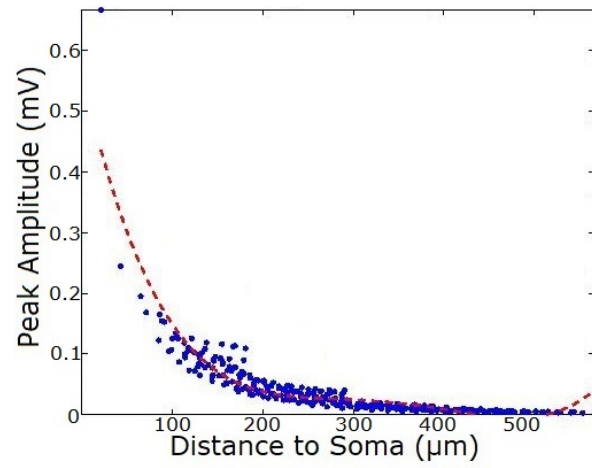
(a) Fish
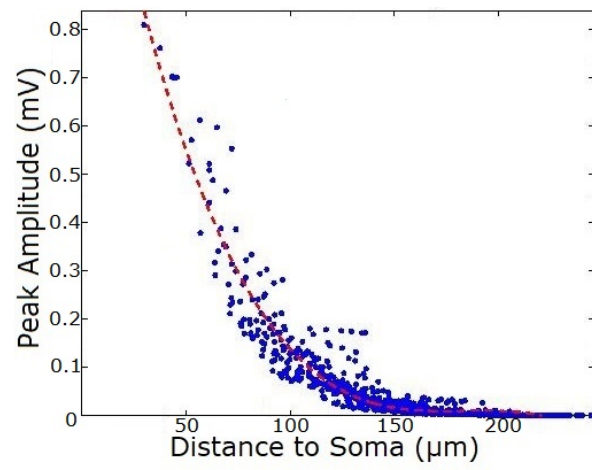
(b) Alligator 2
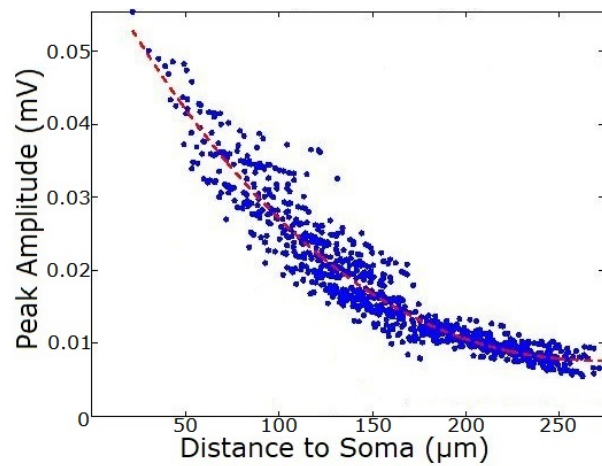
(c) Guinea pig 2

Figure 5.1: Peak amplitude recorded at soma following stimulation at each dendritic compartment in passive models. See Table 5.1 for regression equation terms.

(a) Fish
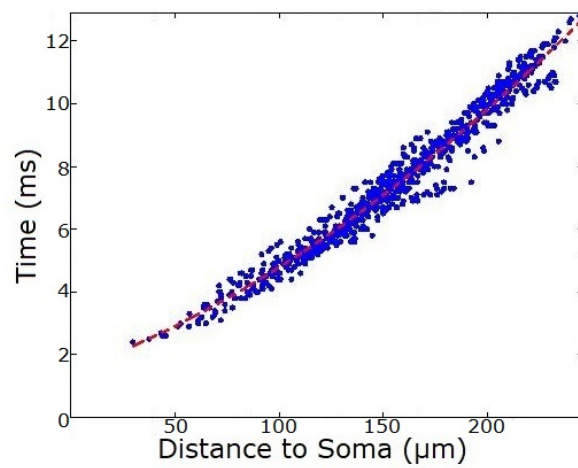
(b) Alligator 2
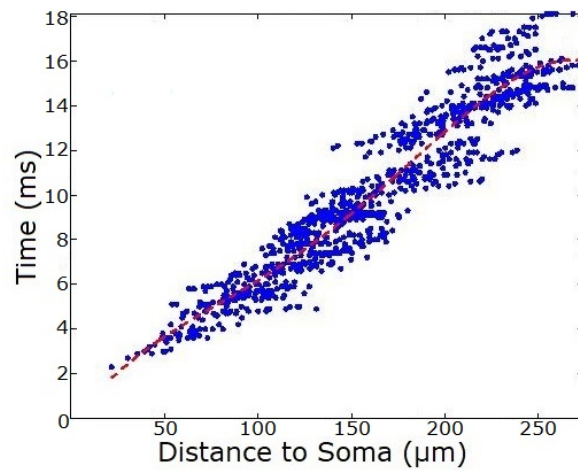
(c) Guinea pig 2

Figure 5.2: Time taken to reach the peak amplitude at soma following dendritic stimulation in passive models - same example cells as previous figure. Data for trend lines can be found in Table 5.1.

Cell	Variance	Covariance
Fish	6.035e-09	-0.005
Alligator 1	1.115e-07	-0.006
Alligator 2	1.134e-08	-0.003
Alligator 3	3.922e-09	-0.006
Alligator 4	8.838e-08	-0.008
Turtle 1	1.725e-09	-0.002
Turtle 2	2.829e-09	-0.002
Turtle 3	3.490e-09	-0.003
Finch 1	1.113e-08	-0.003
Finch 2	1.288e-08	-0.004
Finch 3	3.429e-09	-0.002
Finch 4	1.625e-08	-0.003
Bat 1	5.102e-09	-0.003
Bat 2	2.147e-09	-0.002
Bat 3	1.036e-08	-0.002
Bat 4	1.702e-08	-0.003
Bat 5	2.310e-09	-0.002
Guinea pig 1	6.316e-11	-0.000
Guinea pig 2	8.636e-11	-0.001
Guinea pig 3	3.082e-10	-0.001
Rat 1	2.003e-10	-0.001
Rat 2	9.529e-10	-0.001
Rat 3	2.555e-10	-0.001
Rat 4	5.800e-09	-0.002

Table 5.2: Variance of peak amplitude and covariance between peak amplitude and distance from soma in all passive unspined models.
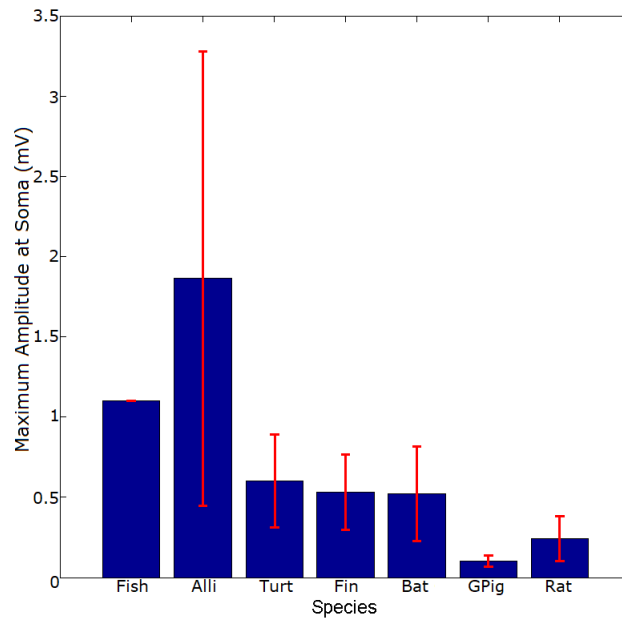
(a) Maximum amplitudes averaged over all cell model results for each species
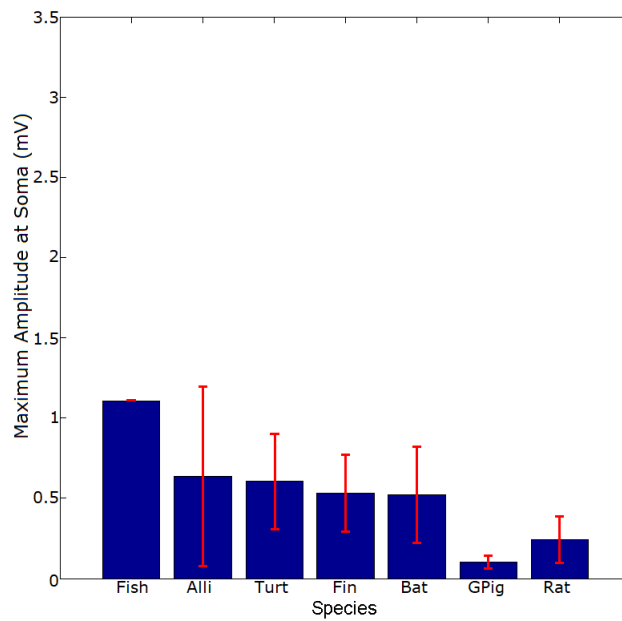
(b) Maximum amplitudes averaged over species with some outliers (Alligator 1 and 4) removed.

Figure 5.3: Maximum voltage amplitude recorded at soma following stimulation in dendritic compartments in passive models averaged over species groups with 95% confidence intervals.

Cell	Variance	Covariance
Fish	3.850	230.818
Alligator 1	6.316	82.852
Alligator 2	5.039	96.203
Alligator 3	19.192	615.842
Alligator 4	18.505	192.181
Turtle 1	15.309	191.533
Turtle 2	5.658	156.186
Turtle 3	2.421	113.762
Finch 1	8.632	103.783
Finch 2	8.984	118.404
Finch 3	10.483	145.323
Finch 4	67.057	268.873
Bat 1	5.403	113.318
Bat 2	13.454	202.839
Bat 3	2.258	36.916
Bat 4	4.216	59.360
Bat 5	24.811	135.995
Guinea pig 1	25.680	290.840
Guinea pig 2	13.813	195.588
Guinea pig 3	72.410	441.936
Rat 1	13.951	189.497
Rat 2	11.677	124.484
Rat 3	16.058	137.365
Rat 4	100.918	309.628

Table 5.3: Variance of time to reach peak amplitude and covariance between the time to reach peak amplitude and distance from soma in all passive unspined models.

	Slope	Intercept	R^2	R
Average Time Taken (ms)	[1.639]	10.000	0.338	0.582
Maximum Time Taken (ms)	[1.053 -0.108 1.183]	19.186	0.275	0.552

Table 5.4: Regression coefficients for the maximum and average time graphs in Figure 5.4
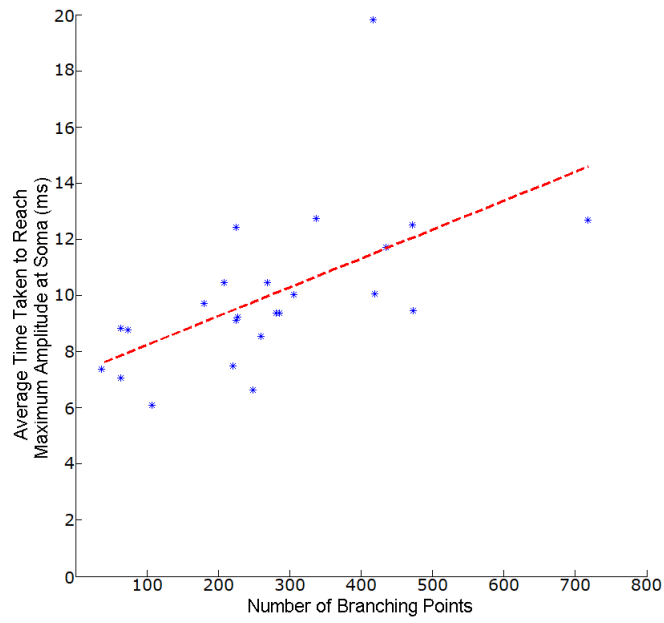
(a) Average time taken to reach peak amplitude in soma
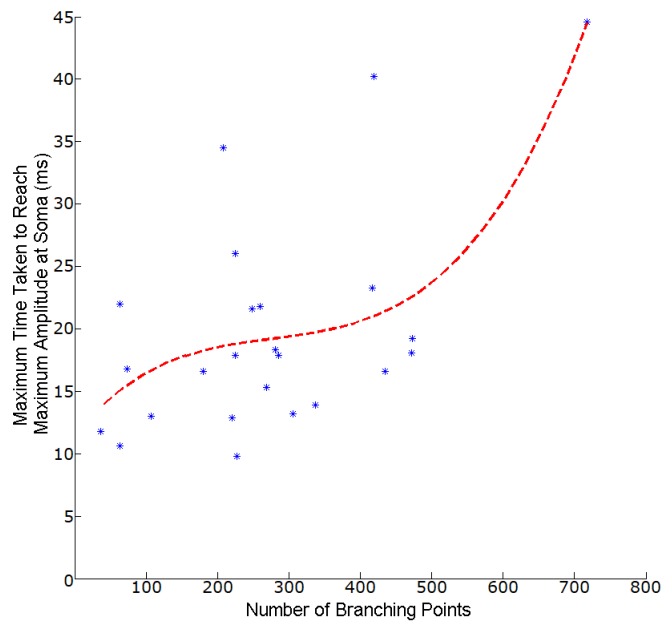
(b) Maximum time taken to reach peak amplitude in soma

Figure 5.4: Average and maximum time to reach peak amplitude in soma following stimulation at compartments in passive models against the number of branch points in the model

Cell Model	Peak Amplitude in Terminal Compartments (mV)
Fish	3.425
Alligator 1	25.056
Alligator 2	14.277
Alligator 3	12.310
Alligator 4	27.113
Turtle 1	5.983
Turtle 2	4.752
Turtle 3	5.473
Finch 1	12.398
Finch 2	9.176
Finch 3	10.851
Finch 4	19.994
Bat 1	16.139
Bat 2	10.110
Bat 3	12.995
Bat 4	14.934
Bat 5	6.964
Guinea pig 1	1.920
Guinea pig 2	2.732
Guinea pig 3	1.403
Rat 1	1.598
Rat 2	1.598
Rat 3	2.253
Rat 4	18.631

Table 5.5: Maximum amplitude at terminal dendritic compartment input sites in passive models

generally lower in the more phylogenetically recent species.

Models that have higher peak amplitudes at soma also have higher voltage attenuation, which seems to be contradictory at first glance. Voltage attenuation is the proportion of voltage at the recording site to that of the input site - not the peak of the voltage that is input to the model. This means that it will vary with the input resistance of each model. The peak amplitude recorded at input sites for each model is given in Table 5.5.

5.3.1.2 Stimulating Soma and Measuring Voltage at Dendritic Compartments

As with the previous section, peak amplitude drops steeply with distance before levelling out (examples in Figure 5.6, same cells as Figure 5.1, and further examples in E.3), with many of the slopes fitting well ($R^2 > 0.75$, see 5.6 for examples and D.2 for full results) to 3rd degree polynomials. These results also
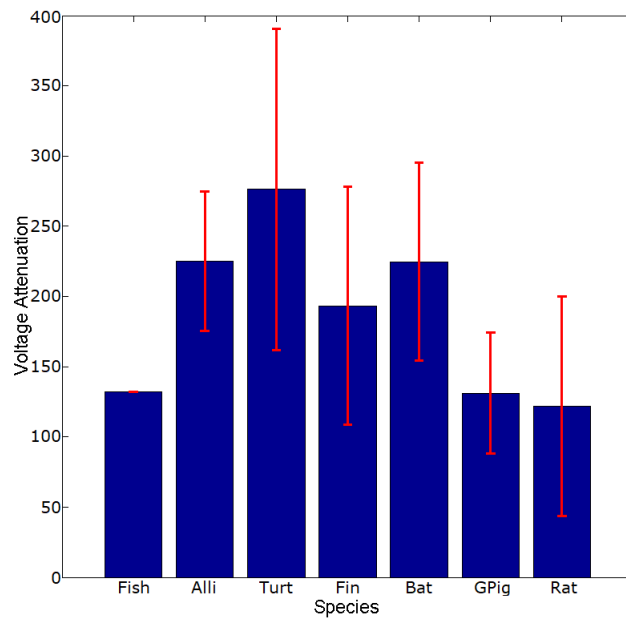
(a) Voltage attenuation averaged over all cell model results for each species
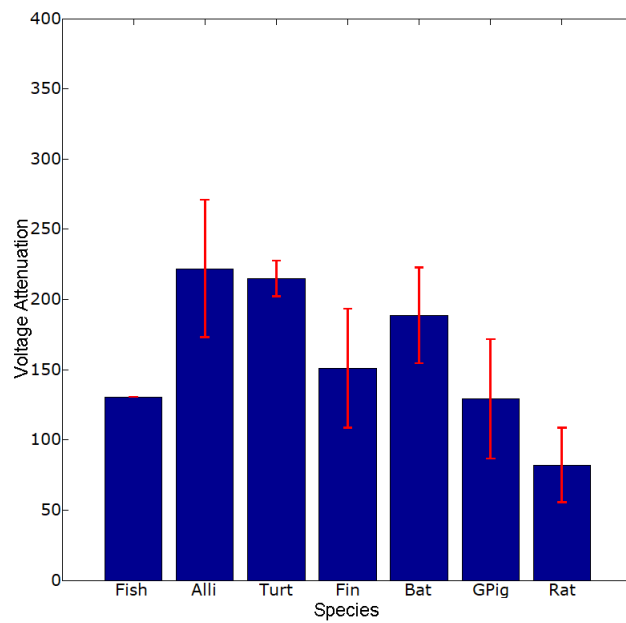
(b) Voltage attenuation averaged over species with some outliers (Turtle 1, Finch 4, Bat 1, Rat 4) removed.

Figure 5.5: Voltage attenuation from terminal compartments to soma in passive models without spines averaged over species with 95% confidence intervals.
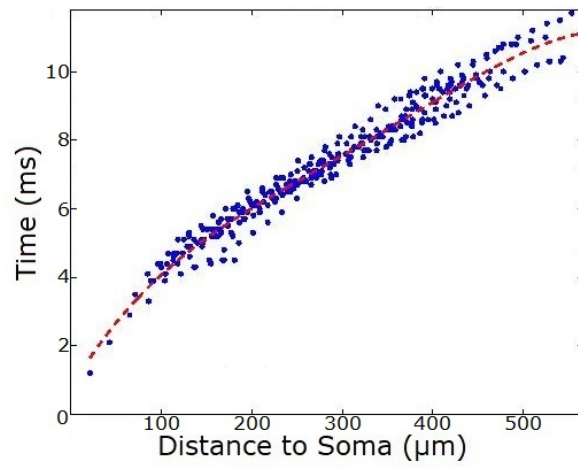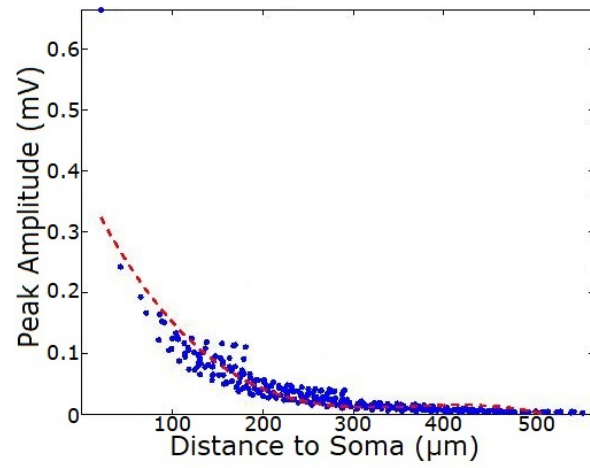
(a) Fish
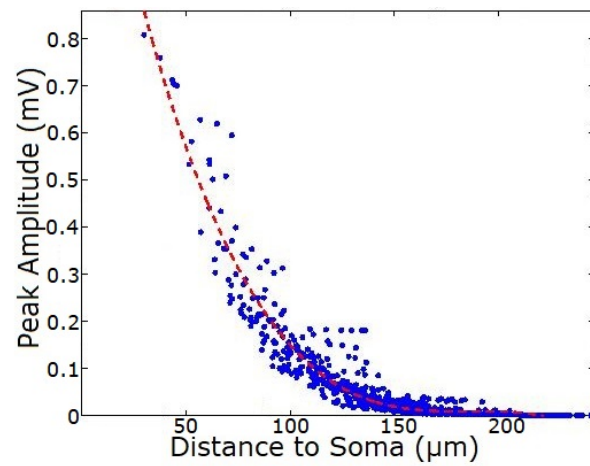
(b) Alligator 2
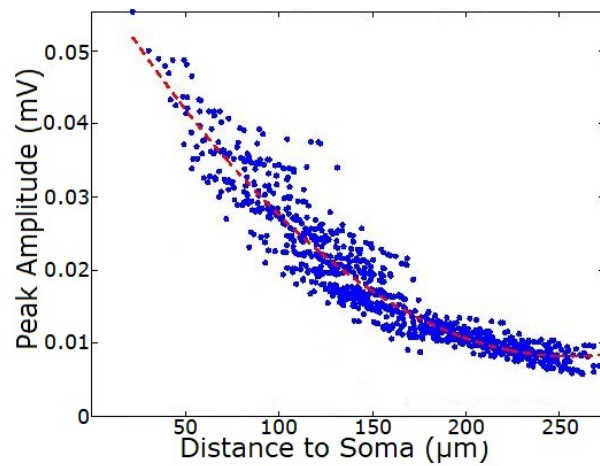
(c) Guinea pig 2

Figure 5.6: Peak amplitude recorded at dendritic compartments following stimulation at the soma in passive models. See Table 5.6 for regression equation terms.
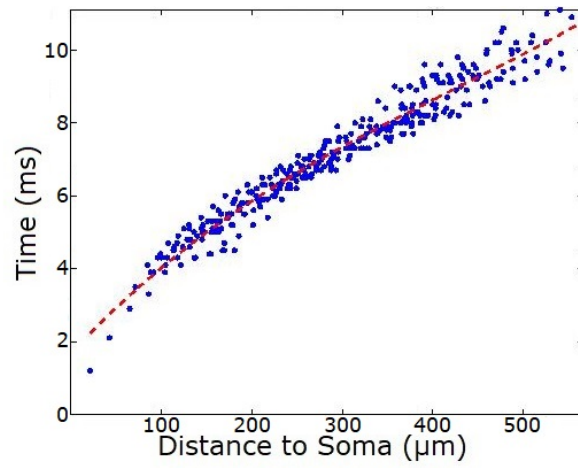
(a) Fish
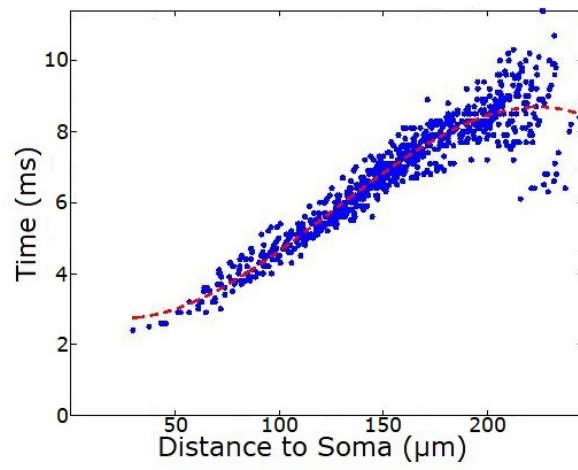
(b) Alligator 2
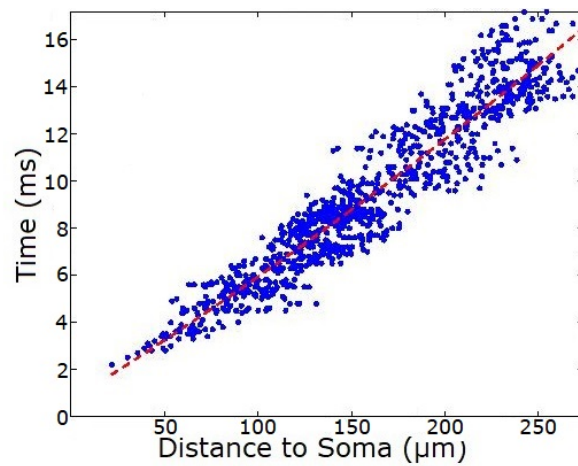
(c) Guinea pig 2

Figure 5.7: Time taken to reach the peak amplitude at dendritic compartments following stimulation at soma in passive models. Data for trend lines can be found in Table 5.6.

Species	Peak Amplitude			Time to Reach Peak Amplitude		
	Slope	Intercept	R^2	Slope	Intercept	R^2
Fish	[-0.013, 0.025, -0.010]	0.013	0.779	[0.044, -0.143, 1.638]	7.250	0.954
Alligator 2	[-0.018, 0.040, -0.028]	0.015	0.919	[-0.124, -0.258, 1.769]	7.028	0.899
Guinea pig 2	[0.002, -0.008]	0.015	0.908	[0.091, 3.256]	9.400	0.898

Table 5.6: Slope and intercept terms for the regression equations for the plots shown in Figures 5.6 and 5.7, and the coefficient of determination (adjusted R^2) for each trend line.

show a variance in the maximum peak amplitude in each model, similarly to the dendrite to soma direction. The highest peak also decreases with phylogenetic rank, with the exception of the alligator cells, shown in Figure 5.8.

The variance in both peak amplitude and the time taken to reach the peak also both show similarities to those seen in the previous experimentation (Table 5.7). Variance in the peak amplitude shows the same magnitude in both sets of experiments. For the variance in time, many of the species groups had a outlier that could skew results. Some of these outliers, such as Finch 4 and Rat 4, have measurable morphological differences to the other cells in their species group (see Section 4.4). Others, like Guinea pig 3, are outliers for less clear reasons. Figure 5.7 shows the time taken to reach peak amplitude against distance from soma for the same example cells as Figure 5.2, with further examples in Appendix E. As in the previous experiments, the time taken often has a nearly linear correlation with distance, as evidenced by the covariance values in Table 5.7. An exception from the positive variance is given in Finch 4 in the appendix.

Despite not having a large difference in the maximum peak amplitude or in the variance of peak amplitudes, the cell Turtle 1 is an outlier in its species group for voltage attenuation in both the dendrite to soma and soma to dendrite directions (see Figure 5.9). The high voltage attenuation in turtle cells in the soma to dendrite direction also disrupts the previous pattern of attenuation decreasing with phylogenetic rank. The peak amplitude at soma (Table 5.8), the input site for this experimentation, also points Turtle 1 as an outlier of its species group.

5.3.1.3 Stimulating Dendritic Spines and Measuring Somatic Voltage

While the scatter graphs (Figures 5.10 and 5.11, same example cells as before, regression coefficients given in Table 5.9) initially seem similar to the previous graphs, adding spine components decreased peak amplitudes and increased the time taken to reach peak amplitudes.

Comparing the species average maximum peak amplitudes recorded when stimulating at spine compartments (Figure 5.12) and at dendritic compartments (Figure 5.3) shows a reduction in peak amplitude by approximately half in many of the species groups.
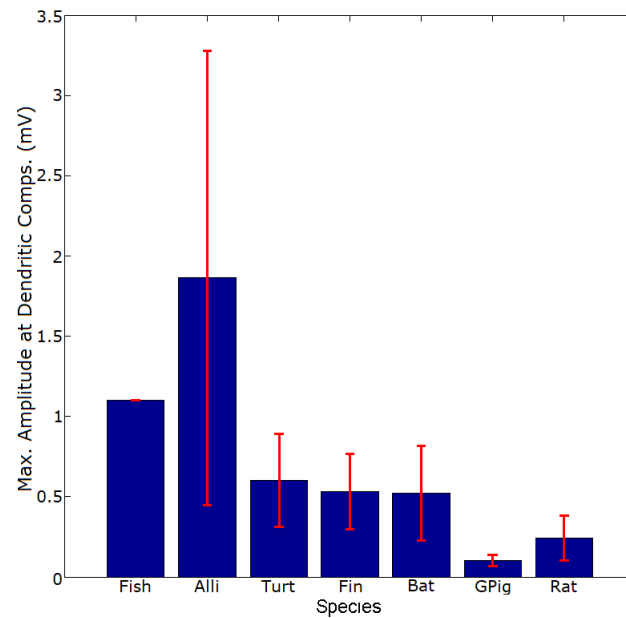
(a) Maximum amplitudes averaged over all cell model results for each species
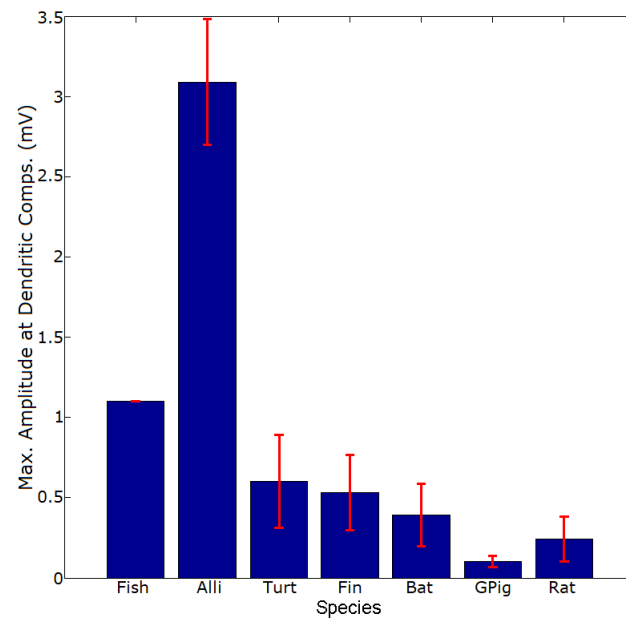
(b) Maximum amplitudes averaged over species with some outliers (Alligator 2 and 3, Bat 4) removed.

Figure 5.8: Maximum voltage amplitude recorded at dendritic compartments following stimulation at the soma averaged over species with 95% confidence intervals.

Cell	Variance	Covariance
Fish	6.012e-09	-0.005
Allig. 1	1.303e-07	-0.007
Allig. 2	1.226e-08	-0.004
Allig. 3	4.145e-09	-0.002
Allig. 4	1.048e-07	-0.003
Turtle 1	1.752e-09	-0.002
Turtle 2	2.830e-09	-0.002
Turtle 3	3.514e-09	-0.003
Finch 1	1.179e-08	-0.003
Finch 2	1.338e-08	-0.004
Finch 3	3.648e-09	-0.002
Finch 4	1.428e-08	-0.003
Bat 1	5.644e-09	-0.003
Bat 2	2.256e-09	-0.002
Bat 3	1.096e-08	-0.002
Bat 4	1.869e-08	-0.003
Bat 5	2.406e-09	-0.002
G. pig 1	6.429e-11	-0.000
G. pig 2	8.765e-11	-0.005
G. pig 3	3.123e-10	-0.001
Rat 1	2.036e-10	-0.002
Rat 2	9.679e-10	-0.001
Rat 3	2.604e-10	-0.001
Rat 4	6.284e-09	-0.001

(a) Variance of peak amplitude and covariance between peak amplitude and distance from soma

Cell	Variance	Covariance
Fish	3.210	209.424
Allig. 1	6.253	8.523
Allig. 2	2.685	67.009
Allig. 3	19.159	-406.468
Allig. 4	12.503	-90.999
Turtle 1	6.902	101.666
Turtle 2	3.590	113.776
Turtle 3	1.708	94.090
Finch 1	5.439	30.056
Finch 2	8.330	21.795
Finch 3	5.856	65.867
Finch 4	16.429	-95.094
Bat 1	6.439	-3.101
Bat 2	9.119	40.381
Bat 3	1.673	31.716
Bat 4	3.947	8.954
Bat 5	15.679	1.398
G. pig 1	21.300	262.395
G. pig 2	11.852	180.395
G. pig 3	54.955	388.318
Rat 1	11.369	170.529
Rat 2	10.231	116.372
Rat 3	13.632	126.326
Rat 4	20.543	-126.961

(b) Variance of time to reach peak amplitude and covariance between the time to reach peak amplitude and distance from soma

Table 5.7: Variance and covariance values for peak amplitude and time to reach peak amplitude when stimulating at the soma and recording in dendritic compartments.
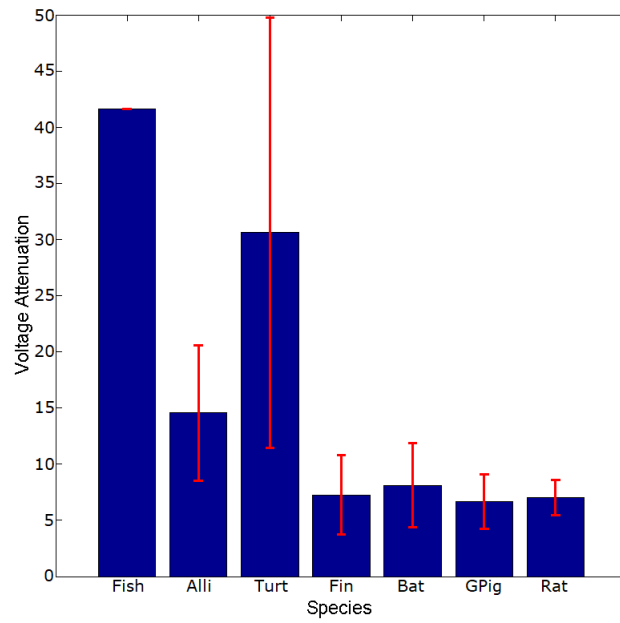
(a) Voltage attenuation averaged over all cell model results for each species
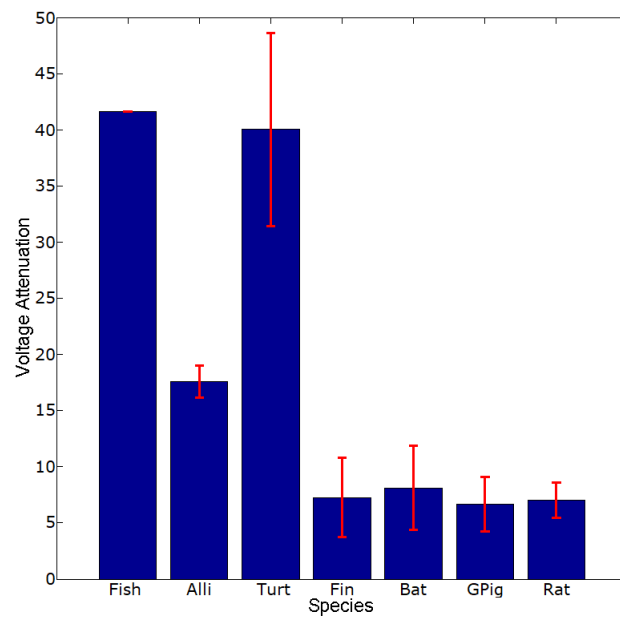
(b) Voltage attenuation averaged over species with some outliers (Alligator 2, Turtle 1) removed.

Figure 5.9: Voltage attenuation from soma to terminal compartments in passive models without spines averaged over species with 95% confidence intervals.

| Cell Model	Peak Amplitude in Soma (mV)
Fish	1.102
Alligator 1	3.291
Alligator 2	0.917
Alligator 3	0.353
Alligator 4	2.890
Turtle 1	0.324
Turtle 2	0.830
Turtle 3	0.654
Finch 1	0.392
Finch 2	0.559
Finch 3	0.318
Finch 4	0.855
Bat 1	0.641
Bat 2	0.219
Bat 3	0.460
Bat 4	1.038
Bat 5	0.251
Guinea pig 1	0.101
Guinea pig 2	0.074
Guinea pig 3	0.134
Rat 1	0.148
Rat 2	0.187
Rat 3	0.178
Rat 4	0.452

Table 5.8: Maximum amplitude at the soma compartment input site in passive models

Species	Peak Amplitude			Time to Reach Peak Amplitude		
	Slope	Intercept	R^2	Slope	Intercept	R^2
Fish	[-0.013, 0.021, -0.000]	0.007	0.692	[2.584]	9.731	0.887
Alligator 2	[-0.010, 0.017, -0.006]	0.004	0.801	[2.868]	12.807	0.511
Guinea pig 2	[0.002, -0.007]	0.009	0.921	[3.765]	10.820	0.893

Table 5.9: Slope and intercept terms for the regression equations for the plots shown in Figures 5.10 and 5.11, and the coefficient of determination (adjusted R^2) for each trend line.
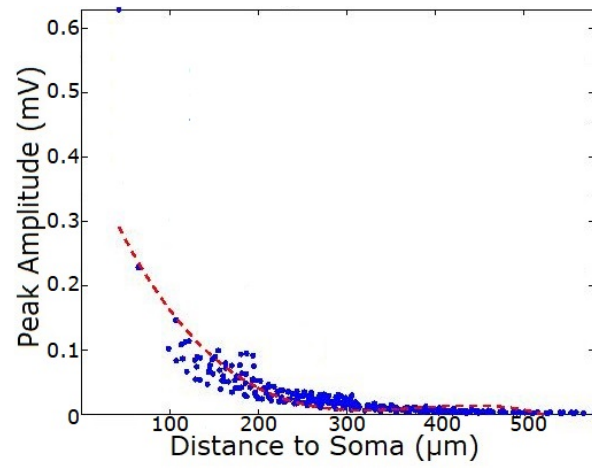
(a) Fish
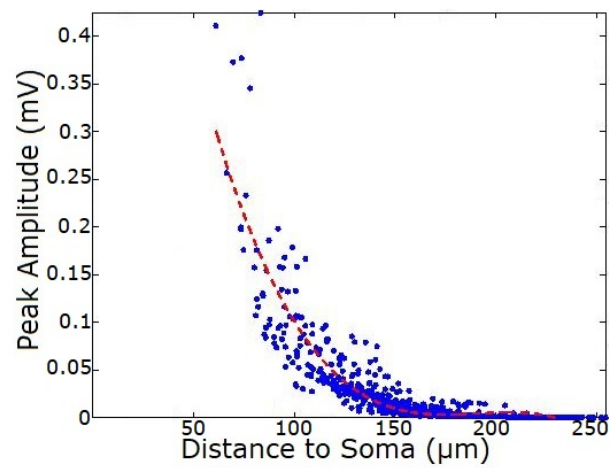
(b) Alligator 2
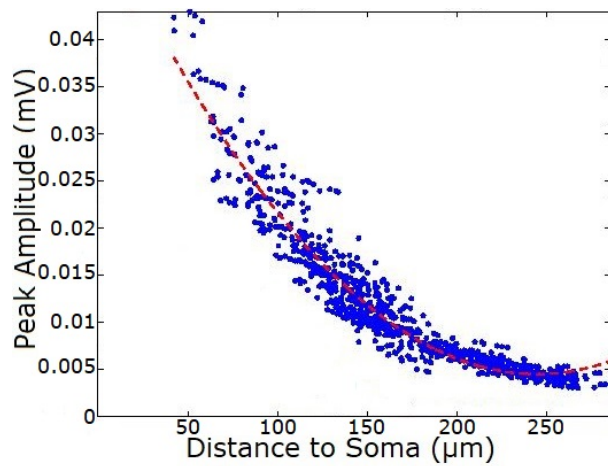
(c) Guinea pig 2

Figure 5.10: Peak amplitude recorded at soma following stimulation at each dendritic spine compartment in passive models. See Table 5.9 for regression equation terms.
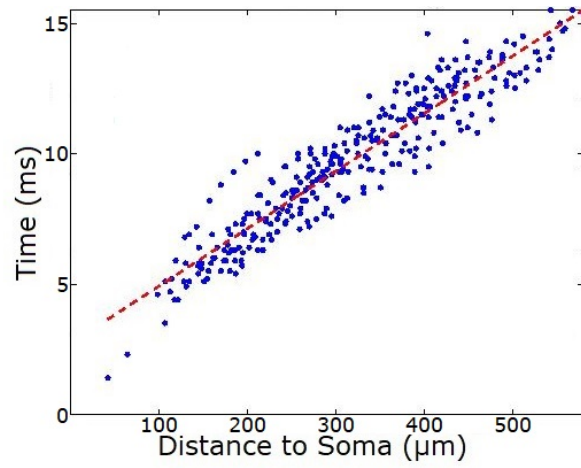
(a) Fish
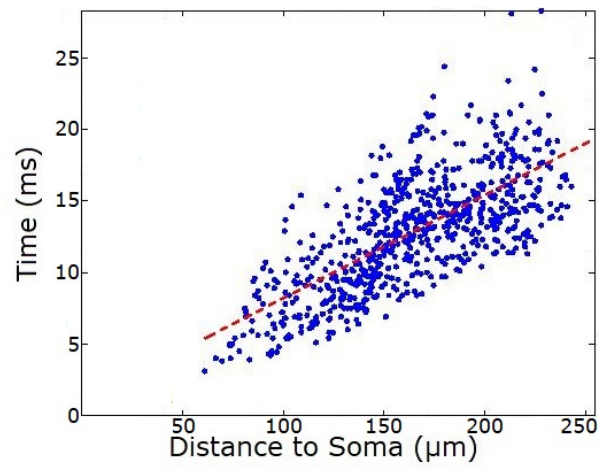
(b) Alligator 2
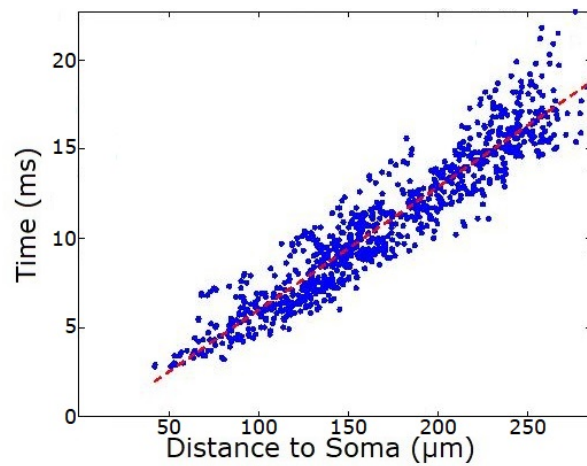
(c) Guinea pig 2

Figure 5.11: Time taken to reach the peak amplitude at soma following stimulation at dendritic spines in passive models. Data for trend lines can be found in Table 5.9.
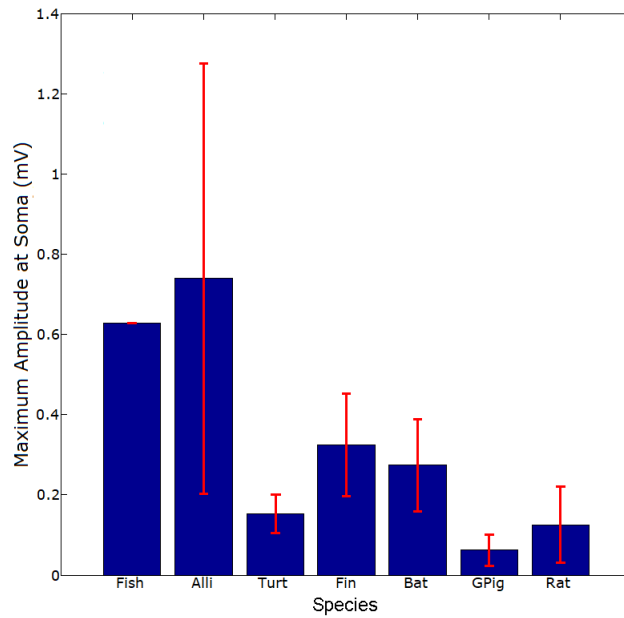
(a) Maximum amplitudes averaged over all cell model results for each species
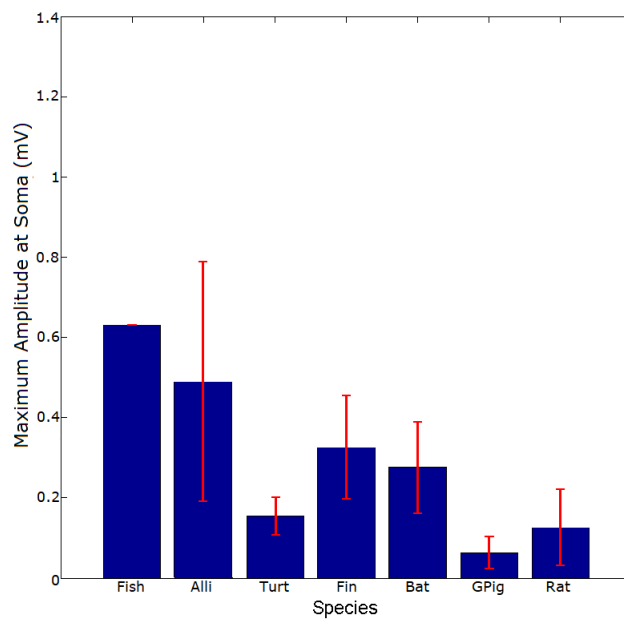
(b) Maximum amplitudes averaged over species with some outliers (Alligator 1) removed.

Figure 5.12: Maximum voltage amplitude recorded at soma following stimulation in dendritic spine compartments averaged over species with 95% confidence intervals.

The increase in time taken to reach peak amplitude in the spined models in comparison to the unspined models was found in all species average groups. This is shown in Figure 5.13, which compares the mean time taken in species groups in each set of experiments. The time taken has a positive linear relationship in almost all cells (see covariance, Table 5.10b), as seen in the other experimentation with passive models. However, an increase in variance in almost all cell results in comparison to the unspined models lead to lower correlation coefficients (Table 5.11) between distance and time in the spined models.

As shown in Figure 5.14, voltage attenuation also increased dramatically in comparison to the unspined models, but as before there does not seem to be any relationship between attenuation and species group.

5.3.2   Active Modelling

The addition of active channels to the models made a significant difference to the results of this experimentation. The relationships between distance from soma and peak amplitude, as well as distance from soma and the time taken to reach the peak amplitude are flat, suggesting there is no effect of input location on peak amplitude or time. This supports results from experimentation with their original guinea pig model by De Schutter and Bower (1994d). Figures 5.15 and 5.16 contain examples of all three experimental conditions from a guinea pig cell, plotting amplitude and time respectively.

These graphs show that in the dendrite→soma direction, there is little variability in voltage recording, or times to reach peak amplitude with respect to distance. Table 5.12, showing the regression coefficients of the graphs, show how in most cases there was no linear correlation at all. When stimulating the soma, the relationship with distance remained present, but was much reduced compared to the passive models. In Figures 5.15 and 5.16, there is a slight positive correlation for both peak amplitude and time taken. Most cells (see Appendix E for more figures) display a negative correlation with the increase in distance.

Adding active channels also greatly increases the amplitude of peak voltages recorded at output sites, although this is less extreme when spines are explicitly modelled. The higher peak amplitudes and low variation across distances also means that voltage attenuation was much lower in active models (see Figures 5.17, 5.18, and 5.19).

5.4   Discussion

The results of the six experimental conditions were designed to create an overview of the electrophysiological behaviour of each cell that could be used to represent the cell in cluster analysis. This was achieved by focusing on three elements in each condition: the peak amplitude at recording sites, the time taken to reach the peak amplitude, and how much voltage attenuated between the two points. With each of the models using the same parameters for the passive

Cell	Variance	Covariance
Fish	1.990e-09	-0.003
Allig. 1	1.690e-08	-0.002
Allig. 2	2.185e-09	-0.001
Allig. 3	1.036e-09	-0.001
Allig. 4	6.420e-09	-0.002
Turtle 1	5.329e-10	-0.001
Turtle 2	4.340e-10	-0.001
Turtle 3	7.798e-10	-0.001
Finch 1	3.556e-09	-0.001
Finch 2	4.295e-09	-0.002
Finch 3	1.229e-09	-0.001
Finch 4	2.402e-09	-0.001
Bat 1	1.639e-09	-0.001
Bat 2	8.925e-10	-0.001
Bat 3	3.193e-09	-0.001
Bat 4	3.487e-09	-0.001
Bat 5	6.088e-10	-0.001
G. pig 1	3.746e-11	-0.000
G. pig 2	5.451e-11	-0.000
G. pig 3	1.443e-10	-0.000
Rat 1	1.049e-10	-0.000
Rat 2	5.489e-10	-0.001
Rat 3	1.290e-10	-0.000
Rat 4	1.046e-09	-0.001

(a) Variance of peak amplitude and covariance between peak amplitude and distance from soma

Cell	Variance	Covariance
Fish	7.525	302.657
Allig. 1	122.371	-141.605
Allig. 2	22.423	70.465
Allig. 3	96.153	-261.801
Allig. 4	133.304	-294.569
Turtle 1	23.786	177.070
Turtle 2	13.566	234.289
Turtle 3	9.704	199.267
Finch 1	102.305	92.387
Finch 2	64.680	15.557
Finch 3	62.104	96.632
Finch 4	167.453	-284.878
Bat 1	58.601	-54.690
Bat 2	71.030	-79.080
Bat 3	29.571	116.319
Bat 4	40.997	29.491
Bat 5	83.464	-126.462
G. pig 1	14.375	210.762
G. pig 2	15.870	205.273
G. pig 3	24.904	255.637
Rat 1	19.767	213.908
Rat 2	19.233	152.537
Rat 3	25.989	175.456
Rat 4	180.031	-317.428

(b) Variance of time to reach peak amplitude and covariance between the time to reach peak amplitude and distance from soma

Table 5.10: Variance and covariance values for peak amplitude and time to reach peak amplitude when stimulating at dendritic spines and recording at the soma.
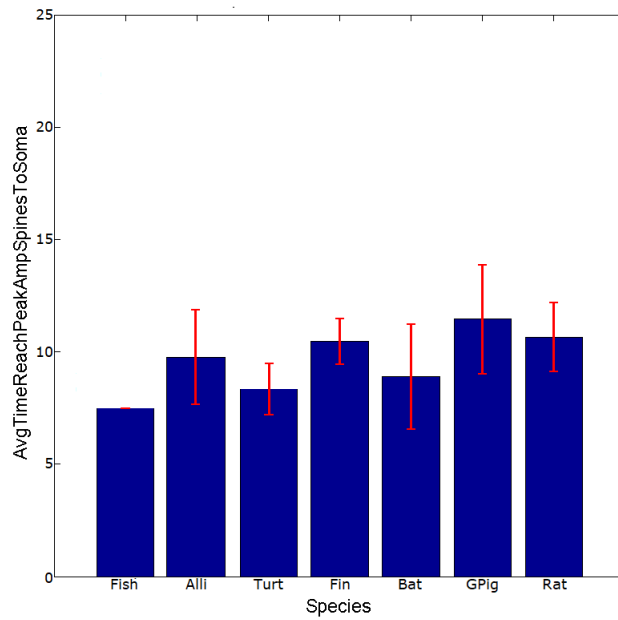
(a) Mean time to reach peak amplitude in spineless passive models, some outliers (Guinea pig 3) removed.
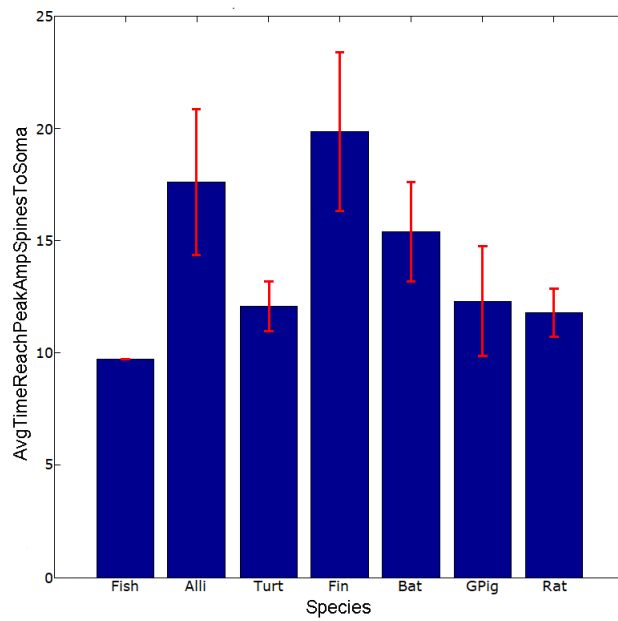
(b) Mean time to reach peak amplitude in spineless passive models, some outliers (Rat 4) removed.

Figure 5.13: Mean time to reach peak amplitude at soma averaged over species with 95% confidence intervals in passive models with and without spines, outliers removed in both cases.

	Correlation Coefficient	
Cell	Unspined Models	Spined Models
Fish	0.979	0.942
Allig. 1	0.973	-0.381
Allig. 2	0.979	0.358
Allig. 3	0.805	-0.431
Allig. 4	0.980	-0.571
Turtle 1	0.667	0.515
Turtle 2	0.862	0.886
Turtle 3	0.969	0.922
Finch 1	0.985	0.277
Finch 2	0.965	0.051
Finch 3	0.962	0.279
Finch 4	0.762	-0.531
Bat 1	0.985	-0.146
Bat 2	0.930	-0.163
Bat 3	0.886	0.847
Bat 4	0.918	0.153
Bat 5	0.475	-0.263
G. pig 1	0.927	0.883
G. pig 2	0.952	0.945
G. pig 3	0.869	0.868
Rat 1	0.943	0.897
Rat 2	0.950	0.935
Rat 3	0.892	0.908
Rat 4	0.705	-0.597

Table 5.11: Correlation coefficient between time take to reach peak amplitude and distance from soma in unspined and spined passive models

Experimental Condition	Peak Amplitude			Time to Reach Peak Amplitude		
	Slope	Intercept	R^2	Slope	Intercept	R^2
Dendrites → Soma	[-0.007]	62.275	0.000	[0.006]	9.059	0.001
Soma → Dendrites	[2.076]	71.008	0.499	[0.174]	9.447	0.337
Spines → Soma	[0.002]	31.739	0.000	[-0.002]	14.624	0.000

Table 5.12: Slope and intercept terms for the regression equations for the plots shown in Figures 5.15 and 5.16, and the coefficient of determination (adjusted R^2) for each trend line.
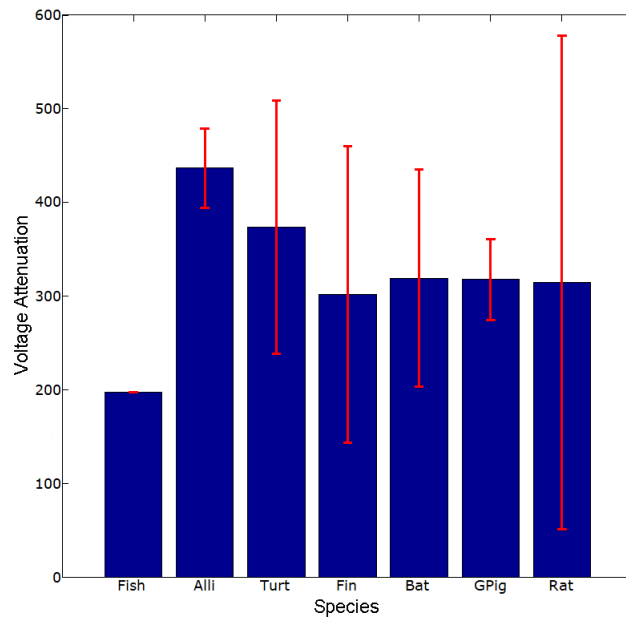
(a) Voltage attenuation averaged over all cell model results for each species
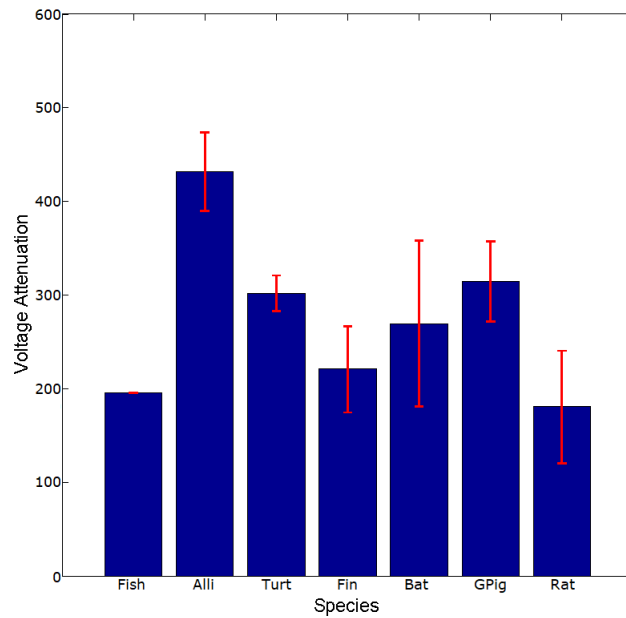
(b) Voltage attenuation averaged over species with some outliers (Turtle 3, Finch 4, Bat 1, Rat 4) removed.

Figure 5.14: Voltage attenuation from spines placed at terminal dendritic compartments and measured at the soma averaged over species with 95% confidence intervals.
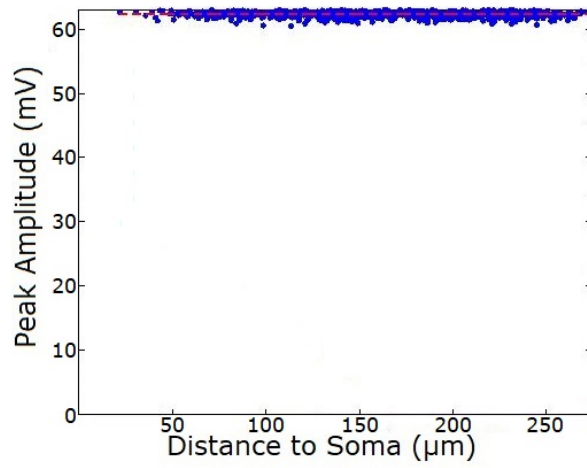
(a) Peak amplitude recorded at soma following stimulation in dendritic compartments
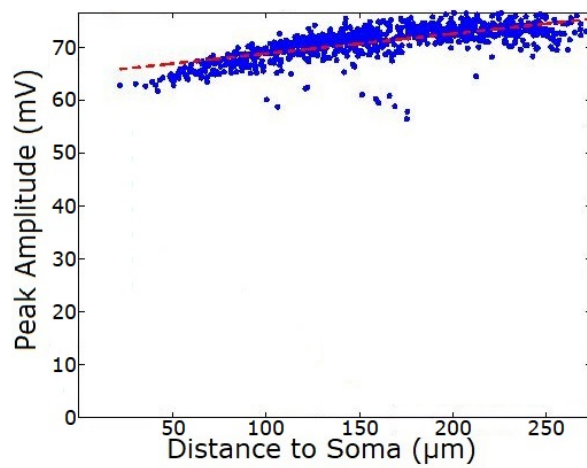
(b) Peak amplitude recorded in dendritic compartments following stimulation at soma
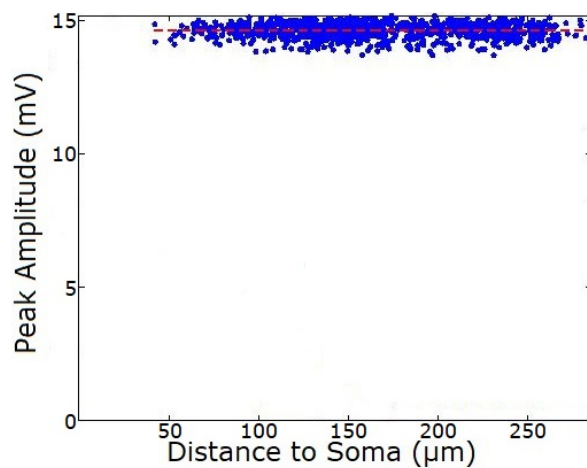
(c) Peak amplitude at soma following stimulation in dendritic spines

Figure 5.15: Peak amplitude recorded following a single spike input, with varying input and recording sites in an active model of cell Guinea pig 2. See Table 5.12 for regression equation terms.
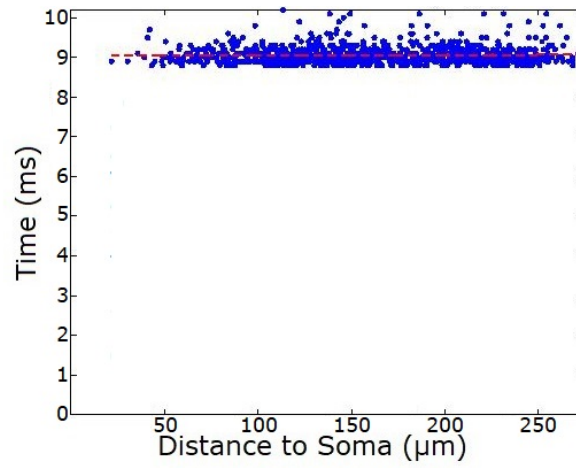
(a) Time take to reach peak amplitude at soma following stimulation in dendritic compartments
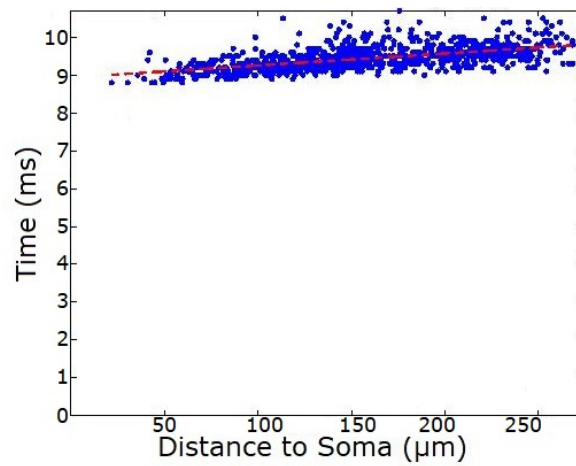
(b) Time taken to reach peak amplitude in dendritic compartments following stimulation at soma
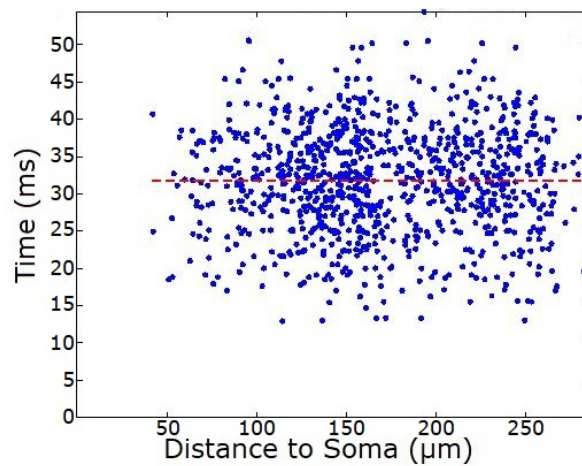
(c) Time taken to reach peak amplitude at soma following stimulation in dendritic spines

Figure 5.16: Time taken to reach peak amplitude following a single spike input, with varying input and recording sites in an active model of cell Guinea pig 2. Data for trend lines can be found in Table 5.12.
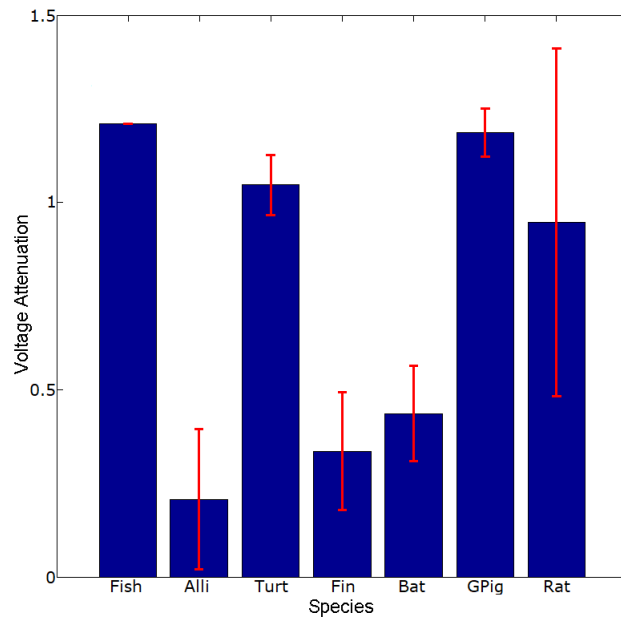
(a) Voltage attenuation averaged over all cell model results for each species
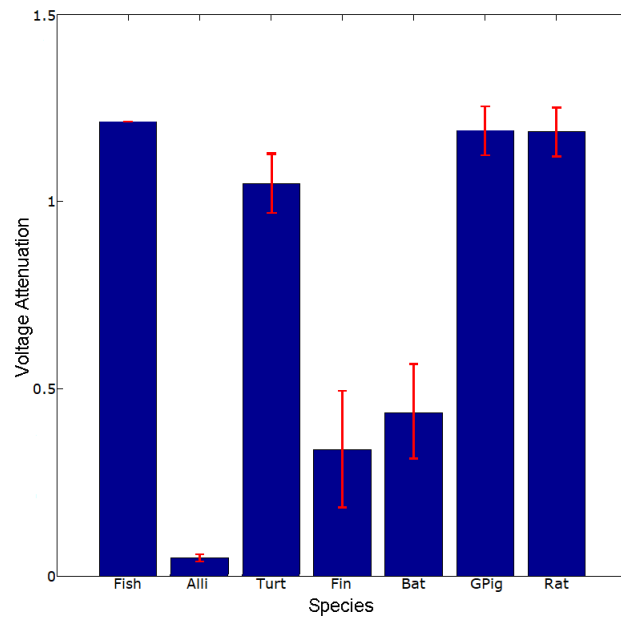
(b) Voltage attenuation averaged over species with some outliers (Alligator 2, Alligator 3, Rat 4) removed.

Figure 5.17: Voltage attenuation from terminal dendritic compartments with active ion channels to the soma averaged over species with 95% confidence intervals.
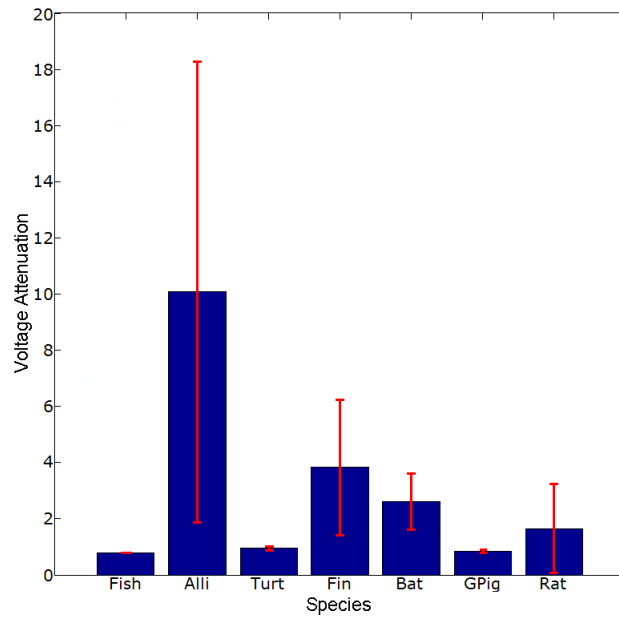
(a) Voltage attenuation averaged over all cell model results for each species
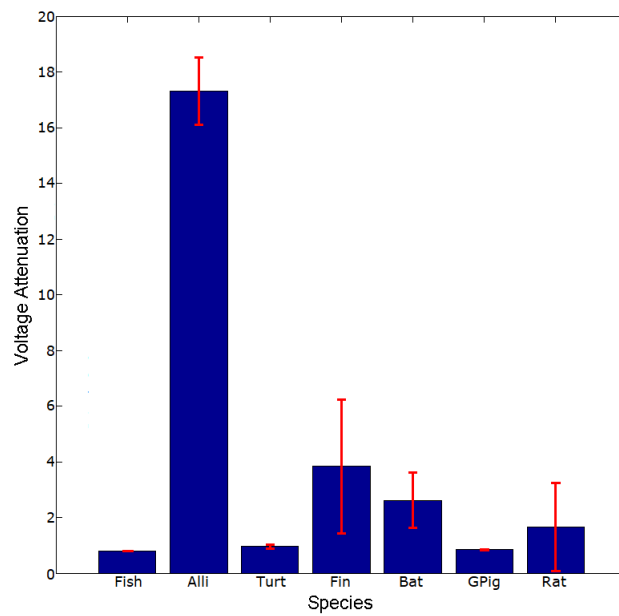
(b) Voltage attenuation averaged over species with some outliers (Alligator 2, Alligator 3) removed.

Figure 5.18: Voltage attenuation from the soma to terminal compartments with active ion channels averaged over species with 95% confidence intervals.
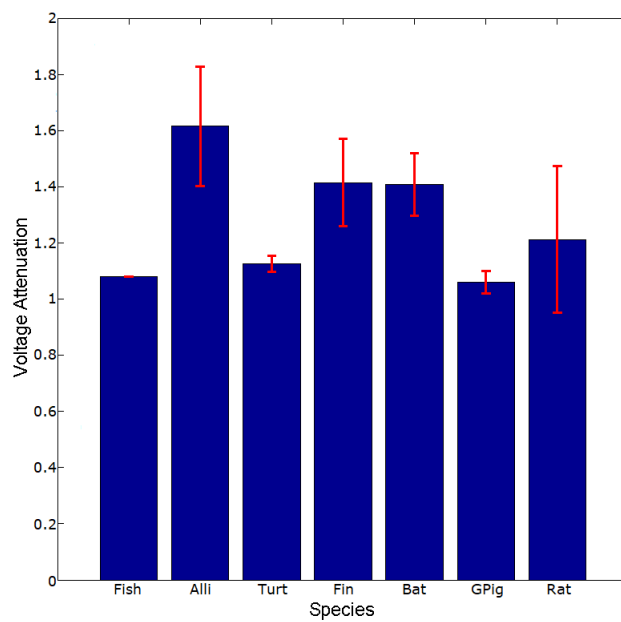
(a) Voltage attenuation averaged over all cell model results for each species

Figure 5.19: Voltage attenuation from terminal dendritic compartments with spines and with active ion channels to the soma averaged over species with 95% confidence intervals.

electrophysiology and active ion channels, it was hoped that differences in the model results would be found to correlate with morphological features. This in investigated further in the next chapter.

Measuring the time taken to reach peak amplitude at recording sites revealed a strong linear correlation with time in passive models. In the active case, the two variables became independent in many cells. This was evidenced by the coefficients of determination derived from plotting these variables with trend lines. However, the time graphs for active models shows signs of quantisation, suggesting the time step for recording output was too large to fully represent the changes over time.

The peak amplitude at a recording site tended to vary more between the cell models than between experimental conditions when passive models were tested. One exception was the decrease seen across all models when the spines were modelled explicitly. The similarities between spineless models in the dendrite→soma and soma→dendrite directions can be explained by the transfer impedance (Koch, 2004).

Transfer impedance is a symmetrical function for finding the change in membrane potential at location j following a change in current at location i. If an identical current change is initiated at location j, than the voltage at i should be identical as had been previously measured at location j. Differences in voltage can still occur without violating this rule. Each compartment has an input resistance, defined as the membrane resistance divided by area (r_m/a). Larger areas decrease resistance, making it easier for current to flow through the membrane. However, this also increases the amount of current necessary for a change in membrane potential to occur. The soma compartment has the largest area in a Purkinje cell model, and therefore the lowest input resistance, and so would require higher current to effect change.

Voltage attenuation in passive models was found to be smaller in the soma → dendrite direction, which is a common property of passive neuron models (Rinzel and Rall, 1974). This is again a product of the differences in input resistance, less current is able to flow through the dendrites away from the soma due to the decrease in radius that increases the resistance; however less current is then needed to effect change in membrane potential. This changes in the active models, where the soma→dendrite voltage attenuation was the highest when averaged over species groups. This could be a factor of changes to the membrane resistance (and by extension, the electrotonic length of compartments) when the membrane includes active channels (Rapp et al., 1992).

Chapter 6

Differences Between Cell Models

6.1 Introduction

In this chapter the results of the exploration of cell morphology in Chapter 4 and of the models of electrophysiological behaviour in Chapter 5 are drawn together to compare and contrast the cells and to look for patterns or groupings within the set. To do this, the data gathered in the previous chapters are organised into feature vectors. A feature vector is comprised of a fixed number of features, which in turn are fixed-length vectors, where each vector is a different measurement from the data. In this work, the features gathered from the data are grouped thematically into different feature vectors. In this format, the data can be used with clustering algorithms, like growing neural gas (GNG) and agglomerative hierarchical clustering (AHC), and statistical tests, such as principal component analysis (PCA).

These methods are useful for defining the variance across the dataset, but also for finding similarities between elements. Using these techniques here is important as groupings in the data may indicate evolutionary changes - particularly if groupings occur along phylogenetic lines. A lack of groupings would be equally as telling, as it could suggest either so little variance that the data is essentially homogeneous, or such high variance that the cells can only be considered as individuals.

The first section, Section 6.2, details the feature vectors used for this work, the techniques used to gather the measurements, and how they were built. Following this, each of the comparative methods used are introduced in Section 6.3. This includes PCA, GNG and AHC, but also a distance metric intended to find variance within species groups, and an image-based clustering method intended to bypass the problems of parametric feature vectors. The results of these methods are given in Section 6.4 and the chapter finishes with a discussion of the results and methodology used in Section 6.5.

6.2   Feature Vectors

A feature vector is a common input to clustering and classification algorithms. The intent is to describe the elements of your data set with a number of features n, such that the observations in the data set can be accurately modelled in an n-dimensional space. Clustering and classification algorithms will then typically try and sort or group the observations based on distance or neighbouring data points. Higher dimensional feature vectors can be desirable for better clustering, which is why many algorithms use a kernel function to inflate the number of dimensions for the data set. However, with a very small sample size, such as that used in this study, this can be counter-productive. Having a much larger number of features than the sample size can lead to an increase in noise-related problems as not all the features will be informative to classification. For this reason multiple feature vectors were used, based around either morphological or electrophysiological aspects of the cells.

6.2.1   Morphological Features

Each of the cells was characterised using several size and branching-based metrics. Some of these were measured using the Trees Toolbox (Cuntz et al., 2010) for Matlab (The MathWorks, 2013), some scripts were also written specifically for this study. Five of the morphological features were based on the size of the cells. Most of these metrics were gathered from neuroConstruct (Gleeson et al., 2007), with the exception of soma radius which is available in the morphology files. These methods are discussed in Section 4.3.1, and the full feature vector is listed in Appendix B.

As the Purkinje cell is noted for its complex branching patterns, it was important that branching metrics were well represented in the clustering stage. Eleven features were chosen that either described branching density, or were dependent on the level of branching in the tree. In the latter category were features like the number of dendritic compartments, which is determined both by cell morphology and electrotonic length. Also included are the number of branching and terminal points. In cases where branch points only bifurcate, the number of terminal points is equal to branching points $+ 1$. These were included as there were cases in both the rat and turtle cells of dendrites splitting into more than two child branches.

The rest of the branching measurements took some method of calculation to be found, as described in Section 4.3.1. The Horton-Strahler number and maximum bifurcation ratio for each tree were taken using purpose-written Matlab scripts; the remaining measures (maximum branch order, maximum and average path length, and average tree asymmetry) required the use of the Matlab toolbox Trees Toolbox written by Cuntz et al. (2010).

6.2.2 Electrophysiological Features

Features for the two electrophysiological vectors were key statistics taken from the passive and active modelling experiments. The active modelling experiments used a passive rather than an active soma so that the same measures could be extracted from each set of results, allowing the analysis to be directly comparable between the two. Using a passive soma stopped the models with active dendrites from producing spikes. As many of the statistics used in the feature vectors concerned maximum amplitudes, it was important that spiking did not occur. In total, fourteen features were selected from the experimental results.

Four different voltage attenuation values were taken from the passive and active models, comprising different directions and different proportions of the dendritic tree. The method for finding voltage attenuation is given in Section 5.3.

Also recorded for the feature vectors were the peak amplitudes reached in the single compartment/spine stimulation experiments, averaged over all results from each cell. Three of these recordings were taken at the soma compartment of the model.

As with the voltage attenuation results, the results from the spineless models are divided into those averaged over the entire dendritic tree, and those averaged over only the dendritic compartments without children. Some terminal points have a relatively short path length to the soma, resulting in lower attenuation than is seen in the tree as a whole. In addition, compartments and spines that had no change, or caused no change at soma when stimulated from these points, were excluded from calculations to avoid problems in the code. In the active case no compartments or spines were removed. For the passive results, almost no compartments were removed in the dendrite to soma direction. Most cells had a small number of removals when testing the opposite direction, however. The largest amount of removals were from the spine stimulation results.

The last of the electrophysiological features are the time-based measurements. These features list the average time taken to reach the peak amplitude following stimulation. As before, these include time taken to reach the peak amplitude at soma following stimulation in dendritic compartments or spines, and vice versa.

6.3 Methods

Before clustering, the feature vectors described in the previous section were converted to Z-scores for normalisation.

The aim of a clustering algorithm is to find the natural groupings in a data set, which are often high-dimensional and have a large number of observations, making it difficult or impossible to find by hand. The effectiveness of clustering algorithms can depend greatly on the size of the data set and selection of features used.

6.3.1   Principal Component Analysis

Principal component analysis (PCA) is a widely used statistical analysis and dimension reduction tool. When applied to a feature vector, it extracts the principal components - additive combinations of the features that capture the variance of the dataset. The first principal component is the combination of features that can explain the highest amount of variance, the second principal component is the combination that explains the most of the remaining variance, and so on.

This is achieved by linearly transforming the data, moving the co-ordinates while maintaining the the relationships between the elements of a vector, such as by rotating the entire vector. The first factor loading vector is designed to transform the data such that maximises the variance along the first axis. The second factor loading must do the same for the second axis and must also be orthogonal to the first. There are several methods for performing PCA. This study uses a Matlab implementation (The MathWorks, 2013) of the eigenvalue decomposition method. The covariance matrix of the data is created and the eigenvectors are calculated to become the principal components (Shlens, 2014).

In this study, PCA was used to find the features that have the highest variance - by finding which features contributed most to the first x principal components that explain $>85\%$ of the variance, and to compare the results of growing neural gas and agglomerative hierarchical clustering.

6.3.2   Growing Neural Gas

The growing neural gas (GNG) algorithm developed by Fritzke (1995) was used for clustering the various feature vectors drawn from the electrophysiological and morphological characteristics of the cells. Growing neural gas is an unsupervised neural network based on competitive Hebbian learning rules.

Unlike the earlier neural gas algorithm (Martinez and Schulten, 1991), GNG begins with only two nodes connected by a single edge, and can add new nodes each time step until it reaches a pre-determined maximum. A new time step begins by finding the two nodes closest to the data, n_1 and n_2. The age of all the edges connecting to n_1 is incremented, and the error (absolute distance between the node and the closest data-point from the input) is taken. Node n_1 and all its connections are then moved towards the input by a fraction of the error. As an interpretation of Hebbian learning rules, if n_1 and n_2 are not already connected by an edge, one is created. If there is already an edge, its age is reset to zero. Any edges above an age limit are then removed, as are any nodes with no edges. A new node n_z can be inserted if the maximum number of nodes has not yet been reached. This node is placed halfway between the existing node n_x that has accrued the highest error and the node n_y with the highest error from the neighbourhood nodes connecting to n_x. The edge between n_x and n_y is removed and replaced with edges connecting n_x and n_y to n_z. Finally, the error variable of all nodes is decreased by a given constant. This will continue until some stopping criterion, such as a maximum number of steps, has been

met.

An advantage of this approach over a regular neural gas algorithm is that it allows the network to find the optimal number of nodes to cluster the input space up to a given maximum. The implementation used in this study is a Java version developed by Fritzke and Loos (2012). The clustering results were then fed into a Matlab (The MathWorks, 2013) script which used PCA as a dimension reduction tool to visualise the cells. The cells were then plotted in PCA-space, either colour-coded by species (showing the clustered GNG nodes) or colour-coded by cluster and labelled.

6.3.3 Agglomerative Hierarchical Clustering

Another clustering technique used on these feature vectors was agglomerative hierarchical clustering, using Ward's method as the similarity measure. Agglomerative clustering first assumes each observation in a feature vector is a cluster that contains one element. It then begins to pair clusters by the similarity measure, until all clusters are grouped together, creating a graph with a binary tree structure.

Ward's method for measuring the suitability of merging one cluster with another is a minimum variance algorithm, it attempts to minimise the increase in variability with each merge. Ward defines the variability as the sum of the square of the Euclidean distance between each element of the cluster and the cluster centre, known as the inner squared distance.

$$d(A, B) = \sqrt{\frac{2n_A n_B}{(n_A + n_B)} \left\| \bar{z}_A - \bar{z}_B \right\|^2} \tag{6.1}$$

Equation 6.1 shows Ward's method as calculated in Matlab (The MathWorks, 2013), as this was the version used in this study. A and B are clusters that comprise n_A and n_B elements respectively, and $\bar{z}_A$ and $\bar{z}_B$ are the centres of each cluster.

6.3.4 Image-Based Clustering

One possible issue with the feature vectors used in this study is that a number of the morphological features rely on the compartmentalisation of the cells. Dendritic compartments are not a natural feature of cells. The creation of compartments relies on electrophysiological parameters, which were unfortunately not derived from the cells used in this study. One attempt at an alternative method of clustering was to use images of the dendritic structure of the cells rather than feature vectors.

To achieve this, images of the cells first had to be obtained. The cell morphology files were loaded into CVAPP (Cannon et al., 1998), a programme with many beneficial features for building compartmental models of cells, including a simple two-dimensional visualisation of cells from morphology files.Unlike other cell types which extend their dendrites in all directions, the Purkinje cell

largely branches within a single plane, making them almost uniquely suited to two-dimensional representation. CVAPP's visualisation tools were chosen over other alternatives as the cells are drawn in a single colour without shading or texture, which helps to maintain a uniformity of the presentation of the cells. Additionally, CVAPP includes axes and graph lines which greatly simplified the process of ensuring the cells were all plotted on a single scale, allowing for cell size to be as much a feature as the branching. Once the images were retrieved from CVAPP, the graph lines were removed from the images and each was cropped to the same dimensions. In addition to the Purkinje cells, the same procedure was followed for images of Deep Cerebellar Nuclei (DCN) neurons (Sultan et al., 2003), so that these cells could be used to verify how well the method worked. An example of the images used can be seen in Figure 6.1.

The images then went through a preprocessing stage so that they would be in the right format for use with the Java GNG algorithm. Firstly, the images were loaded into Matlab, where they were converted to matrices with the same dimensions as the image, with cell of the matrix representing a pixel. Each image used only two colours, allowing them to be represented as a binary matrix; 1 indicating a pixel that was part of the cell and 0 being part of the background.

Each matrix was then mean-centred and had a Fast Fourier Transform (FFT) applied. Applying a Fourier transform to an image is a way to find repeating elements called spatial frequencies. The FFT creates a brightness image of the same size as the input (see Figure 6.2) that describes the number of spatial frequencies that were present in the input, as well as the magnitude of each frequency. The centre pixel of a brightness image is the mean brightness of the input. Each spatial frequency found in the image is represented as two non-black pixels equidistant from the mean; higher frequencies are found further from the mean while lower frequencies are closer. The magnitude of the peak of the frequency is translated to the brightness of the pixel. Orientation of frequencies is also described in the brightness image positioning of the two pixels.

After this, the new FFT image matrices were reformatted as row vectors and added to a single matrix, each row representing one cell image. The final matrix was the put through PCA to reduce the number of features before clustering.

6.4 Results

The clustering results are reported in this section, starting with the findings from the principal component analysis. The PCA results are used as an intermediary to compare the clusters from the agglomerative hierarchical clustering (AHC) and growing neural gas (GNG). This is achieved by using AHC with the relevant principal components for each feature vector and then overlaying the groups on the GNG results.

(a) Bat 1
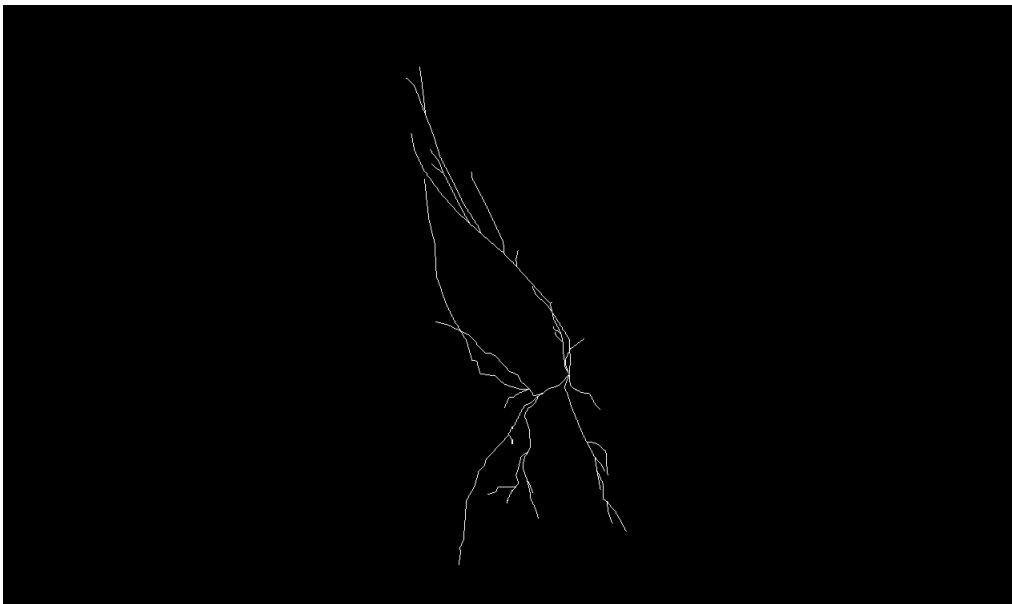
(b) Rat DCN neuron

Figure 6.1: Standardised images used in GNG clustering in place of feature vectors
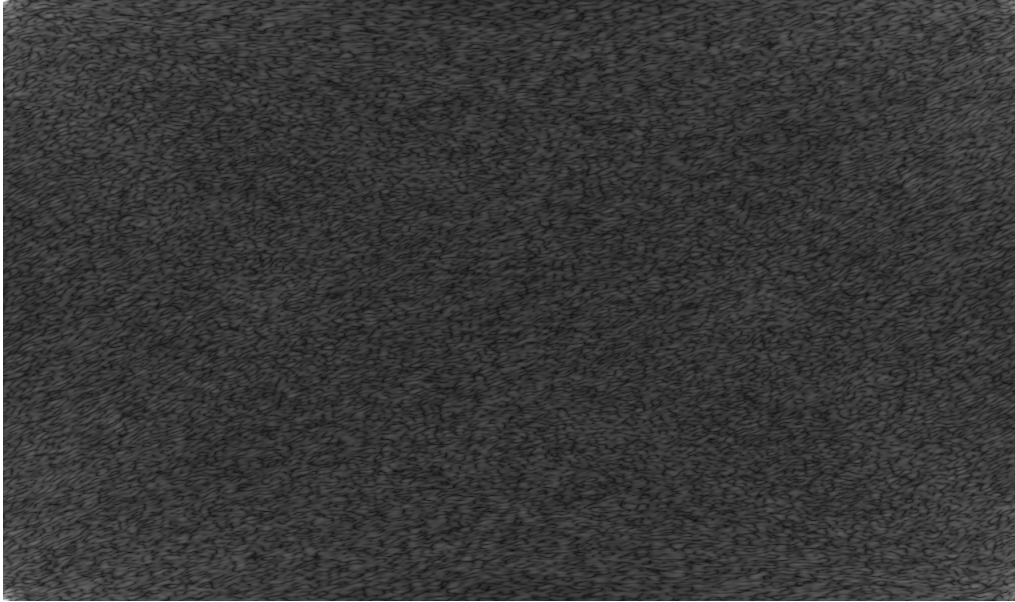
(a) Bat 1
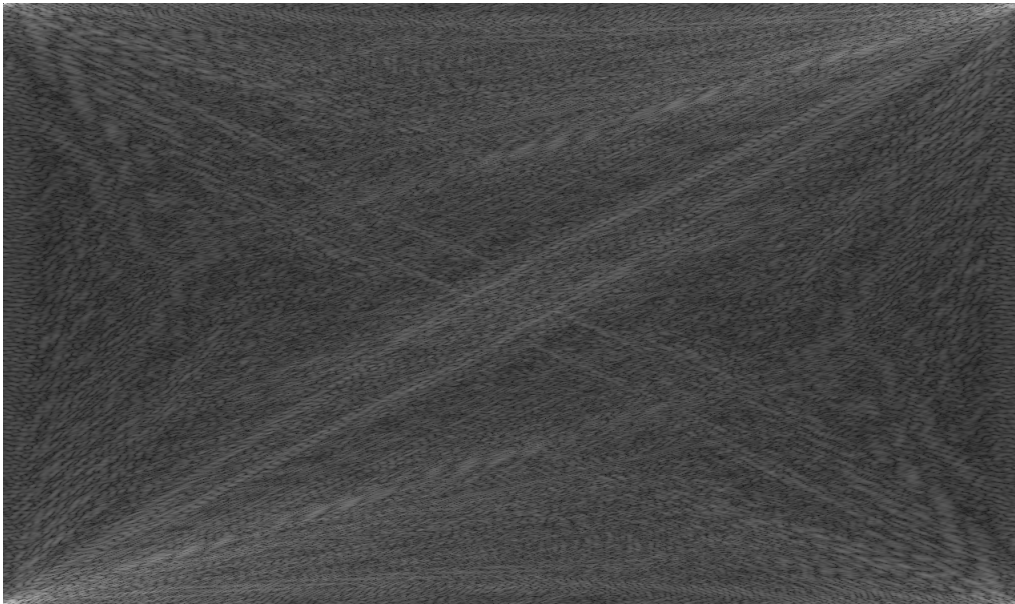
(b) Rat DCN neuron

Figure 6.2: Brightness images created from applying FFT to the cell images in Figure 6.1

6.4.1 PCA

Before beginning PCA, correlation matrices were made for each of the feature vectors. This is a matrix where the Pearson correlation coefficient r is taken between each of the features. Like Kendall's τ (described in Section 4.3.1), r is valued between -1 and 1, with 0 indicating no linear relationship, and 1 and -1 indicating complete positive and negative linear correlations respectively. Table 6.1 shows the results for the morphological feature vector, the corresponding tables for the electrophysiological vectors are given in Appendix F.

In the morphological feature vector, there are three distinct groups with strong linear correlations. The first of these groups contains the number of dendritic compartments, dendritic spines, and branching and terminal points. These metrics can also be seen to have the strongest correlation to the first principal component, demonstrated in Figure 6.3 and Appendix G. The key for abbreviations for morphological features can be found under Table 6.1. This group includes two pairs of features that were known to be related prior to creating the matrix - the number of spines is directly derived from the number of compartments, and for many of the cells the number of terminal points is equal to the number of branch points + 1. The second correlated group, maximum and average path lengths were also already known to be related.

The final correlated group is made up of all of the size metrics except soma radius. As with the other groups, it was clear before correlation that the total dendritic surface area and volume are related to dendritic length and radius. These features have the highest correlation to the second principal component, along with the maximum branch order.

Appendix H shows the first four principal component averaged over species groups, displaying both the in-group variance and the difference between the fish and turtle cells and the other samples. The first four principal components explain 86.15% of the total variance of the feature vector. Plotting the second and fourth components did not reveal any clear patterns, but the third component, which is strongly correlated with the maximum and average path lengths, approximately decreased with phylogenetic rank (see Figure 6.4).

The correlation matrix for the passive electrophysiological features revealed two strongly correlated groups. The first contains six metrics, which are also the six metrics that most strongly correlate to the first principal component (see Figure 6.5 and Appendix G). A key to abbreviations for the electrophysiological features can be found in Appendix F. These include the voltage attenuation from dendritic compartments to the soma and the peak amplitude at the soma following dendritic stimulation, which has a strongly negative linear correlation. Also included in this group is the average peak amplitude at soma following stimulation at terminal compartments, a subset of all dendritic compartments, and the average peak amplitude at soma following stimulation in dendritic spines. The average peak amplitude in dendritic and terminal compartments following stimulation at the soma is also in this group. The second correlated group are all time metrics, many of which are also correlated with the second principal component, although the overlap between these groups is not as high as for the

	NSp	BP	TP	MaxBO	TotLen	TotSA	TotVol	SomRad	AvDCRad	MaxPL	AvPL	AvTA	H-S	MaxBR	AvDCEL
NDC	0.99	0.92	0.90	0.55	0.45	0.13	0.10	-0.16	-0.13	0.51	0.53	-0.42	0.55	-0.14	-0.44
NSp	-	0.92	0.90	0.53	0.47	0.15	0.12	-0.15	-0.11	0.50	0.53	-0.41	0.57	-0.13	-0.45
BP		-	0.99	0.57	0.39	0.25	0.20	-0.17	0.02	0.40	0.44	-0.38	0.65	-0.19	-0.72
TP			-	0.53	0.40	0.28	0.23	-0.16	0.07	0.33	0.37	-0.33	0.64	-0.21	-0.74
MaxBO				-	-0.24	-0.38	-0.25	-0.17	-0.56	0.74	0.67	-0.68	0.32	-0.33	-0.30
TotLen					-	0.86	0.79	0.42	0.66	0.19	0.31	0.12	0.29	0.18	-0.36
TotSA						-	0.93	0.46	0.90	-0.02	0.13	0.28	0.26	0.12	-0.54
TotVol							-	0.72	0.80	0.10	0.26	0.15	0.17	0.05	-0.51
SomRad								-	0.40	0.08	0.17	0.12	-0.28	-0.00	-0.09
AvDCRad									-	-0.27	-0.14	0.40	-0.02	0.15	-0.42
MaxPL										-	0.95	-0.65	0.23	-0.13	-0.10
AvPL											-	-0.54	0.28	-0.17	-0.21
AvTA												-	-0.08	0.12	0.05
H-S													-	-0.03	-0.62
MaxBR														-	0.21

Table 6.1: Correlation matrix for the morphological features. KEY: NDC: Number of dendritic compartments; NSp: Number of dendritic spines; BP: Number of branch points; TP: Number of terminal points; MaxBO: Maximum branch order; TotLen: Total dendritic length; TotSA: Total dendritic surface area; TotVol: Total dendritic volume; SomRad: Soma radius; AvDCRad: Average radius of dendritic compartments; MaxPL: Maximum path length; AvPL: Average path length; AvTA: Average tree asymmetry; H-S: Horton-Strahler number; MaxBR: Maximum bifurcation ratio; AvDCEL: Average electrotonic length of dendritic compartments.
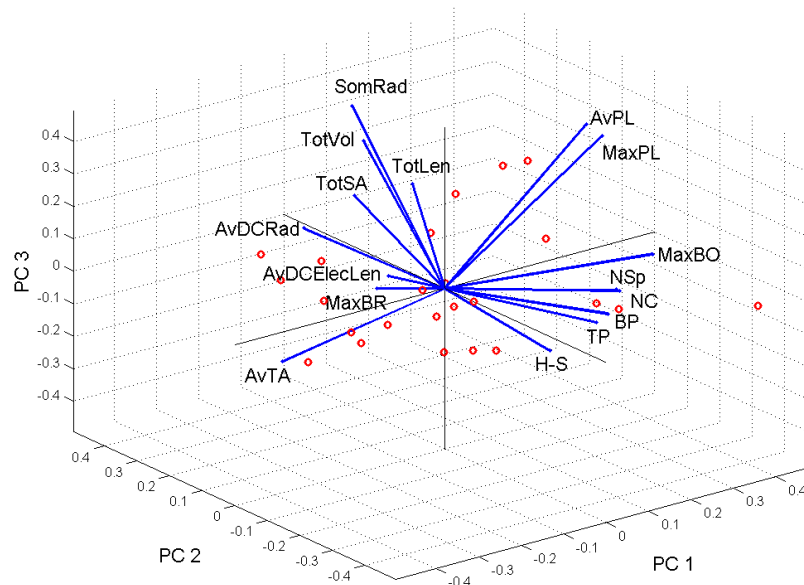
Figure 6.3: The first three principal components plotted with factor loadings for the morphological feature vector

first principal component. Unlike the morphological feature vector, plotting the species average principal components did not reveal potential correlations, these are given in Appendix H. 87.32% of the variance is explained by the first three principal components.

Similar patterns emerge between the correlation matrix for the active electrophysiological features and the first two principal components for the set, see Figure 6.6. One difference was the correlation of the average time to reach peak amplitude following stimulation in dendritic spines to the first principal component and to a group that otherwise comprises the average peak amplitude recorded in dendritic and terminal compartments and in the soma following dendritic/terminal compartment stimulation and the voltage attenuation from terminal compartments to the soma. The second correlated group is made up of the remaining time-based metrics, which are also the four most correlated metrics to the second principal component. The first three principal components are able to explain 88.26% of the feature vector's variance. The full PCA scores for all three feature vectors are listed in Appendix G. Like the passive electrophysiological feature vector, no patterns were found when plotting species average principal components. The third principal component, which is most correlated with the voltage attenuation when stimulating at soma and recording at dendrites, did show the fish cell as a major outlier (see Appendix H).

Once the principal components were found for each of the feature vectors, correlation coefficients were taken between the principal components that ex-
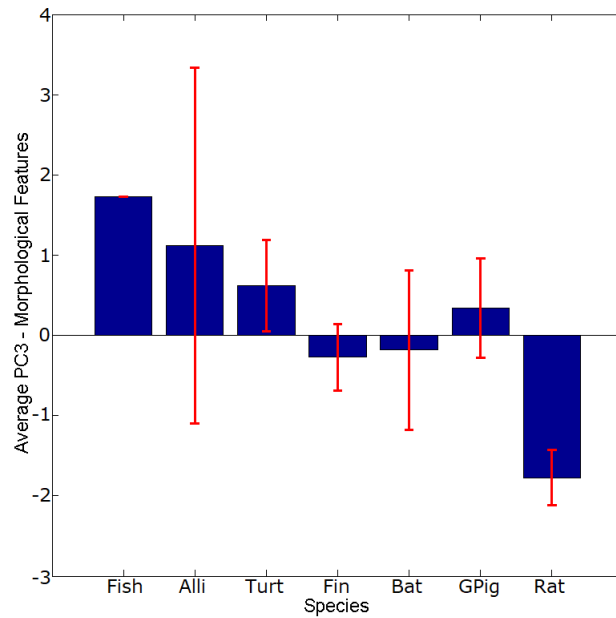
(a) The third morphological principal component averaged over species groups with 95% confidence interval
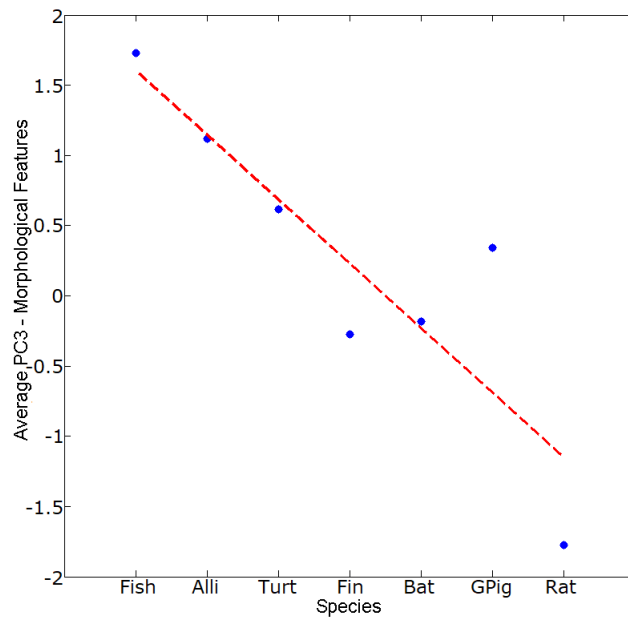
(b) The third morphological principal component averaged over species groups with trend line. (Slope = 0.99, Intercept = 0.23, R^2=0.77)

Figure 6.4: The third PC for the morphological feature vector shown with confidence intervals and trend line
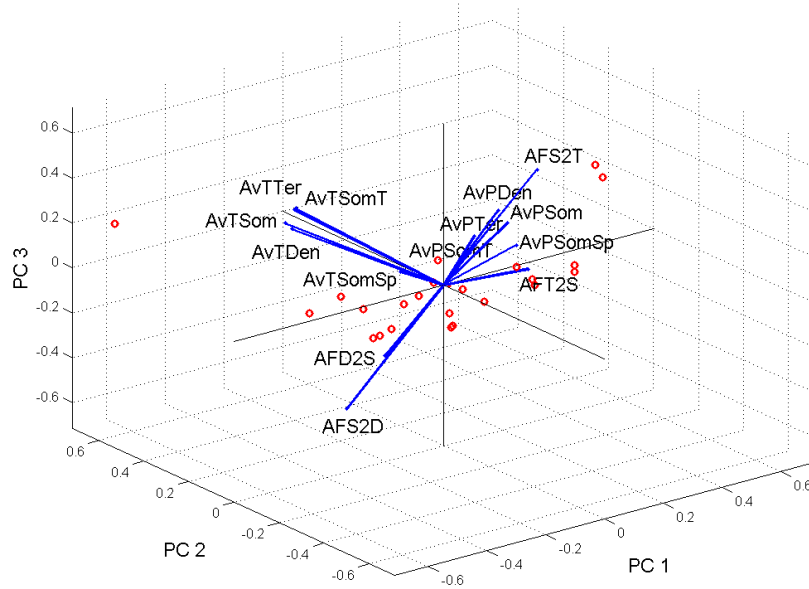
Figure 6.5: The first three principal components plotted with factor loadings for the passive electrophysiological feature vector
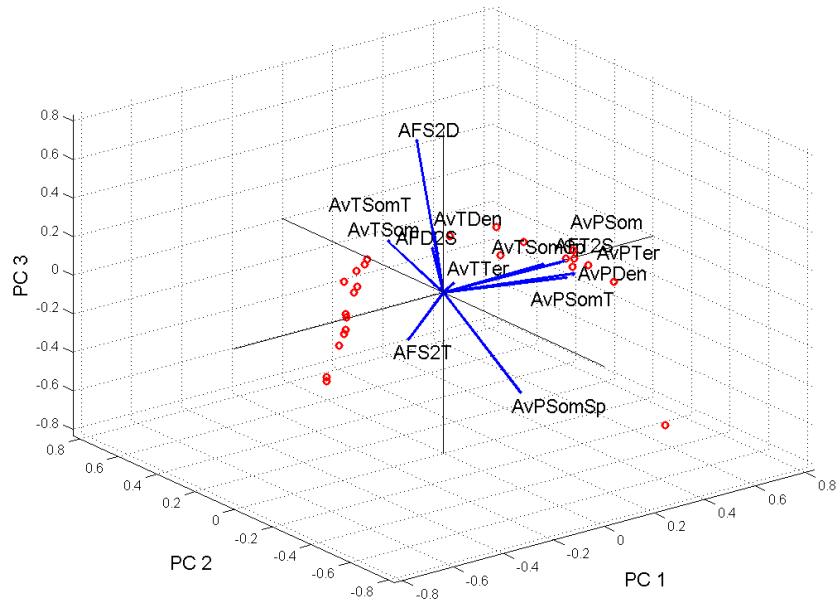
Figure 6.6: The first three principal components plotted with factor loadings for the active electrophysiological feature vector

plained >85% of the variance from each set and recorded in Table 6.2. Between the morphological and passive electrophysiological feature vectors, a strong negative correlation can be seen between the second morphological PC and first electrophysiological PC. This suggests that the size of cells, specifically the average radius of compartments and total dendritic surface area and volume, is negatively correlated with the average peak amplitude recorded at soma following stimulation in dendritic compartments and spines. Additionally, there is a mild positive correlation between the first morphological PC (most correlated to branching and terminal points) and the second electrophysiological PC (average time to reach peak amplitude at soma following stimulation in dendritic compartments or spines), as had been investigated in Section 5.3.1.

Between the morphological principal components and active electrophysiological principal components, only one pair displays a strong linear correlation. The size-correlated second morphological PC has a positive correlation with the first electrophysiological PC. As mentioned above, this PC is most correlated with voltage metrics, but also the time take to reach peak amplitude at soma when stimulating spines. That the first morphological PC is not strongly correlated with any active electrophysiological components suggests that increased dendritic complexity does not have a great effect on Purkinje cell function in vivo.

Finally correlations between the passive and active electrophysiological feature vectors were taken to gain some insight into the changes to behaviour created by the active ion channels. The strongest correlation is a negative correlation between the first PC of each set. This can also be seen in the first PCs plotted over species averages for each set in Appendix G, where many of the species averages are inverted between the two graphs. This could be due to the influence of voltage attenuation on each of these components, which was much higher in the passive models.

6.4.2 Clustering Results

In this section, the results of the growing neural gas and agglomerative hierarchical clustering are given together, due to the large amount of overlap between them. A normalised Hopkins statistic written for Matlab (Fricke, 2012; Zhang et al., 2006) was used to evaluate the clustering tendency of the feature vectors. This statistic compares the distances between the input data with a uniform dataset generated from the original data. In this normalised statistic, a result close to 0.5 indicates that the input data is close to a uniform distribution, while a result nearer to 1.0 would suggest that there are natural clusters in the data. The statistic was averaged over 10,000 runs for each feature vector. The Hopkins statistic is used to question whether clusters found by machine learning techniques truly exist within the data or if they are an artifact of the algorithm. Figure 6.7 shows the GNG clusters plotted in 3-dimensional PCA space. In each graph, the cells are identified by name. Symbols given to data points indicate the GNG cluster they belong to, and the colour of data points indicates species (listed in image caption).

(a) Morphological features

(b) Passive electrophysiological features

(c) Active electrophysiological features
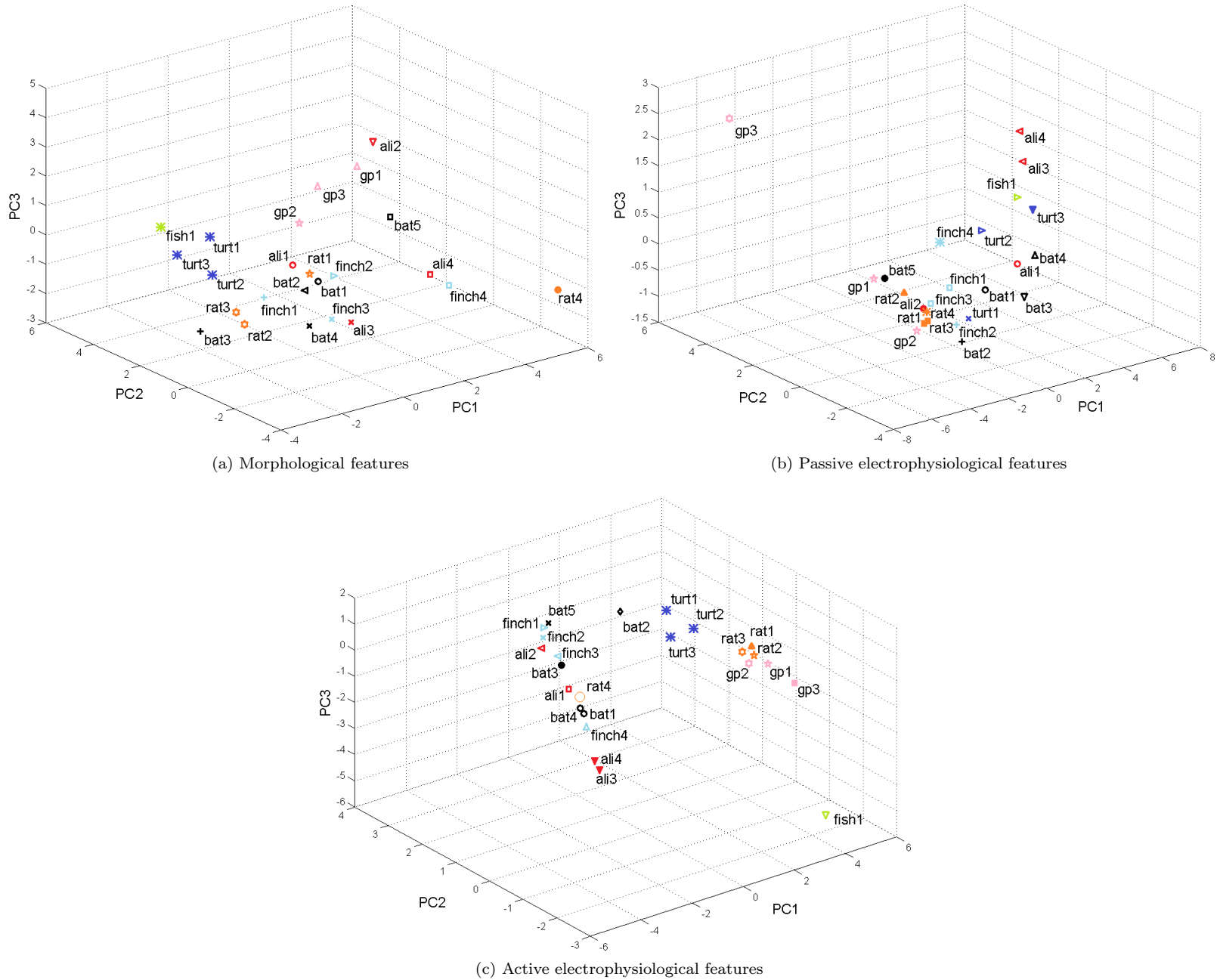
Figure 6.7: Cells plotted in PCA space. Symbols represent clusters designated by GNG, colour indicates species: Green - fish, red - alligator, purple - turtle, blue - finch, black - bat, pink - guinea pig, orange - rat

	Morph. PC1	Morph. PC2	Morph. PC3	Morph. PC4
P.E. PC1	-0.329	-0.749	-0.123	0.042
P.E. PC2	0.544	-0.291	-0.041	-0.361
P.E. PC3	-0.104	0.213	0.230	0.084

(a) Correlation between relevant morphological and passive electrophysiological PCs

	Morph. PC1	Morph. PC2	Morph. PC3	Morph. PC4
A.E. PC1	-0.192	0.833	0.096	0.083
A.E. PC2	-0.282	-0.334	0.300	-0.050
A.E. PC3	0.330	0.204	-0.373	-0.009

(b) Correlation between relevant morphological and active electrophysiological PCs

	P.E. PC1	P.E. PC2	P.E. PC3
A.E. PC1	-0.764	0.052	-0.281
A.E. PC2	-0.365	-0.108	0.164
A.E. PC3	0.071	-0.547	-0.293

(c) Correlation between relevant passive and active electrophysiological PCs

Table 6.2: Correlation coefficients between the relevant principal components of each of the feature vectors

	Alligator	Finch	Bat
Alligator	-	0.741	0.398
Finch	-	-	0.356
Bat	-	-	-

Table 6.3: Pearson's r between the alligator, finch and bat species averages for the morphological feature vector

The GNG results for the morphological feature vector includes only two clusters made up of a single species, one with two rat cells and one with two guinea pig cells. All three turtle cells are also in a single cluster, but are joined with the fish cell. These four cells are visually similar, and have the lowest number of branch points when averaged over species. The alligator, finch and bat cells are clustered together several times. The results given in Section 4.4 also show a lot of overlap between these species groups when morphological features were average over species and plotted. However, the correlation coefficient between species averages for these groups, shown in Table 6.3 only indicates a strong correlation between the alligator and finch cells. The Hopkins statistic for the dataset is 0.57, indicating that natural clusters do not exist in the data.

Clustering the passive electrophysiological feature vector reveals several single-species clusters, including single-species clusters of alligators and finches, unlike the morphological feature vector results. The Hopkins statistic for the feature

	Fish	Alligator	Turtle	Finch	Bat	Guinea pig	Rat
Fish	-	-0.418	-0.026	-0.398	-0.461	0.3953	0.093
Alligator	-	-	-0.712	0.273	0.252	-0.565	-0.437
Turtle	-	-	-	-0.085	-0.038	0.242	0.235
Finch	-	-	-	-	0.747	-0.864	-0.829
Bat	-	-	-	-	-	-0.855	-0.767
Guinea pig	-	-	-	-	-	-	0.939
Rat	-	-	-	-	-	-	-

Table 6.4: Pearson's r between the species averages across the active electrophysiological feature vector

vector is 0.67, suggesting that the data is unlikely to have natural clusters. Both the PCA and GNG clusters have marked Guinea pig 3 as an outlier. Guinea pig 3 has a high score on PC2, the component which correlates highly with time metrics. The feature vector (Appendix B) confirms that the time metrics for this cell are particularly high.

The active electrophysiological feature vector scored a Hopkins statistic of 0.66, again making it unlikely that the data has natural clusters. It is worth noting that this set displays the least cross-species clusters of the three feature vectors. This points to a possible species homogeneity in the behaviour of the active models. The correlation coefficient for species averages (see Table 6.4) suggests that many of the species behave comparably, with the rat and guinea pig cells in particular behaving almost identically.

Agglomerative hierarchical clustering was applied to the relevant principal components for each feature vector and plotted as in Figure 6.8 with the symbols from the GNG clusters for comparison. These results were then added to the PCA-GNG graphs (Figure 6.9) so that the results from all three analyses could be compared.

In the results for the morphological feature vector, 9/12 of the GNG clusters are also grouped by AHC. This is the highest agreement between the clustering techniques of any of the feature vectors: the active electrophysiological feature vector has 7 of the 16 GNG clusters reflected in the AHC groupings, and the passive features only 5 of 15 GNG clusters.

Laying the AHC groupings over the PCA-GNG graphs makes the similarities between the clustering results clearer. The results for all three sets suggest that the GNG cluster granularity was too fine, and that setting the algorithm to favour larger cluster sizes would have improved the agreement between the two techniques.

6.4.3 Image-Based Clustering

The image-based clustering, plotted in Figure 6.10, was unfortunately unsuccessful at clearly classifying cell groups. In the test set, many of the Purkinje neurons are separated from the DCN neurons, though there are overlaps. It

(a) Morphological features

(b) Passive electrophysiological features

(c) Active electrophysiological features
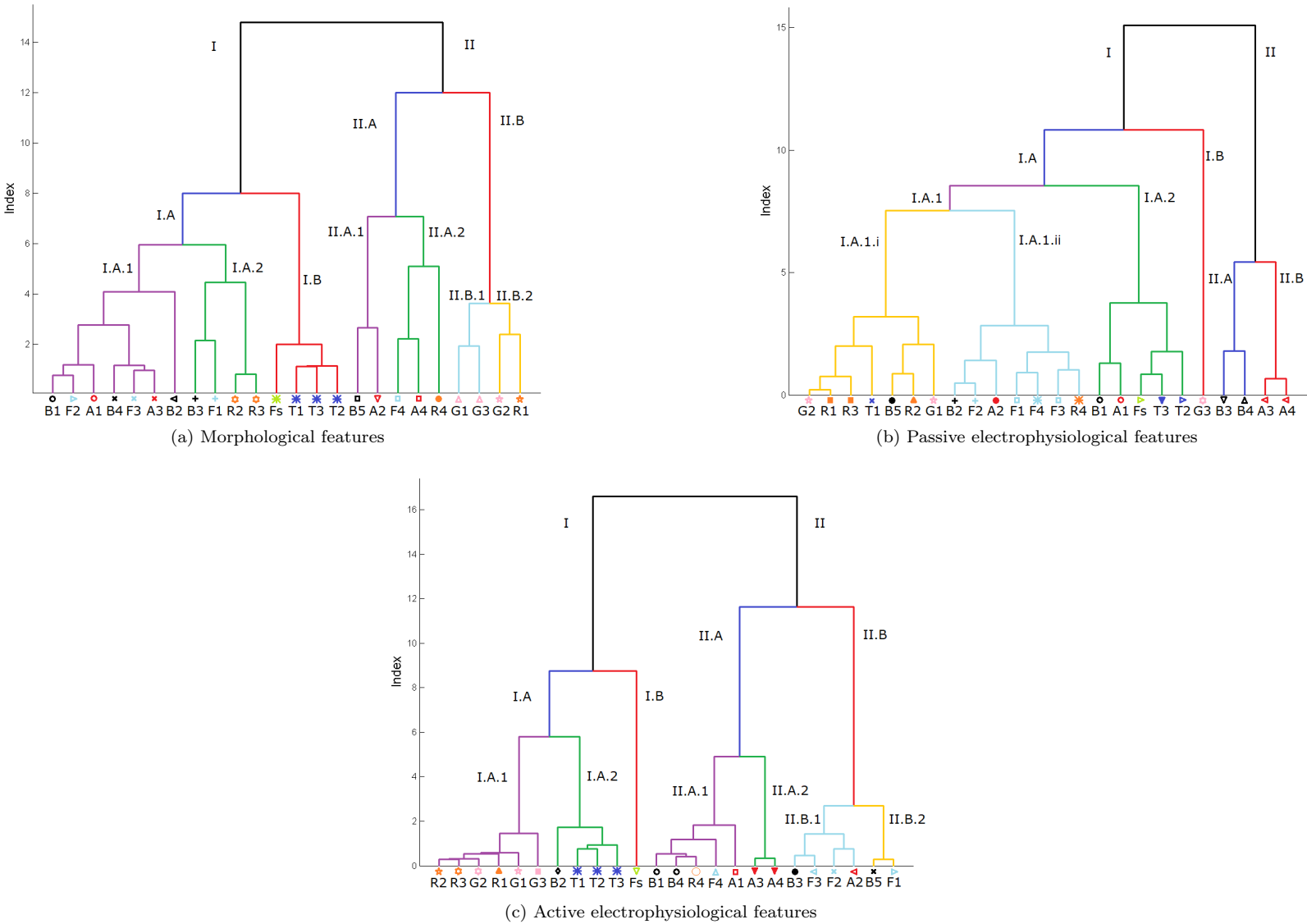
Figure 6.8: Agglomerative hierarchical clustering of the relevant principal components of each feature vector. Symbols represent clusters designated by GNG. Branches coloured for identification

(a) Morphological features

(b) Passive electrophysiological features

(c) Active electrophysiological features
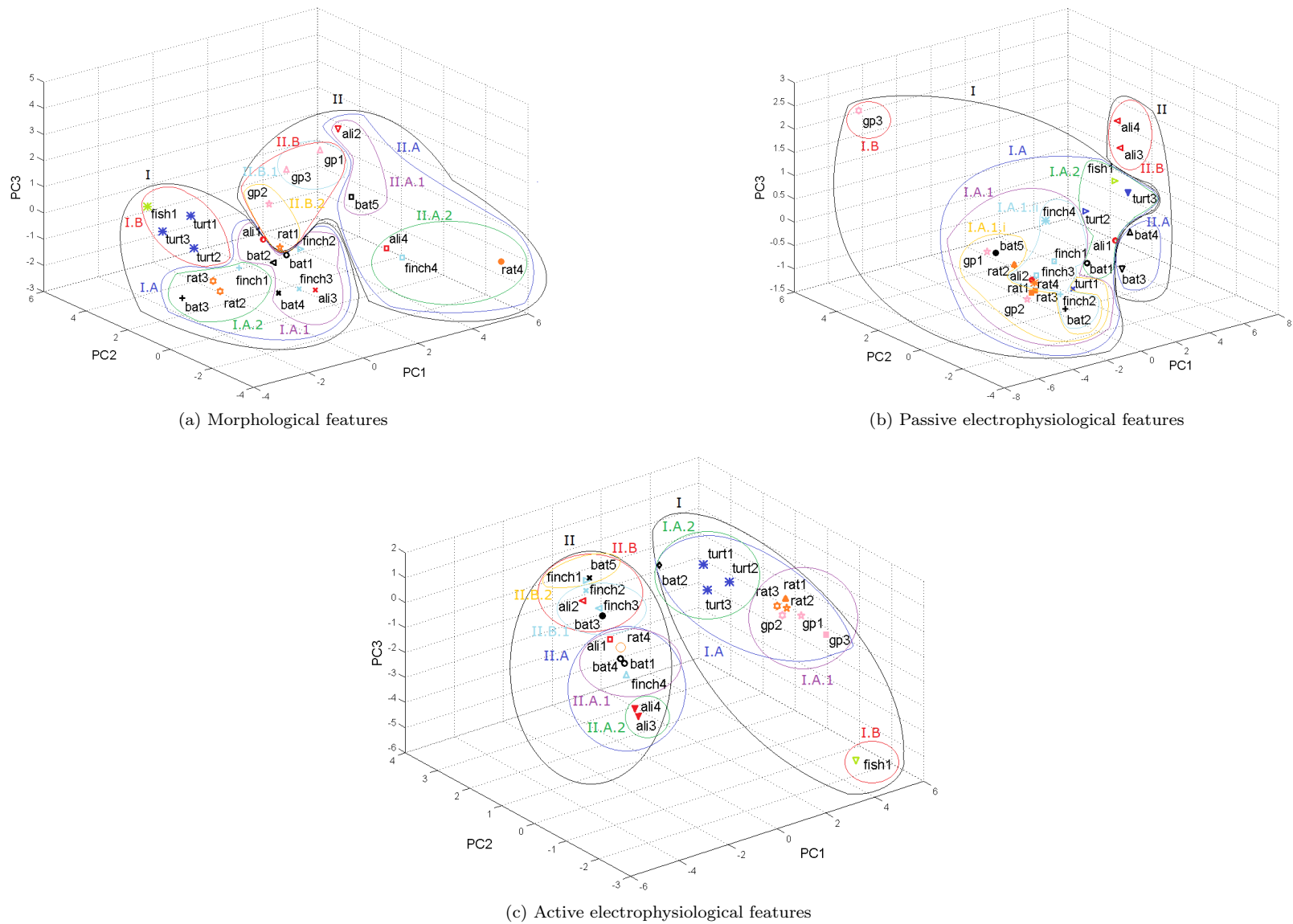
Figure 6.9: Cells plotted in PCA space with both AHC and GNG results. Coloured circles represent AHC clusters, colours indicate branches. Symbols represent clusters designated by GNG, colour indicates species: Green - fish, red - alligator, purple - turtle, blue - finch, black - bat, pink - guinea pig, orange - rat

is likely that there are so few clusters that contain both Purkinje and DCN neurons because the majority of clusters found by GNG contain only a single element.

The results for the Purkinje-only set is also made up of mostly single-element clusters. This is even true for cells that the PCA is able to differentiate, such as Guinea pig 2 and 3.

6.5 Discussion

Clustering is an excellent technique for exploring data for patterns, as was the goal here. Unfortunately, with a dataset as small as the one used in this study, it is difficult to find meaningful results or realistically generalise to a wider population. These problems have previously been discussed in Section 4.5, but are worth repeating here. The small dataset could also be the reason the Hopkins statistic pointed to a lack of natural clusters in all of the feature vectors.

In addition, many of the metrics are rooted in the compartmental models rather than natural features of the cells. Metrics like the number of compartments are dependent on both morphology and electrophysiology, due to compartment length being determined either by branch points or by electrotonic length. It is possible that the variance in the number of compartments could be better reflected by other measures - e.g. number of branching points and total electrotonic length of the dendrite.

Another way of avoiding problems with the chosen metrics was an attempt at non-parametric clustering by using images of the cells. In this case the clustering was unsuccessful, but the wide-spread use of clustering methods for identifying objects in images in other fields suggest that this was a failure of execution rather than technique.

Despite these issues, there were still interesting patterns found in the data. One result from clustering was the recurring overlap of certain species; guinea pig and rat cells often clustered together (Figure 6.7) and displayed strong linear correlation in the active electrophysiological feature vector (Table 6.4), perhaps unsurprisingly as they are both members of the rodent family. Closeness in phylogeny could also explain the relationship between alligator and finch cells. The average morphological metrics for these species are strongly correlated (Table 6.3), and crocodilians are considered to be very close to birds in the phylogenetic tree (Benton and Clark, 1988). Finches and bats did not prove to be strongly correlated but were still often clustered together. There is some evidence that birds and bats share cerebellar adaptions for flight (Kim et al., 2009), suggesting any similarity in Purkinje cells is due to convergent evolution.

Another interesting finding was that the relevant principal components for the active electrophysiological feature vector, while not sharing a relationship with the branching-correlated morphological PCs, were strongly correlated with the size-correlated morphological PCs (Table 6.2).

Branching features had no correlation with electrophysiological features for active models, but size metrics did. The size metrics of each model have influence
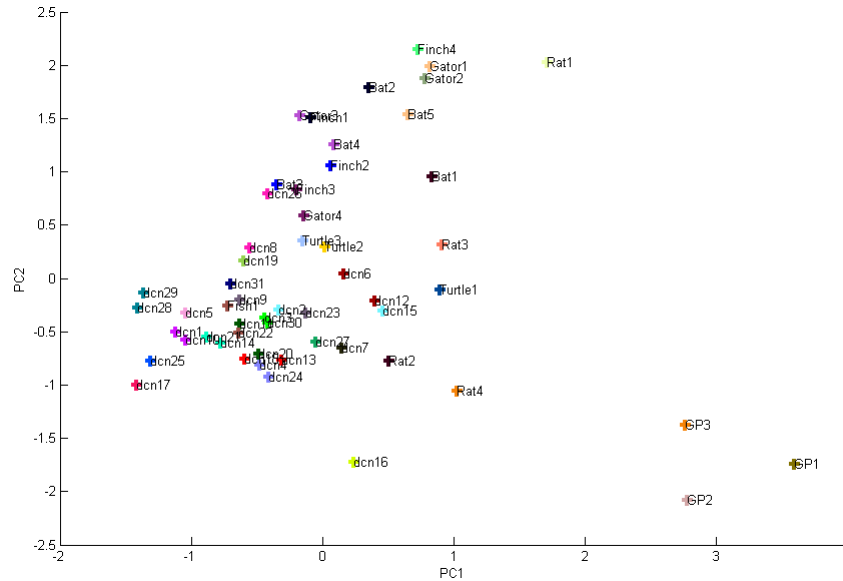
(a) GNG clusters for joint Purkinje cell and DCN neuron image vector
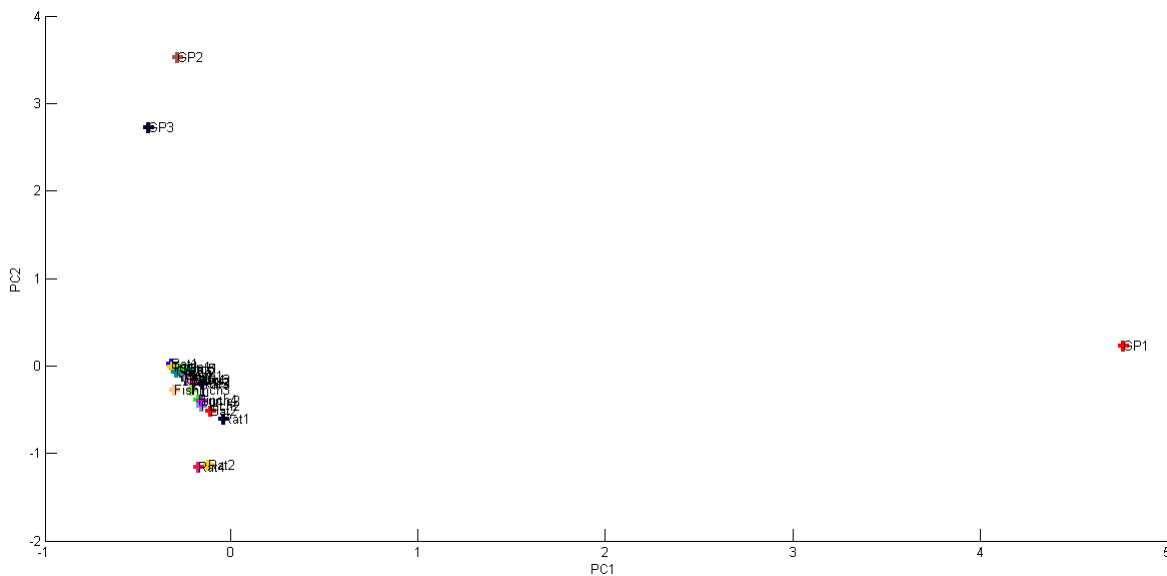
(b) GNG clusters for Purkinje cell only image vector

Figure 6.10: Results of the image-based GNG clustering plotted in PCA space.
Colours indicate the cluster designated by GNG.

on the passive electrophysiological parameters, such as membrane resistance. These parameters do not become less integral to the model with the introduction of active ion channels. Any effect that branching measures have on the behaviour on passive models, however, do appear to be overcome in the active models.

Chapter 7

Information Transfer in the Purkinje Cell

7.1 Introduction

In previous chapters, the cells were compared based on their physical attributes, shape and size, and on their electrophysiology, the tools by which neurons communicate. The final step in this initial exploration of the cells is to attempt to quantify the function of the cells. In this study, this is done by using an information theoretical technique to estimate the information content of spike trains. This gives a final area of comparison, whether information content changes significantly between species groups, to round out this exploration of the cells.

The chapter begins with a background on the history of information theory and basic information theoretical techniques. Background is also given on the use of these techniques in the field of neuroscience. This section also includes a discussion on one of the more difficult aspects of information theory - estimating the probability distribution of the data - by detailing some of the methods attempted in this study before ultimately not being used.

Section 7.3 explains the method of probability distribution estimation that was used, the Kraskov-Stögbauer-Grassberger method, as well as the information theoretic technique the estimation was used for, transfer entropy. The experiments used to create the data for the transfer entropy analysis is also described here. The final two sections report the results of this analysis and discuss what these results may explain about the information transfer through the cell models.

7.2 Background

Information theory is a family of probabilistic measures and the study of the quantification of information. Information theory began as a way to analyse

and optimise communication systems, but has since been used in a wide variety of fields, including neuroscience.

This section is intended to act as background on the basic measures of information theory and it's use in neuroscience. Additionally, a brief overview of the problems of estimating probability distributions for using information theoretical measures is given, as well as some of the methods that were attempted for this study before being discarded.

7.2.1 Shannon Information Theory

Claude Shannon has been an integral force on the fields of computer science and communications. As the first significant work on the limits of noisy communication channels, his paper "A Mathematical Theory of Communication" 1948 was the first to set upper bounds on both the transmission and compression of data.

Information theory was originally devised as a method of quantifying information in order to optimise data compression. While this has obvious applications to signal processing and many aspects of computer science, the concepts first laid out in this paper have since been expanded and generalised as the field of information theory and employed in a vast array of disciplines. Shannon borrowed the concept of entropy from physics to describe the amount of uncertainty in a transmitted message. A message with low uncertainty can be compressed shorter than a message with high uncertainty. For example, '00000000' and '00101110' are the same length when uncompressed, but the low uncertainty, or entropy, of the first message means that it can be compressed much more than the second message without losing any information.

The basis of information theory assumes that all communication channels are inevitably noisy and have an upper bound on their capacity. To send a message through these channels with minimal error, it is therefore important it is compressed so that its transmission does not exceed the channel capacity. Often measured in bits, the entropy of a given message describes the minimum length the message could be compressed to without losing any information. This suggests that messages with a higher entropy contain more information.

Shannon (1948) defined entropy as in Equation 7.1. The base of the logarithm used determines the units for entropy, the use of the natural logarithm here denotes the units as nats.

$$H(X) = -\sum_x \left(p\left(x\right) \ln p\left(x\right) \right) \tag{7.1}$$

Entropy is based on the probability that random variable X takes the value of x given some probability mass function $p(x)$. It could also be thought of as a measure of uncertainty: the less predictable the next value in the data, the higher the entropy becomes. This means that the reverse is also true, a highly predictable or repetitive message would have a very low entropy as it can be compressed much further without the information being lost.

When analysing neural codes, one may look at the entropy of a spike train to understand the rate of information being transmitted, or to look for changes in information transmission when changing aspects of the neuron or its input. However, the analysis of input-output relationships is better served by measuring either the conditional entropy or the mutual information of the input and output messages. These two measures are defined in Equations 7.2 and 7.3 as described in Cover and Thomas (1991).

Conditional entropy places an addition bound on the entropy of a message by assuming it has knowledge of a second message.

$$H\left(X|Y\right) = -\sum_{x,y} p\left(x,y\right) \ln \frac{p\left(x,y\right)}{p\left(y\right)} \tag{7.2}$$

The conditional entropy $H(X|Y)$ of two messages will always be lower than or equal to $H(X)$; there is less uncertainty of X given that Y is known, unless X and Y are completely independent. Mutual information is also a measure of dependence, as it describes the overlap in information between X and Y.

$$MI\left(X;Y\right) = \sum_{x,y} p\left(x,y\right) \ln \frac{p\left(x,y\right)}{p\left(x\right) p\left(y\right)} \tag{7.3}$$

The entropy of X is the upper bound on both conditional entropy and mutual information. In the case of conditional entropy, the upper bound represents the complete independence of the two messages. When measuring mutual information, the upper bound instead means that the two messages are completely dependent as they share the same information exactly.

7.2.2 Information Theoretic Methods Applied to Neuroscience

Information theory has been applied to neuroscience as early as four years after Shannon wrote his paper defining the field when MacKay and McCulloch (1952) attempted to estimate the entropy of spike trains. The aim of their paper was to determine an upper limit of information transmission in neurons. It was suggested that the entropy of a spike train is dependent on its duration, with entropy decreasing as duration increases. Spike train entropy is also dependent on the size of the time bins that spikes are counted in; larger time bins will lower the entropy. This decrease in entropy occurs as the probability of a spike occurring (or being present in a bin) increases.

When using time coding, rather than rate coding, entropy is estimated as in Equation 7.4 (Rieke et al., 1999).

$$\frac{H}{T} \approx \bar{r} \log_2 \left(\frac{e}{\bar{r}\Delta\tau} \right) \tag{7.4}$$

T is the duration of the spike train, $\bar{r}$ the mean firing rate and $\Delta\tau$ the size of the bin. The probability that a spike will occur in the bin is equal to $\bar{r}\Delta\tau$, it is assumed that the bin is suitably small so that this probability is very low. This

equation can also be thought of as finding the information per spike in bits. For rate coding, assuming a larger T than used in Equation 7.4, the entropy for a given spike count (sc) is approximated as:

$$H\left(sc\right) \approx -\sum_n p\left(n\right)\log_2 p\left(n\right) \tag{7.5}$$

In this case $p\left(n\right)$ is the probability of observing n spikes over the time duration T (Rieke et al., 1999). This is also known as the naive estimate as it ignores much of data available in a spike train (Strong et al., 1998). As $\Delta\tau$ becomes smaller, the differences between rate and time coding can become harder to distinguish. For rate coding this means that the maximum possible entropy for a spike count, which is much higher than what would be achieved by a real neuron, can be calculated as in Equation 7.6 (Rieke et al., 1999), where $\bar{n}$ is the mean spike count.

$$H\left(sc\right) \leq \log_2\left(1+\bar{n}\right) + \bar{n}\log_2\left(1+\frac{1}{\bar{n}}\right) \tag{7.6}$$

Calculating entropy is a useful measure of how much information is contained in a message, higher entropy means that there is more uncertainty in the value of symbols in the message, which suggests the message contains a higher amount of information. Entropy gives a good estimate of the information contained in a single message, but neurons are single elements in large systems – their connectivity is one of their most important features.

One way of looking at two related messages is to measure how much of the information contained in a message is new given that a different message has already been seen. As described in the previous section, the conditional entropy of a message x describes how much uncertainty remains in x given that the value of message y is known. If the conditional entropy $H(x|y)$ is the same as $H(x)$ then x and y are independent, whereas a conditional entropy of zero would mean that the message x contains no information that is not already contained in y.

Mutual information has been one of the most widely used information-theoretical tools in neuroscience as it seems to be a natural tool for comparing input and output spike trains. The mutual information of two messages is information common to both messages, it can be defined in many ways using the marginal, joint and conditional entropies of x and y. While it can be calculated as in Section 7.2.1, the most intuitive definition is as follows:

$$MI\left(x;y\right) = H\left(x\right) - H\left(x|y\right) \tag{7.7}$$

This means that while the union of the marginal entropies is equal to the joint entropy, the mutual information is equal to the intersect of these entropies; this relationship is shown in Figure 7.1.

The mechanics of mutual information, entropy and conditional entropy are explored in the previous section. Although there are other uses of information
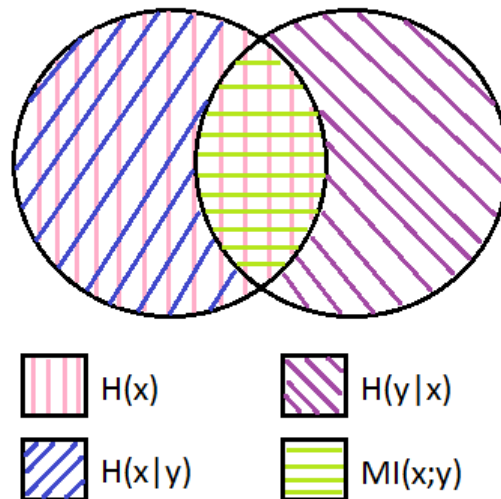
Figure 7.1: The relationship between the marginal and conditional entropies and mutual information of two messages x and y.

theory in neuroscience, many techniques are extensions or modifications of these measures, including transfer entropy.

7.2.3   Probability Distribution Estimation Methods

Information theoretical tools can be used to great effect in neuroscience, but they also come with challenges to overcome. In order to find the entropy of an information source, the probability distribution of how the source generates symbols must be known or estimated. With two different information sources, the mutual information can only be found if the conditional or joint probability distributions are also known or estimated in addition to the singular distributions. To simplify estimations, a simulated input can be randomised based on a known probability distribution; often Poisson or gamma distributions are used to simulate natural spike trains. However, the joint probability of the input and output cannot be derived from the marginal distributions of the input and output unless complete independence is assumed. The following is a summary of probability distribution estimation methods that were investigated for use in this study, but replaced with the Kraskov-Stögbauer-Grassberger (Kraskov et al., 2004) method described in Section 7.3.1.

    The simplest method of estimating a probability distribution first requires that the neuron voltage trace is transformed into a spike train of discrete states by "binning". The trace is split into bins of a fixed width, most often at a resolution that allows only a single spike per bin so that the trace may be represented as a binary string, where a bin containing a 1 corresponds to a
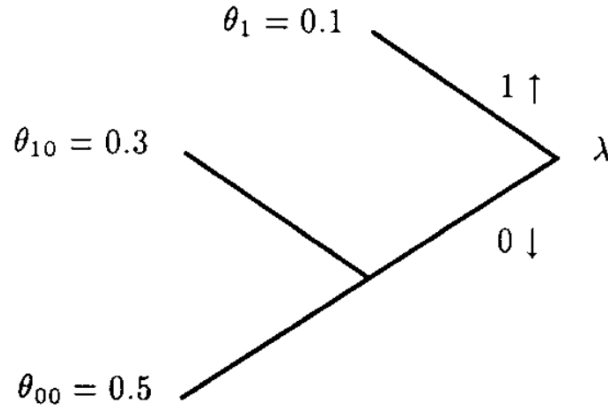
Figure 7.2: Example of a suffix tree from (Willems et al., 1995, fig. 1)

spike at a given time and a 0 is used where there was no spike.

With this discrete spike train the probability of a spike can be estimated as the number of events divided by the number of bins; this is sometimes referred to as a plug-in estimator. The accuracy of this method can be improved by having many output trains of the same length generated by the same input to derive an average number of spikes. Given a large enough sample, this can be an effective method, but its application is limited. The use of binned methods is still highly prevalent, often in conjunction with a bias-correction method like jack-knifing.

When estimating probability distributions a good model will make a minimal amount of assumptions on the nature of both the data and the source. The aim of a weighted context tree (Willems et al., 1995) is to avoid making any assumptions at all by creating a context tree that encompasses any possible source model. Not originally designed for use in neuroscience, it was subsequently used by (London et al., 2002a) to estimate the distribution of binned spike trains to find the synaptic information efficacy (SIE), which is defined as the mutual information between the input to a specific synapse and the output of a neuron.

As described by Willems et al. (1995), the weighted context tree is an extension to the concept of suffix trees. This is a binary tree where edges are labelled either "0" or "1", as in Figure 7.2. The path to any node is denoted a "suffix", and each suffix has a probability. In a suffix tree, the source model is known and all suffixes represented on the tree are known to be generated by the model. A suffix tree model is used to find the conditional probability of a binary information source generating a string (indexed with the most recent symbol at x_0 and earlier symbols with negative numbers) given that a fixed-length suffix string is known.

In a context tree, contexts are possible suffixes and are mapped to the tree in the same way. A context tree is always complete up to the pre-determined depth

parameter D, which represents the length of suffixes. Each context probability is weighted in order to approximate an average over all possible suffix trees.

Probability distributions are estimated by counting the numbers of 1s and separately the number of 0s that follow the context string. Each count and subsequent probability is mapped to a tree so that each node holds the counts given a different context, with the context of the root node being an empty string, and each set of child nodes increasing the context length until D is reached.

At each node, a prior distribution is determined based on the symbol counts. This is a recursive calculation, shown in Equation 7.8, where x is a binary string, a is a binary symbol concatenated to the right side of x, and n is the length of x. $N_x(a)$ is the number of occurrences of binary symbol a in string x (London et al., 2002b).

$$P_e(x \circ a) = \frac{N_x(a) + \frac{1}{2}}{n+1} \cdot P_e(x) \tag{7.8}$$

For leaf nodes, this prior is given as the final estimated probability of a symbol given the context. This prior is better known as the Krichevsky-Trofimov (KT) estimator (Krichevsky and Trofimov, 1981). At any nodes with children the final estimate is derived from the prior of the node, and the final probabilities of its children. This is defined as:

$$P_w \triangleq \frac{1}{2}P_e(x) + \frac{1}{2}P_w^0(x) \cdot P_w^1(x) \tag{7.9}$$

where $P_w^0(x)$ is the final probability of the child node with the extra context symbol "0", $P_w^1(x)$ is the final probability of the child node with the additional context symbol "1", and $P_e(x)$ the prior probability for the given node as calculated from Equation 7.8 (London et al., 2002b). Computationally, these values are worked out in sequence, beginning with the leaf nodes. The probabilities then propagate up the tree such that the value $P_w^\lambda(x)$, the probability at the root node, is the estimated probability for the entire string.

Binning the neural data simplifies it from continuous to discrete time steps. Binning is often thought of as a necessary simplification but any kind of discretisation or compression will lead to information loss. The resolution of time bins can also have a large effect on how much information is estimated to be contained in a segment of neural data. These drawbacks are often thought of as necessary in order to use information theoretical analysis, which is not optimised for continuous data.

A growing family of probability distribution estimators use dimension projection as an alternative, where spike trains are mapped into a feature space for analysis. This approach is particularly useful when handling high-dimensional data. Akin to the use of covariance matrices to find the features of the input most likely to cause spiking in the output, projecting the input and output as vectors in the same space can reveal the boundaries between inputs which do and do not trigger spiking in the output. By projecting the data to some feature space, the data can be represented in a more decompressed manner,

and comparisons can be made using distance-based measures. The Kraskov-Stögbauer-Grassberger method, described in the following section, is one such projection method.

7.3 Methods

Information theory has been applied to neuroscientific data for decades and using many different methods. For this study, only a single measure was applied to the data: transfer entropy. Transfer entropy is a measure of the predictability of a system given that the inputs to and outputs from are known. This chapter describes how this measure was used in three steps. The first sections details the robust method of probability distribution estimation used for the calculation of transfer entropy. This is followed by an explanation of what transfer entropy measures and how it works. The section ends with how the data was generated for analysis with transfer entropy.

7.3.1 The Kraskov-Stögbauer-Grassberger Method

For the probability estimation required for transfer entropy, the Kraskov-Stögbauer-Grassberger (KSG) (Kraskov et al., 2004) method was used. KSG has the benefit of not making assumptions of the model or assuming linearity. It is able to do this by building on box-kernel probability density estimation using a technique based on a method developed by Kozachenko and Leonenko (1987).

The box kernel estimates probability by finding the number of points in a dataset that are within an d-dimensional "box" of set width, r, when projected into an d-dimensional data-space. Data points are given a value of 1 if they are within r, and 0 if not. This is then summed over the number of data points and divided by nr^d; where n is the number of points, r the kernel width, and d the dimensionality of the data. The difference between this technique and the plug-in estimator described in Section 7.2.3 is the position of the box. In the previous plug-in estimator, which similarly counts points in bins, the results is dependent on both the width of bins (generally with spike trains this width is set so that there can never be more than one spike per bin) and the locations of bins in the data-space. While the results of box kernel estimation is still highly dependent on box width, the issue of placement is solved by having boxes centred on each data point.

The main drawback to the box kernel method of estimating probability distributions is the need to set a width value; this is usually remedied by trying a range of widths and assuming the probability distribution with the maximum entropy is the most accurate result. However, the KSG method enhances the box kernel by effectively using a dynamic width value, based on the Kozachenko-Leonenko method (1987) of adapting box kernel estimation for use with entropy estimation through the use of nearest neighbours. This is achieved by having a choosing some k, and then determining the kernel width by the distance of the kth nearest neighbour. Setting a width value can have a huge effect on the

result of standard box-kernel estimation, but KSG results with $k \geq 4$ have been found to be less sensitive to this problem (Kraskov et al., 2004).

For this probability distribution estimation to work with mutual information it needs to be expanded to estimate joint probability distributions. For the KSG method, this was achieved by first finding the k nearest neighbours in the joint data space of X and Y, and then setting a kernel width for each space, r_x and r_y based on the distance to the kth neighbour. KSG proposed two methods for setting the widths, the algorithm used in this study uses the maximum distance of either x or y to the kth neighbour for both widths. The count of data points within r_x and r_y for each element of X and Y takes place in the separate X and Y spaces, and is averaged over the total samples. This can also be expressed as in Equation 7.10 (Kraskov et al., 2004).

$$I(X;Y) = \psi(k) - \langle \psi(n_x + 1) + \psi(n_y + 1) \rangle + \psi(N) \qquad (7.10)$$

Where ψ represents the digamma function, n_x and n_y are the number of points within r_x and r_y respectively, and N is the total number of samples.

Calculating transfer entropy requires three, rather than two, data sources to have their probability distribution functions estimated, as it is a type of conditional mutual information (see Section 7.3.2). In this study, this expansion is implemented as suggested by Gómez-Herrero et al. (2015); widths for the three marginal spaces r_x, r_y and r_z are found using the same method as before in the full X, Y, Z data space. Widths for two joint spaces, r_{xz} and r_{yz} are also set from the maximum distance. Counts then take place in the Z, XZ, and YZ spaces as before in order to find the conditional mutual information using Equation 7.11 (Gómez-Herrero et al., 2015).

$$I(X;Y|Z) = \psi(k) + \langle \psi(n_z + 1) - \psi(n_{xz} + 1) - \psi(n_{yz} + 1) \rangle \qquad (7.11)$$

By using this method, as implemented in JIDT (Lizier, 2014), this study is able to compute continuous transfer entropy without the use of binning or unnecessary model assumptions.

7.3.2 Transfer Entropy

Finding the mutual information between the input to a cell and the resulting output seems like a natural way of applying information theoretical tools to neuroscience, but there are many limitations to this method. A key limitation is the lack of directionality; mutual information is a symmetrical measure, so there is no sense of how much of the shared information has been specifically transferred from input to output.

Transfer entropy is an asymmetric predictive measure. When applied to spike trains, transfer entropy can quantify the reduction in uncertainty in predicting the value of the next time bin in the output, given that the history of the input and output are known. This has been summarised as "what information does the past of I provide about the future of O, that the past of O did not

already provide?" (Wibral et al., 2013). While this does not necessarily imply causation, a higher value of transfer entropy suggests that the combined input and output histories can improve prediction of future states.

$$T_{I \to O} = \sum p\left(o_{n+1}, o_n^{(k)}, i_n^{(l)}\right) \ln \frac{p\left(o_{n+1}|o_n^{(k)}, i_n^{(l)}\right)}{p\left(o_{n+1}|o_n^{(k)}\right)} \tag{7.12}$$

Equation 7.12 describes the transfer entropy from input to output as formalised by Schreiber (2000), which uses the joint and conditional probabilities of the future output (o_{n+1}) and the history of the output ($o_n^{(k)}$) and the input ($i_n^{(l)}$), where n is the current time and k and l are the length of the time windows of the histories, such that $o_n^{(k)} = (o_n, o_{n-1}, \ldots, o_{n-k+1})$ and $i_n^{(l)} = (i_n, i_{n-1}, \ldots, i_{n-l+1})$. Schreiber originally suggested using equal length windows, $k = l$, or setting the output history k to 1. A later study into time delays in transfer entropy by Wibral et al. (2013) broached the subject from the perspective of Wiener's Principle of causality suggested that the output history k should be limited to 1 as this would eliminate the problem of information storage skewing results, and would also allow transfer entropy to represent a causal relationship. Furthermore, they go on to explain that while $k = 1$, the transfer entropy is maximised when the input history l is equal to the delay that occurs between the transmission of information at i and its arrival at o. This means that the true delay can be found by scanning the space of possible delay values until the maximum transfer entropy is found.

An advantage of transfer entropy is the possibility to change the length of the time window of history that is used in calculations. A time delay can also be added to mutual information calculations, but this does not change the symmetry of mutual information. Transfer entropy was intended from conception to avoid making assumptions on the model used and to take into account directionality and delay.

While it is a measure of uncertainty reduction, transfer entropy can also be described as conditional mutual information. As such, the calculation can be written as:

$$T_{I \to O} = MI\left(O^+; I^-|O^-\right), \tag{7.13}$$

where I represents the input, O the output, and $+$ and $-$ the future and past respectively (Wibral et al., 2013).

Transfer entropy was calculated for this study using JIDT (Lizier, 2014), a collection of information theoretic tools for Matlab. Two lists of spikes times were used as input to the transfer entropy algorithm, one from a spine receiving a pre-generated input train, and one from the Purkinje cell soma. The methods of gathering these trains is explained in the next section. The probability distribution of the output spike train was estimated using the KSG method, which is detailed in Section 7.3.1.

JIDT allows the user to define the history lengths and delays on the input and output sources, as well as the time window between each source. Following the recommendations made by Schreiber (2000) the history length of each source was limited to 1 time step. The time window between the history of the input and output sources was shifted backwards over a number of runs in order to find the optimal point of information transfer. The amount of time the window was allowed to run backwards was 50 ms, based on the maximum time to reach peak amplitudes found during earlier experiments using spined models with active channels.

7.3.3 Measuring Information Transfer

For this investigation spiking was imperative, so the active models detailed in Section 5.2.2 were adapted so that the soma compartment was also given active ion channels that would facilitate spiking.

Excepting the active soma, the main change to this set of experimentation from the methods used in Section 5.2.2 was the type of input used. The simulation and output time steps were kept the same as the previous experimentation. Information theory requires large volumes of data to improve the accuracy of the analysis, so each simulation had to last much longer than in previous experiments; in this case there was a ten-fold increase in simulation run time, from two to twenty seconds. The need for increased data also meant that the input could not remain as a single spike.

Five spike trains, each with a twenty second duration, were generated from a gamma distribution with the shape and scale parameters both set to 0.5. These were created from a purposefully written Matlab script, which also performed a slight pruning of spikes to replicate a refractory period of 3 ms after each spike. The final spike trains all had a rate of approximately 10 Hz. Each spike train was presented to a model once, so that the final results could be averaged over multiple runs. These spike trains, referred to as input trains for the rest of the study, were used as the comparison to the output of the cells for the transfer entropy.

In addition to the monitored input trains, each cell was also given background excitatory and inhibitory input. These were randomly generated in GENESIS, but with a fixed seed so the pattern was constant for each simulation. The inhibitory input for all cells was set at 1 Hz, which is commonly used in Purkinje modelling (De Schutter and Bower, 1994b). The frequency of the excitatory input had to be varied due to the wide range of input resistances across the models. In some initial experimentation, setting the excitatory input to a uniform 25 Hz resulted in spiking frequencies of 15-130 Hz. To avoid a large amount of variation in the output of the cell models before the application of the input trains, the background excitatory rates were varied by trial and error until all the cells had a baseline firing rate of 45-55 Hz when not giving the cells any monitored input. For each run the model was presented with three types of input: the monitored, pre-generated excitatory input train, a randomly generated excitatory input with variable frequency, and a randomly generated

inhibitory input with a 1 Hz frequency.

In total, 90 simulations were run for each cell model. The pre-generated input trains were given to the cell in one of four locations and in one of four quantities. The number of input sites was set to either 1, 20, 50 or 100, and these sites were located either proximal, medial or distal to the soma, or were randomly distributed across the tree. This was repeated five times for each of the input trains.

It has been estimated that 50 synchronously firing parallel fibres are required to effect spiking in the Purkinje cell (Barbour, 1993). Smaller input groups were chosen to see if this was effected by location of input sites. Input location was varied to check for a possible morphological effect and also to see whether the randomly distributed group is more effective than localised groups.

Finding transfer entropy requires two sources of data, the past of an input and the past of an output, in order to measure the uncertainty in the future of the output. The algorithm used to calculate the transfer entropy, from the Java Information Dynamics Toolkit (JIDT) (Lizier, 2014), uses the Kraskov-Stögbauer-Grassberger method (Kraskov et al., 2004, see Section 7.3.1 for more on this method) to estimate the probability distributions of the input and output sources. The input and output data were presented as time series data as conductance from a spine receiving input and the voltage at soma respectively. Each was trimmed to remove the first 0.5 seconds of the recordings. The spine stimulated when only one parallel fibre input was simulated was chosen as the recording spine in each experimental condition for consistency.

The length of each input/output pair was analysed for transfer entropy. History of both the input and output was limited to 1 time step (as explained in Section 7.3.2). The delay between input and output windows was tested from 1 to 500 time bins, or 50 ms. This was executed for each input location and number of synchronous inputs, and then repeated for the five different input trains to find an average maximum transfer entropy.

7.4 Results

Transfer entropy measures how well the future values from the output of a system can be predicted given that the history of the output and the input to this system is known. This is computed as conditional mutual information and is intended to represent the information transfer from the input to the output. Transfer entropy was applied to the input to the input of the 24 cell models, conductance at spines receiving input, and the output, the voltage trace from each soma. In this section the results of this analysis is reported as the maximum transfer entropy within a given time window, and the delay between input and output to reach this maximum.

Figure 7.3 shows the maximum transfer entropy in the fish Purkinje model when stimulating different numbers of spines synchronously, and in different positions in the dendritic tree. Each spine group size and position combination was run five times for each model using different randomly generated input spike

trains to give the error bars. The average delay to reach the maximum transfer entropy is plotted in Figure 7.4, which was made in the same way. Regression coefficients for the trend lines are given in Appendix I, as are maximum transfer entropy and corresponding delay values for examples from other species.

A universal observation across all of the cell models was the increase of transfer entropy with the number of spines stimulated synchronously. In many of the cells, this increase can be well fitted linearly with $R^2 > 0.9$, as shown in Figure 7.3. For most species, stimulating groups that were proximal to the soma or randomly distributed across the dendritic produced the largest transfer entropy results. However, as shown in Figure 7.6, the maximum transfer entropy was smallest in the proximal groups for the fish and turtle models in some conditions. For most of the other species, the distal groups produced the smallest maximum transfer entropy, remaining low even in the 100 spine input condition (Appendix I). This is despite the previous experimentation with active models suggesting that distance has very little effect on the amplitude of voltage reaching the soma (see Section 5.3.2).

The delay between input and output history was typically very small, less than 1 ms, when the maximum transfer entropy was in the higher. This can be seen in Figure 7.4, where the stimulation of 50 or more spines in any location produces a small delay with little variability across the different input trains.

Figure 7.5 shows the transfer entropy over delay window for each of the 16 input combinations in the fish cell, averaged over five input trains. Finding transfer entropy requires iteration over the input and output time series for each delay length (here the delay was capped at 50 ms, and used 0.1 ms time steps) starting at each time step in the output series (given that there is a long enough history at that time step, and that it is not the last step in the series) and then averaged over all local values at each step. These averages are shown in this figure, averaged again over the five input trains, spanning the full 50 ms delay window. The higher maximum entropy values seen in the 50 and 100 spine groups peak sooner in the delay window, and have a sharper peak and drop than the values for the smaller spine groups.

To test for a relationship between maximum transfer entropy and the associated delay, the coefficient of correlation was found for each cell, using all input conditions averaged over the five input trains. The results for the example cells are given in Table 7.1. These results suggest some negative linear correlation between the two variables, though only the results of the fish model analysis displays a particularly strong relationship.

The transfer entropy results were also averaged over species groups in order to look for phylogenetic trends. Species average maximum transfer entropy and average associated delay for different input positions when synchronously stimulating groups of 50 spines are plotted in Figure 7.6, with 95% confidence bars. The length of these bars is evidence of high variance within species groups. No obvious increase or decrease of maximum transfer entropy with phylogenetic rank was found, a Kendall's τ analysis also suggests no linear correlation (Table 7.2).
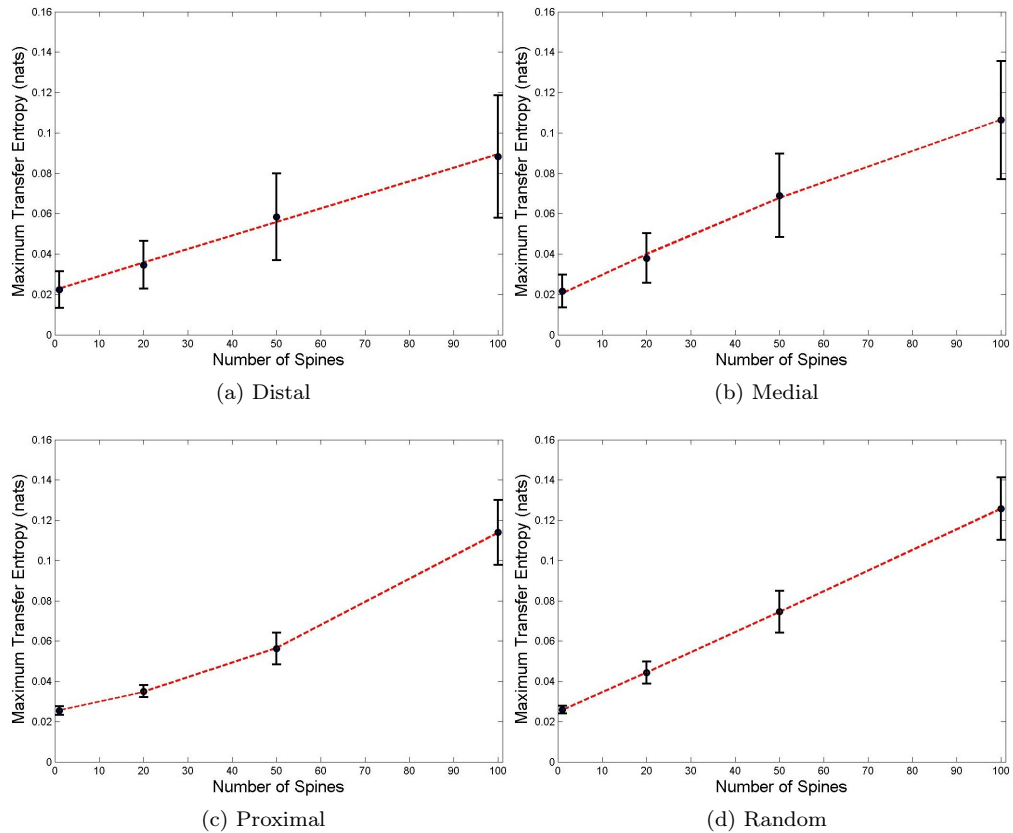
Figure 7.3: Transfer entropy (nats) in the fish Purkinje cell model after stimulating spine groups in different areas of the dendritic tree, averaged over five input trains

Cell Model	R
Fish	-0.774
Alligator 2	-0.576
Turtle 3	-0.618
Finch 4	-0.591
Bat 5	-0.649
Guinea pig 2	-0.618
Rat 1	-0.672

Table 7.1: Correlation coefficient for maximum transfer entropy and corresponding delay

(a) Distal   (b) Medial

(c) Proximal   (d) Random
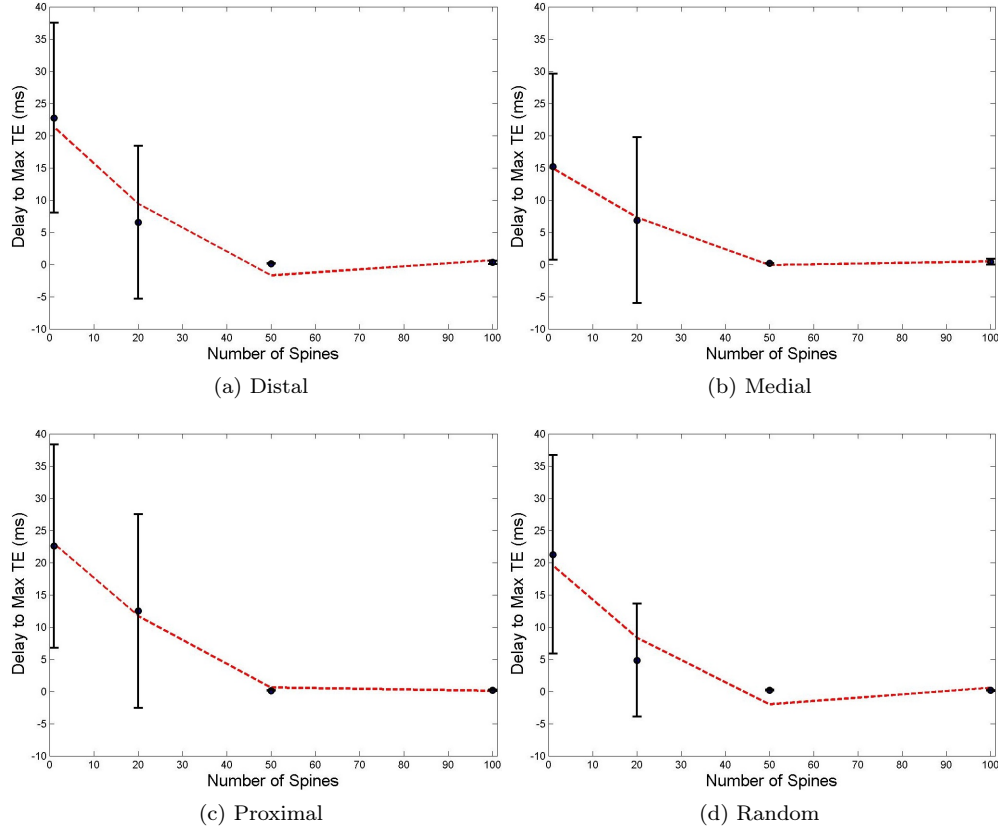
Figure 7.4: Delay (ms) between input and output to find the maximum transfer entropy in the fish Purkinje cell model after stimulating spine groups in different areas of the dendritic tree, averaged over five input trains

Input Position	τ	p
Distal	-0.143	0.773
Medial	-0.143	0.773
Proximal	0.143	0.773
Random	-0.333	0.381

(a) Maximum transfer entropy

Input Position	τ	p
Distal	0.562	0.238
Medial	0.143	0.773
Proximal	0.619	0.069
Random	0.514	0.164

(b) Delay

Table 7.2: Kendall's τ for species average maximum transfer entropy and delay at different input positions when stimulating groups of 50 spines against phylogenetic rank

(a) distal

(b) medial

(c) proximal

(d) random
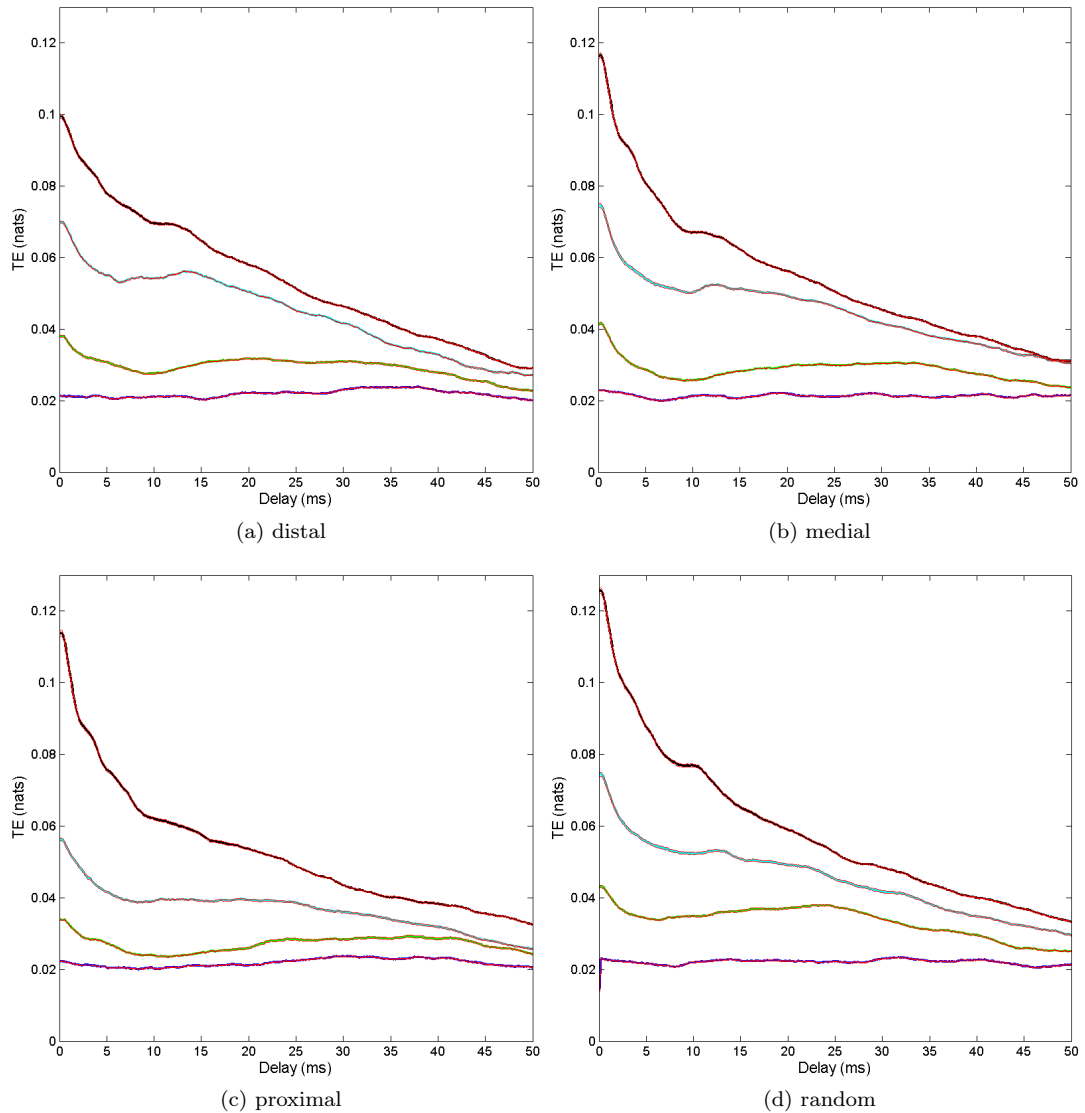
Figure 7.5: Transfer entropy over the 50 *ms* delay window containing maximum transfer entropy in the fish Purkinje cell after stimulating spine groups in different areas of the dendritic tree, averaged over five input trains. Number of spines stimulated indicated by line colour: Blue = 1 spine, green = 20 spines, cyan = 50 spines, black = 100 spines. Red lines are the standard error for each group.
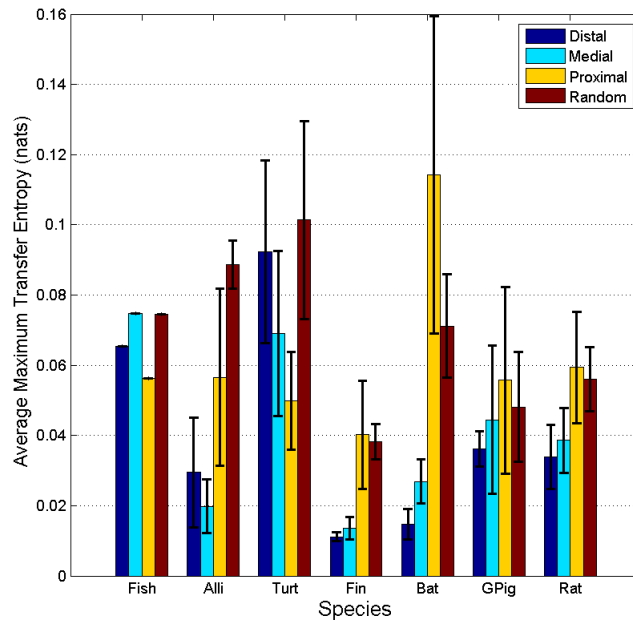
(a) Average maximum transfer entropy
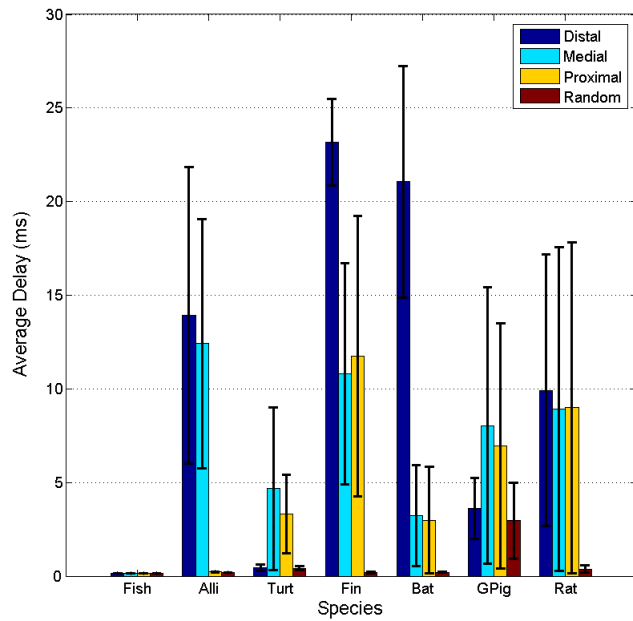
(b) Average delay

Figure 7.6: The average maximum transfer entropy (nats) for each species group when synchronously stimulating groups of 50 spines and the average delay to the maximum transfer entropy (ms) with 95% confidence intervals

7.5 Discussion

The use of information theoretical techniques in the analysis of spike trains spans almost the entire history of information theory. Transfer entropy, despite being a much more recent development, has also seen much use in the field. This is due to two advantages that transfer entropy has over traditional information theoretical measures, Firstly, the inclusion of the history of data sources, as well as an adjustable delay between input and output makes it well suited for time series data. Additionally, as an asymmetrical measure, the results imply a direction, or flow of information that is lacking in mutual information.

As mentioned in Section 2.3.1, it is thought that 50 synchronous parallel fibre inputs are required for the Purkinje cell to spike (Barbour, 1993). Measuring the maximum transfer entropy when inputting the pre-generated spike train at only a single spine allows for an approximate measure of how much of the possible information transfer is just chance interactions with the background activation. With a few exceptions, including the fish cell, maximum transfer entropy for a single input was below 0.02 nats. Based on this, 0.025 nats could be used as a conservative baseline transfer entropy, with values below this threshold considered noise.

Whether the synchronous stimulation of 20 spines was enough to cross this threshold was dependent on the cell model. For some, such as Rat 1 (see Appendix I) 20 synchronous inputs had an effect on transfer entropy only when they were proximal to the soma. In other models, this could also be achieved when spines receiving synchronous input were distributed across the dendritic tree. This could be misleading, however, as only one random distribution was tested for each model. In a larger study, there would be permutations of the random spines chosen to reduce possible bias.

The delay times for the 1 and 20 spine groups displayed more variance and across the results tended to be longer when the maximum transfer entropy failed to reach the noise threshold of 0.025 nats. As Figure 7.5 shows an early peak and definitive drop of transfer entropy in the larger spine groups, and Table 7.1 suggests some correlation for higher transfer entropy values with shorter delay times, a longer delay could also be an indicator of noise. Higher transfer entropy values often had delay times of less than 1 ms, suggesting very quick information transfer in the Purkinje cell, if accurate. This is noticeably quicker than the time to reach peak amplitude at soma in active models following stimulation at spines reported in Section 5.3.2, though it is possible this is partly an artifact of the passive soma.

Section 5.3.2 also reported that there was little variation in the active results based on the distance between compartments receiving inputs and the recording compartment. Sensitivity to distance from soma was found in all of the cell models when measuring transfer entropy. The models used in the two experiments had two differences; whether the soma compartment was modelled passively or actively, and the presence of background excitatory and inhibitory input. One possible explanation for this key difference in results is the introduction of noise through the background inputs, which would potentially effect

distal inputs more than those close to the soma. Further experimentation without background input is recommended to test this hypothesis, as it could mean that input location is not as location-independent as currently believed.

As with the other experimentation within this study, this is intended as an initial exploration of the data and source of questions rather than answers. While there was no correlation between maximum transfer entropy and phylogenetic rank found, a similar approach with a larger dataset could examine whether this is indicative of a conservation of function in the Purkinje cell. The extent to which transfer entropy depends on distance from the soma would also be an area of potential interest. These results do, however, lend some additional evidence to the requirement of a minimum approximately 50 spines receiving synchronous activation to effect the Purkinje soma.

Chapter 8

Conclusion

The cerebellum is a structure that is present in all vertebrates, but grows larger and more morphologically complex through evolution. Its neural circuitry and the neurons themselves also follow the pattern of growth, in size and number, and increased dendritic complexity. Despite this, the strict organisation of cells – particularly the unique arrangement of Purkinje cells – is a constant feature of the cerebellum, from primates back to the simplest cerebella found in fish.

Unfortunately, the majority of research into the cerebellum and Purkinje cells takes place using samples from a small number of vertebrate species, with phylogenetic orders like Rodentia vastly over-represented. The aim of this work was to take the first steps in exploring a greater range of species. Three areas were chosen for this exploration: morphology, electrophysiology, and information theory.

Purkinje cells have been famous for their dendritic morphology since the first sketches by Ramon y Cajal demonstrated their immense complexity. However this is not common to all species, the fish and turtle cells used in this study have far simpler dendritic structures. The Kendall's τ analysis in Chapter 4 lends statistical evidence to the increase of branching with phylogenetic rank, the Kruskal-Wallis results also finding that the number of branching points is statistically dissimilar between species groups. Research into cell numbers in the cerebellum suggests that there is an increase in numbers of both the excitatory granule cells, whose parallel fibres synapse onto Purkinje cells in huge numbers, and the inhibitory interneurons. A possible hypothesis for the increase in branching that cold be investigated further is that it is a necessary adaption for the increase in inputs.

Passive modelling was undertaken on the cells despite knowing that Purkinje cells have a number of active ion channels as it was felt that any morphological effect would be easier to distinguish without the added complication of ion channels amplifying voltage. In passive models, both maximum amplitude and time to reach peak amplitude are highly dependent on distance. Referring back to Section 3.2.1.1, this is not surprising as current is a function of both time and distance. Input resistance has an important effect on the cell, as a higher

input resistance results in a larger change in voltage in response to current changes. This is reflected in both the amplitude of peak voltages recorded, and in the attenuation of voltage in these results. It is possible that the specific morphological changes are able to compensate for any related change in voltage attenuation. For example, the attenuation in the turtle cells would be related to the length of dendrites, while in the alligator cells it would be most connected to the small diameter of its dendrites and resulting high resistance. The correlation between the principal component associated with size metrics and the principal component most associated with peak amplitude at soma in both the passive and active modelling results could lend some support to this hypothesis.

Finding similarities in the results from the active models is much more difficult than those for the passive models due to the often non-linear result. However, much of the active results mirror what was seen in those from the passive modelling. One major difference between the two is the linear correlation with distance is almost completely absent for both voltage amplitude and time. Many in vitro studies of Purkinje cells show that different species generate similar spiking patterns and firing frequencies in response to the same stimulation. It is possible that had the active model experimentation been expanded to include spiking, these results would also have been replicated here.

A downfall to the clustering results is the small number of cells available for the study makes drawing conclusions difficult. Testing for cluster tendency with the Hopkins statistic indicated that there are no strong clusters present in the data. Unfortunately,with such a small dataset it is unclear whether this is due to clusters not existing within the data or their not being enough examples for clustering to occur. Some patterns emerged despite this limitation, suggesting further investigation could be warranted. The three groups emerged of species that were more likely to be clustered together all had some phylogenetic similarity. The fish and turtle cells, which both come from species with flat, rather than foliated cerebella, were often clustered due to their low branching and similar size. The three guinea pig cells and three of the rat cells (one rat cell was a strong outlier in both morphology and electrophysiological results) were also often clustered together in some combination. These two species are the closest phylogenetically of any of the other samples used in this study as they are both rodents. Finally, the alligator, finch, and bat cells were also often clustered, though Pearson's R for the morphological features of these species suggests that only the alligator and finch have any strong correlation. This grouping may be explained by the closeness of alligators and birds phylogenetically, as well as the possibility that the Purkinje cells of birds and bats have converged on the same adaptions for the challenges of flight.

As the background of the specimens that the cells were taken from is unknown, it is not possible to say whether any of these results are related to the cells of these species or outside factors. One such area where this is an issue is cell size. Size based metrics were found to have statistically significant differences between species groups, but this could be effected by many things, with the age of donor animals being a large factor. Any further investigation into these hypotheses should aim to have not only a larger dataset, but a better

record of the origin of specimens to prepare for any potential bias.

Two factors were emphasised through the transfer entropy results. Firstly, for many of the cells, 50-100 synchronous inputs are a minimum for meaningful transferral of information to soma, which is largely consistent with earlier estimations. The results suggest that large synchronous inputs have influence on the output of the cell for a very brief time on a very fast time scale. More surprisingly, based on the active modelling results, was that the distance of inputs highly effected the predicted information transfer. Under the conditions tested here, inputs received at spines that were further from the soma are less likely to transfer information even when large groups are activated.

This study was intended to find questions about the Purkinje cells of different species that would benefit from a larger-scale study. As a cell famed for its dendritic morphology, the study was an exploration of how influential this structure is on behaviour. Firstly, the results of morphological analysis suggest that branching does indeed increase with phylogenetic rank. The actual size of the cell is somewhat determined by species but not by rank. Though the passive modelling results displayed slight correlation with branching, cell size was a factor in both passive and active modelling results. Information transfer was effected by distance from the soma, but the cell models with the some of the highest dendritic lengths - fish and turtle cells - were also the cells with some of the highest transfer entropy from distal inputs. These results put forward the argument that there is a lot more work to do in this area. Further cluster analysis could potentially find patterns that do not exist in a sample as small as the one used here. Morphology is correlated with phylogenetic rank - but to what extent is that true in a wider sample? Active modelling results are fairly homogeneous, but whether that is true in vivo or an artifact of using the same parameters across cells could be explored. Information theoretical analysis did not suggest phylogenetic increase or decrease in information transfer, but would more accurate modelling of the number of inputs each Purkinje cell is estimated to receive in different species affect this result?

Future Work To extend this work the first recommendation would be that many of the analyses attempted here would be greatly improved with a larger sample of cells; the exploratory nature of this work produces a number of hypothesis that could produce interesting results if investigated more fully. The most pressing recommendation is to increase the range of species typically used in studies. This could be used to more fully test if the increase in branching with phylogenetic rank is truly a trend in nature, or just of the samples used here. This would be further improved if the age of donor species is known and kept constant for each cell.

The genesis of the cerebellum is older than many other sections of the brain, and its lack of specialisation allows it to be present in all vertebrates with little change to its structure, or presumably its function. This makes it an interesting target for evolutionary studies when there is biological data to support the work. However, increasing the variety of species tested would be useful across the field

of neuroscience. An understanding of what changes in a cell, as well as what is conserved, is critical for seeing which elements are important to the function of that cell.

To further test models of Purkinje cells, increasing the number of cell models with electrophysiological parameters derived from the same animal as the cell morphology that are not rodent cells would be greatly beneficial. There is evidence that ion channel distribution and spiking behaviour has similarities in vastly distinct species, but further testing in this area could provide insight into the function of Purkinje cells and how much it has changed through evolution.

A larger sample set would also make potential clustering results far more robust and therefore much more interesting. This would be true whether the homogeneity between cell features, as suggested by the low Hopkins statistic of the feature vectors, proves true for a larger sample, but would also be true if natural clusters can be found. This recommendation for larger datasets also extends to the image-based investigation attempted within this study. Although the clustering here proved untenable, its successes in other fields reassures that it could be a useful tool given the right images and pre-processing techniques.

Furthermore, clustering is a strong technique for pattern finding in data and these methods of quantifying cell morphology could be applied to many different groups of cells. This could include populations of cells from the same species at different ages, or populations of healthy cells and those in different stages of neurodegeneration.

Bibliography

Albus, J. S. (1971). A theory of cerebellar function. *Math. Biosci.*, 10(1):25–61.

Altman, J. (1972). Postnatal development of the cerebellar cortex in the rat. ii. phases in the maturation of purkinje cells and of the molecular layer. *Journal of Comparative Neurology*, 145(4):399–463.

Alvarez-Otero, R., Regueira, S. D., and Anadon, R. (1993). New structural aspects of the synaptic contacts on purkinje cells in an elasmobranch cerebellum. *J. Anat.*, 182(Pt 1):13.

Andersen, B. B., Korbo, L., and Pakkenberg, B. (1992). A quantitative study of the human cerebellum with unbiased stereological techniques. *J. Comp. Neurol.*, 326(4):549–560.

Armstrong, D. and Rawson, J. (1979). Activity patterns of cerebellar cortical neurones and climbing fibre afferents in the awake cat. *The Journal of Physiology*, 289(1):425–448.

Barbour, B. (1993). Synaptic currents evoked in purkinje cells by stimulating individual granule cells. *Neuron*, 11(4):759–769.

Bell, C. (2002). Evolution of cerebellum-like structures. *Brain. Behav. Evol.*, 59(5-6):312–326.

Bell, C. C., Han, V., and Sawtell, N. B. (2008). Cerebellum-like structures and their implications for cerebellar function. *Annu. Rev. Neurosci.*, 31:1–24.

Benton, M. J. and Clark, J. M. (1988). Archosaur phylogeny and the relationships of the crocodylia. *The phylogeny and classification of the tetrapods*, 1:295–338.

Bernander, O., Douglas, R. J., Martin, K., and Koch, C. (1991). Synaptic background activity influences spatiotemporal integration in single pyramidal cells. *Proceedings of the National Academy of Sciences*, 88(24):11569–11573.

Bloedel, J. and Llinas, R. (1969). Neuronal interactions in frog cerebellum. *J. Neurophysiol.*, 32(6):871–880.

Bloedel, J. R. (1992). Functional heterogeneity with structural homogeneity: how does the cerebellum operate? *Behav. Brain Sci.*, 15(04):666–678.

Bower, J. (1994). *Movement Control*, chapter Is the cerebellum a motor control device?, pages 112–113. Cambridge Univ Press.

Bower, J. and Beeman, D. (1998). *The book of GENSIS: exploring realistic neural models with the GEneral NEural SImulation System.*, chapter Ion Channels in Bursting Neurons, pages 97–130. Telos, Springer, New York.

Bower, J. M., Beeman, D., and Hucka, M. (2003). *The GENESIS simulation system.* MIT Press.

Bower, J. M. and Woolston, D. C. (1983). Congruence of spatial organization of tactile projections to granule cell and purkinje cell layers of cerebellar hemispheres of the albino rat: vertical organization of cerebellar cortex. *Journal of Neurophysiology*, 49(3):745–766.

Braitenberg, V. and Preissl, H. (1994). *Movement Control*, chapter Why is the output of the cerebellum inhibitory?, pages 113–115. Cambridge Univ Press.

Brand, S., Dahl, A., and Mugnaini, E. (1976). The length of parallel fibers in the cat cerebellar cortex. an experimental light and electron microscopic study. *Experimental Brain Research*, 26(1):39–58.

Cannon, R., Turner, D., Pyapali, G., and Wheal, H. (1998). An on-line archive of reconstructed hippocampal neurons. *Journal of neuroscience methods*, 84(1):49–54.

Carroll, R. (1977). *Patterns of evolution, as illustrated by the fossil record*, chapter Patterns of amphibian evolution: An extended example of the incompleteness of the fossil record, pages 405–438. Developments in Palaeontology and Stratigraphy. Elsevier Science.

Chan, C. and Nicholson, C. (1986). Modulation by applied electric fields of purkinje and stellate cell activity in the isolated turtle cerebellum. *J. Physiol. (Lond.)*, 371(1):89–114.

Clark, D. A., Mitra, P. P., and Wang, S. S.-H. (2001). Scalable architecture in mammalian brains. *Nature*, 411(6834):189–193.

Cole, K. S. (1968). Membranes, ions and impulses: A chapter of classical biophysics.

Cover, T. and Thomas, J. (1991). *Elements of information Theory.* Wiley.

Cuntz, H., Forstner, F., Borst, A., and Häusser, M. (2010). One rule to grow them all: a general theory of neuronal branching and its practical application. *PLoS Comput. Biol.*, 6(8):e1000877.

Dayan, P. and Abbott, L. (2001). *Theoretical neuroscience: Computational and mathematical modelling of neural systems.* MIT Press.

de Ruiter, M. M., De Zeeuw, C. I., and Hansel, C. (2006). Voltage-gated sodium channels in cerebellar purkinje cells of mormyrid fish. *J. Neurophysiol.*, 96(1):378–390.

De Schutter, E. and Bower, J. M. (1994a). An active membrane model of the cerebellar purkinje cell. i. simulation of current clamps in slice. *J. Neurophysiol.*, 71(1):375–400.

De Schutter, E. and Bower, J. M. (1994b). An active membrane model of the cerebellar purkinje cell ii. simulation of synaptic responses. *J. Neurophysiol.*, 71(1):401–419.

De Schutter, E. and Bower, J. M. (1994c). Simulated responses of cerebellar purkinje cells are independent of the dendritic location of granule cell synaptic inputs. *Proceedings of the National Academy of Sciences*, 91(11):4736–4740.

De Schutter, E. and Bower, J. M. (1994d). Simulated responses of cerebellar purkinje cells are independent of the dendritic location of granule cell synaptic inputs. *Proceedings of the National Academy of Sciences*, 91(11):4736–4740.

De Schutter, E. and Steuber, V. (2009). Patterns and pauses in purkinje cell simple spike trains: experiments, modeling and theory. *Neuroscience*, 162(3):816–826.

DeBraga, M. and Rieppel, O. (1997). Reptile phylogeny and the interrelationships of turtles. *Zoological Journal of the Linnean Society*, 120(3):281–354.

Denk, W. and Svoboda, K. (1997). Photon upmanship: why multiphoton imaging is more than a gimmick. *Neuron*, 18(3):351–357.

Eccles, J. C., Llinas, R., and Sasaki, K. (1966b). The excitatory synaptic action of climbing fibres on the purkinje cells of the cerebellum. *The Journal of Physiology*, 182(2):268–296.

Farrell, A. (2011). *Encyclopedia of Fish Physiology: From Genome to Environment.* Elsevier Science.

Finger, T. E. (1978). Cerebellar afferents in teleost catfish (lctaluridae). *Journal of Comparative Neurology*, 181(1):173–181.

Fox, C. A. and Barnard, J. W. (1957). A quantitative study of the purkinje cell dendritic branchlets and their relationship to afferent fibres. *J. Anat.*, 91(Pt 3):299.

Fricke, M. (2012). Hopkins statistic (matlab). last accessed: 21/12/2015.

Fritzke, B. (1995). *Advances in Neural Information Processing Systems 7*, chapter A growing neural gas network learns topologies, pages 625–632. MIT Press.

Fritzke, B. and Loos, H. (2012). Demogng. last accessed: 26/11/2015.

Gess, R. W., Coates, M. I., and Rubidge, B. S. (2006). A lamprey from the devonian period of south africa. *Nature*, 443(7114):981–984.

Gleeson, P., Steuber, V., and Silver, R. A. (2007). neuroconstruct: a tool for modeling networks of neurons in 3d space. *Neuron*, 54(2):219–235.

Gómez-Herrero, G., Wu, W., Rutanen, K., Soriano, M. C., Pipa, G., and Vicente, R. (2015). Assessing coupling dynamics from an ensemble of time series. *Entropy*, 17(4):1958–1970.

Greenwood, P. H., Rosen, D. E., Weitzman, S. H., Myers, G. S., et al. (1966). Phyletic studies of teleostean fishes, with a provisional classification of living forms. bulletin of the amnh; v. 131, article 4.

Han, V. Z., Zhang, Y., Bell, C. C., and Hansel, C. (2007). Synaptic plasticity and calcium signaling in purkinje cells of the central cerebellar lobes of mormyrid fish. *J. Neurosci.*, 27(49):13499–13512.

Harris, K. M. and Stevens, J. (1988). Dendritic spines of rat cerebellar purkinje cells: serial electron microscopy with reference to their biophysical characteristics. *J. Neurosci.*, 8(12):4455–4469.

Harvey, R. and Napper, R. (1988). Quantitative study of granule and purkinje cells in the cerebellar cortex of the rat. *J. Comp. Neurol.*, 274(2):151–157.

Harvey, R. and Napper, R. (1991). Quantitativ studies on the mammalian cerebellum. *Prog. Neurobiol.*, 36(6):437–463.

Hashimoto, M. and Hibi, M. (2012). Development and evolution of cerebellar neural circuits. *Development, growth & differentiation*, 54(3):373–389.

Heck, D. and Sultan, F. (2002). Cerebellar structure and function: making sense of parallel fibers. *Human movement science*, 21(3):99–109.

Hillman, D. (1969). Morphological organization of frog cerebellar cortex: a light and electron microscopic study. *J. Neurophysiol.*, 32(6):818–846.

Hodgkin, A. L. and Huxley, A. F. (1939). Action potentials recorded from inside a nerve fibre. *Nature*, 144(3651):710–711.

Hodgkin, A. L. and Huxley, A. F. (1952). A quantitative description of membrane current and its application to conduction and excitation in nerve. *J. Physiol. (Lond.)*, 117(4):500.

Hodgkin, A. L., Huxley, A. F., and Katz, B. (1952). Measurement of current-voltage relations in the membrane of the giant axon of loligo. *J. Physiol. (Lond.)*, 116(4):424–448.

Hodgkin, A. L. and Katz, B. (1949). The effect of sodium ions on the electrical activity of the giant axon of the squid. *J. Physiol. (Lond.)*, 108(1):37.

Horton, R. E. (1945). Erosional development of streams and their drainage basins; hydrophysical approach to quantitative morphology. *Geological society of America bulletin*, 56(3):275–370.

Hounsgaard, J. and Midtgaard, J. (1988). Intrinsic determinants of firing pattern in purkinje cells of the turtle cerebellum in vitro. *J. Physiol. (Lond.)*, 402:731.

Hounsgaard, J. and Midtgaard, J. (1989). Synaptic control of excitability in turtle cerebellar purkinje cells. *J. Physiol. (Lond.)*, 409:157.

Ito, M. (2006). Cerebellar circuitry as a neuronal machine. *Prog. Neurobiol.*, 78(3):272–303.

Iwaniuk, A. N., Hurd, P. L., and Wylie, D. R. (2006a). Comparative morphology of the avian cerebellum: I. degree of foliation. *Brain. Behav. Evol.*, 68(1):45–62.

Jacobs, B., Johnson, N. L., Wahl, D., Schall, M., Maseko, B. C., Lewandowski, A., Raghanti, M. A., Wicinski, B., Butti, C., Hopkins, W. D., et al. (2014). Comparative neuronal morphology of the cerebellar cortex in afrotherians, carnivores, cetartiodactyls, and primates. *Frontiers in neuroanatomy*, 8:24.

Jacquemin, S. J., Cicimurri, D. J., Ebersole, J. A., Jones, M., Whetstone, Z., and Ciampaglio, C. N. (2016). Quantifying heterodonty in the late devonian (upper famennian) sharks cladoselache and ctenacanthus from the ohio shale, usa. *PalArch's Journal of Archaeology of Egypt/Egyptology*, 13(1).

Jerison, H. (1973). *Evolution of the Brain and Intelligence*. Academic Press.

Joyce, W. G. (2007). Phylogenetic relationships of mesozoic turtles. *Bulletin of the Peabody Museum of Natural History*, 48(1):3–102.

Kendall, M. G. (1938). A new measure of rank correlation. *Biometrika*, 30(1/2):81–93.

Kendall, M. G. (1945). The treatment of ties in ranking problems. *Biometrika*, pages 239–251.

Kim, J.-Y., Marzban, H., Chung, S.-H., Watanabe, M., Eisenman, L. M., and Hawkes, R. (2009). Purkinje cell compartmentation of the cerebellum of microchiropteran bats. *J. Comp. Neurol.*, 517(2):193–209.

Koch, C. (2004). *Biophysics of computation: information processing in single neurons.* Oxford university press.

Kozachenko, L. and Leonenko, N. N. (1987). Sample estimate of the entropy of a random vector. *Problemy Peredachi Informatsii*, 23(2):9–16.

Kraskov, A., Stögbauer, H., and Grassberger, P. (2004). Estimating mutual information. *Phys. Rev. E*, 69(6):066138.

Krichevsky, R. and Trofimov, V. (1981). The performance of universal encoding. *IEEE Transactions on Information Theory*, 27(2):199–207.

Kriwet, J., Kiessling, W., and Klug, S. (2009). Diversification trajectories and evolutionary life-history traits in early sharks and batoids. *Proceedings of the Royal Society of London B: Biological Sciences*, 276(1658):945–951.

Kruskal, W. H. and Wallis, W. A. (1952). Use of ranks in one-criterion variance analysis. *Journal of the American statistical Association*, 47(260):583–621.

Larsell, O. (1932). The cerebellum of reptiles: chelonians and alligator. *J. Comp. Neurol.*, 56(2):299–345.

Lizier, J. T. (2014). Jidt: An information-theoretic toolkit for studying the dynamics of complex systems. *arXiv preprint arXiv:1408.3270.*

Llinás, R. (1971a). Frog cerebellum: bilogical basis for a computer model. *Math. Biosci.*, 11(1-2):137–151.

Llinás, R., Bloedel, J., and Roberts, W. (1969). Antidromic invasion of purkinje cells in frog cerebellum. *J. Neurophysiol.*, 32(6):881–891.

Llinás, R. and Hess, R. (1976). Tetrodotoxin-resistant dendritic spikes in avian purkinje cells. *Proceedings of the National Academy of Sciences*, 73(7):2520–2523.

Llinás, R. and Nicholson, C. (1971). Electrophysiological properties of dendrites and somata in alligator purkinje cells. *J. Neurophysiol.*, 34(4):532–551.

Llinás, R., Nicholson, C., Freeman, J. A., and Hillman, D. E. (1968). Dendritic spikes and their inhibition in alligator purkinje cells. *Science*, 160(3832):1132–1135.

Llinás, R. and Sugimori, M. (1980a). Electrophysiological properties of in vitro purkinje cell somata in mammalian cerebellar slices. *J. Physiol. (Lond.)*, 305:171–195.

Llinás, R. and Sugimori, M. (1980b). Electrophysiological properties of in vitro purkinje cell dendrites in mammalian cerebellar slices. *J. Physiol. (Lond.)*, 305:197–213.

Llinás, R. and Sugimori, M. (1992). *The Cerebellum Revisited*, chapter The electrophysiology of the cerebellar Purkinje cell revisited, pages 167–181. Springer-Verlag.

Llinás, R., Walton, K., and Lang, E. (2004). *The Synaptic Organisation of the Brain*, chapter Cerebellum, pages 271–309. OUP USA.

London, M., Schreibman, A., Häusser, M., Larkum, M. E., and Segev, I. (2002a). The information efficacy of a synapse. *Nat. Neurosci.*, 5(4):332–340.

London, M., Shcreibman, A., and Segev, I. (2002b). Estimating information theoretic quantities of spike-trains using the context tree weighting algorithm. *Nature neuroscience*, 5.

Lyell, C. (1871). *The Student's Elements of Geology*. J. Murray.

MacKay, D. M. and McCulloch, W. S. (1952). The limiting information capacity of a neuronal link. *Bull. Math. Biophys.*, 14(2):127–135.

Marjanović, D. and Laurin, M. (2007). Fossils, molecules, divergence times, and the origin of lissamphibians. *Systematic Biology*, 56(3):369–388.

Marmont, G. (1949). Studies on the axon membrane. i. a new method. *Journal of Cellular and Comparative Physiology*, 34(3):351–382.

Marr, D. (1969). A theory of cerebellar cortex. *J. Physiol. (Lond.)*, 202(2):437–470.

Martinez, T. and Schulten, K. (1991). *Artificial neural networks*, chapter A "neural gas" network learns topologies, pages 397–402. Elsevier Science Publishers.

Maseko, B. C., Jacobs, B., Spocter, M. A., Sherwood, C. C., Hof, P. R., and Manger, P. R. (2012). Qualitative and quantitative aspects of the microanatomy of the african elephant cerebellar cortex. *Brain. Behav. Evol.*, 81(1):40–55.

Mel, B. W. (1993). Synaptic integration in an excitable dendritic tree. *Journal of neurophysiology*, 70(3):1086–1101.

Messer, M., Weiss, A. S., Shaw, D. C., and Westerman, M. (1998). Evolution of the monotremes: phylogenetic relationship to marsupials and eutherians, and estimation of divergence dates based on α-lactalbumin amino acid sequences. *Journal of Mammalian Evolution*, 5(1):95–105.

Midtgaard, J. (1992). Stellate cell inhibition of purkinje cells in the turtle cerebellum in vitro. *J. Physiol. (Lond.)*, 457(1):355–367.

Miyamura, Y. and Nakayasu, H. (2001). Zonal distribution of purkinje cells in the zebrafish cerebellum: analysis by means of a specific monoclonal antibody. *Cell Tissue Res.*, 305(3):299–305.

Miyasho, T., Takagi, H., Suzuki, H., Watanabe, S., Inoue, M., Kudo, Y., and Miyakawa, H. (2001). Low-threshold potassium channels and a low-threshold calcium channel regulate ca 2+ spike firing in the dendrites of cerebellar purkinje neurons: a modeling study. *Brain Res.*, 891(1):106–115.

Mugnaini, E. (1983). The length of cerebellar parallel fibers in chicken and rhesus monkey. *Journal of Comparative Neurology*, 220(1):7–15.

Napper, R. and Harvey, R. (1988). Quantitative study of the purkinje cell dendritic spines in the rat cerebellum. *J. Comp. Neurol.*, 274(2):158–167.

Near, T. J., Eytan, R. I., Dornburg, A., Kuhn, K. L., Moore, J. A., Davis, M. P., Wainwright, P. C., Friedman, M., and Smith, W. L. (2012). Resolution of ray-finned fish phylogeny and timing of diversification. *Proceedings of the National Academy of Sciences*, 109(34):13698–13703.

Nelson, M. and Rinzel, J. (1998). *The book of GENSIS: exploring realistic neural models with the GEneral NEural SImulation System.*, chapter The Hodgkin-Huxley Model, pages 29–50. Telos, Springer, New York.

Nernst, W. (1888). Zur kinetik der in lösung befindlichen körper. *Z. phys. Chem*, 2(9):613–679.

Palay, S. L. and Chan-Palay, V. (2012). *Cerebellar cortex: cytology and organization*. Springer Science & Business Media.

Palkovits, M., Magyar, P., and Szentágothai, J. (1971). Quantitative histological analysis of the cerebellar cortex in the cat: Ii. cell numbers and densities in the granular layer. *Brain Res.*, 32(1):15–30.

Paul, D. and Roberts, B. (1977). Studies on a primitive cerebellar cortex: I. the anatomy of the lateral-line lobes of the dogfish, scyliorhinus canicula. *Proceedings of the Royal Society of London B: Biological Sciences*, 195(1121):453–466.

Paulin, M. G. (1993). The role of the cerebellum in motor control and perception. *Brain. Behav. Evol.*, 41(1):39–50.

Pichitpornchai, C., Rawson, J., and Rees, S. (1994). Morphology of parallel fibres in the cerebellar cortex of the rat: an experimental light and electron microscopic study with biocytin. *Journal of Comparative Neurology*, 342(2):206–220.

Purves, D., Augustine, G., Fitzpatrick, D., Hall, W., LaMantia, A.-S., and White, L., editors (2012). *Neuroscience*. Sinauer Associates, Inc., 5th edition.

Rall, I. and Agmon-Snir, H. (1998). *Methods in neuronal modeling: from ions to networks*, chapter Cable Theory for Dendritic Neurons, pages 27–92. MIT Press.

Rall, W. (1959). Branching dendritic trees and motoneuron membrane resistivity. *Exp. Neurol.*, 1(5):491–527.

Rall, W. (1964). Theoretical significance of dendritic trees for neural input-output relations. *Neural theory and modeling.*

Rall, W. (1967). Distinguishing theoretical synaptic potentials computed for different soma-dendritic distributions of synaptic input. *J. Neurophysiol.*, 30(5):1138–1168.

Rall, W. (1969a). Time constants and electrotonic length of membrane cylinders and neurons. *Biophys. J.*, 9(12):1483–1508.

Rall, W. (1969b). Distributions of potential in cylindrical coordinates and time constants for a membrane cylinder. *Biophys. J.*, 9(12):1509–1541.

Rámon y Cajal, S. (1911). Histologie du systeme nerveux de l'homme et des vertébrés. *Madrid: Consejo Superior de Investigaciones Cientificas.*

Rapp, M., Segev, I., and Yarom, Y. (1994). Physiology, morphology and detailed passive models of guinea-pig cerebellar purkinje cells. *J. Physiol. (Lond.)*, 474(1):101.

Rapp, M., Yarom, Y., and Segev, I. (1992). The impact of parallel fiber background activity on the cable properties of cerebellar purkinje cells. *Neural Comput.*, 4(4):518–533.

Rieke, F., Warland, D., de Ruyter van Steveninck, R., and Bialek, W. (1999). *Spikes: Exploring the Neural Code.* MIT Press.

Rinzel, J. and Rall, W. (1974). Transient response in a dendritic neuron model for current injected at one branch. *Biophysical Journal*, 14(10):759–790.

Roth, A. and Häusser, M. (2001). Compartmental models of rat cerebellar purkinje cells based on simultaneous somatic and dendritic patch-clamp recordings. *J. Physiol. (Lond.)*, 535(2):445–472.

Roth, A. and van Rossum, M. (2009). *Computational modeling methods for neuroscientists*, chapter Modeling Synapses, pages 139–160.

Rowe, T. (1988). Definition, diagnosis, and origin of mammalia. *Journal of Vertebrate Paleontology*, 8(3):241–264.

Schreiber, T. (2000). Measuring information transfer. *Phys. Rev. Lett.*, 85(2):461.

Segev, I. (1998). *The book of GENSIS: exploring realistic neural models with the GEneral NEural SImulation System.*, chapter Cable and compartmental models of dendritic trees, pages 51–78. Telos, Springer, New York.

Segev, I. and Burke, R. (1998). *Methods in neuronal modeling: from ions to networks*, chapter Compartmental Models of Complex Neurons, pages 93–136. MIT Press.

Shannon, C. (1948). A mathematical theory of communication. *Bell Technical Journal*, 27:379–423, 623–656.

Shelton, D. (1985). Membrane resistivity estimated for the purkinje neuron by means of a passive computer model. *Neuroscience*, 14(1):111–131.

Shlens, J. (2014). A tutorial on principal component analysis. *arXiv preprint arXiv:1404.1100*.

Spain, W., Schwindt, P., and Crill, W. (1987). Anomalous rectification in neurons from cat sensorimotor cortex in vitro. *J. Neurophysiol.*, 57(5):1555–1576.

Sterratt, D., Graham, B., Gillies, A., and Willshaw, D. (2011). *Principles of computational modelling in neuroscience.* Cambridge Univ Press.

Strahler, A. N. (1952). Hypsometric (area-altitude) analysis of erosional topography. *Geological Society of America Bulletin*, 63(11):1117–1142.

Strong, S. P., Koberle, R., van Steveninck, R. R. d. R., and Bialek, W. (1998). Entropy and information in neural spike trains. *Physical review letters*, 80(1):197.

Sultan, F. (1999). A model of temporal and activity-dependent mechanisms underlying the phylogenetic development of cerebellar molecular interneuron morphology. *Neurocomputing*, 26:285–291.

Sultan, F. (2005). Why some bird brains are larger than others. *Curr. Biol.*, 15(17):R649–R650.

Sultan, F. and Bower, J. M. (1998). Quantitative golgi study of the rat cerebellar molecular layer interneurons using principal component analysis. *J. Comp. Neurol.*, 393(3):353–373.

Sultan, F. and Braitenberg, V. (1993). Shapes and sizes of different mammalian cerebella. s study in quantitative comparative neuroanatomy. *J. Hirnforsch.*, 34:79–79.

Sultan, F., Czubayko, U., and Thier, P. (2003). Morphological classification of the rat lateral cerebellar nuclear neurons by principal component analysis. *J. Comp. Neurol.*, 455(2):139–155.

The MathWorks, I. (2013). Matlab release 2013a.

Vitt, L. and Caldwell, J. (2013). *Herpetology: An Introductory Biology of Amphibians and Reptiles.* Elsevier Science.

Vladimirescu, A. and Pederson, D. (1981). A computer program for the simulation of large scale integrated circuits. In *IEEE Proc Int. Symp. on Circuits and Systems*.

Voogd, J. and Glickstein, M. (1998). The anatomy of the cerebellum. *Trends in cognitive sciences*, 2(9):307–313.

Wibral, M., Pampu, N., Priesemann, V., Siebenhühner, F., Seiwert, H., Lindner, M., Lizier, J. T., and Vicente, R. (2013). Measuring information-transfer delays. *PloS one*, 8(2):e55809.

Willems, F. M., Shtarkov, Y. M., and Tjalkens, T. J. (1995). The context-tree weighting method: basic properties. *IEEE Transactions on Information Theory*, 41(3):653–664.

Yamada, W., Koch, C., and Adams, P. (1989). *Methods in neuronal modelling: From synapses to networks*, chapter Multiple channels and calcium dynamics, pages 97–133. MIT Press.

Yopak, K. E., Lisney, T. J., Collin, S. P., and Montgomery, J. C. (2007). Variation in brain organization and cerebellar foliation in chondrichthyans: sharks and holocephalans. *Brain. Behav. Evol.*, 69(4):280–300.

Zhang, J., Leiderman, K., Pfeiffer, J. R., Wilson, B. S., Oliver, J. M., and Steinberg, S. L. (2006). Characterizing the topography of membrane receptors and signaling molecules from spatial patterns obtained using nanometer-scale electron-dense probes and electron microscopy. *Micron*, 37(1):14–34.

Appendix A

Images of Purkinje Cells

Each of the cells used in modelling experiments. Each is labelled with a number for identification in tables (such as Table D.1 in Appendix D). Scale bar is 50 μm. Visualised using neuroConstruct (Gleeson et al., 2007). Guinea pig cells (Figure A.6) originally used in (Rapp et al., 1994).
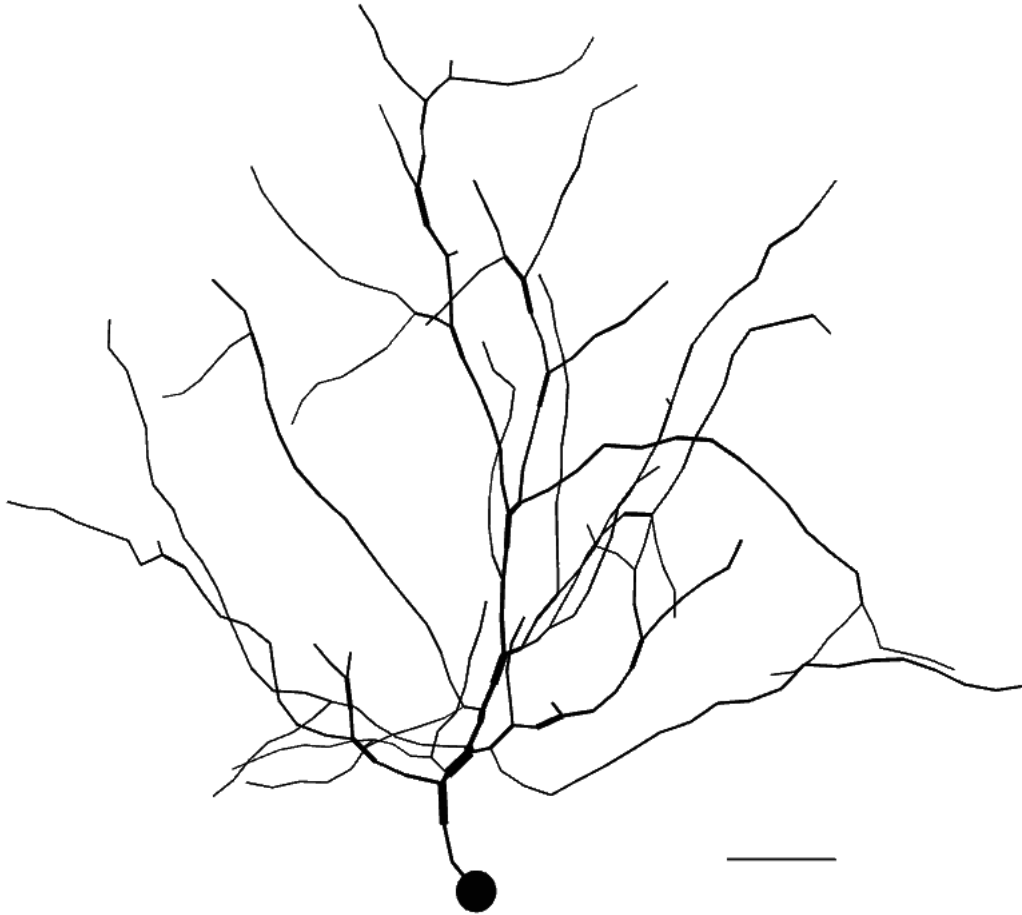
Figure A.1: Fish Purkinje cell

(a) Alligator 1

(b) Alligator 2

(c) Alligator 3
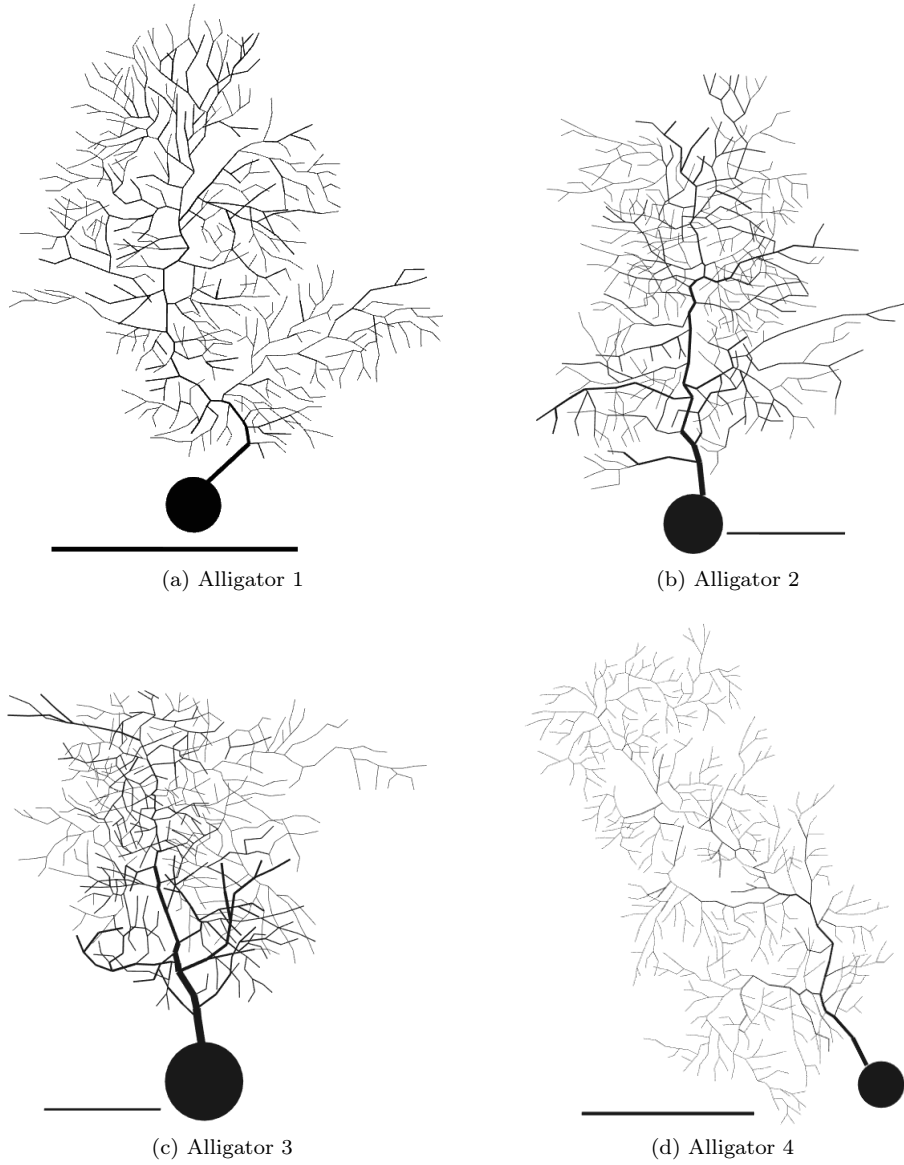
(d) Alligator 4

Figure A.2: Alligator Purkinje cells
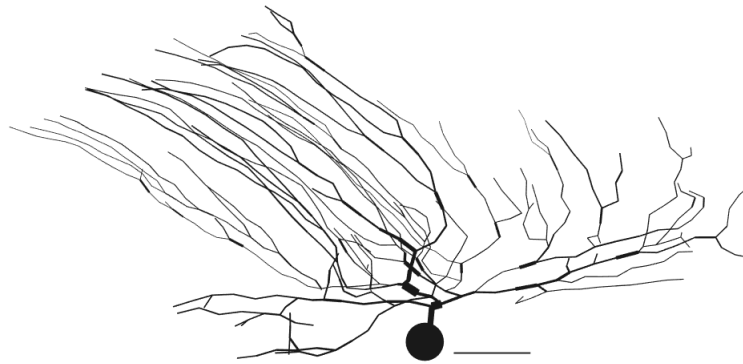
(a) Turtle 1
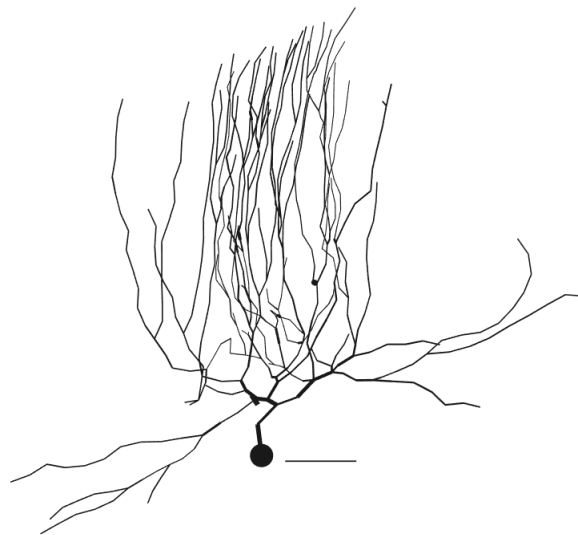
(b) Turtle 2
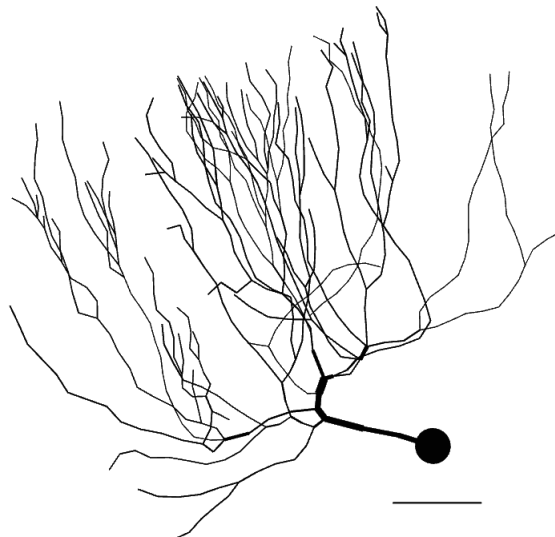
(c) Turtle 3

Figure A.3: Turtle Purkinje Cells

(a) Finch 1

(b) Finch 2

(c) Finch 3

(d) Finch 4
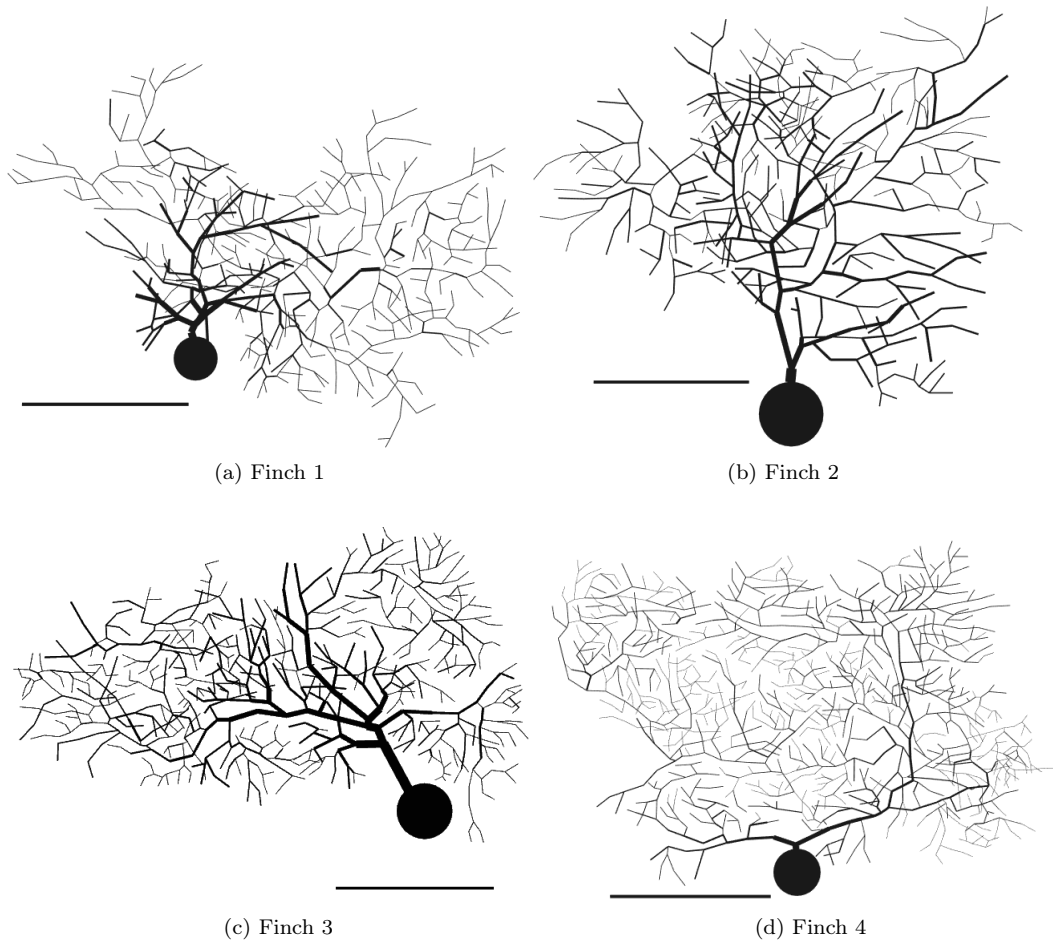
Figure A.4: Finch Purkinje Cells

(a) Bat 1

(b) Bat 2

(c) Bat 3

(d) Bat 4

(e) Bat 5
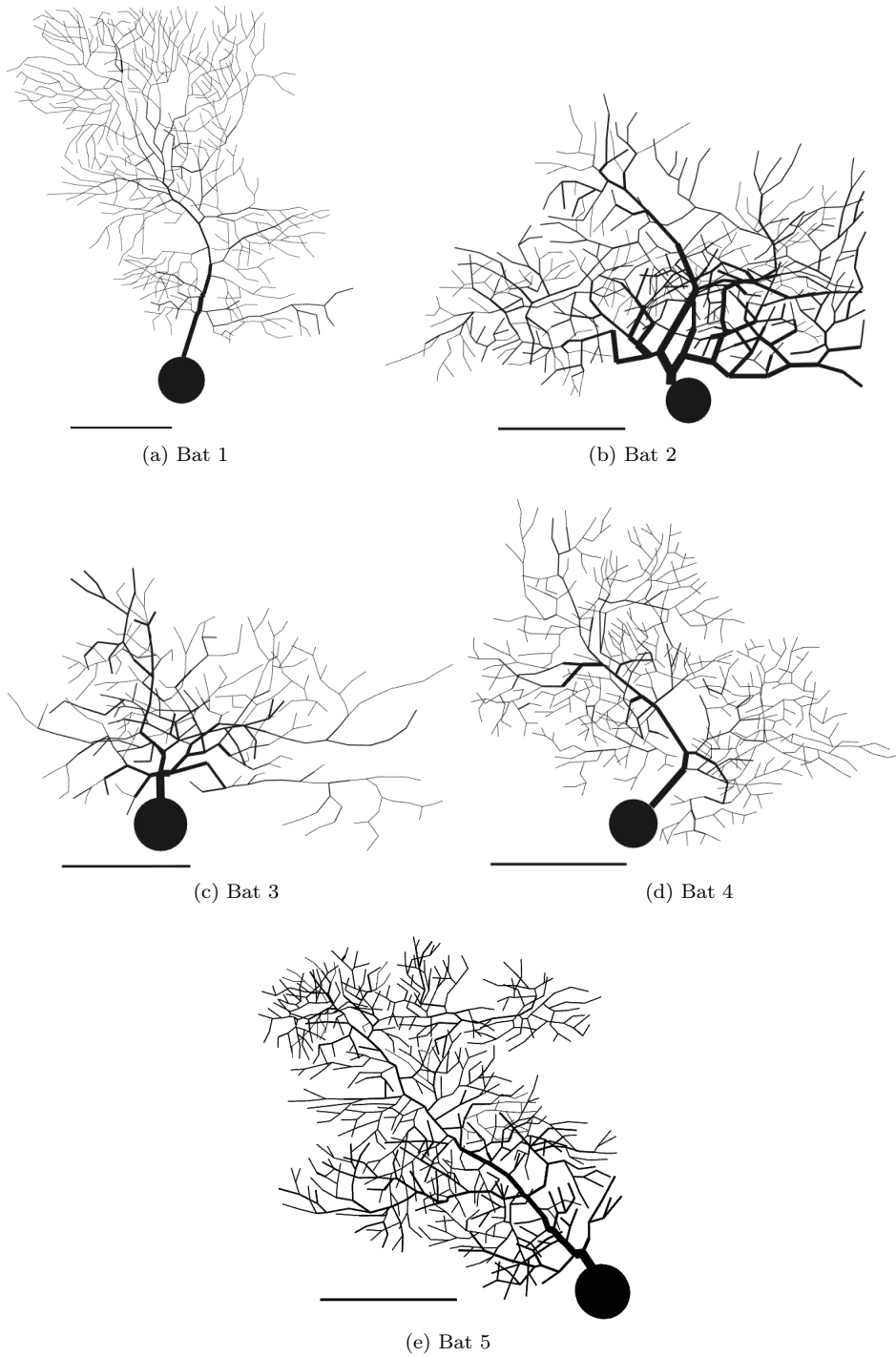
Figure A.5: Bat Purkinje Cells

(a) Guinea pig 1
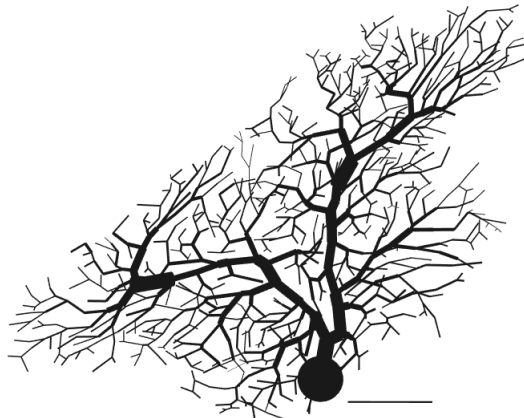
(b) Guinea pig 2
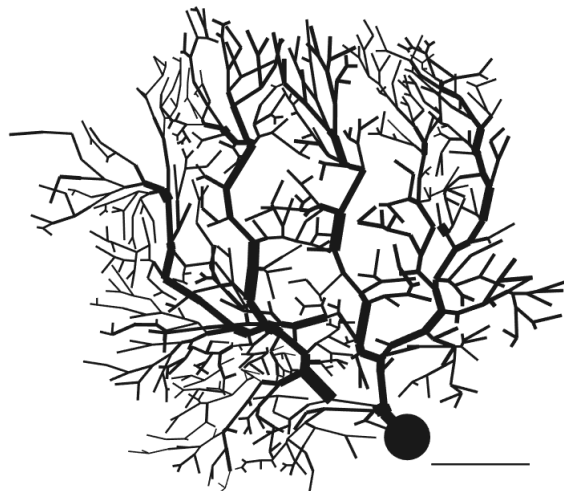
(c) Guinea pig 3

Figure A.6: Guinea pig Purkinje Cells

(a) Rat 1

(b) Rat 2

(c) Rat 3

(d) Rat 4
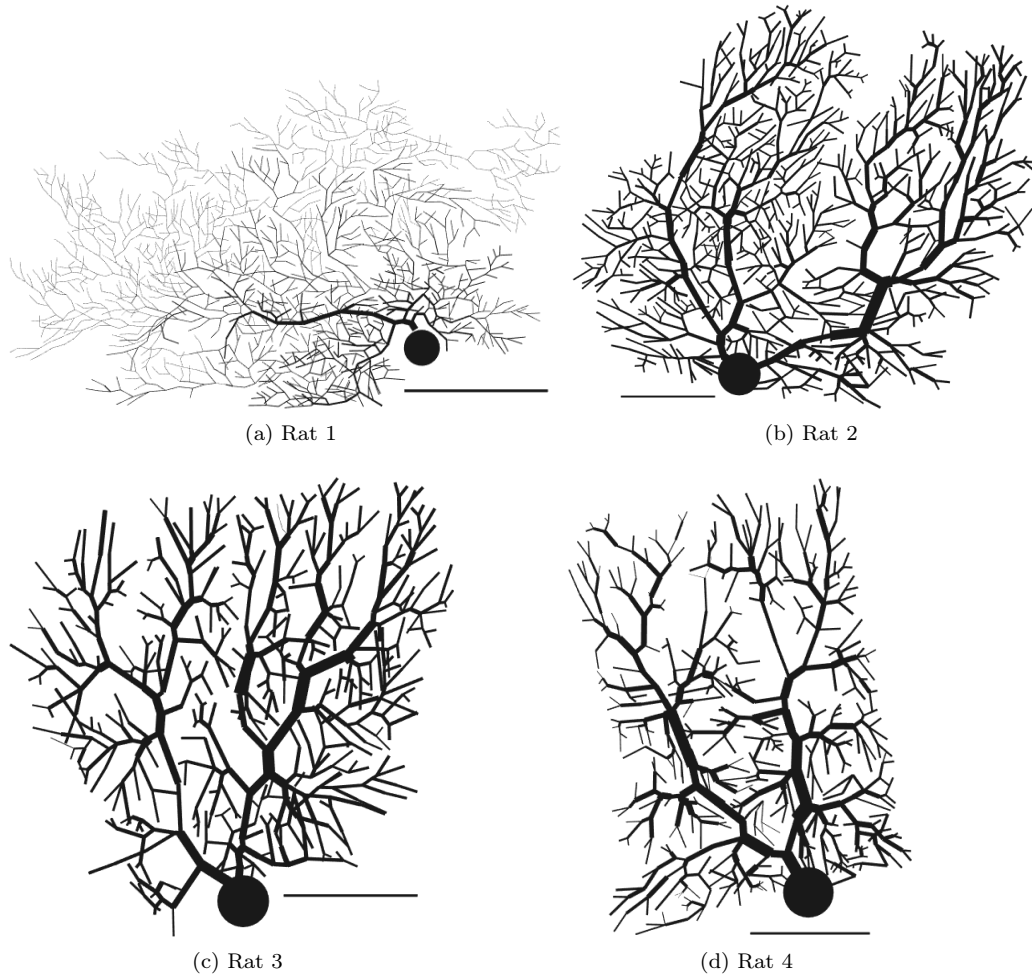
Figure A.7: Rat Purkinje Cells

Appendix B

Full Feature Vectors

The following tables give the full feature vectors containing values from the 24 cells. The methods used to create these vectors are given in Section 4.3.1 for the morphological features and Section 5.2 for electrophysiological features,

Cell	nDendC	nDendSp	nBrP	nTrmP
Fish	330	303	37	38
Alligator 1	800	733	221	222
Alligator 2	788	729	225	226
Alligator 3	759	697	260	261
Alligator 4	866	7761	306	307
Turtle 1	640	588	73	76
Turtle 2	574	529	63	69
Turtle 3	574	527	63	67
Finch 1	506	478	180	181
Finch 2	758	690	286	287
Finch 3	570	525	208	209
Finch 4	1217	1133	435	436
Bat 1	896	847	225	226
Bat 2	674	618	227	228
Bat 3	371	340	107	109
Bat 4	698	648	248	249
Bat 5	907	817	337	338
Guinea pig 1	1145	1084	472	473
Guinea pig 2	991	941	419	420
Guinea pig 3	915	860	417	418
Rat 1	1118	1030	473	564
Rat 2	620	571	269	302
Rat 3	643	587	281	324
Rat 4	1928	1778	718	719

Table B.1: First part of the 16-dimensional morphological feature vector. KEY: nDendC: Number of dendritic compartments; nDendSp: Number of dendritic spines; nBrP: Number of branch points; nTrmP: Number of terminal points

Cell	MaxBO	TotLen (μm)	TotSA (μm^2)	TotVol (μm^3)
Fish	13	5169.06	25622.31	15332.65
Alligator 1	29	4733.05	7458.50	9093.12
Alligator 2	43	4529.43	9501.75	21003.34
Alligator 3	33	2733.95	1930.79	1336.55
Alligator 4	48	2849.62	1822.94	1388.08
Turtle 1	12	7049.19	21045.48	13037.41
Turtle 2	12	6756.34	21987.58	7948.88
Turtle 3	10	7077.61	21299.06	12206.71
Finch 1	26	3245.20	6828.42	5663.08
Finch 2	35	4120.88	8241.23	6547.82
Finch 3	29	2825.45	3825.76	1648.45
Finch 4	40	4663.05	3886.27	1922.97
Bat 1	28	4946.85	6083.81	6979.35
Bat 2	31	4387.92	9764.55	5160.13
Bat 3	17	2439.22	4852.84	5498.57
Bat 4	28	3573.09	4453.93	3465.70
Bat 5	50	5092.66	11018.25	8659.91
Guinea pig 1	29	10839.87	60630.05	35475.89
Guinea pig 2	24	8357.72	40998.33	26063.77
Guinea pig 3	25	8128.17	50722.78	28521.30
Rat 1	23	8143.32	40298.73	22022.63
Rat 2	20	4271.51	21246.42	11455.40
Rat 3	20	4093.74	20040.52	12708.19
Rat 4	43	6948.88	5323.70	1501.83

Table B.2: Second part of the 16-dimensional morphological feature vector. KEY: MaxBO: Maximum branch order; TotLen: Total dendritic length; TotSA: Total dendritic surface area; TotVol: Total dendritic volume

Cell	SomRad (μm)	AvgDCRad (μm)	MaxPL	AvgPL
Fish	11.19	1.39	35	18.40
Alligator 1	12.59	0.32	36	19.45
Alligator 2	16.85	0.37	62	30.92
Alligator 3	6.71	0.15	39	22.50
Alligator 4	6.79	0.12	60	27.00
Turtle 1	12.47	0.81	39	17.98
Turtle 2	8.20	0.95	36	17.39
Turtle 3	12.00	0.82	32	18.26
Finch 1	10.42	0.48	32	17.11
Finch 2	10.63	0.43	37	17.35
Finch 3	6.63	0.34	35	18.48
Finch 4	7.38	0.20	51	24.55
Bat 1	11.57	0.26	39	20.94
Bat 2	8.99	0.53	41	17.87
Bat 3	10.50	0.39	20	10.76
Bat 4	8.99	0.27	35	14.67
Bat 5	11.88	0.53	55	28.50
Guinea pig 1	13.38	1.40	49	28.43
Guinea pig 2	12.69	1.21	38	21.60
Guinea pig 3	11.80	1.59	52	27.63
Rat 1	11.38	1.27	27	14.12
Rat 2	9.69	1.27	21	12.86
Rat 3	10.60	1.20	22	11.46
Rat 4	6.29	0.20	52	26.18

Table B.3: Third part of the 16-dimensional morphological feature vector. KEY: SomRad: Soma radius; AvgDCRad: Average dendritic compartment radium; MaxPL: Maximum path length; AvgPL: Average path length

Cell	AvgTA	H-S	MaxBifRat	AvgDendCompEL
Fish	0.34	4	8.64	0.085
Alligator 1	0.35	5	6.15	0.067
Alligator 2	0.30	5	3.17	0.063
Alligator 3	0.35	6	5.80	0.061
Alligator 4	0.33	6	2.87	0.060
Turtle 1	0.35	5	7.60	0.080
Turtle 2	0.35	5	7.50	0.077
Turtle 3	0.37	5	9.80	0.086
Finch 1	0.35	5	3.30	0.061
Finch 2	0.32	5	4.91	0.056
Finch 3	0.32	6	2.92	0.058
Finch 4	0.32	6	7.17	0.057
Bat 1	0.36	6	3.71	0.069
Bat 2	0.33	6	18.33	0.062
Bat 3	0.35	5	7.14	0.071
Bat 4	0.35	6	4.63	0.063
Bat 5	0.34	5	2.69	0.050
Guinea pig 1	0.34	7	4.50	0.029
Guinea pig 2	0.35	6	12.67	0.034
Guinea pig 3	0.35	6	5.40	0.030
Rat 1	0.35	6	3.80	0.041
Rat 2	0.36	6	5.00	0.039
Rat 3	0.36	5	3.20	0.040
Rat 4	0.31	6	5.00	0.056

Table B.4: Fourth part of the 16-dimensional morphological feature vector. KEY: AvgTA: Average tree asymmetry; H-S: Horton-Strahler number; MaxBifRat: Maximum bifurcation ratio; AvgDendCompEL: Average dendritic compartment electrotonic length

	Voltage Attenuation			
Cell	TrmComp →Soma	Soma →TrmComp	DendComp→Soma	Soma→DendComp
Fish	132.25	41.63	1.00	0.99
Alligator 1	287.30	16.18	0.99	0.99
Alligator 2	202.69	5.48	0.99	1.00
Alligator 3	169.91	18.03	0.98	0.99
Alligator 4	241.23	18.61	0.98	0.99
Turtle 1	224.53	11.73	1.00	1.00
Turtle 2	211.50	35.66	1.00	1.00
Turtle 3	392.75	44.43	1.00	1.00
Finch 1	136.46	7.97	0.99	1.00
Finch 2	196.82	5.33	0.99	1.00
Finch 3	126.27	3.77	0.99	1.00
Finch 4	314.02	11.98	0.99	1.00
Bat 1	357.75	12.23	0.99	1.00
Bat 2	214.28	4.36	1.00	1.00
Bat 3	147.70	4.65	0.98	1.00
Bat 4	225.23	13.22	0.99	0.99
Bat 5	178.78	6.14	1.00	1.00
Guinea pig 1	143.69	7.39	1.00	1.00
Guinea pig 2	161.47	4.28	1.00	1.00
Guinea pig 3	88.35	8.35	1.00	1.00
Rat 1	100.79	9.16	1.00	1.00
Rat 2	56.19	6.49	1.00	1.00
Rat 3	92.53	7.17	1.00	1.00
Rat 4	237.69	5.36	0.99	1.00

Table B.5: First part of the 14-dimensional passive electrophysiological feature
vector

	Average Peak Depolarisation (mV)			
	At Soma		At Dendritic Compartments	
Cell	All Compartments	Terminal Compartments	All Compartments	Terminal Compartments
Fish	0.04	0.03	0.04	0.03
Alligator 1	0.06	0.05	0.06	0.06
Alligator 2	0.03	0.06	0.05	0.06
Alligator 3	0.11	0.15	0.14	0.18
Alligator 4	0.12	0.11	0.19	0.16
Turtle 1	0.02	0.03	0.03	0.03
Turtle 2	0.03	0.02	0.03	0.02
Turtle 3	0.04	0.01	0.04	0.02
Finch 1	0.06	0.07	0.06	0.07
Finch 2	0.05	0.06	0.05	0.06
Finch 3	0.06	0.10	0.07	0.10
Finch 4	0.05	0.06	0.07	0.07
Bat 1	0.04	0.05	0.04	0.05
Bat 2	0.04	0.05	0.05	0.05
Bat 3	0.10	0.09	0.11	0.10
Bat 4	0.08	0.07	0.10	0.08
Bat 5	0.03	0.04	0.03	0.04
Guinea pig 1	0.01	0.01	0.01	0.01
Guinea pig 2	0.02	0.02	0.02	0.02
Guinea pig 3	0.02	0.02	0.02	0.02
Rat 1	0.02	0.02	0.02	0.02
Rat 2	0.03	0.03	0.03	0.03
Rat 3	0.03	0.02	0.03	0.03
Rat 4	0.04	0.08	0.06	0.08

Table B.6: Second part of the 14-dimensional passive electrophysiological feature vector. Peak amplitudes when averaged either over all dendritic compartments or only terminal dendritic compartments.

	Average Time Taken to Reach Peak Amplitude (ms)			
	At Soma		At Dendritic Compartments	
Cell	All Compartments	Terminal Compartments	All Compartments	Terminal Compartments
Fish	7.38	8.22	7.09	8.58
Alligator 1	7.49	7.01	6.79	7.20
Alligator 2	12.42	8.92	9.17	9.29
Alligator 3	8.55	6.84	6.82	7.06
Alligator 4	10.04	7.50	6.99	7.51
Turtle 1	8.76	8.22	7.76	8.60
Turtle 2	8.84	9.02	8.10	9.60
Turtle 3	7.07	8.11	6.68	8.62
Finch 1	9.72	8.90	8.26	9.46
Finch 2	9.37	8.17	8.09	8.46
Finch 3	10.45	8.94	8.74	9.29
Finch 4	11.72	9.71	9.01	10.08
Bat 1	9.11	8.07	7.60	8.28
Bat 2	9.24	7.93	7.59	8.28
Bat 3	6.08	6.49	5.81	6.58
Bat 4	6.63	6.43	5.86	6.52
Bat 5	12.75	11.33	11.26	11.83
Guinea pig 1	12.50	12.47	11.59	13.41
Guinea pig 2	10.07	10.25	9.48	10.83
Guinea pig 3	19.82	20.01	17.95	22.15
Rat 1	9.45	9.58	10.07	10.18
Rat 2	10.47	10.69	10.97	11.19
Rat 3	9.37	9.50	9.88	9.99
Rat 4	12.69	9.14	6.99	9.42

Table B.7: Third part of the 14-dimensional passive electrophysiological feature vector. Time taken to reach peak amplitudes when averaged either over all dendritic compartments or only terminal dendritic compartments.

Cell	Average Peak Depolarisation At Soma (Stimulation At Spines) (mV)	Average Time To Reach Peak Depolarisation At Soma (Stimulation At Spines) (ms)
Fish	0.03	9.73
Alligator 1	0.02	12.81
Alligator 2	0.02	17.91
Alligator 3	0.05	20.02
Alligator 4	0.05	19.62
Turtle 1	0.02	12.29
Turtle 2	0.02	11.01
Turtle 3	0.02	12.94
Finch 1	0.03	17.02
Finch 2	0.03	16.65
Finch 3	0.03	21.83
Finch 4	0.02	23.92
Bat 1	0.02	15.80
Bat 2	0.03	15.42
Bat 3	0.05	12.66
Bat 4	0.04	13.82
Bat 5	0.02	19.29
Guinea pig 1	0.01	11.31
Guinea pig 2	0.01	10.82
Guinea pig 3	0.01	14.78
Rat 1	0.01	11.18
Rat 2	0.02	12.88
Rat 3	0.02	11.33
Rat 4	0.02	24.00

Table B.8: Fourth part of the 14-dimensional passive electrophysiological feature vector. Peak amplitudes when averaged either over all dendritic compartments or only terminal dendritic compartments.

	Voltage Attenuation			
Cell	TrmComp →Soma	Soma →TrmComp	DendComp→Soma	Soma→DendComp
Fish	1.21	0.79	1.13	-3.032
Alligator 1	0.42	2.57	1.27	0.992
Alligator 2	0.32	3.13	1.57	0.981
Alligator 3	0.05	17.92	1.24	0.987
Alligator 4	0.04	16.69	1.34	0.985
Turtle 1	0.98	1.01	2.59	2.595
Turtle 2	1.12	0.89	2.03	2.030
Turtle 3	1.04	0.95	1.83	1.833
Finch 1	0.36	2.83	1.44	0.899
Finch 2	0.53	1.89	1.30	0.980
Finch 3	0.31	3.17	1.47	0.924
Finch 4	0.14	7.42	1.29	0.992
Bat 1	0.26	4.31	1.28	0.995
Bat 2	0.54	1.84	8.89	0.902
Bat 3	0.57	1.68	1.18	1.039
Bat 4	0.30	3.22	1.23	0.987
Bat 5	0.51	0.19	1.30	0.948
Guinea pig 1	1.17	0.85	1.32	1.323
Guinea pig 2	1.14	0.88	1.21	1.214
Guinea pig 3	1.25	0.80	1.02	1.016
Rat 1	1.23	0.81	1.84	1.841
Rat 2	1.20	0.83	1.49	1.487
Rat 3	1.12	0.89	1.28	1.281
Rat 4	0.24	4.06	1.42	1.424

Table B.9: First part of the 14-dimensional active electrophysiological feature vector

	Average Peak Depolarisation (mV)			
	At Soma		At Dendritic Compartments	
Cell	All Compartments	Terminal Compartments	All Compartments	Terminal Compartments
Fish	74.14	76.77	88.14	76.77
Alligator 1	15.30	2.31	14.40	1.32
Alligator 2	23.19	10.24	17.13	4.46
Alligator 3	13.14	0.14	13.33	0.29
Alligator 4	13.44	0.14	13.43	0.33
Turtle 1	60.25	47.12	56.38	46.91
Turtle 2	60.74	47.56	66.84	53.73
Turtle 3	55.88	42.89	57.22	45.25
Finch 1	30.19	17.18	21.93	8.93
Finch 2	22.84	9.91	19.41	6.51
Finch 3	24.67	11.76	20.94	8.93
Finch 4	14.22	1.22	13.47	0.46
Bat 1	13.97	0.97	13.53	0.53
Bat 2	64.84	51.83	42.00	29.10
Bat 3	16.93	3.93	16.29	3.19
Bat 4	14.51	1.53	13.95	0.87
Bat 5	27.20	14.16	21.73	8.79
Guinea pig 1	78.94	65.94	90.39	77.37
Guinea pig 2	75.27	62.29	84.00	71.09
Guinea pig 3	79.50	66.52	96.16	83.32
Rat 1	74.02	61.05	88.21	75.22
Rat 2	74.63	61.62	87.11	74.17
Rat 3	75.30	62.28	82.79	69.79
Rat 4	16.06	3.05	13.89	1.10

Table B.10: Second part of the 14-dimensional active electrophysiological feature
vector. Peak amplitudes when averaged either over all dendritic compartments
or only terminal dendritic compartments.

	Average Time Taken to Reach Peak Amplitude (ms)			
	At Soma		At Dendritic Compartments	
Cell	All Compartments	Terminal Compartments	All Compartments	Terminal Compartments
Fish	8.23	8.23	8.78	16.85
Alligator 1	9.01	9.07	7.32	7.26
Alligator 2	16.06	16.07	9.07	9.79
Alligator 3	1.47	1.48	1.14	1.15
Alligator 4	2.32	2.34	1.30	1.27
Turtle 1	11.88	11.91	14.33	14.38
Turtle 2	11.17	11.31	13.16	13.49
Turtle 3	11.90	11.89	14.35	14.64
Finch 1	16.75	16.81	16.08	16.43
Finch 2	15.15	15.21	13.98	14.07
Finch 3	14.07	14.19	9.56	9.66
Finch 4	5.58	5.60	2.16	2.14
Bat 1	6.10	6.14	3.71	3.83
Bat 2	13.13	13.14	14.04	14.01
Bat 3	11.49	11.51	10.79	10.30
Bat 4	6.65	6.70	5.14	5.04
Bat 5	16.12	16.11	15.53	15.62
Guinea pig 1	8.34	8.34	8.68	8.71
Guinea pig 2	9.06	9.06	9.45	9.47
Guinea pig 3	6.92	6.92	7.83	7.83
Rat 1	8.81	8.81	9.08	9.10
Rat 2	8.91	8.91	9.18	9.19
Rat 3	9.48	9.49	9.59	9.61
Rat 4	8.07	8.05	2.86	3.38

Table B.11: Third part of the 14-dimensional active electrophysiological feature vector. Time taken to reach peak amplitudes when averaged either over all dendritic compartments or only terminal dendritic compartments.

Cell	Average Peak Depolarisation At Soma (Stimulation At Spines) (mV)	Average Time To Reach Peak Depolarisation At Soma (Stimulation At Spines) (ms)
Fish	22.19	35.14
Alligator 1	13.70	11.39
Alligator 2	14.09	20.35
Alligator 3	13.12	4.79
Alligator 4	13.29	5.56
Turtle 1	15.48	27.31
Turtle 2	15.42	30.90
Turtle 3	16.32	26.29
Finch 1	14.49	23.44
Finch 2	13.98	18.90
Finch 3	13.86	20.85
Finch 4	13.32	11.67
Bat 1	13.30	11.47
Bat 2	14.46	24.67
Bat 3	13.79	15.24
Bat 4	13.58	10.01
Bat 5	13.98	22.52
Guinea pig 1	14.56	32.49
Guinea pig 2	14.62	31.85
Guinea pig 3	15.10	35.25
Rat 1	14.54	29.53
Rat 2	14.46	31.01
Rat 3	14.07	32.54
Rat 4	13.56	15.95

Table B.12: Fourth part of the 14-dimensional active electrophysiological feature vector

Appendix C

Kendall's Rank Coefficient and Kruskal-Wallis Test Full Results

Kendall's rank and Kruskal-Wallis test results for all the morphological features, including results for species groups with outliers removed.

Metric	τ	p (2-tailed)
nDendC	0.619	0.069
nDendSp	0.619	0.069
nBrP	0.619	0.069
nTrmP	0.714	0.030
maxBO	-0.048	1.000
totLen	0.333	0.381
totSurfA	0.238	0.562
totVol	0.048	1.000
somRad	-0.238	0.562
avgDendCmpRad	0.238	0.562
maxPL	-0.048	1.000
avgPL	-0.048	1.000
avgTA	0.143	0.773
H-S	0.781	0.017
maxBifRatio	-0.333	0.381
avgDendCmpEL	-0.619	0.069

(a) Kendall's τ for full species groups

Metric	τ	p (2-tailed)
nDendC	0.524	0.136
nDendSp	0.524	0.136
nBrP	0.619	0.069
nTrmP	0.619	0.069
maxBO	-0.098	0.884
totLen	0.238	0.562
totSurfA	0.143	0.773
totVol	0.143	0.773
somRad	0.143	0.773
avgDendCmpRad	0.238	0.562
maxPL	-0.048	1.000
avgPL	-0.238	0.562
avgTA	-	-
H-S	-	-
maxBifRatio	-0.429	0.239
avgDendCmpEL	-0.619	0.069

(b) Kendall's τ for species groups minus outlying results. avgTA and H-S had no outliers.

Table C.1: Kendall's τ and p-values for all morphological features

Metric	H	p (2-tailed)
nDendC	9.939	0.127
nDendSp	9.589	0.143
nBrP	15.362	0.018
nTrmP	16.231	0.013
maxBO	13.666	0.034
totLen	14.417	0.025
totSurfA	16.701	0.010
totVol	12.612	0.050
somRad	7.315	0.293
avgDendCmpRad	15.446	0.017
maxPL	6.811	0.339
avgPL	9.654	0.140
avgTA	6.857	0.334
H-S	10.409	0.109
maxBifRatio	7.946	0.242
avgDendCmpEL	10.804	0.003

(a) H for full species groups

Metric	H	p (2-tailed)
nDendC	12.876	0.045
nDendSp	12.600	0.050
nBrP	15.336	0.018
nTrmP	16.376	0.012
maxBO	14.716	0.023
totLen	12.979	0.043
totSurfA	16.983	0.009
totVol	14.910	0.021
somRad	10.153	0.118
avgDendCmpRad	18.579	0.005
maxPL	9.624	0.141
avgPL	14.937	0.021
avgTA	-	-
H-S	-	-
maxBifRatio	9.654	0.140
avgDendCmpEL	19.124	0.004

(b) H for species groups minus outlying results. avgTA and H-S had no outliers.

Table C.2: Morphological features with statistically significant H values

Appendix D

Regression Coefficients

Regression coefficients for all the cell models, corresponding to Tables 5.1, 5.6, 5.9, and 5.12 in Section 5.3.

Species	Peak Amplitude Slope	Intercept	R^2	Time to Reach Peak Amplitude Slope	Intercept	R^2
Fish	[-0.006, 0.009, 0.014, -0.006, -0.034]	0.024	0.892	[-0.047, 0.050, 0.039, 1.812]	7.453	0.964
Alligator 1	[-0.025, 0.045, 0.010, -0.025, -0.015]	0.010	0.931	[0.054, 0.257, -0.033, 2.019]	8.573	0.952
Alligator 2	[-0.019, 0.037, -0.021]	0.013	0.913	[0.162, 2.224]	7.332	0.967
Alligator 3	[0.003, -0.009, -0.002, 0.024, 0.004, -0.038]	0.019	0.554	[-0.423, 0.241,1.474,3.140]	11.923	0.663
Alligator 4	[0.042, -0.112, 0.031, 0.035]	0.009	0.842	[-0.168, -0.178, 0.947, 4.621]	9.834	0.974
Turtle 1	[-0.007, 0.017, -0.015]	0.014	0.809	[0.146, 0.231, -0.483, -0.616, 2.677]	8.866	0.464
Turtle 2	[-0.008, 0.019, -0.010]	0.007	0.788	[-0.121, 2.034]	8.975	0.742
Turtle 3	[-0.008, 0.019, -0.017]	0.013	0.934	[1.489]	7.080	0.937
Finch 1	[0.006, -0.005, -0.036, 0.064, -0.032]	0.006	0.892	[0.081, 2.901]	10.376	0.970
Finch 2	[-0.008, 0.041, -0.048]	0.011	0.842	[-0.023, 0.204, 3.016]	9.521	0.940
Finch 3	[-0.004, 0.023, -0.039]	0.022	0.855	[0.221, 0.336, 2.672]	9.051	0.942
Finch 4	[0.006, -0.030, 0.042, -0.012]	-0.002	0.926	[0.177, 0.617, 0.063, -1.108, 2.956]	11.836	0.893
Bat 1	[-0.002, 0.005, -0.007, 0.014, -0.020]	0.010	0.884	[-0.014, -0.072, 0.058, 0.424, 2.246]	8.834	0.977
Bat 2	[-0.003, 0.022, -0.045]	0.021	0.844	[-0.220, 0.235, 3.987]	9.221	0.873
Bat 3	[-0.003, -0.001, 0.041, -0.083]	0.069	0.793	[-0.072, -0.50, 1.500]	6.152	0.788
Bat 4	[-0.016, 0.037, -0.042]	0.038	0.805	[0.157, 0.455, 1.594]	6.220	0.905
Bat 5	[-0.007, 0.023, -0.020]	0.005	0.926	[0.134, 4.104]	13.265	0.962
Guinea pig 1	[-0.001, 0.003, -0.005]	0.011	0.910	[-0.159, 0.183, 5.004]	12.343	0.861
Guinea pig 2	[-0.000, 0.002, -0.008]	0.015	0.913	[-0.100, -0.212, 0.391, 3.938]	9.995	0.910
Guinea pig 3	[0.000, -0.003, 0.002, -0.002]	0.013	0.481	[-0.135, -0.052, 0.734, 0.182, 6.667]	19.731	0.755
Rat 1	[-0.002, -0.002, 0.017, -0.013, 0.003, -0.012]	0.006	0.787	[0.737, 2.095, 0.677, -1.745, 2.817]	12.814	0.793
Rat 2	[0.000, -0.002, 0.004, -0.007]	0.011	0.931	[0.044, 0.246, 3.394]	9.211	0.894
Rat 3	[0.011, -0.018]	0.018	0.820	[-0.044, -0.282, -0.129, 3.727]	10.569	0.909
Rat 4	[0.001, -0.001, 0.002, -0.011]	0.021	0.823	[-0.174, -0.257, 0.618, 4.182]	9.290	9.813

Table D.1: Regression coefficients for plotting peak amplitude and time to reach
peak amplitude when stimulating in dendritic compartments and recording at
soma in passive models without spines.

	Peak Amplitude			Time to Reach Peak Amplitude		
Species	Slope	Intercept	R^2	Slope	Intercept	R^2
Fish	[-0.013, 0.025, -0.010]	0.013	0.779	[0.044, -0.143, 1.638]	7.250	0.954
Alligator 1	[-0.161, 0.117, 0.140]	-0.051	0.900	[-0.517, 1.108]	7.344	0.742
Alligator 2	[-0.018, 0.040, -0.028]	0.015	0.919	[-0.124, -0.258, 1.769]	7.028	0.899
Alligator 3	[-0.100, 0.024, -0.018]	0.013	0.481	[1.100]	0.191	0.262
Alligator 4	[-0.094, 0.203, -0.017]	-0.049	0.843	[1.449]	7.002	0.767
Turtle 1	[-0.007, 0.017, -0.016]	0.015	0.808	[1.604]	7.771	0.410
Turtle 2	[-0.008, 0.019, -0.010]	0.008	0.787	[-0.291, 1.485]	8.407	0.647
Turtle 3	[-0.007, 0.020, -0.018]	0.013	0.935	[-0.089, 1.209]	6.782	0.915
Finch 1	[-0.005, 0.467, -0.066]	0.016	0.871	[-0.627, 1.226]	9.375	0.735
Finch 2	[-0.008, 0.042, -0.051]	0.013	0.837	[1.699]	8.267	0.754
Finch 3	[-0.004, 0.023, -0.042]	0.024	0.861	[-0.475, 1.823]	8.477	0.780
Finch 4	[-0.026, 0.071, -0.025]	-0.011	0.912	[1.255]	9.019	0.604
Bat 1	[-0.017, 0.030, -0.014]	0.006	0.893	[-0.429, 0.944]	8.040	0.644
Bat 2	[0.001, -0.003, -0.001, 0.030, -0.050]	0.020	0.845	[1.583]	7.595	0.526
Bat 3	[0.028, -0.089]	0.082	0.790	[1.134]	5.818	0.779
Bat 4	[-0.016, 0.039, -0.050]	0.044	0.812	[1.175]	5.864	0.842
Bat 5	[-0.007, 0.023, -0.021]	0.005	0.920	[-0.674, 1.966]	11.943	0.762
Guinea pig 1	[-0.001, 0.003, -0.005]	0.011	0.904	[4.229]	11.602	0.843
Guinea pig 2	[0.002, -0.008]	0.015	0.908	[0.091, 3.256]	9.400	0.898
Guinea pig 3	[0.000, -0.003, 0.002, -0.002]	0.013	0.478	[6.483]	17.963	0.768
Rat 1	[-0.002, 0.006, -0.007]	0.011	0.926	[3.162]	8.867	0.883
Rat 2	[0.011, -0.018]	0.018	0.082	[3.021]	9.984	0.900
Rat 3	[0.004, -0.013]	0.021	0.802	[3.277]	8.948	0.792
Rat 4	[-0.020, 0.037, -0.007]	-0.002	0.774	[1.134]	8.916	0.406

Table D.2: Regression coefficients for plotting peak amplitude and time to reach peak amplitude when stimulating in the soma and recording at dendritic compartments in passive models without spines.

	Peak Amplitude			Time to Reach Peak Amplitude		
Species	Slope	Intercept	R^2	Slope	Intercept	R^2
Fish	[-0.013, 0.021, -0.000]	0.007	0.692	[2.584]	9.731	0.887
Alligator 1	[-0.070, 0.032, 0.080]	-0.022	0.776	[3.212]	20.019	0.205
Alligator 2	[-0.010, 0.017, -0.006]	0.004	0.801	[2.868]	12.807	0.511
Alligator 3	[-0.009, 0.019, -0.004]	-0.003	0.922	[5.457]	17.913	0.758
Alligator 4	[-0.027, 0.050, 0.009]	-0.017	0.730	[4.880]	19.617	0.349
Turtle 1	[-0.004, 0.010, -0.010]	0.009	0.715	[3.275]	12.287	0.516
Turtle 2	[-0.003, 0.010, -0.010]	0.006	0.818	[3.264]	12.943	0.785
Turtle 3	[-0.004, 0.011, -0.010]	0.007	0.890	[2.873]	11.009	0.851
Finch 1	[-0.012, 0.027, -0.011]	-0.001	0.848	[7.177]	21.830	0.769
Finch 2	[-0.010, 0.023, -0.010]	0.001	0.749	[5.143]	17.023	0.785
Finch 3	[-0.005, 0.015, -0.014]	0.007	0.784	[5.408]	16.648	0.671
Finch 4	[-0.013, 0.032, -0.002]	-0.009	0.802	[5.041]	23.924	0.389
Bat 1	[-0.011, 0.015, -0.001]	0.000	0.816	[3.686]	15.798	0.542
Bat 2	[-0.004, 0.019, -0.024]	0.008	0.775	[5.890]	15.415	0.688
Bat 3	[-0.004, 0.021, -0.039]	0.030	0.686	[4.603]	12.656	0.717
Bat 4	[-0.010, 0.017, -0.009]	0.012	0.732	[3.657]	13.823	0.503
Bat 5	[-0.006, 0.013, -0.006]	0.000	0.852	[4.770]	19.286	0.697
Guinea pig 1	[-0.001, 0.002, -0.004]	0.006	0.865	[3.346]	11.312	0.779
Guinea pig 2	[0.002, -0.007]	0.009	0.921	[3.765]	10.820	0.893
Guinea pig 3	[-0.003, 0.004, -0.001]	0.005	0.528	[4.333]	14.777	0.754
Rat 1	[0.004, -0.009]	0.007	0.865	[3.989]	11.180	0.805
Rat 2	[0.009, -0.014]	0.013	0.813	[4.109]	12.881	0.874
Rat 3	[0.004, -0.010]	0.015	0.083	[4.629]	11.333	0.825
Rat 4	[0.007, -0.008, -0.008, 0.004]	0.003	0.710	[6.057]	23.995	0.528

Table D.3: Regression coefficients for plotting peak amplitude and time to reach peak amplitude when stimulating in dendritic spine compartments and recording at soma in passive models.

	Peak Amplitude			Time to Reach Peak Amplitude		
Species	Slope	Intercept	R^2	Slope	Intercept	R^2
Fish	[-0.055]	60.666	0.003	[0.024]	8.231	0.008
Alligator 1	$[1.203 \times 1^{-6}]$	0.135	6.227×1^{-8}	[-0.001]	1.469	2.950×1^{-5}
Alligator 2	[-0.005]	2.303	2.880×1^{-4}	[-0.025]	9.013	4.510×1^{-4}
Alligator 3	[-0.025]	10.189	2.051×1^{-4}	[-0.012]	16.056	2.093×1^{-4}
Alligator 4	[0.001]	0.443	0.002	[0.006]	2.320	0.001
Turtle 1	[-0.056]	47.251	0.003	[0.035]	11.875	0.004
Turtle 2	[-0.018]	47.742	0.001	[0.005]	11.169	0.001
Turtle 3	[0.006]	42.882	8.260×1^{-5}	[-0.001]	11.904	7.346×1^{-6}
Finch 1	[0.121]	11.676	0.001	[0.072]	14.065	0.002
Finch 2	[0.053]	17.170	7.663×1^{-5}	[0.016]	16.748	1.794×1^{-4}
Finch 3	[-0.066]	9.835	0.002	[-0.008]	15.151	9.766×1^{-5}
Finch 4	[5.897]	1.220	3.533×1^{-5}	[0.008]	5.583	1.727×1^{-4}
Bat 1	[-0.001]	0.970	2.496×1^{-4}	$[9.942 \times 1^{-5}]$	6.097	2.029×1^{-8}
Bat 2	[0.115]	51.836	0.001	[-0.001]	13.131	8.240×1^{-7}
Bat 3	[-0.028]	3.934	0.001	[-0.053]	11.491	4.980×1^{-4}
Bat 4	[-0.006]	1.515	0.002	[-0.036]	6.651	0.002
Bat 5	[0.074]	14.205	0.001	[-0.019]	16.115	0.001
Guinea pig 1	[0.003]	65.941	9.642×1^{-5}	[-6.133]	8.340	2.064×1^{-5}
Guinea pig 2	[-0.007]	62.275	3.045×1^{-4}	[0.006]	9.059	0.001
Guinea pig 3	[0.012]	66.496	0.001	[7.408]	6.915	2.435×1^{-5}
Rat 1	[0.014]	61.016	2.750×1^{-4}	[-9.262]	8.809	5.181×1^{-5}
Rat 2	[0.024]	61.633	0.002	[-0.005]	8.911	4.766×1^{-4}
Rat 3	[-0.015]	62.295	0.001	[0.005]	9.485	2.967×1^{-4}
Rat 4	[-0.003]	3.059	1.606×1^{-4}	[-0.001]	8.058	5.059×1^{-9}

Table D.4: Regression coefficients for plotting peak amplitude and time to reach peak amplitude when stimulating in dendritic compartments and recording at soma in active models without spines.

	Peak Amplitude			Time to Reach Peak Amplitude		
Species	Slope	Intercept	R^2	Slope	Intercept	R^2
Fish	[-2.117, 4.728]	77.291	0.551	[-0.137, 0.236]	8.923	0.114
Alligator 1	[-0.341, 0.335, 0.281]	-0.125	0.895	[1.056, -0.346, -3.578]	2.850	0.823
Alligator 2	[0.083, 0.100, -1.077]	1.317	0.664	[0.100, -0.886, -2.211]	8.405	0.452
Alligator 3	[-4.480]	4.118	0.690	[-5.584]	9.433	0.683
Alligator 4	[-0.242, 0.595, -0.179]	-0.107	0.864	[0.153, -0.792, -1.138]	4.570	0.577
Turtle 1	[-0.539, -1.615, -3.315]	45.042	0.093	[0.224, 0.081, 0.890]	14.230	0.275
Turtle 2	[-1.374, 0.393]	55.222	0.035	[1.153]	13.168	0.400
Turtle 3	[-1.549]	44.221	0.012	[1.231]	14.359	0.298
Finch 1	[1.199, 3.447, -10.852]	4.735	0.733	[0.182, -2.249, -4.390]	12.903	0.517
Finch 2	[0.902, 2.167, -8.795]	7.042	0.676	[-0.538, -1.575, 0.236]	17.464	0.197
Finch 3	[0.747, -0.149, -5.442]	6.559	0.762	[0.568, -0.801, -2.705]	14.828	0.162
Finch 4	[-0.107, 0.448, -0.465]	0.067	0.795	[0.298, -0.633, -2.143]	4.612	0.431
Bat 1	[0.028, 0.206, -0.575]	0.327	0.775	[0.515, -0.653, -3.325]	4.783	0.766
Bat 2	[2.450, 0.235, -25.929]	26.385	0.694	[-0.244, -0.560, 1.911]	14.837	0.190
Bat 3	[0.112, -0.071, -1.645]	3.342	0.364	[0.129, -0.410, -1.077]	11.567	0.058
Bat 4	[0.045, -0.639]	0.901	0.538	[-0.141, -0.853, -1.039]	6.654	0.308
Bat 5	[0.953, 0.360, -7.518]	8.298	0.692	[0.243, -1.099, -1.997]	16.614	0.312
Guinea pig 1	[-0.630, -782,, 3.173]	78.191	0.836	[0.042, -0.792, -0.130]	8.753	0.184
Guinea pig 2	[2.076]	71.008	0.499	[0.174]	9.447	0.165
Guinea pig 3	[0264, -1.394, 1.203]	84.590	0.514	[0.076, 0.007, 0.001]	7.831	0.186
Rat 1	[0.165, -0.444, 3.143]	75.649	0.614	[0.036, -0.151, -0.170]	9.223	0.275
Rat 2	[-1.374, 0.393]	75.364	0.574	[-0.019, -0.077, 0.114]	9.245	0.400
Rat 3	[-0.666, 2.015]	70.618	0.649	[0.139]	9.591	0.298
Rat 4	[-0.283, 0.759, -0.419]	0.212	0.531	[0.117, -0.093, -2.056]	6.574	0.267

Table D.5: Regression coefficients for plotting peak amplitude and time to reach peak amplitude when stimulating in the soma and recording at dendritic compartments in active models without spines.

	Peak Amplitude			Time to Reach Peak Amplitude		
Species	Slope	Intercept	R^2	Slope	Intercept	R^2
Fish	[0.085]	19.512	0.004	[0.229]	35.142	0.004
Alligator 1	[-0.078, 0.032, 0.096]	13.055	0.742	[-0.644]	4.772	0.263
Alligator 2	[-0.007, 0.025, -0.026]	13.676	0.329	[-0.005]	11.396	6.022×1^{-6}
Alligator 3	[0.026,-0.037]	14.066	0.052	[0.037]	20.39	8.000×1^{-5}
Alligator 4	[-0.031. 0.054, 0.018]	13.239	0.628	[-0.156, 0.0389, -0.139]	5.201	0.427
Turtle 1	[0.010]	15.488	0.001	[-0.050]	27.231	8.112×1^{-5}
Turtle 2	[-0.007]	15.425	1.958×1^{-4}	[0.471]	30.949	0.005
Turtle 3	[-0.023]	16.311	0.002	[0.237]	26.234	0.002
Finch 1	[-0.045]	13.860	0.063	[0.214]	21.148	0.002
Finch 2	[-0.073]	14.492	0.040	[0.036]	23.316	2.494×1^{-5}
Finch 3	[-0.031]	31.979	0.038	[-0.334, 0.075]	19.252	0.006
Finch 4	[-0.014, 0.036, -0.006]	13.292	0.605	[0.063, 0.041, -0.398]	11.607	0.025
Bat 1	[-0.036]	13.299	0.340	[-0.177]	11.438	0.010
Bat 2	[-0.033]	14.451	0.010	[0.135]	24.499	3.367
Bat 3	[-0.048]	13.790	0.144	[0.209]	15.244	0.004
Bat 4	[-0.010, 0.019, -0.017]	13.553	0.464	[0.098,-0.121,-0.278]	10.158	0.021
Bat 5	[0.010, -0.023]	13.974	0.024	[-0.005]	22.483	1.413×1^{-6}
Guinea pig 1	[0.004]	14.559	0.001	[0.352]	32.487	0.006
Guinea pig 2	[-0.002]	14.624]	6.956×1^{-5}	[0.002]	31.739	8.901×1^{-8}
Guinea pig 3	[0.010, -0.022, 0.007]	15.123	0.009	[0.535]	33.339	0.001
Rat 1	[-0.005]	14.541	0.001	[-0.043]	15.952	0.001
Rat 2	[0.001]	14.461	2.807×1^{-5}	[0.060]	29.519	1.227×1^{-4}
Rat 3	[0.001]	14.073	2.653×1^{-5}	[-0.492, -0.350, 1.223]	31.016	0.002
Rat 4	[0.017, -0.017]	13.539	0.181	[-0.357]	33.339	00.1

Table D.6: Regression coefficients for plotting peak amplitude and time to reach peak amplitude when stimulating in dendritic spine compartments and recording at soma in active models.

Appendix E

Peak Amplitude and Time Plots

Additional plots to those shown in Section 5.3, giving examples from the other species used in the study.

(a) Turtle 3

(b) Finch 4

(c) Bat 5

(d) Rat 2

Figure E.1: Peak amplitude recorded at soma following stimulation at each dendritic compartment in passive models without spines. Corresponding regression coefficients are listed in Table D.1 as: Turtle 3, Finch 4, Bat 5, Rat 2

(a) Turtle 3

(b) Finch 4

(c) Bat 5

(d) Rat 2
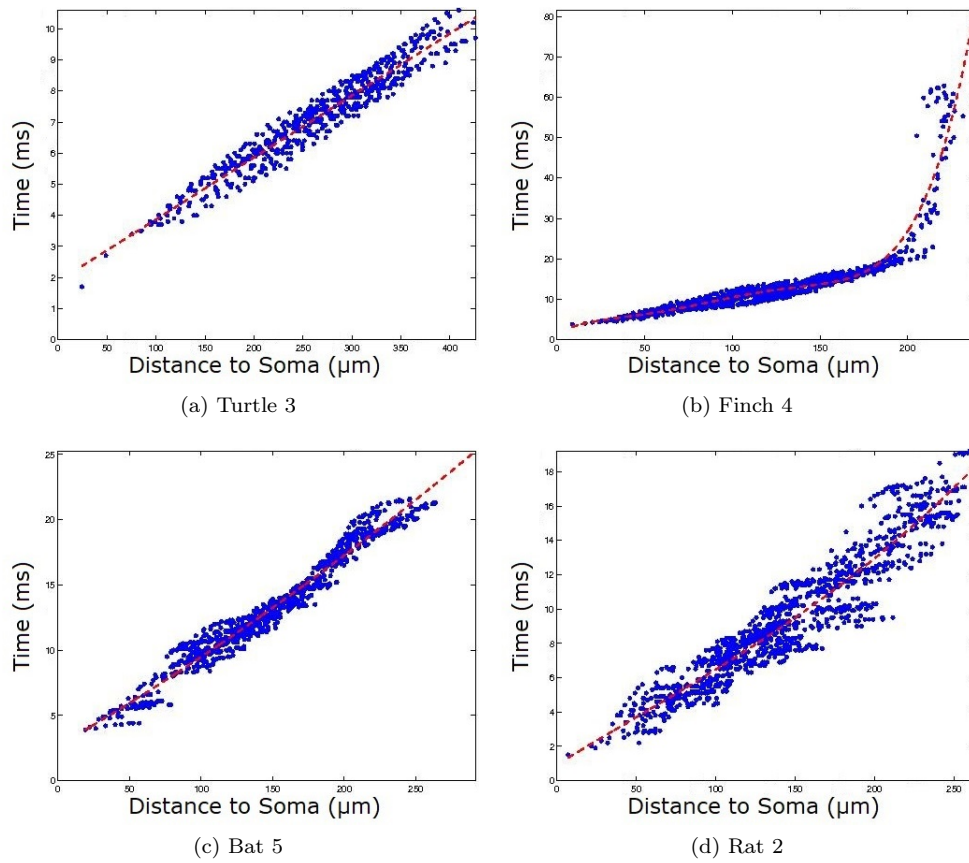
Figure E.2: Time to reach peak amplitude recorded at soma following stimulation at each dendritic compartment in passive models without spines. Corresponding regression coefficients are listed in Table D.1 as: Turtle 3, Finch 4, Bat 5, Rat 2

(a) Turtle 3

(b) Finch 4

(c) Bat 5

(d) Rat 2
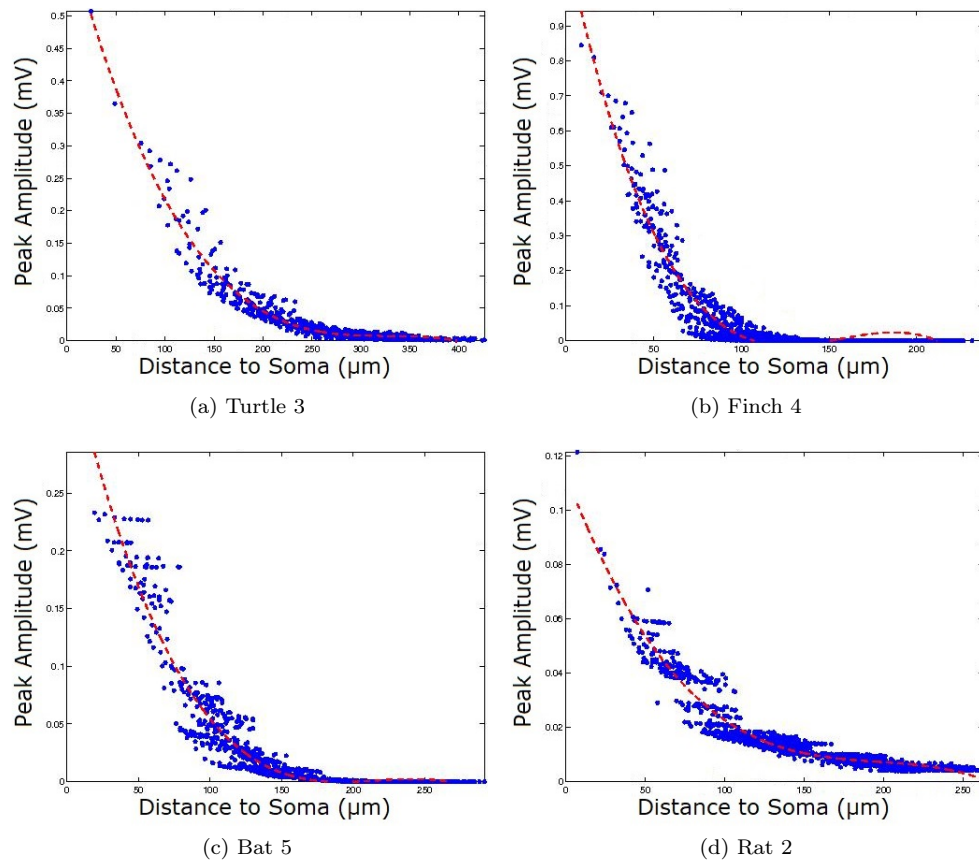
Figure E.3: Peak amplitude recorded at dendritic compartments following stimulation at the soma in passive models without spines. Corresponding regression coefficients are listed in Table D.2 as: Turtle 3, Finch 4, Bat 5, Rat 2

(a) Turtle 3

(b) Finch 4

(c) Bat 5

(d) Rat 2
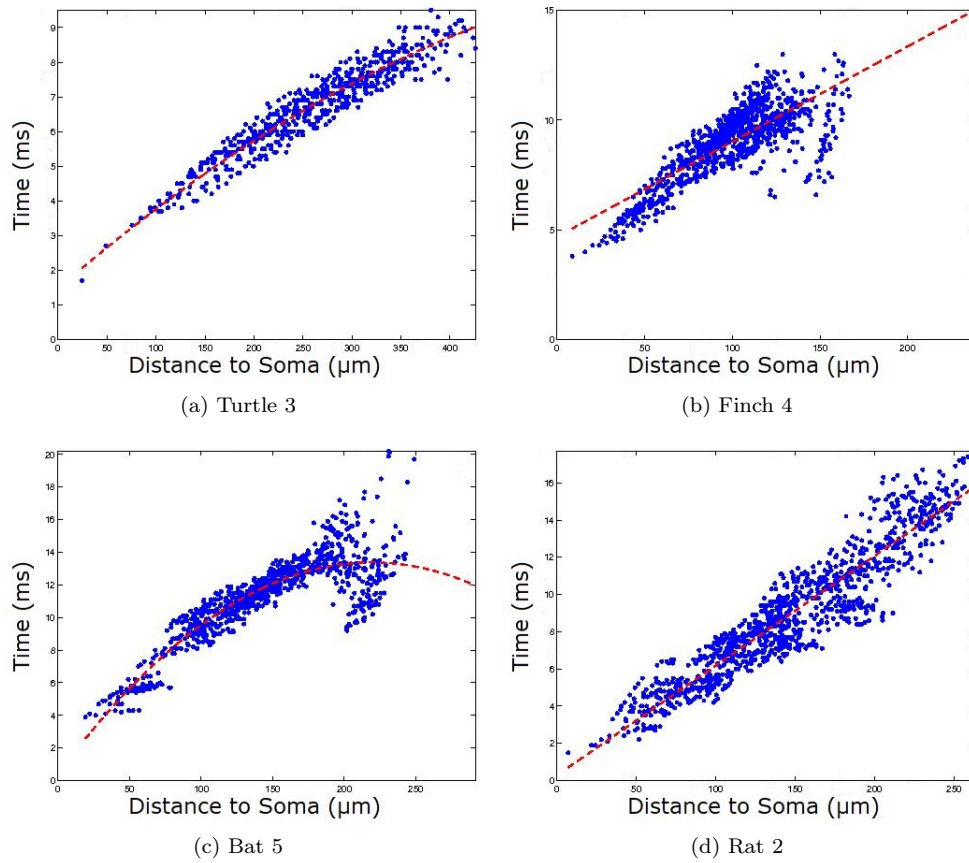
Figure E.4: Time to reach peak amplitude recorded at dendritic compartments following stimulation at the soma in passive models without spines. Corresponding regression coefficients are listed in Table D.2 as: Turtle 3, Finch 4, Bat 5, Rat 2

(a) Turtle 3

(b) Finch 4

(c) Bat 5

(d) Rat 2
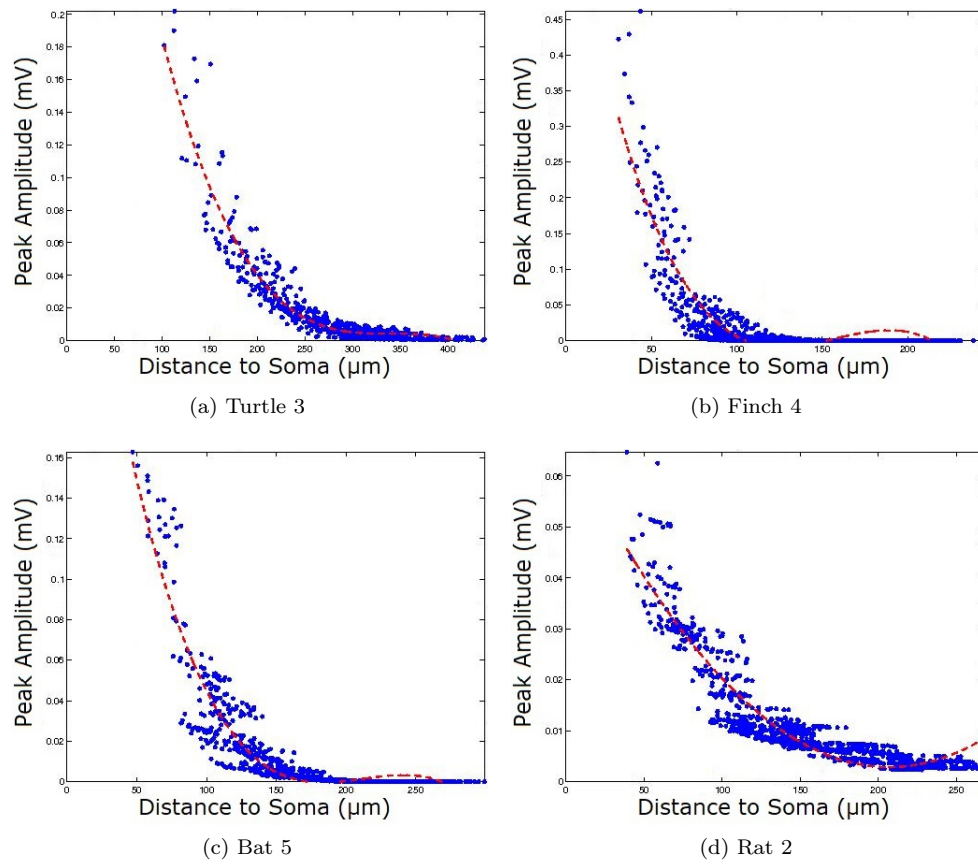
Figure E.5: Peak amplitude recorded at soma following stimulation at each dendritic spine compartment in passive models. Corresponding regression coefficients are listed in Table D.3 as: Turtle 3, Finch 4, Bat 5, Rat 2

(a) Turtle 3

(b) Finch 4

(c) Bat 5

(d) Rat 2
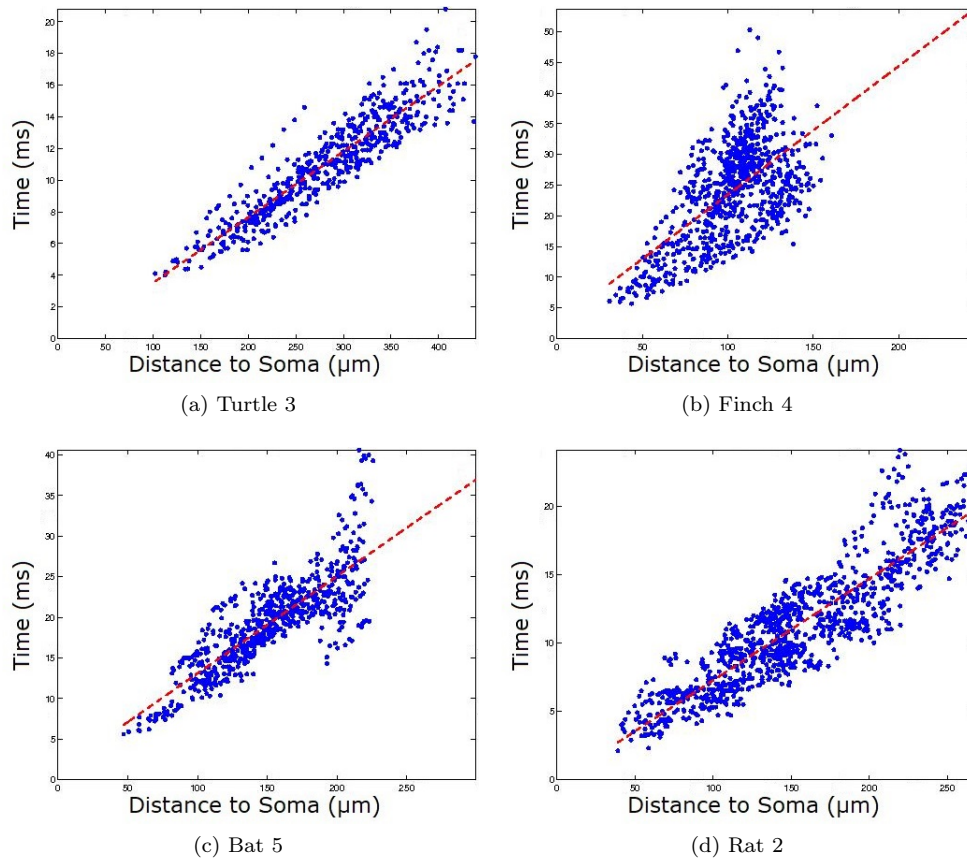
Figure E.6: Time to reach peak amplitude recorded at soma following stimulation at each dendritic spine compartment in passive models. Corresponding regression coefficients are listed in Table D.3 as: Turtle 3, Finch 4, Bat 5, Rat 2

(a) Turtle 3

(b) Finch 4

(c) Bat 5

(d) Rat 2
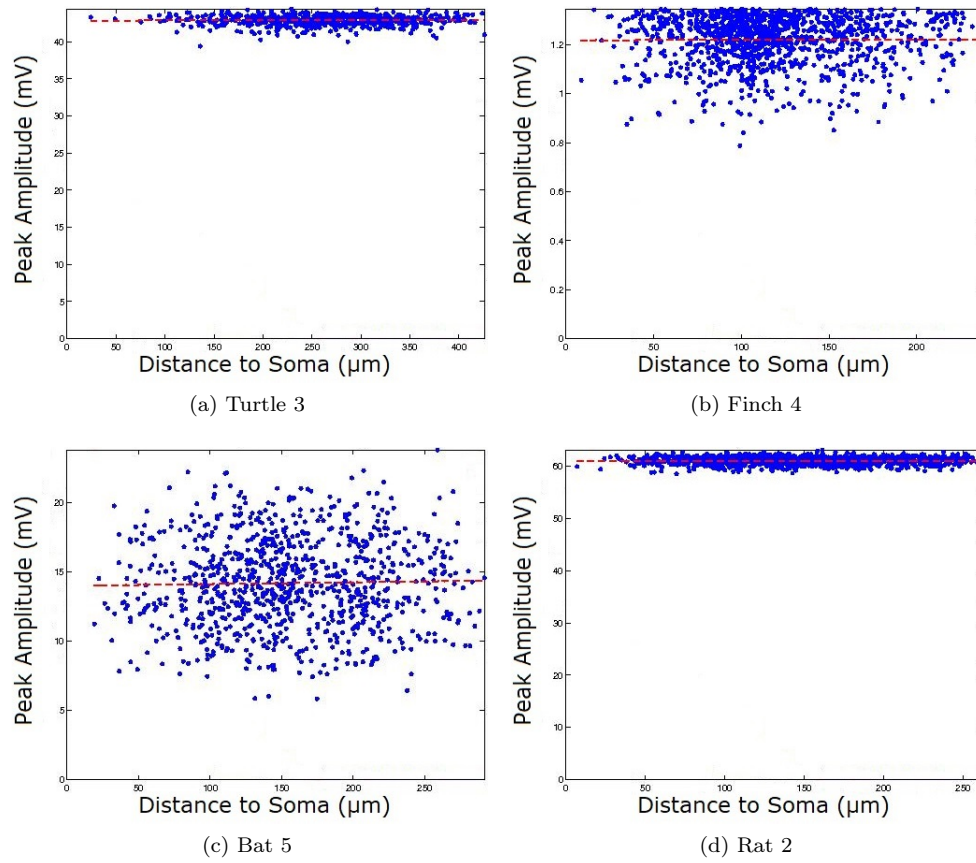
Figure E.7: Peak amplitude recorded at soma following stimulation at each dendritic compartment in active models without spines. Corresponding regression coefficients are listed in Table D.4 as: Turtle 3, Finch 4, Bat 5, Rat 2

(a) Turtle 3

(b) Finch 4

(c) Bat 5

(d) Rat 2
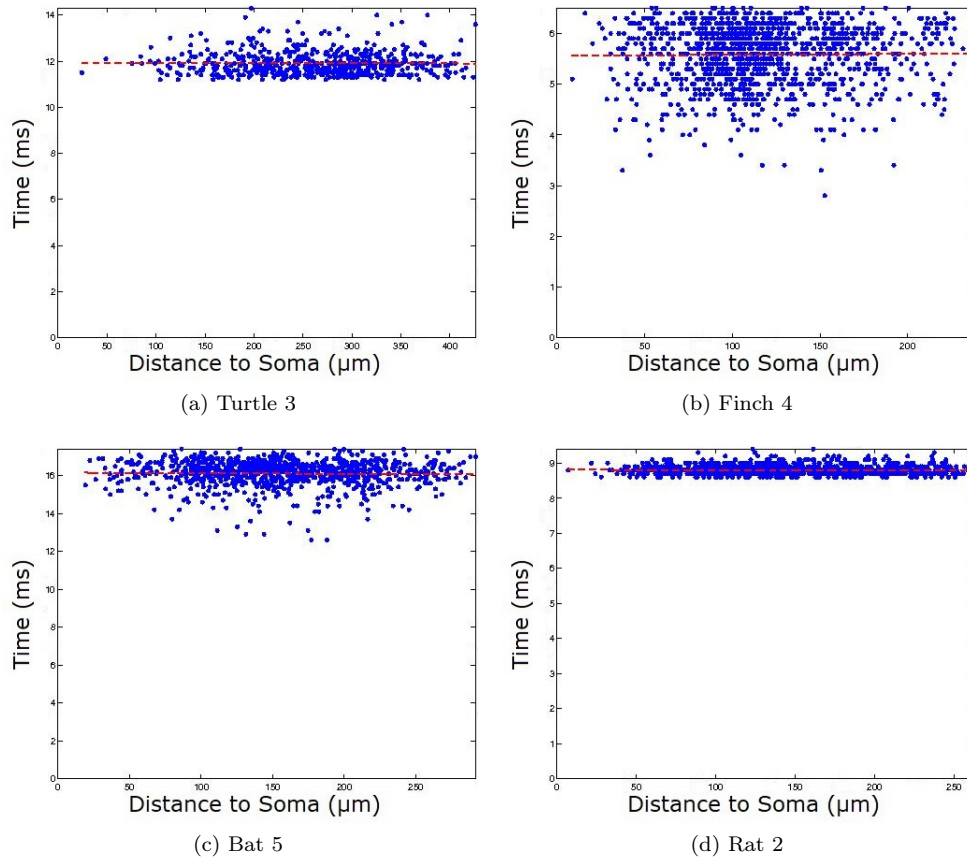
Figure E.8: Time to reach peak amplitude recorded at soma following stimulation at each dendritic compartment in active models without spines. Corresponding regression coefficients are listed in Table D.4 as: Turtle 3, Finch 4, Bat 5, Rat 2

(a) Turtle 3

(b) Finch 4

(c) Bat 5

(d) Rat 2
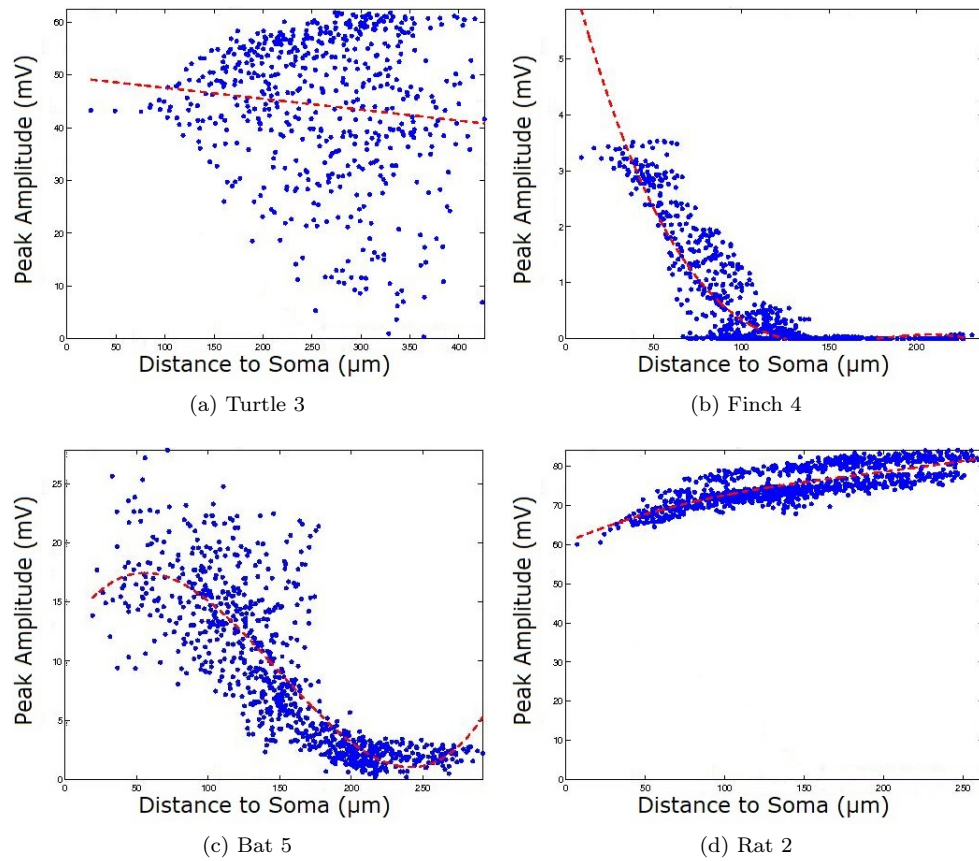
Figure E.9: Peak amplitude recorded at dendritic compartments following stimulation at the soma in active models without spines. Corresponding regression coefficients are listed in Table D.5 as: Turtle 3, Finch 4, Bat 5, Rat 2

(a) Turtle 3

(b) Finch 4

(c) Bat 5

(d) Rat 2
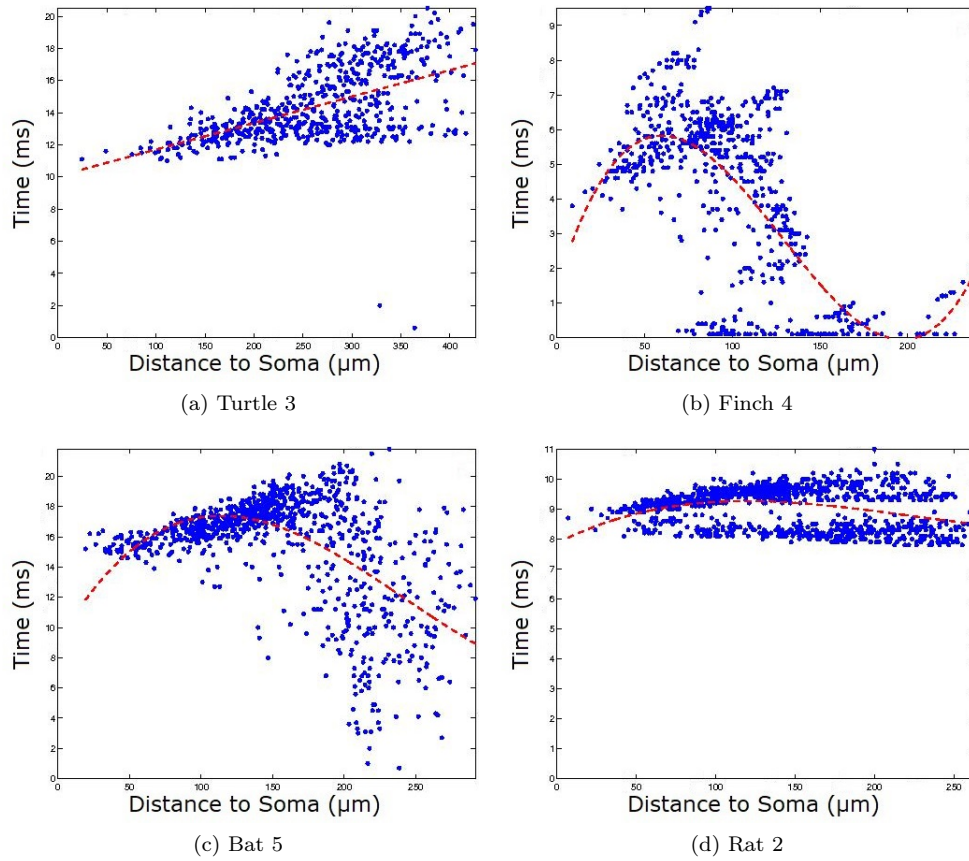
Figure E.10: Time to reach peak amplitude recorded at dendritic compartments following stimulation at the soma in active models without spines. Corresponding regression coefficients are listed in Table D.5 as: Turtle 3, Finch 4, Bat 5, Rat 2

(a) Turtle 3

(b) Finch 4

(c) Bat 5

(d) Rat 2
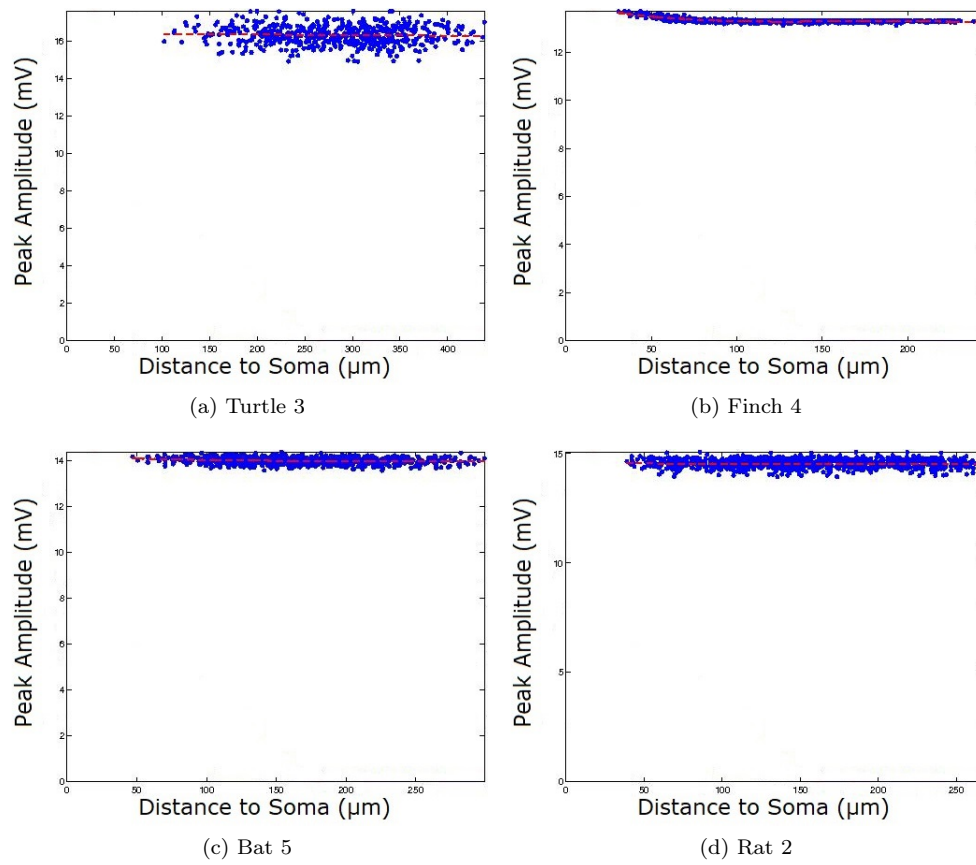
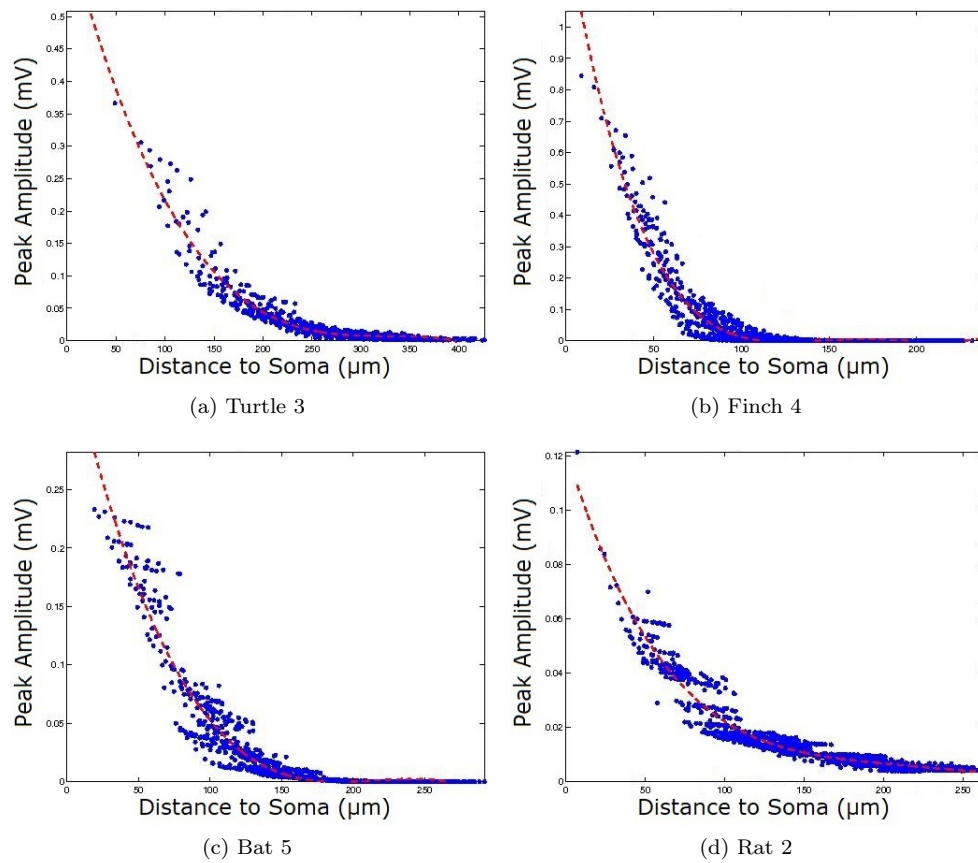Figure E.11: Peak amplitude recorded at soma following stimulation at each dendritic spine compartment in active models. Corresponding regression coefficients are listed in Table D.6 as: Turtle 3, Finch 4, Bat 5, Rat 2

(a) Turtle 3

(b) Finch 4

(c) Bat 5

(d) Rat 2
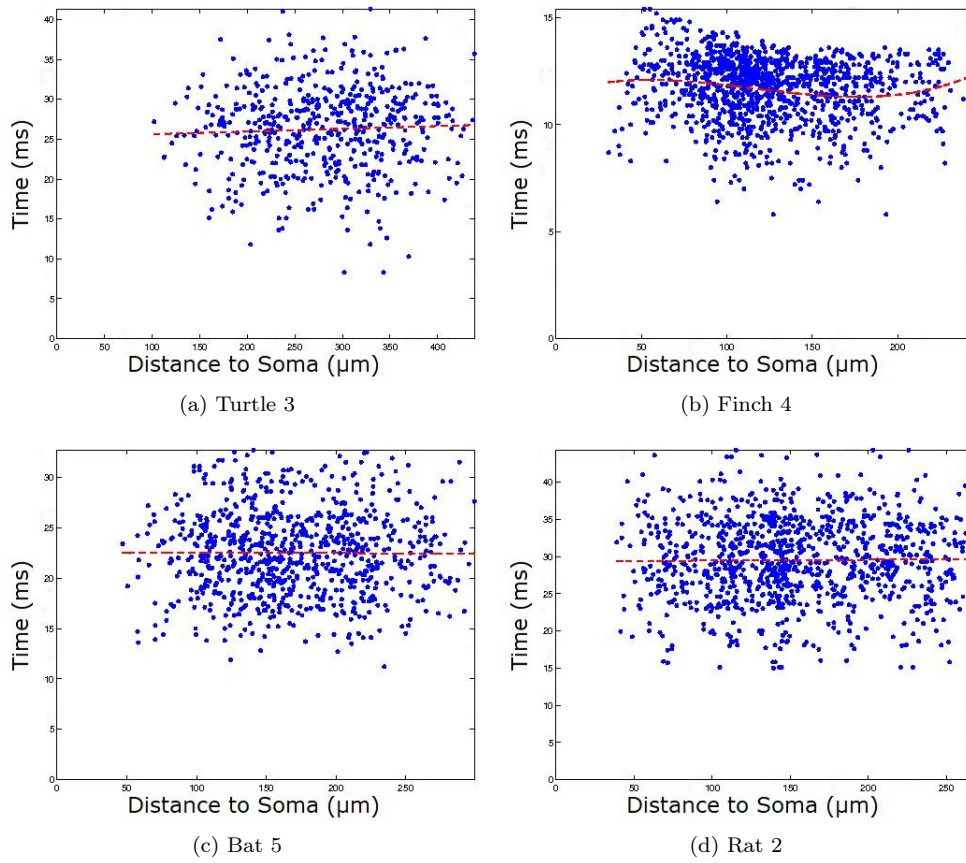
Figure E.12: Time to reach peak amplitude recorded at soma following stimulation at each dendritic spine compartment in active models. Corresponding regression coefficients are listed in Table D.6 as: Turtle 3, Finch 4, Bat 5, Rat 2

Appendix F

Correlation Matrices

Full correlation matrices for the passive and active electrophysiological feature vectors. The morphological correlation matrix is given in Section 6.4.

	AFS2T	AFD2S	AFS2D	AvPS	AvPST	AvPD	AvPT	AvTS	AvTST	AvTD	AvTT	AvPSSp	AvTSSp
AFT2S	0.389	-0.178	-0.326	0.129	0.088	0.183	0.110	-0.291	-0.405	-0.499	-0.404	0.087	0.253
AFS2T	-	-0.046	-0.553	0.048	-0.172	0.043	-0.121	-0.376	-0.208	-0.305	-0.191	0.040	-0.309
AFD2S		-	0.757	-0.979	-0.891	-0.977	-0.924	0.348	0.516	0.536	0.520	-0.951	-0.413
AFS2D			-	-0.740	-0.554	-0.753	-0.627	0.478	0.506	0.538	0.502	-0.699	-0.092
AvPS				-	0.875	0.958	0.901	-0.409	-0.541	-0.552	-0.545	0.967	0.366
AvPST					-	0.870	0.990	-0.177	-0.458	-0.456	-0.467	0.877	0.679
AvPD						-	0.917	-0.300	-0.494	-0.511	-0.502	0.911	0.443
AvPT							-	-0.184	-0.453	-0.451	-0.462	0.887	0.639
AvTS								-	0.899	0.872	0.889	-0.480	0.327
AvTST									-	0.969	0.999	-0.612	-0.047
AvTD										-	0.967	-0.613	-0.076
AvTT											-	-0.614	-0.068
AvPSSp												-	0.344

Table F.1: Correlation matrix for the passive electrophysiological features. KEY: AFT2S: Attenuation factor terminal compartments → soma; AFS2T: Attenuation factor soma → terminal compartments; AFD2S: Attenuation factor dendritic compartments →soma; AFS2D: Attenuation factor soma → dendritic compartments; AvPS: Average peak amplitude at soma (stimulation at dendritic compartments); AvPST: Average peak amplitude at soma (stimulation at terminal compartments); AvPD: Average peak amplitude in dendritic compartments (stimulation at soma); AvPT: Average peak amplitude in terminal compartments; AvTS: Average time to reach peak amplitude at soma (stimulation at dendritic compartments); AvTST: Average time to reach peak amplitude at soma (stimulation at terminal compartments); AvTD: Average time to reach peak amplitude in dendritic compartments; AvTT: Average time to reach peak amplitude in terminal compartments; AvPSSp: Average peak amplitude at soma (stimulation at spinal compartments); AvTSSp: Average time to reach peak amplitude at soma (stimulation at spinal compartments)

	AFS2T	AFD2S	AFS2D	AvPS	AvPST	AvPD	AvPT	AvTS	AvTST	AvTD	AvTT	AvPSSp	AvTSSp
AFT2S	-0.662	-0.008	0.016	0.936	0.933	0.955	0.957	0.116	0.114	0.443	0.502	0.557	0.918
AFS2T	-	-0.109	-0.030	-0.544	-0.538	-0.496	-0.499	-0.633	-0.632	-0.685	-0.686	-0.354	-0.732
AFD2S		-	0.086	0.218	0.201	0.019	0.021	0.228	0.227	0.318	0.268	0.007	0.105
AFS2D			-	-0.013	-0.114	-0.049	-0.049	0.092	0.093	0.142	-0.165	-0.677	-0.069
AvPS				-	0.994	0.974	0.975	0.069	0.066	0.392	0.451	0.523	0.926
AvPST					-	0.973	0.975	0.057	0.054	0.377	0.471	0.606	0.927
AvPD						-	1.000	-0.057	-0.060	0.263	0.340	0.531	0.898
AvPT							-	-0.053	-0.055	0.269	0.348	0.540	0.900
AvTS								-	1.000	0.859	0.795	0.092	0.354
AvTST									-	0.859	0.794	0.090	0.352
AvTD										-	0.940	0.284	0.572
AvTT											-	0.574	0.643
AvPSSp												-	0.579

Table F.2: Correlation matrix for the active electrophysiological features. KEY: AFT2S: Attenuation factor terminal compartments → soma; AFS2T: Attenuation factor soma → terminal compartments; AFD2S: Attenuation factor dendritic compartments →soma; AFS2D: Attenuation factor soma → dendritic compartments; AvPS: Average peak amplitude at soma (stimulation at dendritic compartments); AvPST: Average peak amplitude at soma (stimulation at terminal compartments); AvPD: Average peak amplitude in dendritic compartments (stimulation at soma); AvPT: Average peak amplitude in terminal compartments; AvTS: Average time to reach peak amplitude at soma (stimulation at dendritic compartments); AvTST: Average time to reach peak amplitude at soma (stimulation at terminal compartments); AvTD: Average time to reach peak amplitude in dendritic compartments; AvTT: Average time to reach peak amplitude in terminal compartments; AvPSSp: Average peak amplitude at soma (stimulation at spinal compartments); AvTSSp: Average time to reach peak amplitude at soma (stimulation at spinal compartments)

Appendix G

Principal Component Analysis Factor Loadings

Factor loadings from principal component analysis on the three feature vectors listed in Appendix B. The results of this analysis are given in Section 6.4, and discussed in Section 6.5.

	PC1	PC2	PC3	PC4	PC5	PC6	PC7	PC8
NC	0.363	-0.063	-0.106	0.178	-0.348	0.044	0.077	0.010
NSp	0.364	-0.051	-0.107	0.182	-0.342	0.049	0.091	-0.016
BP	0.374	-0.012	-0.205	-0.026	-0.098	-0.168	0.042	0.121
TP	0.365	0.010	-0.239	-0.060	-0.130	-0.196	0.039	0.106
MaxBO	0.257	-0.303	0.154	-0.184	0.199	-0.122	0.176	0.277
TotLen	0.197	0.356	0.089	0.277	-0.241	0.210	-0.080	-0.130
TotSA	0.127	0.442	0.038	0.014	0.091	0.058	-0.222	-0.027
TotVol	0.130	0.418	0.216	-0.104	0.076	-0.068	0.067	-0.162
SomRad	-0.008	0.273	0.440	-0.198	-0.168	-0.183	0..658	-0.158
AvDCRad	0.011	0.445	-0.022	-0.056	0.040	-0.152	-0.416	0.243
MaxPL	0.254	-0.151	0.449	0.106	0.174	0.212	-0.150	0.176
AvPL	0.275	-0.077	0.444	0.046	0.159	0.298	-0.099	0.222
AvTA	-0.191	0.249	-0.271	-0.057	-0.046	0.569	0.382	0.577
H-S	0.264	0.022	-0.294	0.058	0.522	0.390	0.190	-0.521
MaxBR	-0.082	0.101	-0.017	0.785	0.346	-0.362	0.257	0.215
AvDCElecLen	-0.268	-0.177	0.213	0.362	-0.378	0.254	-0.069	-0.196
Var %	*39.422*	*27.338*	*12.237*	*7.155*	*4.573*	*3.618*	*2.880*	*1.783*
Cum. Var %	*39.422*	*66.760*	*78.997*	*86.152*	*90.725*	*94.344*	*97.224*	*99.007*

(a) First eight PCA factor loadings

	PC9	PC10	PC11	PC12	PC13	PC14	PC15	PC16
NC	-0.095	0.018	0.178	-0.041	0.372	-0.029	0.154	0.698
NSp	-0.159	-0.046	0.189	-0.043	0.277	-0.218	0.133	-0.697
BP	-0.134	0.035	-0.232	0.130	-0.489	-0.516	-0.396	0.110
TP	-0.041	0.274	-0.240	0.078	-0.245	0.703	0.188	-0.096
MaxBO	0.543	0.223	-0.211	-0.376	0.268	-0.125	-0.053	-0.043
TotLen	0.585	-0.302	0.087	-0.112	-0.182	0.197	-0.314	-0.016
TotSA	0.189	-0.005	-0.392	0.141	-0.006	-0.316	0.644	0.024
TotVol	-0.240	0.078	-0.376	0.173	0.513	0.109	-0.446	-0.032
SomRad	-0.031	0.121	0.221	-0.074	-0.256	-0.061	0.180	0.030
AvDCRad	-0.120	0.443	0.401	-0.398	-0.024	-0.057	-0.089	-0.006
MaxPL	0..092	0.299	0.302	0.615	-0.051	0.016	-0.030	-0.019
AvPL	-0.432	-0.345	-0.158	-0.405	-0.179	0.120	0.069	0.026
AvTA	-0.010	0.084	-0.052	0.079	0.038	0.005	-0.047	-0.010
H-S	-0.041	0.242	0.121	-0.162	-0.075	-0.019	-0.004	0.015
MaxBR	-0.045	-0.020	-0.025	-0.006	0.019	0.017	0.019	0.001
AvDCElecLen	-0.044	0.538	-0.363	-0.177	-0.101	-0.061	-0.044	-0.008
Var %	*0.337*	*0.245*	*0.212*	*0.149*	*0.027*	*0.016*	*0.006*	*0.002*
Cum. Var %	*99.344*	*99.589*	*99.810*	*99.494*	*99.977*	*99.992*	*99.999*	*100.000*

(b) Second eight PCA factor loadings

Table G.1: Factor loadings from the principal component analysis of the morphological feature vector.

	PC1	PC2	PC3	PC4	PC5	PC6	PC7
AFT2S	0.117	-0.225	0.133	0.739	0.539	0.069	-0.213
AFS2T	0.057	-0.340	0.650	0.092	-0.493	0.364	0.128
AFD2S	-0.328	-0.165	-0.124	0.092	-0.244	-0.115	-0.107
AFS2D	-0.276	0.072	-0.487	0.059	0.032	0.702	0.206
AvPSom	0.328	0.143	0.097	-0.158	0.210	0.273	-0.036
AvPSomT	0.302	0.274	-0.089	0.040	-0.234	-0.003	-0.334
AvPDen	0.321	0.177	0.138	-0.059	0.233	-0.057	0.679
AvPTer	0.309	0.267	-0.013	0.023	-0.134	-0.150	-0.150
AvTSom	-0.213	0.426	0.157	0.204	-0.017	-0.098	0.319
AvTSomT	-0.275	0.304	0.295	-0.018	0.118	0.157	-0.099
AvTDen	-0.279	0.311	0.207	-0.101	0.104	-0.126	-0.245
AvTTer	-0.276	0.295	0.305	-0.027	0.120	0.187	-0.150
AvPSomSp	0.331	0.109	0.011	-0.195	0.038	0.412	-0.298
AvTSomSp	0.133	0.365	-0.154	0.559	-0.441	0.041	0.072
Var %	*57.255*	*21.151*	*8.911*	*8.194*	*2.154*	*0.959*	*0.497*
Cum. Var %	*57.255*	*78.406*	*87.317*	*95.510*	*97.665*	*98.623*	*99.120*

(a) First seven PCA factor loadings

	PC8	PC9	PC10	PC11	PC12	PC13	PC14
AFT2S	-0.108	0.081	0.081	0.054	0.050	0.028	0.020
AFS2T	-0.124	0.183	0.067	-0.017	-0.065	-0.005	0.010
AFD2S	0.073	0.129	-0.005	0.709	0.478	0.057	0.018
AFS2D	-0.236	0.282	0.042	-0.072	0.000	-0.024	0.005
AvPSom	0.254	0.209	-0.457	0.512	-0.348	-0.127	-0.046
AvPSomT	-0.410	0.080	-0.116	0.050	-0.043	0.643	0.228
AvPDen	0.054	0.201	0.094	0.032	0.444	0.266	0.059
AvPTer	-0.434	0.285	-0.023	-0.037	0.284	-0.623	-0.172
AvTSom	-0.332	-0.304	0.287	0.389	-0.390	-0.078	-0.039
AvTSomT	0.021	-0.165	-0.262	-0.100	0.256	-0.202	0.695
AvTDen	0.251	0.644	0.414	-0.072	-0.155	0.088	0.013
AvTTer	-0.037	-0.170	-0.281	-0.108	0.278	0.219	-0.652
AvPSomSp	0.183	-0.357	0.590	0.152	0.213	-0.054	-0.009
AvTSomSp	0.529	-0.036	-0.078	-0.142	0.016	-0.041	-0.043
Var %	*0.394*	*0.186*	*0.152*	*0.075*	*0.066*	*0.005*	*0.002*
Cum. Var %	*99.514*	*99.701*	*99.852*	*99.928*	*99.993*	*99.998*	*100.00*

(b) Second seven PCA factor loadings

Table G.2: Factor loadings from the principal component analysis of the passive electrophysiological feature vector.

	PC1	PC2	PC3	PC4	PC5	PC6	PC7
AFT2S	0.340	-0.158	0.106	-0.140	0.034	-0.254	-0.158
AFS2T	-0.284	-0.190	-0.055	0.218	0.750	0.448	0.093
AFD2S	0.069	0.145	0.136	0.926	-0.200	-0.090	0.048
AFS2D	-0.035	0.091	0.758	-0.098	0.284	-0.343	0.433
AvPSom	0.336	-0.185	0.131	0.129	0.029	0.172	-0.022
AvPSomT	0.338	-0.194	0.046	0.132	0.024	0.150	0.006
AvPDen	0.318	-0.258	0.103	-0.035	0.023	0.143	-0.066
AvPTer	0.320	-0.256	0.099	-0.033	0.035	0.125	-0.027
AvTSom	0.152	0.480	-0.008	-0.095	-0.057	0.321	0.231
AvTSomT	0.151	0.481	-0.008	-0.096	-0.055	0.318	0.231
AvTDen	0.248	0.371	0.052	0.022	0.374	-0.158	-0.453
AvTTer	0.276	0.309	-0.193	0.038	0.344	-0.178	-0.222
AvPSomSp	0.235	-0.093	-0.558	0.060	0.200	-0.420	0.586
AvTSomSp	0.359	-0.046	0.041	-0.070	-0.082	0.290	0.257
Var %	*52.734*	*24.511*	*11.013*	*7.058*	*2.390*	*1.460*	*0.608*
Cum. Var %	*52.734*	*77.244*	*88.257*	*95.315*	*97.704*	*99.164*	*99.772*

(a) First seven PCA factor loadings

	PC8	PC9	PC10	PC11	PC12	PC13	PC14
AFT2S	-0.584	0.531	-0.298	-0.163	0.010	0.009	-0.018
AFS2T	-0.152	0.184	-0.044	-0.033	0.007	0.000	0.000
AFD2S	-0.089	0.166	0.076	0.072	0.014	-0.008	-0.006
AFS2D	0.071	-0.090	-0.020	0.076	-0.011	0.000	0.023
AvPSom	0.065	-0.365	-0.208	-0.387	-0.338	-0.015	-0.586
AvPSomT	0.039	-0.379	-0.407	-0.105	0.269	0.076	0.637
AvPDen	-0.147	-0.045	0.451	0.344	-0.600	0.032	0.295
AvPTer	-0.130	-0.123	0.383	0.282	0.660	-0.086	-0.321
AvTSom	-0.277	-0.061	-0.007	-0.049	-0.034	-0.698	0.076
AvTSomT	-0.270	-0.041	0.040	0.008	0.034	0.705	-0.067
AvTDen	0.193	0.017	0.404	-0.447	0.079	0.014	0.148
AvTTer	0.162	-0.062	-0.383	0.615	-0.081	-0.026	-0.167
AvPSomSp	-0.038	-0.079	0.175	-0.149	-0.024	0.003	0.012
AvTSomSp	0.604	0.582	-0.045	-0.022	0.023	-0.008	0.007
Var %	*0.145*	*0.058*	*0.013*	*0.010*	*0.001*	*0.000*	*0.000*
Cum. Var %	*99.918*	*99.976*	*99.989*	*99.999*	*100.00*	*100.000*	*100.000*

(b) Second seven PCA factor loadings

Table G.3: Factor loadings from the principal component analysis of the active electrophysiological feature vector.

Appendix H

Principal Components Averaged Over Species

Significant principal components for the three feature vectors averaged over species groups.
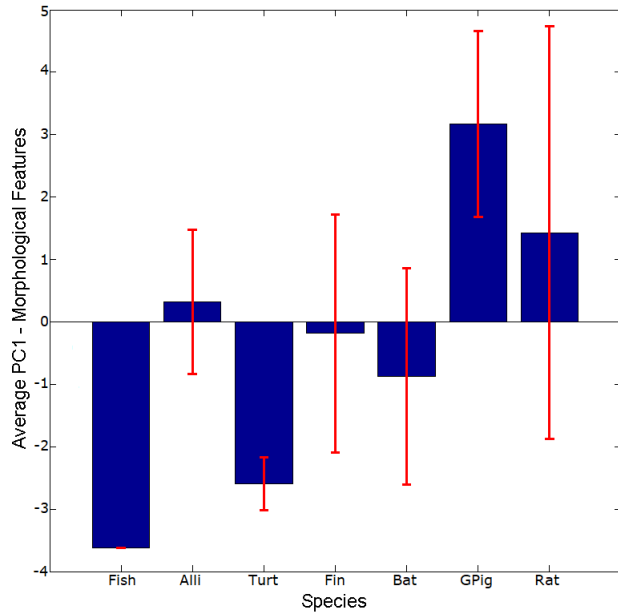
(a) First principal component
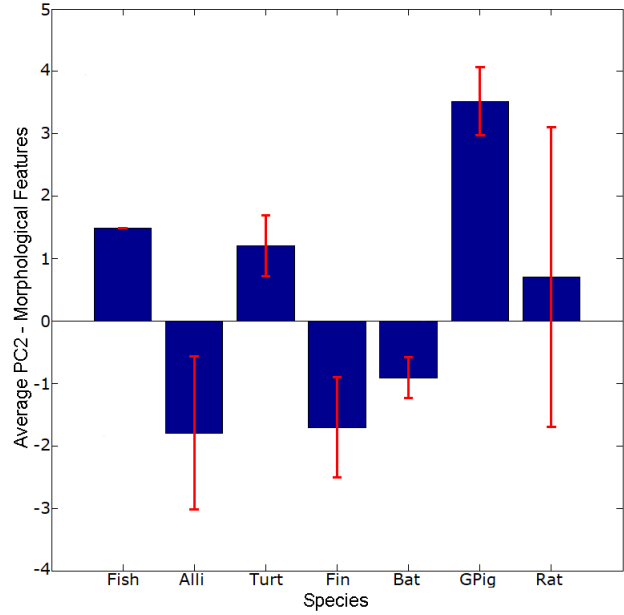
(b) Second principal component
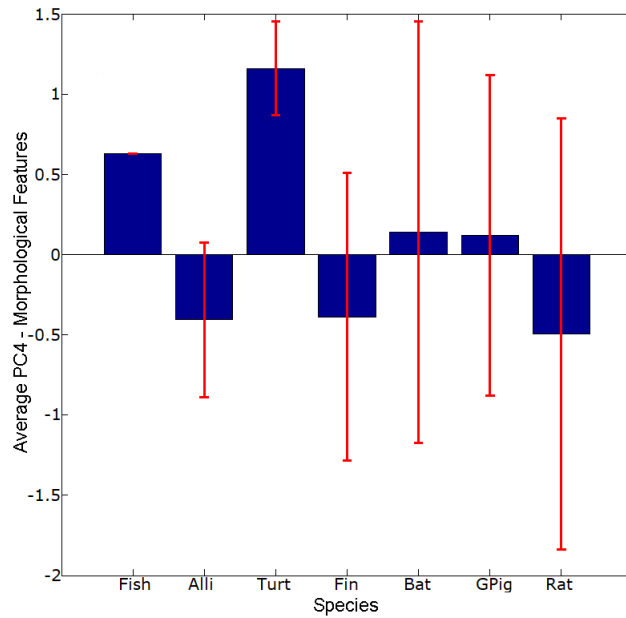
(c) Fourth principal component

Figure H.1: The first, second, and fourth morphological principal components averaged over species groups with 95% confidence interval

(a) First principal component
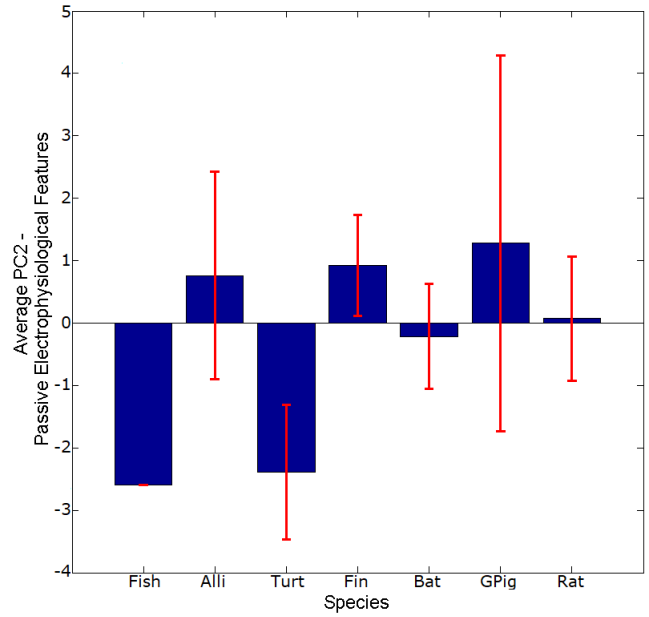
(b) Second principal component
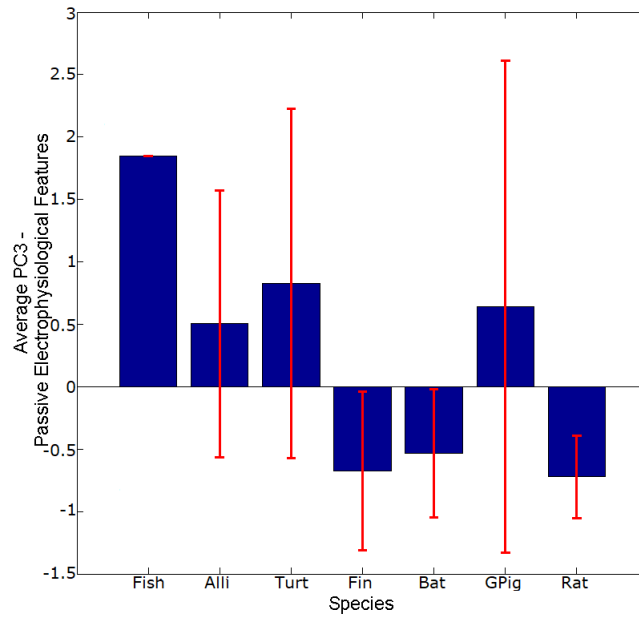
(c) Third principal component

Figure H.2: The first to third passive electrophysiological principal components averaged over species groups with 95% confidence interval

(a) First principal component

(b) Second principal component

(c) Third principal component

Figure H.3: The first to third active electrophysiological principal components averaged over species groups with 95% confidence interval

Appendix I

Maximum Transfer Entropy, Delays, and Regression Coefficients

Maximum transfer entropy and corresponding delays from example models from each species, as well as regression coefficients for trend lines, including those for the fish cell given in Figure 7.3 and 7.4.

Cell	Number inputs	Average maximum TE (nats)	Slope	Intercept	R^2
Fish	1	0.026	[0.033]	0.057	0.997
	20	0.039			
	50	0.066			
	100	0.100			
Alligator 1	1	0.013	[-0.014, 0.043]	0.065	0.971
	20	0.033			
	50	0.075			
	100	0.096			
Turtle 3	1	0.016	[0.009, 0.028]	0.034	0.996
	20	0.020			
	50	0.040			
	100	0.087			
Finch 4	1	0.015	[0.004, 0.003]	0.014	0.972
	20	0.014			
	50	0.014			
	100	0.026			
Bat 5	1	0.010	[0.000, -0.004, 0.000, 0.005]	0.011	1.000
	20	0.010			
	50	0.012			
	100	0.011			
Guinea pig 2	1	0.006	[0.042]	0.040	0.985
	20	0.012			
	50	0.046			
	100	0.098			
Rat 1	1	0.014	[0.014]	0.027	0.994
	20	0.018			
	50	0.030			
	100	0.044			

Table I.1: Average maximum transfer entropy (nats) when measuring input from distal spine groups

Cell	Number inputs	Average delay (ms)	Slope	Intercept	R^2
Fish	1	23.88	[10.203, -13.112]	0.008	0.855
	20	6.42			
	50	0.16			
	100	0.18			
Alligator 1	1	31.10	[14.870, -16.380]	-3.062	0.445
	20	0.78			
	50	0.14			
	100	0.34			
Turtle 3	1	24.14	[13.402, -20.639, 0.000, 5.816]	-0.630	1.000
	20	0.36			
	50	0.26			
	100	0.40			
Finch 4	1	21.50	[-8.812, -6.252]	23.999	0.995
	20	25.46			
	50	22.32			
	100	0.28			
Bat 5	1	27.28	[-12.635, -0.859]	37.661	0.977
	20	33.38			
	50	37.92			
	100	14.16			
Guinea pig 2	1	17.36	[7.645, -9.200]	-0.649	0.620
	20	2.36			
	50	0.48			
	100	0.14			
Rat 1	1	15.90	[3.827, -8.154]	4.880	0.973
	20	11.14			
	50	3.06			
	100	0.90			

Table I.2: Average delay (ms) to reach maximum transfer entropy when measuring from distal spine groups

Cell	Number inputs	Average maximum TE (nats)	Slope	Intercept	R^2
Fish	1	0.025	[0.040]	0.065	0.997
	20	0.042			
	50	0.075			
	100	0.117			
Alligator 1	1	0.014	[-0.007, 0.020]	0.037	0.950
	20	0.022			
	50	0.042			
	100	0.052			
Turtle 3	1	0.016	[0.016, 0.019]	0.021	0.989
	20	0.017			
	50	0.023			
	100	0.075			
Finch 4	1	0.015	[0.005]	0.020	0.949
	20	0.017			
	50	0.023			
	100	0.026			
Bat 5	1	0.009	[0.012, 0.015]	0.013	0.986
	20	0.011			
	50	0.015			
	100	0.055			
Guinea pig 2	1	0.006	[0.062]	0.064	0.981
	20	0.023			
	50	0.086			
	100	0.143			
Rat 1	1	0.014	[0.031]	0.043	0.993
	20	0.025			
	50	0.052			
	100	0.082			

Table I.3: Average maximum transfer entropy (nats) when measuring input from medial spine groups

Cell	Number inputs	Average delay (ms)	Slope	Intercept	R^2
Fish	1	19.06	[7.816, -10.601]	0.698	0.946
	20	6.84			
	50	0.14			
	100	0.20			
Alligator 1	1	17.62	[9.820, -15.381, 0.000, 4.624]	-0.412	1.000
	20	0.16			
	50	0.30			
	100	0.22			
Turtle 3	1	25.26	[-11.229]	15.41	0.992
	20	22.68			
	50	13.36			
	100	0.34			
Finch 4	1	27.16	[14.680, -22.149, 0.000, 5.507]	-0.392	1.000
	20	1.08			
	50	0.44			
	100	0.66			
Bat 5	1	28.08	[9.700, -15.722]	4.100	0.997
	20	15.68			
	50	1.36			
	100	0.38			
Guinea pig 2	1	22.92	[12.759, -19.725, 0.000, 5.575]	-0.693	1.000
	20	0.24			
	50	0.16			
	100	0.16			
Rat 1	1	24.06	[10.887, -12.819]	-1.300	0.610
	20	2.86			
	50	0.34			
	100	0.20			

Table I.4: Average delay (ms) to reach maximum transfer entropy when measuring from medial spine groups

Cell	Number inputs	Average maximum TE (nats)	Slope	Intercept	R^2
Fish	1	0.025	[0.010, 0.035]	0.050	1.000
	20	0.035			
	50	0.056			
	100	0.114			
Alligator 1	1	0.014	[0-0.042, 0.055]	0.114	0.802
	20	0.090			
	50	0.112			
	100	0.115			
Turtle 3	1	0.016	[0.051]	0.058	0.982
	20	0.022			
	50	0.069			
	100	0.125			
Finch 4	1	0.014	[0.006, 0.006]	0.015	0.958
	20	0.015			
	50	0.015			
	100	0.034			
Bat 5	1	0.011	[0.054]	0.069	0.977
	20	0.052			
	50	0.072			
	100	0.142			
Guinea pig 2	1	0.006	[-0.016, 0.077]	0.091	0.977
	20	0.038			
	50	0.109			
	100	0.164			
Rat 1	1	0.014	[-0.015,0.036]	0.060	0.962
	20	0.032			
	50	0.069			
	100	0.082			

Table I.5: Average maximum transfer entropy (nats) when measuring input from proximal spine groups

Cell	Number inputs	Average delay (ms)	Slope	Intercept	R^2
Fish	1	22.56	[8.380, -12.971]	2.555	0.992
	20	12.48			
	50	0.14			
	100	0.18			
Alligator 1	1	6.32	[3.441, -5.346, 0.000, 1.5540]	-0.036	1.000
	20	0.20			
	50	0.20			
	100	0.18			
Turtle 3	1	16.50	[8.811, -13.704, 0.000, 3.861]	0.130	1.000
	20	0.78			
	50	0.72			
	100	0.54			
Finch 4	1	25.58	[-13.358]	18.870	0.821
	20	34.56			
	50	15.08			
	100	0.26			
Bat 5	1	23.62	[13.188, -20.464, 0.000, 5.898]	-0.724	1.000
	20	0.18			
	50	0.18			
	100	0.16			
Guinea pig 2	1	16.26	[9.061, -14.053, 0.000, 4.051]	-0.461	1.000
	20	0.16			
	50	0.16			
	100	0.16			
Rat 1	1	25.10	[14.029, -21.795, 0.000, 6.309]	-0.787	1.000
	20	0.16			
	50	0.18			
	100	0.14			

Table I.6: Average delay (ms) to reach maximum transfer entropy when measuring from proximal spine groups

Cell	Number inputs	Average maximum TE (nats)	Slope	Intercept	R^2
Fish	1	0.026	[0.001, 0.043]	0.067	1.000
	20	0.044			
	50	0.075			
	100	0.126			
Alligator 1	1	0.014	[-0.019, 0.061]	0.090	0.998
	20	0.051			
	50	0.101			
	100	0.138			
Turtle 3	1	0.016	[0.006, 0.031]	0.038	0.982
	20	0.020			
	50	0.045			
	100	0.089			
Finch 4	1	0.014	[-0.004, 0.029]	0.045	0.997
	20	0.027			
	50	0.051			
	100	0.077			
Bat 5	1	0.009	[0.013, 0.057]	0.056	0.0982
	20	0.036			
	50	0.061			
	100	0.156			
Guinea pig 2	1	0.006	[0.055]	0.061	0.989
	20	0.029			
	50	0.079			
	100	0.130			
Rat 1	1	0.014	[0.031]	0.043	0.976
	20	0.021			
	50	0.054			
	100	0.082			

Table I.7: Average maximum transfer entropy (nats) when measuring input from randomly distributed spine groups

Cell	Number inputs	Average delay (ms)	Slope	Intercept	R^2
Fish	1	21.26	[9.253, -11.582]	-0.330	0.799
	20	4.84			
	50	0.16			
	100	0.18			
Alligator 1	1	13.54	[7.487, -11.470, 0.000, 3.201]	-0.289	1.000
	20	0.28			
	50	0.20			
	100	0.36			
Turtle 3	1	25.40	[11.145, -13.496]	-0.628	0.692
	20	4.42			
	50	0.62			
	100	0.48			
Finch 4	1	15.82	[8.751, -13.695, 0.000, 4.054]	-0.303	1.000
	20	0.24			
	50	0.32			
	100	0.20			
Bat 5	1	30.62	[17.060, -26.354, 0.000, 7.431]	-0.957	1.000
	20	0.30			
	50	0.18			
	100	0.20			
Guinea pig 2	1	23.90	[13.348, -20.686, 0.000, 5.935]	-0.749	1.000
	20	0.18			
	50	0.16			
	100	0.16			
Rat 1	1	31.56	[13.914, -16.674]	-1.311	0.587
	20	3.80			
	50	0.96			
	100	0.18			

Table I.8: Average delay (ms) to reach maximum transfer entropy when measuring from randomly distributed spine groups